# Towards Micro-Imaging with Dissolution Dynamic Nuclear Polarisation

By

## Adam P. Gaunt



Thesis submitted to the
University of Nottingham
for the degree of Doctor of Philosophy

April 2018

The hand that rocks the cradle is the hand that rules the world.
*Granny*[1]

---

[1]Otherwise known as Ruth Newton. Original words by the poet William Ross Wallace

# Abstract

Nuclear magnetic resonance (NMR) of small samples and nuclei with a low gyromagnetic ratio is intrinsically insensitive due to the received signal dependence on Boltzmann's statistics. This insensitivity can be partially overcome through the application of hyper-polarisation techniques such as Dissolution Dynamic Nuclear Polarisation (D-DNP). It is hoped that the hyper-polarised $^{13}$C signal received from labelled small molecules could facilitate imaging of metabolic and transporter processes in biological systems. In order to realise this, appropriate molecules and experimental hardware must be used.

A detailed description of the experimental set-up used for carrying out D-DNP is given and the system is characterised. the advantageous use of a dual iso-centre magnet system is elucidated with optimisation of acquisition of fast relaxing molecules. such a system allows for interrogation of processes with short relaxation times, not possible with traditional, stand-alone polarisers.

To acquire the maximum amount of hyper-polarised $^{13}$C signal in an imaging experiment, parallel acquisition techniques have been implemented and the hardware designed with such goals in mind. Multiple coils have been used to allow accelerated image acquisition. As such this work has validated the SENSE algorithm for artefact free, image reconstruction on the micro-scale. These techniques require an array of coils which add to the complexity of the design of the probehead. Decoupling methods and array coil construction must be considered the methods used to ensure well isolated coils, such as geometric decoupling, are presented.

The novel fabrication and implementation of micro-coils for imaging and spectroscopy of nL scale samples is presented this will help facilitate the acquisition of images showing metabolic processes in active transport in cells. By placing the coils close to the sample it is possible to gain sensitivity relative to the mass of the sample in question. To achieve signal detection on the order of nL a novel, flexible micro-coil array has been fabricated and the results of NMR experiments carried out on both protons and $^{13}$C are shown. This is the final stage before integrating the coils with the D-DNP system. The acquisition of $^{13}$C signal with the micro-coils displays optimal electronic characteristics when compared with other detectors presented in the literature.

The final goal of the work is to produce a system that is capable of micro imaging in small biological samples such as the Xenopus Oocyte with a view to monitoring metabolic processes and transportation without the need for the use of the large fluorescing proteins (GFP's) that have been used in previous work (1). The need for GFP's attached to metabolites results in the measured data being non-physical as the fluorescing protein is often much larger than the molecule being transported. It is hoped that the use of hyper-polarised small molecules (such as pyruvic acid) may be able to remove this need for GFP's in the study of metabolite transportation.

# Acknowledgements

A wise woman once said *"You don't need to be clever to do a PhD, you just have to work hard"*.. and my god was she right!

It is difficult to find the necessary words to thank all the appropriate people, however I shall make an attempt at this point.

First of all I would like to acknowledge the IMRCDT and thank my supervisor Dr Walter Köckenberger for giving me the opportunity to do something really interesting and meet some amazing people along the way. I would also like to thank Alexey Potapov and Marcel Utz for agreeing to do my viva and making it a much better experience than was anticipated.

It is important to mention the other members of staff at UoN who have helped with my project regardless of if it was their job to do so. Thanks to Paul Glover for his help with electronics. A huge thank you to Chris Mellor: without your help much of the work in this thesis would not have been possible. Another thank you must go to my friends at NTU (Rob, Ed and Mike to name but a few), a fantastic institution and I can say now that I have really seen the light!

I must thank all my friends in the MR centre as it is you who make it such a fun and happy place to work, you are all too many to mention by name but you have played a large part in my life in the last 4 years which I cherish and will take with me. A special mention needs to go to The Barn back row crew (Simon too) who have had to put up with me and my mess since we moved in. A further mention must go to Sheila who always made me smile first thing in the morning after a cold wet cycle in.

I can not pass up the opportunity to say thank you to Elena K and Elena B. You two have helped to keep me sane, keep me fit, challenging me and also provided me with some very useful and stimulating discussions.

Of course I must thank my (self appointed) therapist, drinking buddy and SEOP expert Fraser Hill-Casey. You have gone above and beyond the call of duty in pursuit of our happiness and shared misery alike.

To all the K-team (past and present) it has been a pleasure to serve along side you all. To Ben Henderson McGeorge, Ed (Brother) Breeds and Dan Wisnewski you have given me some truly unforgeable experiences while con-

ferencing with you.. (although the jury is out on weather all of the experiences can be classed as good). A big thank you goes to Sank and Jim who were around in the early stages of my PhD and taught me how to be an experiential NMR scientist. Thank you to all the later additions to the K-team, Fed, Anto and Tommy (and Jamie briefly), you all deserve a medal for putting up with me.

Finally I must thank my entire family and my amazing partner Charlotte who have all given me nothing but unconditional love, relentless patients and endless support throughout the course of my PhD. As well as this you have provided sage council at various times over the last 4 years to help me face the troubles that come with a PhD. Without you all I certainly would have struggled, I can not express my gratitude enough.

Thank you!

# Contents

# Chapter 1

# Introduction

Nuclear magnetic resonance (NMR) spectroscopy and imaging provide a unique, non-invasive approach to monitoring of systems ranging from medical applications to food stuffs. NMR is used to examine (for example) time varying interactions like protein folding (2), moisture migration in pork pies (3) and most significantly, in vivo clinical diagnostics (4). There are few spectroscopic techniques that give the user such a high level of control over the observed information as NMR spectroscopy. With NMR it is possible to extract useful information about chemical structure, local environment and molecular motion for a given experiment. However the technique suffers from an intrinsic lack of sensitivity when compared with other spectroscopic and imaging techniques meaning often many hours of averaging are required which compromises the time resolution of the experiment (5). One of the reasons that the poor sensitivity arises is because NMR relies on differences in populations of energy levels that occur when nuclear spins experience a magnetic field. These population differences are governed by Boltzmann statistics giving rise to only very small population differences and as such, low levels of detectable signal. Therefore, in order to conduct experiments on small sample volumes techniques to maximise the sensitivity and available signal need to be employed.

One such technique demonstrating the possibility of polarisation transfer, known as dynamic nuclear polarisation (DNP) conducted by Overhauser in the 1950s, in the solid state (6). Taking advantage of the electron polarisation a theoretical enhancement of 660 is achievable for $^1$H nuclear spins, due to the ratio of the gyromagnetic ratio of the electron and proton. This was later expanded into liquid state NMR with a technique known as dissolution dynamic nuclear polarisation (D-DNP) which was initially developed by Ardenkjaer-Larsen *et al* and achieves reported signal enhancements of more than 10000 (7). The limiting factor of this D-DNP is the nuclear relaxation time, $T_1$. Over time the spin system returns to the equilibrium state governed by Boltzmann statistics. Therefore in order to optimise the data acquisition in any hyper-polarised experiment it is important to limit the time required

to carry out the dissolution and measurement.

Often the nature of the D-DNP experiment means that it is not possible to acquire signal from nuclear spins with a short $T_1$ relaxation time due to the sample transfer time from solid to liquid state. However with the dual iso-centre magnet D-DNP system at the University of Nottingham the dissolution and sample transfer is carried out in under a second, which allows the single scan measurement of fast relaxing molecules (8).

The large signal enhancement achieved in D-DNP experiments may open the possibility of observation of small numbers of spins. To optimise the signal acquisition in small samples it is important to place the detector as physically close to the sample as possible. Hoult *et al.* demonstrated that this is the case through the principal of reciprocity (9), showing that the strength of the signal received is directly proportional to the time dependent field produced by that coil. Therefore in order to observe nL sample volumes micro detector coils are beneficial.

It is thought that a combination of micro detectors and hyper-polarisation may elucidate NMR microscopy with a view to imaging of metabolic process and molecular transport in cells. Experiments using other spectroscopic techniques have been carried out to monitor such processes, however they require the attachment of large green fluorescing proteins (GFP) to the metabolites (1) which reduces the biological relevance of the result. By hyper-polarising $^{13}$C on spin labelled small molecules in the dual iso-centre magnet, and using micro-detectors, it is hoped that signal can be detected during these biological processes.

Due to the nature of hyper-polarised signal, it is important that any imaging sequence be optimised for a rapid acquisition. Therefore, sub-Nyquist sampling of $k$-space is employed which requires multiple receivers in order to allow artefact free reconstruction of the images. The hardware needed to achieve has been developed and is presented in this document.

Chapter 2 presents the information required to understand the NMR and imaging experiments presented in later chapters. The basic principals of NMR are presented and some imaging methods are also shown, along with a brief discussion of resolution in MRI.

Chapter 3 presents the basic concepts of hyper-polarisation and DNP and discusses the main polarisation transfer mechanisms in DNP. A general overview of the traditional hardware required for conducting D-DNP experiments is also presented. Chapter 4 shows how the dual iso-centre magnet at the University of Nottingham allows a rapid dissolution compared with traditional, stand alone polariser systems. Experimental results for the characterisation of the system in the solid and liquid state are shown. A series of $^{13}$C experiments on biologically relevant small molecules were carried out and presented in this chapter. This was done in order to determine the $T_1$ relaxation time and the achievable $^{13}$C polarisation of the molecule with a view of use in an

imaging experiment.

Chapter 5 presents parallel imaging and under-sampling such as sensitivity encoding (SENSE) (10). The benefits of under-sampling of $k$-space in terms of acquisition time are demonstrated and results of simulations that were carried out to determine the optimum configuration for a coil array capable of micro imaging are shown. It is demonstrated in this chapter that the SENSE algorithm is not affected by the small FOV as long as the receiver coils have an appropriate geometry. The results of the in chapter 5 simulations were used to determine the design for the prototype micro imaging probe-head. The building of a micro-imaging coil array, including the problems encountered , are presented in chapter 6. This chapter contains the results of imaging experiments carried out to characterise the probe-head and to demonstrate that artefact free reconstruction of under-sampled micron scale resolution images is achievable.

Chapter 7 explains why it is necessary to use small detectors to detect signal from smaller sample volumes. A review of micro-fabricated NMR detectors in current literature is presented. It was decided based on the information given in this chapter that an array of planar micro-coils is the optimum configuration for achieving parallel micro-image. The fabrication and characterisation of the novel, flexible micro-coils designed to be wrapped around the topology of any given sample, is presented in this chapter. The flexibility of the coils maximises the filling factor and allows the coils to be easily positioned about the sample. Experiments demonstrating that the coils are suitable for multiple working frequencies ($^{13}$C and $^{1}$H) are shown and an examination of magnetic susceptibility effects on the detector is given.

Finally, in chapter 8 the conclusions reached in each of the chapters are given. A brief outline of the potential outlook of the project along with the further work to be done in order to achieve the original objectives of micro-imaging of biological processes with hyper-polarised $^{13}$C labelled small molecules.

# Chapter 2

# NMR Theory

## 2.1 Introduction

In this chapter the basic concepts behind NMR will be discussed. Zeeman splitting, the gyromagnetic ratio, population differences and the importance of these to NMR will be explained. Presentation of some typical NMR experiments and pulse sequences will be explained along with some of the interactions that occur within a spin system. Knowledge of these interactions will aid the better understanding of how molecules can be characterised with NMR and how the spin system interacts in order to provide a mechanism of polarisation transfer.

The fundamentals of MRI and acquisition methods, such as FLASH, RARE and EPI will be presented and the feasibility for using these imaging sequences for micro-imaging and their benefits when acquiring hyper-polarised signals will be discussed. The limits on the resolution in MRI will also be presented.

This chapter should enable the reader to understand why the novel hardware presented in the subsequent chapters has been developed as well as presenting the required information to fully understand the physical limitations and constraints upon any NMR microscopy equipment and experiment

## 2.2 Nuclear Spin

The concept of NMR (and MRI) relies entirely on the fact that many nuclei posses an intrinsic property known as nuclear spin. This is the term describing the angular momentum that is innate in many quantum particles. This was first observed by Pauli when looking at emission spectra of alkali metal in the 1920's. However the first measurement of spin was in the Stern-Gerlach experiment (11) which demonstrated how electron spin angular momentum is
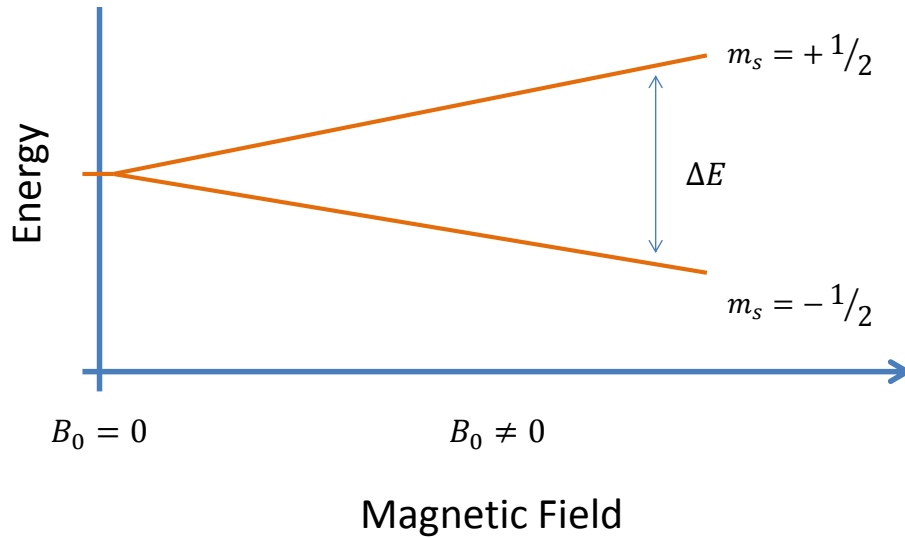
Figure 2.1: Zeeman splitting - the energy level separation increases with magnetic field strength. The levels relate to either spin $|\alpha\rangle$ or spin $|\beta\rangle$ energy states. $\Delta E = E_{+\frac{1}{2}} - E_{-\frac{1}{2}} = h\nu$ is the energy difference between the $+\frac{1}{2}$ and the $-\frac{1}{2}$ spin states.

quantized and is split into $(2I+1)$ energy levels in the presence of a magnetic field gradient, where $I$ is the spin angular momentum quantum number (11). This splitting is known as Zeeman splitting and it is the manipulation of the populations of these different energy levels that allows NMR signal to be acquired.

The phenomena of quantization of the intrinsic angular momentum in atomic particles occurs when there are odd numbers of protons, neutrons, or both. The total spin angular momentum, given by the vector operator $\vec{J}_{tot}$, is described by $\sqrt{I[I+1]}\hbar$, where $I$ denotes the spin quantum number and $\hbar$ is Plank's constant divided by $2\pi$. The value of $I$ that a given nucleus takes is determined by its physical properties. There are three rules which can be used to determine the value:

(1) Nuclei with an odd mass number will have half-integer spin.
(2) Nuclei with even mass number and charge will have zero spin.
(3) Nuclei with even mass number and an odd charge number have integer spin values.

Analogous to angular momentum, spin can also be described with operators which obey the commutation relations:

$$\left[\hat{I}_k, \hat{I}_l\right] = i\varepsilon_{klm}\hat{I}_m, \tag{2.1}$$

for $k, l, m \in [x, y, z]$. $\varepsilon_{klm}$ is the Levi-Civita symbol and the components of the single spin operator $\hat{I}$ are given by:

12

Table 2.1: Typical interaction strengths at high $(> 0.5T)$ magnetic field strengths (12).

| Interaction | Typical frequency range (Hz) |
| --- | --- |
| Scalar coupling | $10^0 - 10^2$ |
| Nuclear dipole coupling | $10^0 - 10^3$ |
| hyperfine coupling[1] | $10^3 - 10^8$ |
| Nuclear Zeeman interaction | $10^8$ |
| Electron Zeeman Interaction | $10^{10}$ |

$$\hat{I}_m = \frac{\hbar}{2}\sigma_m, \tag{2.2}$$

where $m \in [x, y, z]$. When considering spin $1/2$ nuclei the term $\sigma_m$ represents the Pauli matrices, which are split into the three matrices to describe the orthogonal spin operators, these $x, y$ and $z$ Pauli matrices are shown in Equation 2.3.

$$\sigma_x = \begin{pmatrix} 0 & 1 \\ 1 & 0 \end{pmatrix}, \sigma_y = \begin{pmatrix} 0 & -i \\ i & 0 \end{pmatrix}, \sigma_z = \begin{pmatrix} 1 & 0 \\ 0 & -1 \end{pmatrix}. \tag{2.3}$$

Each one of these Hermitian matrices represents the observables in the space which then allows the way that the spin interacts with its environment to be expressed.

## 2.3   Spin Interactions

There are many different interactions that take place within the spin system, which affect the nuclei, and the acquired NMR spectrum in different ways. Table 2.1 gives an example of some of the interactions and the magnitude of the effect they have in the spin system (12).

In order to be able to properly understand how the NMR spectrum is formed and how hyper-polarisation is generated it is important to consider how spins interact with each other as well as with applied magnetic fields.

### 2.3.1   Zeeman Interaction

A static magnetic field applied to the spin system causes a splitting in the energy levels known as Zeeman splitting (13). The Hamiltonian describing

---

[1]This is highly nuclei dependent.

the Zeeman interaction for a magnetic field (conventionally) applied along the $z$-axis is given by:

$$\hat{H} = -\bar{\mu} \cdot \bar{B}. \tag{2.4}$$

The term $\bar{\mu}$ denotes the magnetic moment of a quantum particle, which is proportional to its spin,

$$\bar{\mu} = \gamma \vec{I}, \tag{2.5}$$

where $\gamma$ is the proportionality constant, referred to as the gyromagnetic ratio and $\vec{I}$ is the spin angular momentum. By substitution of Equation 2.5 into Equation 2.4 and considering a magnetic field acting only along $z$, the Hamiltonian describing the Zeeman interaction is found.

$$\hat{H}_z = -\gamma B_0 \hat{I}_z, \tag{2.6}$$

where $I_z$ is the $z$ component of the spin angular momentum operator $\hat{I}$ shown in Equation 2.2 and for a spin $-\frac{1}{2}$ nuclei the operator is given by the Pauli matrix as shown above in Equation 2.3. $B_0$ is the applied magnetic field, which acts along the z-axis. The matrix representation of the Zeeman Hamiltonian is,

$$\hat{H}_z = \begin{pmatrix} -\frac{\hbar}{2}\gamma B_0 & 0 \\ 0 & \frac{\hbar}{2}\gamma B_0 \end{pmatrix}, \tag{2.7}$$

which shows how, from the diagonal elements of the matrix, a spin $\frac{1}{2}$ nuclei can occupy one of two different energy levels, whose energy scales with magnetic field strength.

### 2.3.2 Chemical Shift

The chemical shift is the interaction that gives rise to nuclei having different, distinguishable frequencies along the NMR spectrum and allows characterisation of a molecule based on this information. The change in frequency position is due to the interaction between the nuclei and its local environment (i.e. the electron cloud of surrounding nuclei).

Nuclear or molecular electron clouds interact strongly with the magnetically active nuclei being observed in the NMR experiment, which acts as a form of shielding from the static $B_0$ field and gives the nuclei a "chemical fingerprint" depending on its position in the molecule. This effect was discovered in the 1950's and has been fundamental in characterising the structure of molecules in chemistry ever since (14). Table 2.2 shows the chemical shift positions of some common chemical groups.

Table 2.2: List of $^{13}C$ chemical shift values for different molecular environments (12).

| Molecular Environment | $^{13}C$ Chemical Shift (ppm) |
|---|---|
| $R - CH_3$ | $8 - 35$ |
| $R2 - CH_2$ | $15 - 50$ |
| $R_3CH$ | $20 - 60$ |
| $R_4C$ | $30 - 40$ |
| $C - O$ | $50 - 80$ |
| $C - N$ | $40 - 60$ |

The difference between the methyl $(CH_3)$ group and the highly shifted carbonyl group $(C - O)$ in Table 2.2 is due to the fact that the oxygen reduces the electron density of the carbon site and causes a de-shielding of the $^{13}$C, thus causing the peak from the isochromat to appear further to the left of the spectrum as the frequency increases.

Chemical shift is denoted as a reference from a zero shift position in the spectrum. The zero chemical shift position is given by well shielded molecules such as TMS (Tetramethylsilane). TMS has a high electron density which allows it to be well shielded and causes it to have a chemical shift of $\delta = 0$ ppm, where $\delta$ denotes the relative chemical shift. However TMS is not water soluble so in water other molecules such as sodium salts are used. The chemical shift is often expressed in ppm which is calculated using Equation 2.8. Due to the field dependence it is convenient to measure this in ppm and relative to a fixed (0 ppm) position. This facilitates the comparison of molecular structures that have been analysed at different field strengths.

$$\text{Chemical shift in ppm} = \frac{\delta(\text{Hz}) \times 10^6}{\omega_0/2\pi}. \quad (2.8)$$

The chemical shift is a two step process whereby the applied magnetic field induces currents in the electron cloud of the molecules in the system and then in turn these currents generate their own small magnetic fields (12). The path of the electrons is governed by the shape of the molecule and therefore the field induced by the current around the molecule is dependent on the molecules orientation rather than the applied magnetic field. In liquids the random motion and tumbling of the molecules means that the dependence on molecular orientation is averaged out so only isotropic terms govern the chemical shift position of a molecule in a liquid state NMR spectrum. The fact that the chemical shift is caused by induced molecular currents creating a slight perturbation in the magnetic field means that the chemical shift is field dependent.

The Hamiltonian that describes the chemical shift is the Zeeman Hamiltonian, with a further term added for taking into account the electron's

shielding effect as shown in Equation 2.9.

$$\hat{H}_0 = \hat{H}_{\text{static}} + \hat{H}_{\text{cs}}, \tag{2.9}$$

where $\hat{H}_{\text{static}}$ is the Zeeman Hamiltonian and $\hat{H}_{\text{cs}}$ is the term describing the contribution of the induced magnetic field. This is given by:

$$\hat{H}_{cs} = -\sigma_i \omega_0 \hat{I}_z. \tag{2.10}$$

Due to the motional averaging that the tumbling molecules of a liquid experience, the tensorial shielding effect of the electron cloud is reduced down to only its isotropic components $\sigma_i$. This is found by taking the trace of the diagonal components of the chemical shift tensor (15).

### 2.3.3   J-coupling

Scalar coupling, or **J**-coupling is known as an intra-molecular interaction as it links the nuclear spins in the spin system via the local electrons. **J**-coupling is a short range, intra-molecular interaction that generally only acts through covalently bonded nuclei, it is therefore known as a through-bond interaction.

Two uncoupled spins with different chemical shift values will give rise to two separate peaks in an NMR spectrum. The two spin system will have 4 energy levels but 2 pairs of equivalent coherences, as represented by the blue and orange arrows on the left hand side of Figure 2.2. When **J**-coupling is introduced, it has the effect of shifting the energy levels so that there are now individual distinguishable coherences, which leads to there being 4 individual peaks in the spectrum. This is known as J-splitting and is seen on the right hand side of Figure 2.2.

The Hamiltonian that describes the effect of **J**-coupling on the spin system is given by:

$$\hat{H}_J = 2\pi J_{jk} \hat{I}_j \hat{I}_k \tag{2.11}$$

Where $I_{j,k}$ are the operators describing the interacting spins and $J_{jk}$ is a $3 \times 3$ real matrix containing the coupling values. The factor of $2\pi$ is present in Equation 2.11 because the coupling values are quoted in Hz. The energy levels are shifted by the coupling which results in there being four different coherences between the NMR transition instead of the two available in the uncoupled system (12), as shown in Figure 2.2 and Table 2.3. Coherences correspond to a change in the quantum state of the spin and, in NMR only a change of $\pm 1$ is allowed due to the selection rules.
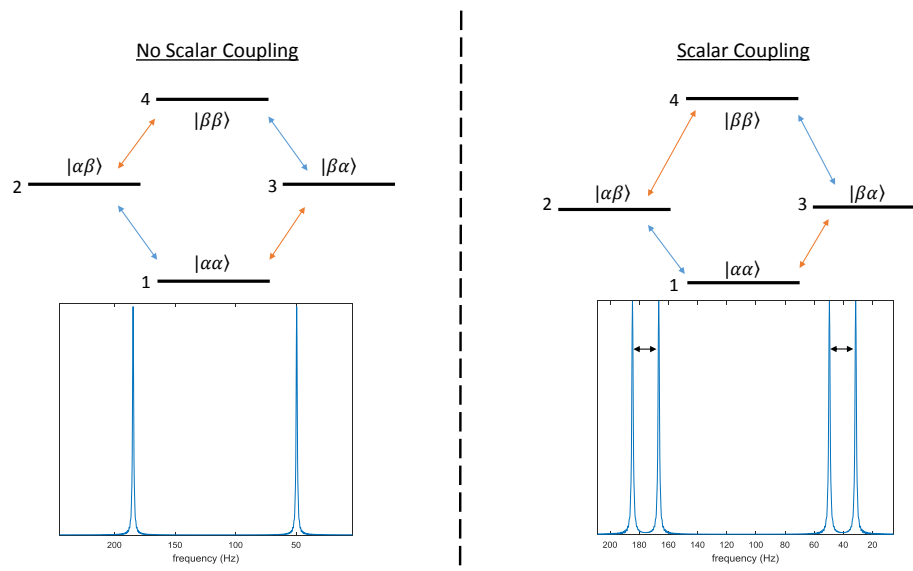
Figure 2.2: The LHS shows the energy level diagram for a two, inequivalent, spin system where there is no scalar coupling between the spins and the spectrum that is produced from the spins. Thee RHS shows the energy level diagram from two inequivalent, coupled spins. The blue and orange arrows represent the different coherences (transitions between the states) and the black arrows represent the J-splitting.

Table 2.3: Energy levels for two coupled spins

| Spin States | Energy | Energy Level Number |
|---|---|---|
| $\alpha\alpha$ | $+\omega_{0,1} + \omega_{0,2} + {}^{1}/_{4}J_{1,2}$ | 1 |
| $\alpha\beta$ | $+\omega_{0,1} - \omega_{0,2} - {}^{1}/_{4}J_{1,2}$ | 2 |
| $\beta\alpha$ | $-\omega_{0,1} + \omega_{0,2} - {}^{1}/_{4}J_{1,2}$ | 3 |
| $\beta\beta$ | $-\omega_{0,1} - \omega_{0,2} + {}^{1}/_{4}J_{1,2}$ | 4 |

In the liquid state the random molecular tumbling causes motional averaging in the system leading to only the isotropic part of the coupling matrix being retained so that $J_{jk} = \frac{1}{3}\left(J_{xx}^{jk} + J_{yy}^{jk} + J_{zz}^{jk}\right)$.

A key point that arises when looking at the energy level terms in Table 2.3 and the Hamiltonian in Equation 2.11, is that unlike the chemical shift, there is no field dependence on the splitting of the energy levels due to the scalar coupling.

## 2.3.4   Dipolar Interaction

The direct dipole-dipole interaction is the direct coupling as a result of the magnetic fields produced by two spins located close to each other and it is that which predominantly drives the spin lattice relaxation process. Dipole-dipole coupling also facilitates the spin diffusion process that allows polarisa-

17

tion transferred from electrons to the nuclear spins in DNP, to then be passed to the bulk nuclei in the solid state (16). For this reason it is a highly important term in the spin system when considering NMR and dynamic nuclear polarisation.

In the solid state, the dipole-dipole interaction causes line broadening in the NMR spectrum, however in the liquid state the motional averaging causes the dipolar interaction to average to zero. For an isotropic liquid the Hamiltonian describing the dipole-dipole interaction is given as $\hat{H}_{DD} \cong 0$ and therefore can be omitted.

Unlike the **J**-coupling the dipole-dipole interaction is a though-space interaction rather than though-bond and is described for the solid state by the Hamiltonian:

$$\hat{H}_{DD} = d_{jk}(3\hat{I}_{z,j}\hat{I}_{z,k} - \hat{I}_j\hat{I}_k), \tag{2.12}$$

and $d_{jk}$ is the secular dipole-dipole coupling between spin $j$ and $k$ which is given by:

$$d_{jk} = b_{jk}\frac{1}{2}\left(3\cos^2\Theta_{jk} - 1\right). \tag{2.13}$$

The term $b_{jk}$ in Equation 2.13 contains the distance dependent terms in the dipole-dipole coupling Hamiltonian, and is given by Equation 2.14,

$$b_{jk} = -\frac{\mu_0}{4\pi}\frac{\gamma_j\gamma_k\hbar}{r_{jk}^3}. \tag{2.14}$$

Equation 2.13 shows the dependence on the orientation in the dipole-dipole interaction. Due to the random motion and tumbling of molecules in a liquid, this term is averaged out so therefore has little effect on the spectrum. However in solids the motion is heavily restricted and therefore a much broader spectral line arises. This broadening can be reduced significantly due to spinning the sample at the "Magic Angle". This experimental procedure takes advantage of the $3\cos^2\Theta_{jk} - 1$ term in the Hamiltonian, therefore, by placing the sample at $54.7^o$ to the magnetic field and spinning it, this term is reduced.

## Populations and Energy Levels

The signal in the NMR experiment is dependent upon the population differences between (for a spin $\frac{1}{2}$ nuclei) the two energy states that arise due to the Zeeman splitting. Given that one state is a higher energy level than the
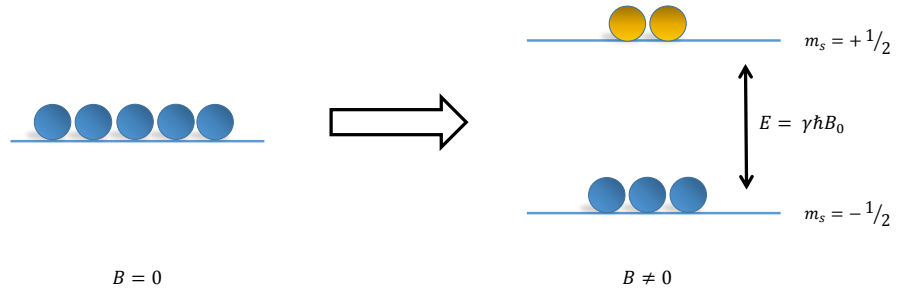
Figure 2.3: The circles represent the populations of the energy levels. For no applied external magnetic field (left) there is no energy level splitting and no polarisation. When a field is applied the levels split and there is a difference in the populations of the two levels.

other, at thermal equilibrium there will be a slight difference in the populations of the states. The difference in the populations follows Boltzmann's formula shown in Equation 2.15. This equation defines the population of any given state $(m)$, where the number of states is $m = 2I + 1$.

$$P_m = \frac{N}{Z} \exp\left(\frac{m\gamma\hbar B_0}{K_B T}\right), \qquad (2.15)$$

$$Z = \sum_m \exp\left(\frac{-E_m}{K_B T}\right), \qquad (2.16)$$

where $N$ is the total number of spins in the system and $Z$ is the partition function, summing over all the states for normalising the numerator in Equation 2.15. The polarisation $(P_0)$ is the fractional difference in the populations given, for a spin $\frac{1}{2}$, by:

$$P_0 = \frac{p_\alpha - p_\beta}{p_\alpha + p_\beta}. \qquad (2.17)$$

When $K_B T >> E$, Curie's limit applies (where $\tanh x \simeq x$) and the polarisation can be expressed as:

$$P_0 \approx \frac{\gamma\hbar B_0}{2K_B T}, \qquad (2.18)$$

this is known as the high temperature approximation.

The magnetisation in a non-zero, static magnetic field will give a value $(M)$ for the portion of the spins that are aligned with the field and will contribute to the NMR signal. Before application of the high temperature approximation the magnetisation is given by,

19

$$M = N\gamma\hbar \tanh\left(\frac{\gamma\hbar B_0}{2K_B T}\right). \tag{2.19}$$

Once again, due to the hyperbolic tangent in Equation 2.19, for high temperatures it is feasible to simplify this equation,

$$M \approx \frac{N\left(\gamma\hbar\right)^2 B_0}{4K_B T}. \tag{2.20}$$

where N is the number of spins. The total magnetisation is directly proportional to the SNR so therefore, if there are fewer spins in the system the total amount of magnetisation is less and in turn the SNR is decreased. This has profound consequences when attempting an NMR or MRI experiment on a microscopic scale, as there may only be sample volumes on the order of nano or pico litres, containing on the order of $10^{12} - 10^{16}$ spins.

### 2.3.5    Signal-to-Noise

There are many factors effecting SNR however for the purposes of MR-microscopy a significant limiting factor is that the region of interest is greatly reduced compared with macroscopic MRI and as such the sample volume is also reduced. This is obstructive to the received signal level as the number of spins contributing to the total magnetisation is fewer. One equation that attempts to define the SNR was derived by Callaghan (14) for a solenoid is given as:

$$SNR = \frac{N\gamma^3\hbar^2 B_0^2}{4K_B T_s}\sqrt{\frac{\mu_0 Q}{4K_B T_{eff}(BW)V_{coil}}}, \tag{2.21}$$

where $N$ is the total number of spins being measured in the system, $T_s$ is the temperature of the sample and $T_{eff}$ is an effective temperature that combines the temperature of the sample with the equivalent noise temperature of the coil and the pre-amplifier (17; 18; 19). $Q$ is the Q factor of the coil, $BW$ is the bandwidth of the receiver and $V_{coil}$ is the volume of the coil. The equation takes into account the operating frequency given the magnetic field and the effect this has on both the received signal. The effect of reducing the volume of the coil to improve the SNR as well as other hardware considerations that need to be taken into account to achieve high resolution micro imaging is described in more detail in Chapter 4.

From Equation 2.21 it is clear that the number of spins in the system and the level of polarisation (due to the dependence of the applied magnetic field) will partly determine the achievable resolution and the limit of detection. From this it becomes clear that a method for increasing the level of polarisation

to a higher than thermal state (i.e. DNP) may facilitate detection of small ($\sim 10^{15}$) numbers of spins.

## 2.4 Bloch Equations

The way in which the magnetisation behaves when in the presence of a magnetic field and when fields in other directions are applied can be described by the Bloch equations. In the presence of a magnetic field a magnetic moment $\mu$ will experience a torque $\vec{T}$, given the analogous nature of spin angular momentum with classical angular momentum the rate of change magnetisation is derived from the equations governing angular momentum:

$$\frac{d\vec{J}}{dt} = \vec{T} = \vec{\mu} \times \vec{B}. \tag{2.22}$$

The rate of change in angular momentum $\vec{J}$, is given by the cross product of the magnetic moment and the applied magnetic field vector.

Given Equation 2.5, and summing over all the individual magnetic moments in order to consider the total magnetisation vector $\vec{M}$, we see that the rate of change in the magnetisation, and as such, the motion of the magnetisation in a given applied field, is described by Equation 2.23,

$$\frac{d\vec{M}}{dt} = \gamma \vec{M} \times \vec{B}. \tag{2.23}$$

If the applied magnetic field is aligned with the z-axis, Equation 2.23 gives the result:

$$\dot{M}_x = \gamma \left( M_y B_z \right)$$
$$\dot{M}_y = \gamma \left( -M_x B_z \right)$$
$$\dot{M}_z = 0. \tag{2.24}$$

### 2.4.1 Ehrenfest Theorem

This same result can also be derived from the quantum mechanical perspective using Ehrenfest theorem (20). The time evolution of the expectation values of the spin component operators shows how the classical mechanics is contained within the quantum mechanical picture as a limiting case. Calculating the time evolution of the expectation value of the $\hat{I}_x$ spin operator gives:

$$\frac{d\left\langle \hat{I}_x \right\rangle}{dt} = \frac{1}{i\hbar}\left\langle \left[ \hat{H}, \hat{I}_x \right] \right\rangle + \left\langle \frac{\delta \hat{I}_x}{\delta t} \right\rangle. \tag{2.25}$$

$\hat{H}$ is the Zeeman Hamiltonian as shown by Equation 2.6 and the term $\left\langle \frac{\delta \hat{I}_x}{\delta t} \right\rangle = 0$ so therefore can be neglected. After expansion of the commutator brackets the result is given as,

$$\frac{d\left\langle \hat{I}_x \right\rangle}{dt} = \gamma B_z \left\langle \hat{I}_y \right\rangle, \tag{2.26}$$

which yields the same result as shown in the solution to $\dot{M}_x$ in Equation 2.24. What the equation demonstrates is that in the presence of a homogeneous magnetic field the magnetisation along the z-axis is constant, however the magnetisation along x and y will precess in the transverse plane. The precession frequency is known as the Larmor frequency ($\omega_0$), given by:

$$\omega_0 = -\gamma B_0. \tag{2.27}$$

It is the Larmor frequency that determines the resonant frequency of the NMR experiment and it is also directly related to the frequency equivalent to the energy difference between the spin $+\frac{1}{2}$ and $-\frac{1}{2}$ states, caused by the Zeeman splitting.

It is possible to perturb the equilibrium magnetisation by the application of an RF pulse. The processes in which the magnetisation returns to its equilibrium state (as determined by the Boltzmann's formula in Equation 2.18) are collectively known as relaxation. One of which is known as longitudinal relaxation, by which, after an initial excitation to equalise the energy levels, the precessing magnetisation in the x,y plane returns to thermal equilibrium, to become oriented back along the z-axis. The second is a de-phasing of the magnetisation which is precessing in the x,y plane, known as transverse relaxation. The Bloch equations that include the effect on the magnetisation due to relaxation are given by:

$$\dot{M}_x = \gamma \left( M_y B_z - M_z B_y \right) - M_x/T_2,$$
$$\dot{M}_y = \gamma \left( M_z B_x - M_x B_z \right) - M_y/T_2,$$
$$\dot{M}_z = \gamma \left( M_x B_y - M_y B_x \right) - \left( \frac{M_z - M_0}{T_1} \right), \tag{2.28}$$

where $T_2$ is the time constant that corresponds to the transverse relaxation rate and $T_1$ is the equivalent time constant for the longitudinal relaxation (15). The process of relaxation is discussed in more detail in section 2.5.

## 2.4.2 RF Excitation

In NMR the spin system is perturbed by a transverse oscillating magnetic field, or RF pulse. The Bloch equations shown in Equation 2.23 and 2.28 can be used to simulate the effect of such a field, applied in an arbitrary direction, on the magnetisation. Hence it is possible to simulate the effect of RF pulses on the magnetisation vector. In this circumstance $\vec{B}$ is now made up of two orthogonal fields, one static $(B_z)$ acting along the z-axis and one time dependent oscillating field $(B_1(t))$, rotating with a frequency $\omega_1$, which is applied along either x or y. The equation describing the sum of the static and time dependent field is given by,

$$\vec{B} = B_z\mathbf{k} + \vec{B}_1(t)\mathbf{i}, \tag{2.29}$$

The circularly polarised component of the time dependent field, which is oscillating at $\omega_0$, can be expressed as,

$$\vec{B}_1(t) = B_1 \cos \omega_0 t\mathbf{i} - B_1 \sin \omega_0 t\mathbf{j}, \tag{2.30}$$

where $\mathbf{i}, \mathbf{j}$ and $\mathbf{k}$ are unit vectors acting along x, y and z respectively (21). In order to be able to easily solve the Bloch equations for the time varying field it is convenient to transform the frame of reference from the laboratory to a rotating frame of reference, which is rotating with the time varying field. This is achieved by application of a transformation matrix ($\mathbf{T}$),

$$\vec{M}_{rot} = \mathbf{T}\vec{M}, \tag{2.31}$$

$$\mathbf{T} = \begin{pmatrix} \cos(\omega_{rf}t) & \sin(\omega_{rf}t) & 0 \\ -\sin(\omega_{rf}t) & \cos(\omega_{rf}t) & 0 \\ 0 & 0 & 1 \end{pmatrix}, \tag{2.32}$$

where $\omega_{rf} = \gamma B_1$. The solution to the Bloch equations in the rotating frame are,

$$\dot{M}_x = -M_y\Delta\omega - \frac{M_x}{T_2},$$
$$\dot{M}_y = M_x\Delta\omega + M_z\omega_1 - \frac{M_y}{T_2},$$
$$\dot{M}_z = M_y\omega_1 - \left(\frac{M_z - M_0}{T_1}\right), \tag{2.33}$$
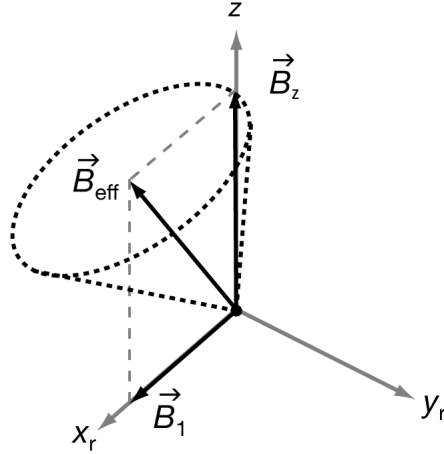
Figure 2.4: The effective field is a combination of the on and off resonance components of the $B_1$ field as represented in the rotating frame. When there is a significant off resonant component the magnetisation precesses in a conical fashion about the effective field.

where $\Delta\omega = \omega_0 - \omega_1$ and $\omega_1 = \gamma B_1$, with $B_1$ being the magnitude of the oscillating magnetic field. The effective field observed by the magnetisation is given by,

$$B_{eff} = \sqrt{B_z^2 + |B_1|^2} \qquad (2.34)$$

If the applied pulse is on resonance then the magnetisation vector will rotate about the direction of the pulse. However, an off resonance pulse (where $\omega_1 \neq \omega_0$) causes the effective field about which the the magnetisation rotates to be off axis and therefore will precess about $B_{eff}$, as demonstrated by Figure 2.4 (14).

It has been shown through the Bloch equations that the two components of the $B_1(t)$ field rotate clockwise and anticlockwise in the transverse plane at the Larmor precession frequency which causes the magnetisation vector to rotate into the transverse plane though a given angle. For a full rotation of the magnetisation vector into the transverse plane a flip angle of $\pi/2$ rad is required. The angle that the magnetization vector moves from the longitudinal plane is known as the flip angle, and the size of the flip angle ($\beta$) is determined by:

$$\beta = -\gamma B_1 \tau, \qquad (2.35)$$

where $\tau$ is the duration of the $B_1$ field.

The $B_1$ field effects the populations of the energy levels by inducing transitions between the energy levels. The populations of the energy levels will

become equal after a given duration, which is a $\pi/2$ pulse and further application of the pulse past this point will eventually invert the populations (a $\pi$ pulse).

## 2.5 Relaxation

The processes that cause the magnetization to return to its equilibrium values are known collectively as relaxation. There are two types of relaxation to consider, longitudinal, associated with the return of the magnetisation vector to align with the applied static field and the transverse relaxation, a dephasing of the magnetisation as it precesses in the transverse plane.

### 2.5.1 Longitudinal Relaxation

Spin-lattice, or $T_1$, relaxation is the process that occurs immediately after an RF pulse and it is the process by which the population differences return to equilibrium levels, reducing the magnetisation in the $xy$-plane and growing the magnetisation vector along $z$. The effect of the $T_1$ on the magnetisation vector has been shown in Equation 2.33 and the component that contributes to the longitudinal relaxation is given by,

$$\frac{dM_z}{dt} = -\frac{M_z - M_0}{T_1},\qquad(2.36)$$

which has the solution,

$$M_z(t) = M_0 + (M_z(0) - M_0)\exp\left(-\frac{t}{T_1}\right).\qquad(2.37)$$

In Equation 2.37, $T_1$ is the characteristic time constant that governs the rate at which the magnetisation returns to equilibrium.

The mechanisms that cause this relaxation are usually due to dipolar or quadrupolar interactions, however in the case of spin $\frac{1}{2}$ nuclei, the interaction is purely magnetic (12), meaning that there is no electronic driven relaxation (i.e. quadrupolar). Relaxation occurs when there are fluctuations in the local magnetic field on the order of the Larmor frequency which induce NMR transitions. Local field fluctuations are caused by other nearby dipoles in the lattice, thus giving rise to the term spin-lattice relaxation. However, these fluctuations can be also caused by the field and other interactions, such as the chemical shift anisotropy. It is worth considering how molecular motion affects the relaxation times, as shown in Figure 2.5, where the effect of a molecule with fast or slow motion in the liquid state, compared with the Larmor frequency, is displayed in terms of its $T_1$. The magnitude of the
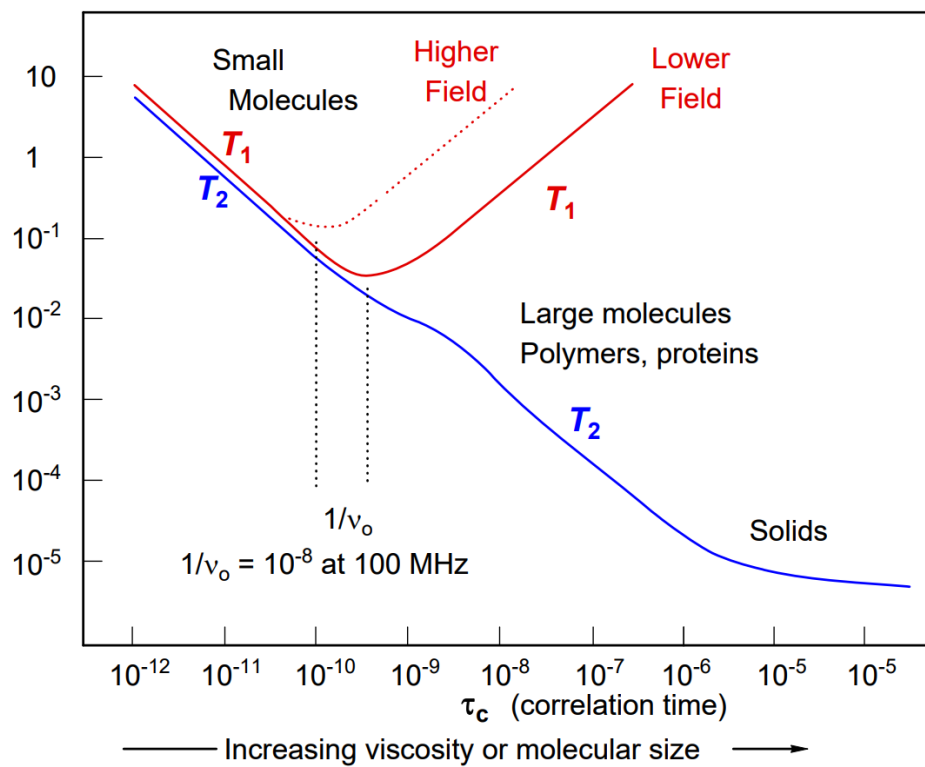
Figure 2.5: The schematic shows how the efficiency of the $T_1$ and $T_2$ relaxation (measured in seconds) changes due to molecular motion(14). The correlation time is the correlation between the Larmor frequency and the molecular motion. When the two are equivalent the $T_1$ relaxation is most efficient. The figure is adapted from Boembergen, Purcell and Pound, 1948.
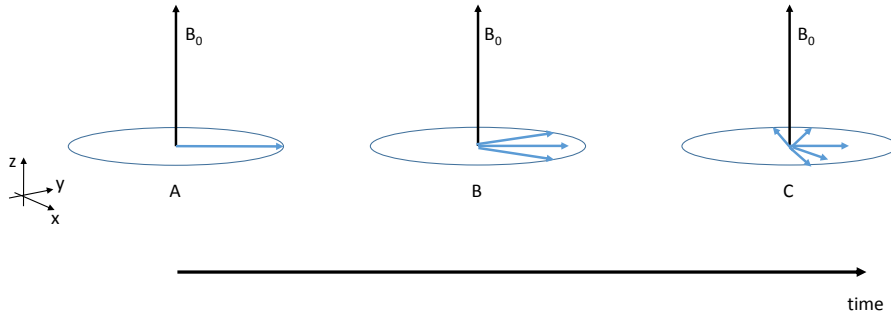
Figure 2.6: The blue arrows represent the precessing magnetisation vector in the $xy$ plane. At A $M_{xy}(t) = M_{xy}(0)$ and the strength of the signal is at its maximum. At B and C the magnetisation is de-phasing.

though-space dipolar interaction $(b_{jk})$ is given by Equation 2.14, and motion of the molecules in liquid state NMR means that the dipolar interaction is averaged out so the effect on the spectrum is negligible, however motion on the order of the Larmor frequency still drives spin-lattice relaxation (14). Most efficient relaxation happens when the molecular rotation and tumbling is closest to the Larmor frequency.

## 2.5.2   Transverse Relaxation

Transverse relaxation acts on the magnetisation in the x,y plane and it is this form of relaxation that determines the lifetime of the x,y magnetisation. Over time the coherences between the individual magnetic moments breaks down, thus leading to a decrease of the magnetisation vector $(M_{x,y})$. This is caused by the small variations in the local magnetic field experienced by the spins, which means that they no longer precess in phase. Transverse relaxation is described in the Bloch equations as,

$$\frac{dM_{x,y}}{dt} = -\frac{M_{x,y}}{T_2}$$

(2.38)

The solution provides a decay envelope that follows an exponential process given by,

$$M_{xy}(t) = M_{x,y}(0) \exp\left(\frac{-t}{T_2}\right),$$

(2.39)

27

where $T_2$ is the time constant that it takes the magnetisation to reduce by $1/e$ from the initial value. The longitudinal magnetisation remains invariant to the transverse relaxation.

$T_2$ relaxation is caused by the random motion of the spins in the system causing local variation in the magnetic field. The measured value for the transverse relaxation after a single $90^o$ pulse is typically much shorter than the theoretical value of $T_2$. This is a result of imperfections in the magnetic field and magnetic susceptibility effects which cause a local shift in the precession frequency, leading to a de-phasing faster than predicted due to spin-spin interactions. The term describing the complete transverse relaxation is known as $T_2^*$ which contains both the effect on the magnetisation due to the spin interactions and due to the hardware related field inhomogeneities such as the inhomogeneity in the polarising field due to the presence of the RF coil. The $T_2^*$ is given by,

$$\frac{1}{T_2^*} = \frac{1}{T_2} + \frac{1}{T_2'}, \tag{2.40}$$

where $T_2'$ is the time constant associated with the de-phasing to the inhomogeneity of the magnetic field.

## 2.6   The Free Induction Decay

Through the process of induction, when a coil of wire is placed orthogonally to a rotating magnetic field a voltage will be induced across the coil. The nuclear magnetisation can be thought of, in a semi-classical sense, as a magnetic dipole which precesses about a given magnetic field and as such, will generate a voltage in a coil placed orthogonally to it. In order for magnetisation to be observed it needs to be precessing in an plane orthogonal to one of the polarising field. The oscillating voltage that is generated in the coil, after a $90^o$ pulse, by the precessing spins is known as the Free Induction Decay (FID) (22).

The FID (decaying sinusoid) shown in blue in the left hand side of Figure 2.7 has its length determined by the $T_2^*$ relaxation rate. The modulation, which is given by Equation 2.27 and changes in the local magnetic field determines the spectral position after carrying out a Fourier transform. As the magnetisation de-phases in the transverse plane, the strength of the oscillating signal decreases. It will be shown later that the $T_2$ and $T_2^*$ have profound consequences for the achievable resolution in both NMR and MRI. The length of the decay envelope of the FID determines the linewidth of the spectrum after the Fourier transform.
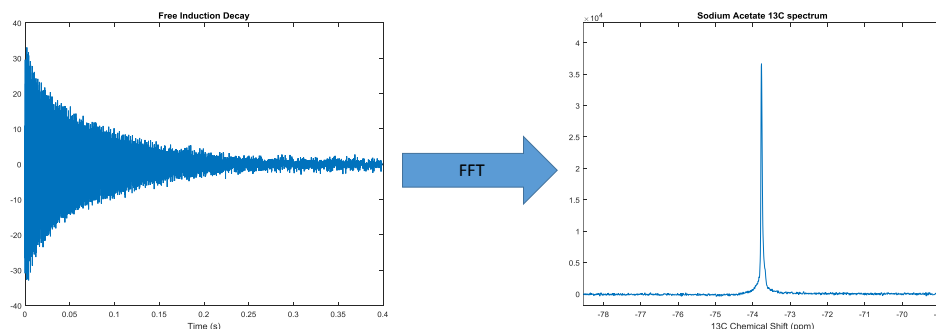
Figure 2.7: LHS: A $^{13}$C time domain signal for Sodium Acetate after a 90 degree pulse, carried out at 9.4 T. RHS: Frequency domain spectrum for sodium acetate following the application of a Fourier transform to the time domain signal.

## 2.6.1   The Fourier transform

In order to the frequency components of the oscillating voltages that are detected at the receiver a Fourier transform is applied to the FID. In essence, the Fourier transform breaks the NMR signal down into individual frequency components, giving a representation of the quantity of each of the different frequencies. This is computationally laborious as it requires $N^2$ multiplications which can be made more efficient if the number of points in the series is on the order of $N = 2^n$, where n is a small integer. In this circumstance, as shown by Cooley and Tukey in 1965 (23) the discreet Fourier transform can be broken down into smaller steps of $NlogN$ multiplications, thus making it faster. It is this trick that gives it the name Fast Fourier transform.

The digitization of the spectrum by the spectrometer must occur at a rate that is twice that of the fastest oscillation in the received signal, obeying the Nyquist sampling condition (24) where the sampling rate must be twice the highest frequency to be sampled in order to correctly interpret the received signal. In NMR the use of quadrature detection means that it is feasible to sample at the same rate as the highest frequency. If under-sampling of the FID occurs, the spectrum will not be a faithful representation of the position of the peaks as frequencies that are not sampled correctly will cause aliasing.

If the duration that the receiver gate is open for greatly extends past the length of the FID then the SNR of the spectrum will deteriorate as only noise is collected during this period. In order to maintain high digital resolution and collect as little noise as possible the zero filling of the FID (padding with zeros) allows the digital resolution to be increased without spoiling the SNR.

Apodizatoin or smoothing filters can be applied to the FID to reduce the noise in the spectrum. This is achieved by multiplying the raw data by an
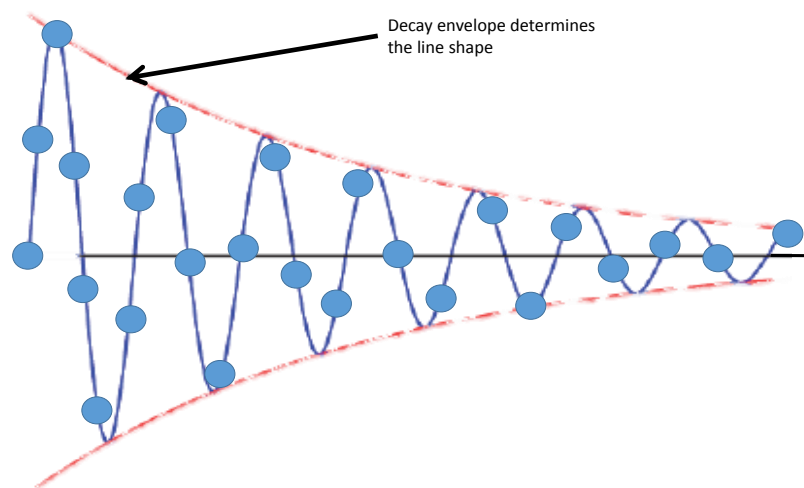
Figure 2.8: The oscillating signal is discretised by the digitizer in the spectrometer, converting a continuous signal into discreet points. This is then transformed with an Fast Fourier transform where the line-shape of the peaks are determined by the decay envelope of the FID.

exponential function to accelerate the decay of the FID while also reducing the noise. This has the effect on the frequency domain of broadening the lines in the spectrum but reducing the noise. In high resolution imaging it is important to ensure that the broadening being introduced by the filter is less than the pixel spacing otherwise the resolution will deteriorate (25; 14).

## 2.7 The Spin Echo

In MR microscopy the resolution is determined partly by the duration over which signal may be sampled and therefore it is beneficial for the transverse relaxation rate to be as long as possible. This means that the increased transverse relaxation observed in the FID due to field inhomogeneity $(T_2^*)$ can severely hamper microscopic acquisition. Hahn was the first to understand that by using multiple RF pulses it is possible to remove the spurious relaxation effects caused by instrumentation and that the signal lost in the FID to $T_2^*$ relaxation could be refocused in order to measure $T_2$ (26). Initially Hahn used a $90^o$ pulse followed by another one after some delay to collect what is known as a Hahn echo. However, Carr and Purcell used a $180^o$ pulse for the second excitation which inverts all of the isochromats which is shown in Figure 2.9 (27).

The spin echo sequence is useful as the de-phasing that occurs due to the inhomogeneity in the magnetic field is inverted so that the isochromats re-phase to form an echo. This de-phasing and the re-phasing due to the application of the $180^o$ pulse is demonstrated in Figure 2.10, where the

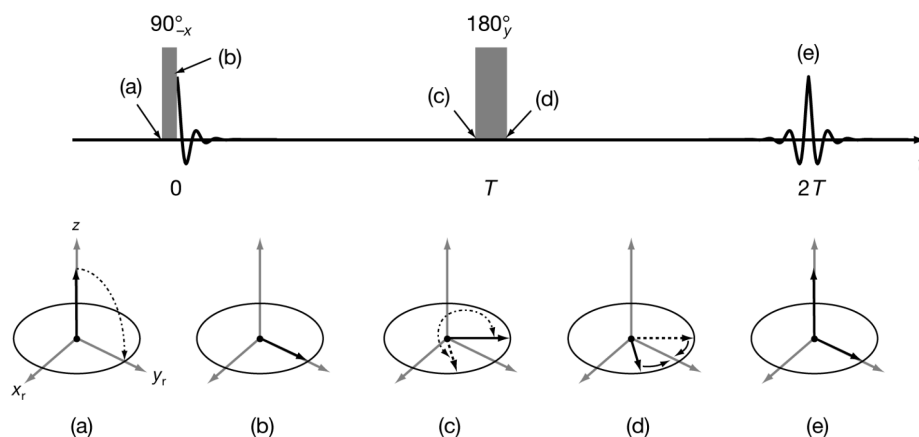Figure 2.9: The spin echo sequence as used by Carr and Purcell. The magnetisation, as viewed from the rotating frame, is tipped into the transverse plane where the FID decays with a rate contestant of $T_2^*$, after some time $(T)$ a refocussing pulse is applied and the magnetisation vectors are inverted whereby they then refocus to form an echo at time $2T$.

magnetisation vector is broken down into isochromats represented by the different colours (28).

By varying the time between the initial $90^o$ pulse and the refocussing $180^o$ pulse the magnitude of the echo will change and by collecting multiple experiments, it is then possible to fit Equation 2.39 to extract the value for $T_2$. It was also realised that multiple refocussing pulses could be carried out in the same experiment to produce a train of echoes which allow $T_2$ to be extracted in a single experiment. This pulse sequence was developed by Carr, Purcell, Meiboom and Gill and as such is known as the CPMG sequence, it is shown in Figure 2.11 (29). The initial FID decays with $T_2^*$ however the echo train decays with $T_2$. In MR-microscopy the high gradient strengths required to achieve the small voxel sizes mean that the $T_2^*$ is very short and therefore the spin echo plays a vital role.

# 2.8   Spatial Encoding

In NMR it is preferable to achieve the most homogeneous field possible, this is in order to get high resolution spectra with well resolved lines. If the field has significant inhomogeneity then the different isochromats of the magnetisation across the sample will precess at different frequencies, and therefore broaden the lines of the NMR spectrum. However this negative effect in NMR can be harnessed and used to great effect when attempting to generate images.

In order to carry out magnetic resonance imaging (MRI) Lauterbur showed that it is necessary to intentionally apply a well defined field inhomogeneity in the form of field gradients (30; 31). The well defined gradient means that
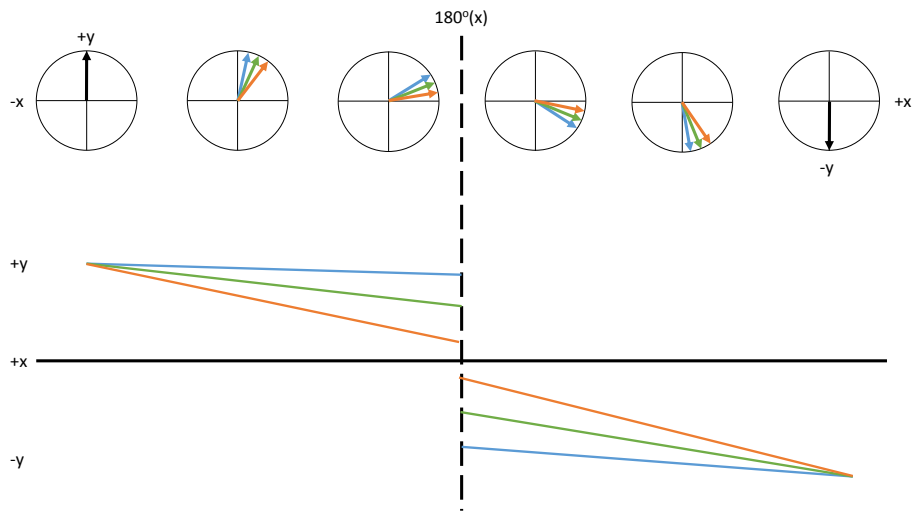
Figure 2.10: Top: Vector diagram demonstrating how the magnetisation vector is broken up into isochromats whereby they de-phase and are then refocussed by the $180^o$ pulse. Below this is the phase diagram for the evolution of the isochromats.
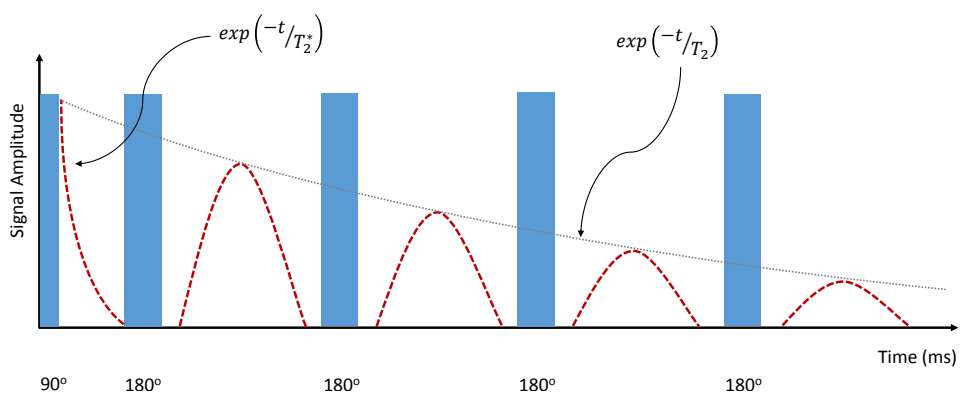


Figure 2.11: The CPMG pulse sequence, which is a $90^o$ pulse followed by a train of $180^o$ pulses. This sequence demonstrates how true $T_2$ values can be extracted from the NMR experiment by the use of the spin echo.
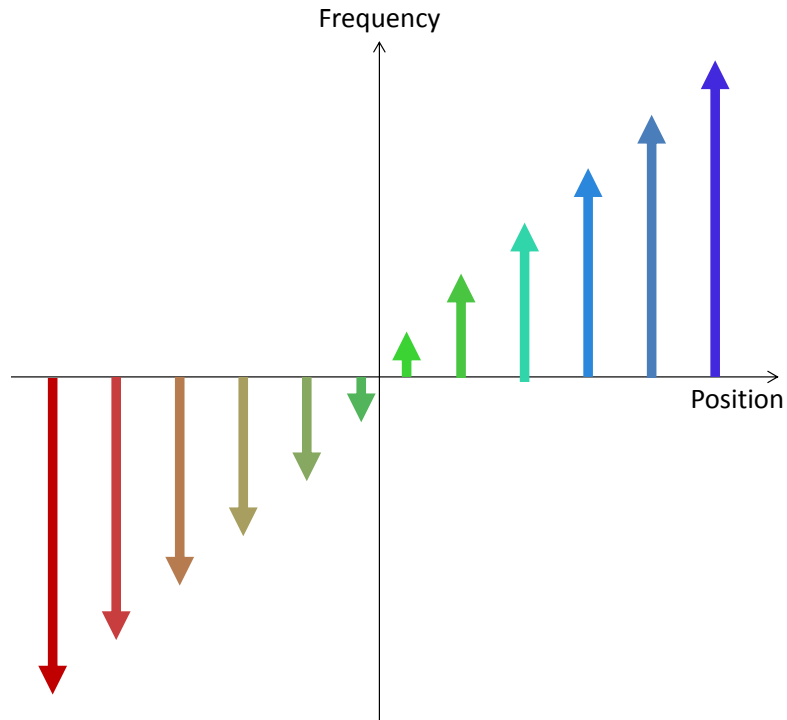
Figure 2.12: Under the application of a field gradient the spins in the sample will precess at varying frequencies which depend on the total field that they experience.

the Larmor frequency becomes spatially dependant across the sample, which allows the magnetisation to be spatially encoded, as shown by Figure 2.12. Therefore, when the Fourier transform is applied, instead of showing the individual frequency components within a molecule as in NMR, the individual frequency components that are created due to the gradient encoding are shown. This is essentially a density map of the spins along the direction of the applied gradient.

The effect of an applied gradient on the Larmor frequency is:

$$\omega\left(\mathbf{r}\right) = \gamma B_0 + \gamma \mathbf{G}.\mathbf{r}. \tag{2.41}$$

Equation 2.41 defines how the frequency of the spins changes with the position in relation to the gradient. $\mathbf{G}$ is the field gradient strength in units of Tesla per metre, defined as the **grad** of the pulsed field parallel to the static applied magnetic field $\left(B_0\right)$. The term $\mathbf{r}$ describes a position in the sample. This linear relationship between frequency and position is the fundamental relation that allows images to be constructed.
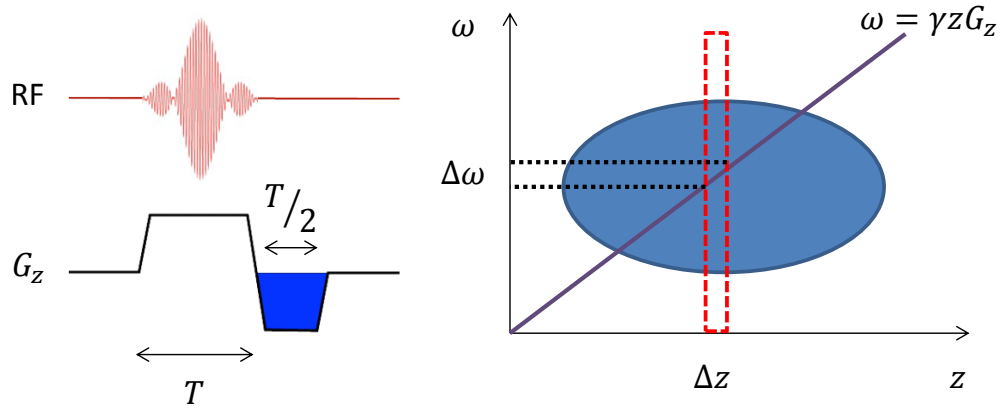
Figure 2.13: Left: A slice selective RF pulse is applied which consists of a sinc pulse and a gradient. The refocussing gradient (shown in blue) is to reverse the phase modulation imparted by the gradient. Right: during the application of a linear gradient (purple) a RF pulse with bandwidth $\Delta\omega$ is applied which excites only a small portion of the magnetisation (red dashed box).

## 2.8.1 Slice Selection

The technique to selectively excite a portion of the magnetisation is known as slice selection and is done through the application of a linear gradient, typically along the z-axis, during the RF excitation pulse. The gradient enforces a linear distribution of the Larmor frequency across the sample, meaning that only a portion of the isochromats are tipped into the transverse plane leaving the magnetisation outside of the chosen slice width unperturbed. The thickness of the slice is determined by the gradient strength, $G_z$, and the bandwidth of the RF pulse $\Delta\omega$, and is defined by,

$$\Delta z = \frac{\Delta\omega}{\gamma G_z}. \tag{2.42}$$

Therefore, from Equation 2.42, it is possible to reduce the slice thickness by increasing the gradient strength or reducing the bandwidth of the RF pulse (14). Figure 2.13 shows how the bandwidth of the RF pulse effects the slice thickness for a given gradient strength. The gradient is applied during the RF excitation and then reversed for half of the duration to ensure a re-phasing of the spins, this is to counteract the de-phasing that is introduced by the initial slice select gradient (32).

## 2.8.2 Phase-Frequency Encoding

A general mathematical expression for the spatially encoded signal, $S\left(k_x, k_y\right)$, can be derived given knowledge of the applied gradients and their durations. The term $k_{x,y}$ are components of $k$-vector which describes the position in

reciprocal space (or $k$-space) introduced by Mansfield (31; 33; 34) and is given by,

$$\mathbf{k} = \frac{\gamma \mathbf{G} t}{2\pi},$$ (2.43)

where $\mathbf{G}$ is the gradient strength and $t$ is the duration the gradient is applied for. This $k$-space data array can then be Fourier transformed along each direction to give the frequency domain image.

In conventional MRI, using a single detection coil, every point in the $k$-space array must be sampled to allow an artefact free reconstruction. Missing lines of $k$-space results in the Nyquist limit not being achieved and therefore it is not possible to accurately distinguish different frequencies. This results in overlapping of features in the image, a problem which will be discussed in more detail in chapter 5.

Position in $k$-space is navigated by either changing the gradient strength or allow the spin system to evolve over a given time period while a static field gradient is being applied. The $k$-space describes, in the time domain, the number of wavelengths per unit distance or the rate of change in phase with distance. The direction of sampling in $k$-space is determined by the direction of the gradient, $\mathbf{G}$.

The received spatially encoded signal due to the applied magnetic field gradients is given by,

$$S\left(k_x, k_y\right) = \int_{-a/2}^{a/2} \left[ \iint_{-\infty}^{\infty} \rho\left(x, y, z\right) exp\{i2\pi \left(k_x x + k_y y\right)\}dxdy \right] dz.$$ (2.44)

The outer integral represents the averaging across the slice thickness ($a$) and can be ignored when considering the spatially encoded signal within a slice (14). $\rho\left(x, y, z\right)$ is the spin density at a given position which is calculated from the inverse Fourier transform of Equation 2.45 which gives,

$$\rho\left(x, y\right) = \iint_{-\infty}^{\infty} S\left(k_x, k_y\right) exp\{-i2\pi \left(k_x x + k_y y\right)\}dk_x dk_y.$$ (2.45)

The nature of the reciprocal space can be visualised in Figure 2.15.

A simple spin echo imaging pulse sequence is shown in Figure 2.14, which shows how the magnetisation is manipulated to fill up lines of $k$-space. First a gradient is applied during the RF excitation to select a slice, then a gradient ($G_{phase}$) is applied along the y-axis to impose a sinusoidal modulation of the phase of the magnetisation across the image, as shown in Figure 2.15. A refocusing RF pulse is applied (this time not slice selective) and finally a readout gradient along the x direction is applied during the echo in order to

35
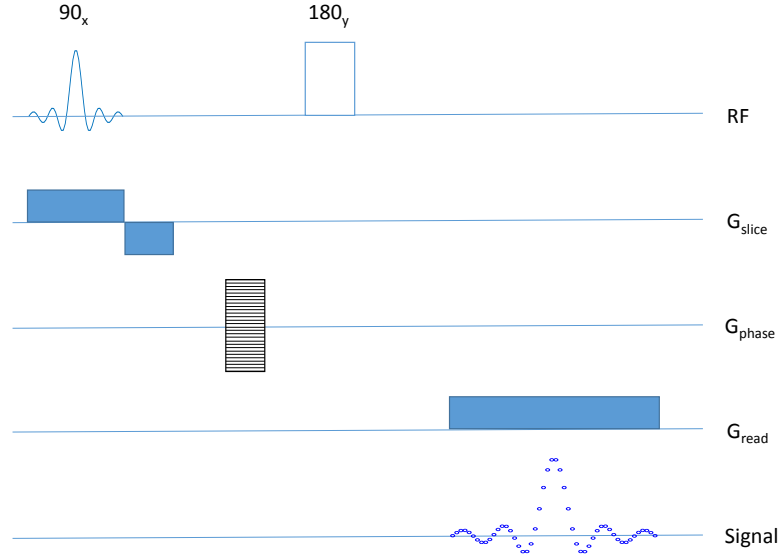
Figure 2.14: Spin echo pulse sequence for MRI Cartesian $k$-space acquisition with slice selective excitation and non-slice selective refocussing pulse.

encode the spins in the read direction. Due to the nature of reciprocal space the distance between points in $k$-space is equivalent to the size of the field of view (FOV),

$$FOV_{x,y} = \frac{1}{\Delta k_{x,y}} = \frac{1}{\gamma G_{x,y} \Delta t_{x,y}}. \tag{2.46}$$

The term defining the time between sampled points during the application of the gradient in Equation 2.46, $t_{x,y}$, is associated with a spatial coordinate to distinguish between the duration of the gradient along the x or y axis respectively. Due to the reciprocal nature of the $k$-space the pixel spacing in the image domain is given by,

$$pixel_{x,y} = \frac{1}{N_{x,y} \Delta k_{x,y}}, \tag{2.47}$$

where $N_{x,y}$ is the number of points collected in the x or y directions of the $k$-space. Therefore, in the frequency encoding (read) direction, where the $k$-space is traversed by application of a constant gradient and the magnetisation is allowed to evolve, the resolution is determined by the duration of the echo and the size of the FOV in the read direction is inversely proportional to the time step between the sampled points (19). The maximum resolution in the phase encoding direction is related to the gradient strength as this is only applied to impart a phase modulation so that it is possible to distinguish between the frequency encoded lines as shown in Figure 2.15.
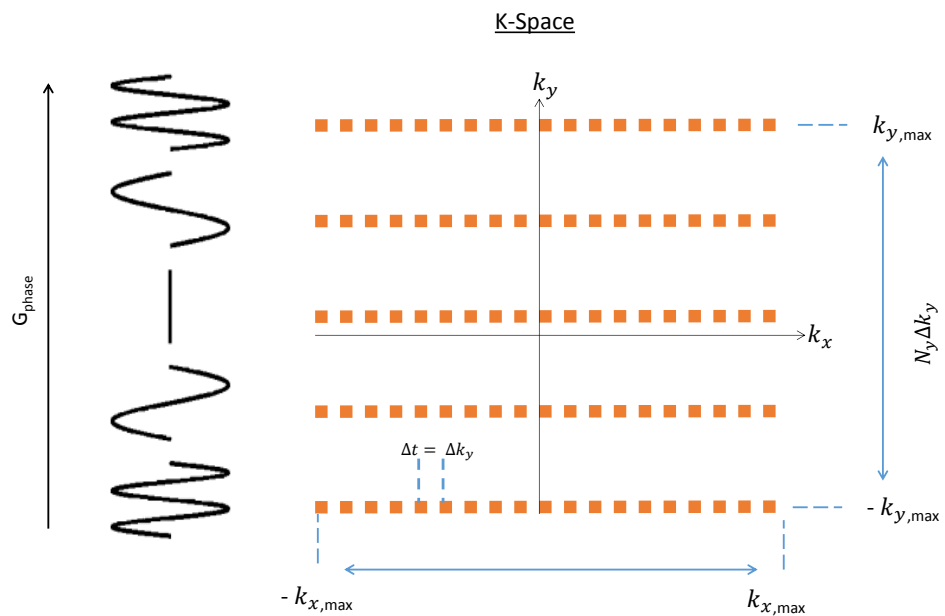
Figure 2.15: Phase modulation due to phase encoding gradient across $k$-space. The strength of the phase encoding gradient is changed to impose different phase modulations along this direction. The number of points collected in the read direction $(k_x)$ determines the number of pixels and the FOV size along the x direction in the image domain.

Given that the the read out direction in $k$-space must be traversed by applying a static gradient for a fixed time, each extra line requires further time. For imaging of hyper-polarised samples this is time in which the signal is returning to thermal equilibrium. Therefore removing lines of $k$-space without reducing the FOV size is useful. This however requires specialised hardware to avoid artefacts being generated. The techniques and the hardware required for accelerated MRI will be discussed in chapter 5.

**FLASH**

In order to reduce the time required to sample the entire $k$-space, it is preferable to limit the waiting time between acquisitions of each of the lines. After a $90^o$ pulse the repetition time between acquisitions $(T_r)$ is governed by the $T_1$ of the sample, as the magnetisation must recover before another line of $k$-space can be acquired. To speed up the repetition time the flip angle can be reduced so that the recovery of the magnetisation is quicker.

Haase *et al.* showed that small flip angles $(\theta)$ could be used for selective excitation and that the signal due to the small flip angle is proportional to $\sin\theta$, with the remaining z magnetisation proportional to $\cos\theta$ (35; 36). By using a train of small flip angles it possible to reduce $T_r$ and collect the entirety of $k$-space in a much shorter time. The optimal flip angle for a thermally polarised system is determined by the Ernst angle. This type of imaging is known as FLASH or Fast Low Angle SHot imaging and uses a

Figure 2.16: RARE pulse sequence with echo train of 4. The phase encoding is applied before the echo allow distinction between echoes and applied after to rewind the phase. The gradient lobes either side of the slice selective pulse are crusher gradients to de-phase magnetisation excited outside of the selected slice. The gradients marked by red and green lines correspond to lines showing how the $k$-space is navigated.
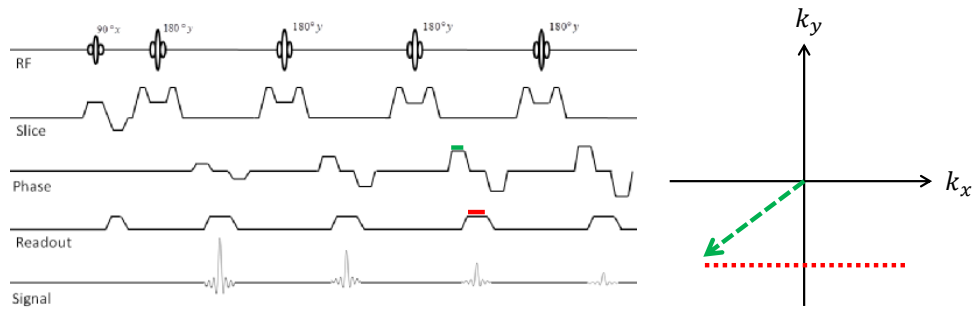
simple gradient echo for the read out of the signal.

Typically small flip angle pulse sequences are not preferable in MR microscopy as the SNR reduction increases the acquisition time, however when considering microscopy with the application of a hyper-polarised sample, FLASH becomes a more realistic possibility. Given that hyper-polarised samples are in a higher than thermal equilibrium state there is a necessity to avoid saturation of the magnetisation through large RF pulses in order to sample the full $k$-space.

**RARE**

In order to improve acquisition time Mansfield showed that the echo train, as displayed in the CPMG pulse sequence in Figure 2.11, can be encoded so that each echo represents a different line in the k-space (37). This was developed further by Hennig *et al.* to produce the Rapid Acquisition with Relaxation Enhancement (RARE) sequence, shown in Figure 2.16 (38).

The RARE sequence is attractive for MR-microscopy as the spin echo sequence means an echo train is used and as such, the relaxation is determined by $T_2$ rather than $T_2^*$, making the acquisition less sensitive to inhomogeneity in the magnetic field. Typically it is preferable to sample the central regions of $k$-space first as these contain the low frequency values, with the higher frequency values contributing more to the finer detail of the image. The $k$-space trajectory and the RARE pulse sequence are presented in Figure 2.16. In this sequence the initial excitation pulse is followed by a train of refocussing pulses, analogous to the CPMG sequence, however a phase encoding gradient is applied to allow encoding in the phase direction of the different echoes. A rewind phase encoding gradient is applied after the echo so as to return to the centre of k-space before the next refocussing pulse is applied.
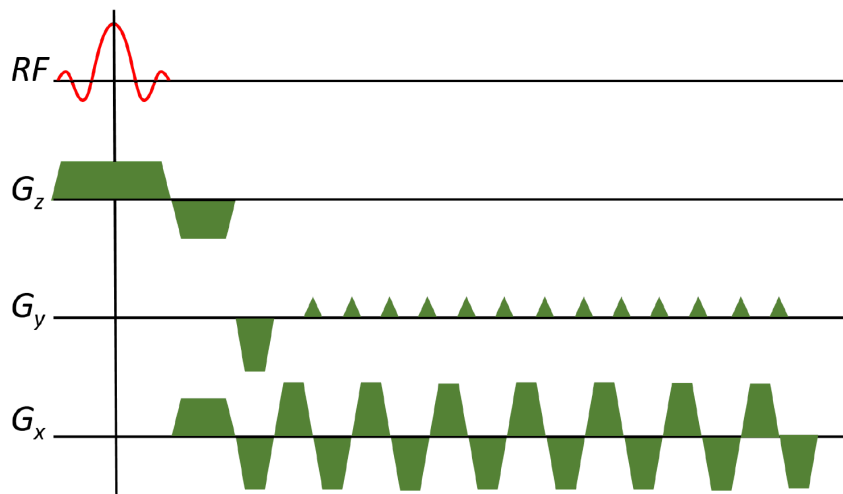
Figure 2.17: Echo Planar Imaging (EPI) pulse sequence where the read gradient is modulated to produce a gradient echo and a blip gradient is applied between gradient echoes to move through the phase direction of $k$-space.

**Echo Planar Imaging**

Developed by Mansfield in the late 1970's, Echo Planar Imaging (EPI) is a technique for collecting an entire $k$-space in a single shot. The pulse sequence, shown in Figure 2.17, is significantly faster than the sequences simple spin echo sequence previously presented as it samples the entire $k$-space with only a single RF excitation pulse (34; 37).

The GE-EPI sequence starts with an initial RF excitation pulse, followed by the application of gradients in order start the acquisition at the $\pm k_{x,y,\text{max}}$ position in $k$-space. Following this, a series of gradient echoes are generated by rapidly switching the readout gradient, where each fills a line in $k$-space. After each echo a blip gradient is applied in the phase encoding direction to move to another line in $k$-space. The EPI pulse sequence is illustrated in Figure 2.17, where $G_z$ is the slice selective gradient, $G_y$ is the phase encoding gradient and $G_x$ is the frequency encoding gradient.

The EPI pulse sequence requires large bandwidths to allow sampling of the entire $k$-space and as such the SNR suffers. It also has the problem that the acquisition time is limited by $T_2^*$ which puts limitation to the resolution. The rapid gradient switching and the very high gradients required for microscopy means that EPI is difficult to use for this application as the vibrations caused by the switching gradient could cause blurring in the image.

## 2.9 Resolution

The resolution in MRI is related to the SNR as the signal is proportional to the number of spins being measured, which means that as the volume of the voxel reduces the number of spins does also. Hardware can be changed to improve the detection for small numbers of spins, however there are still diffusive and magnetic susceptibility effects, along with the relaxation time which all limit the resolution (14). Ciobanu *et. al.* (39) have achieved a voxel size of $3.7 \times 3.3 \times 3.3 \mu m$ at 9 tesla with gradient strengths of $50 \, T/m$, with the use of micro coils (19; 39). However, these images are of protons in free water, a much more favourable medium than a low concentration low-gamma nuclei confined within biological tissue. The number of spins in the $40 \mu m$ voxel as presented by (19) is approximately $\sim 10^{12}$ and an SNR of 1 is achieved for a single scan when there are approximately $5 \times 10^{13}$ spins, this means that significant averaging is required to attain a suitable SNR (19; 39). Smaller in-plane resolution has been achieved, with Lee *et al.* producing a $1 \mu m$ resolution image at $14.1T$ with $10 \, T/m$ gradients, however the overall voxel volume was $75 \mu m^3$ as the slice thickness was larger to improve the SNR and shorten acquisition times (40).

In a homogeneous spin system, without translational motion of the molecules between voxels, the resolution limit is defined by the $T_2$ (or $T_2^*$), due to the fact that the pixel size is inversely proportional to the size of the $k$-space, and it is the duration of the echo that governs the maximum length the read gradient can be applied for. The optimum nearest next neighbour pixel spacing ($\Delta x_{opt}$) for the $T_2$ broadening limit is given by,

$$\Delta x_{opt} = \left( 2/N\pi T_2 \right) \left( 2\pi/\gamma G \right),$$

(2.48)

where $N$ is the number of points sampled along the read encoding direction of the $k$-space. Therefore the optimal resolution for the $T_2$ broadening limit is when the acquisition time is $\pi T_2$. However, in a system where there are boundaries and the molecules are free to move and tumble, the resolution may be considerably effected by the field variations due to magnetic susceptibility and the motion of the molecules.

### 2.9.1 Susceptibility

The boundaries within a sample between areas of different magnetic susceptibility ($\chi_m$) are sources of local field variations (41). The field offset due to the samples magnetic susceptibility adds to the applied magnetic field and the field within a sample ($B_0^s$) can be calculated as,

$$B_0^s = (1 + \chi_m) B_0.$$

(2.49)

This local field variation adds linearly with an applied magnetic field gradient which gives a linear shift to the signal,

$$S(t) = \iint \rho(x,y) exp \left[ i\gamma G t_x \left( x + \frac{\Delta B_0(x,y)}{G_x} \right) \right]$$
$$exp\left[ i\gamma G_y t_y y \right] exp\left[ i\gamma \Delta B_0(x,y) t_y \right] dxdy, \quad (2.50)$$

where $\Delta B_0(x,y)$ is the local field variation relative to the applied static magnetic field, $G_x$ is the the frequency encoding gradient and $G_y$ is the phase encoding gradient. $t_{x,y}$ pertains to the duration for which the different gradients are applied.

For a typical imaging sequence such as the one presented in Figure 2.16, the effect of the local field variation is to shift the image element (x,y) by $\Delta B_0(r)/G_x$ along the read direction (x) (42). The effect on a given pixel along the read direction is described by,

$$\Delta x_{shift} = \frac{\Delta B_0(r)}{G_x}, \quad (2.51)$$

and the phase shift due to the local magnetic field $(\Delta \Phi_{local})$ is given by,

$$\Delta \Phi_{local} = exp\left[ i\gamma B_0(x,y) t_y \right], \quad (2.52)$$

although this only has an effect on the image for gradient echo based sequences as the spin echo refocusses the phase distortion. As the FOV is reduced the imaging bandwidth is also reduced, where the bandwidth is given by,

$$BW = \gamma N \Delta x G_x, \quad (2.53)$$

and $N\Delta x$ is the width of the FOV in the read direction. When the $BW$ becomes comparable to the frequency shift due to susceptibility variation, $\gamma \Delta B_0$, image distortions occur. Therefore to preserve an artefact free image the field variation across a single pixel due to the applied magnetic field gradient must be larger than the field variation due to susceptibility effects.

## 2.9.2 Diffusion

Since the resolution in the read duration is dependent on the magnetisation de-phasing and re-phasing in the presence of a field gradient, it is important to understand how motion of the spins affects the final outcome.

Translational motion in the form of molecular self diffusion of the molecules in a liquid state sample gives rise to random fluctuation of the local Larmor frequency and it is this motion that provides the limitation on resolution in NMR microscopy (14; 42). The average distance travelled under random self diffusion is given by

$$\Delta x_{diff} = \sqrt{2Dt}, \tag{2.54}$$

where $D$ is the self diffusion coefficient. During the image acquisition the self diffusion becomes a limiting factor on the resolution when $\Delta x_{diff}$ is on the order of the pixel spacing. Where the line broadening contribution in the read gradient direction due to diffusion is given by (14)

$$\Delta f_{diff} = 0.6 \left( \gamma^2 G^2 D / 3 \right)^{1/3}. \tag{2.55}$$

By comparing the diffusive broadening with the effect of $T_2$ a resolution limit for a fixed SNR can be obtained which is shown to be

$$\Delta x = C \left[ \Delta x_{diff} \Delta x_{opt}^2 \right], \tag{2.56}$$

where $C$ is a constant equal to 1.34 (14; 25). An important feature of diffusive attenuation and the resolution limit is that it is not solely the motion of the molecule (i.e. the possibility of a given isochromat moving across pixels on the time scale of the acquisition) that limits the resolution as the line broadening due to phase evolution also contributes. The signal phase is changed due to diffusion though a magnetic field gradient and this causes attenuation in the signal between successive pulses (43). The motion of the molecule during the presence of a gradient causes a phase shift in the magnetisation which is given by,

$$\phi = -\frac{2}{3}\gamma^2 G^2 D t^3 \tag{2.57}$$

This phase shift can be exploited by adding diffusion weighting gradients either side of the refocussing pulse in the spin echo sequence to generate a diffusion weighted image contrast and measure the diffusivity. Gradients are applied in multiple directions in order to measure a mean diffusion direction. The ratio of echo amplitudes with and without the presence of a gradient is given by the Stejskal-Tanner equation (44),

$$S(G)/S(0) = exp \left[ -\gamma^2 G^2 \delta^2 D \left( \Delta - \delta/3 \right) \right], \tag{2.58}$$

where $G$ is the diffusion weighting gradient strength, $\delta$ is the duration that each of the gradients are applied for and $\Delta$ is the time between the start of the first gradient and the start of the second gradient. Table 2.4 shows typical

ranges of diffusion coefficients for various systems that are often observed in NMR and MRI.

Table 2.4: Table showing typical range of diffusion coefficients (14)

| System | Diffusion Coefficient D ($cm^2/s$) |
|---|---|
| small molecule in water | $1 - 1.5 \times 10^{-5}$ |
| small protein in water | $10^{-8}$ |
| Protein in membrane | $10^{-10}$ |

## 2.10   Summary

In this chapter the basic concepts behind NMR were introduced and it was explained how the spin system interacts with itself and the surrounding environment. This is relevant for any further discussions of how (for example) polarisation can be transferred between spins and what mechanisms affect the lifetime of the polarisation.

An explanation of MRI and how different image acquisition sequences work has been presented, and finally a discussion of the limits on resolution was provided. This is essential to consider how micro imaging of hyper-polarised might be carried out and what resolution is achievable.

# Chapter 3

# Hyper-polarisation

## 3.1 Introduction

The aim of this chapter is to provide a general overview of the field of hyper-polarisation and give an insight as to how dissolution dynamic nuclear polarisation (D-DNP) works. Knowledge of these concepts will also prove to be important for understanding many of the design constraints on the hardware presented and will allow the reader to gain perspective on the reasoning behind decisions regarding hardware development.

In this chapter a number of the different techniques for creating a hyper-polarised NMR signal will be explained and the benefits and disadvantages will be briefly discussed. The available methods for engendering a liquid state hyper-polarised signal will be examined along with some reasons as to why a dissolution system may be preferable to other rapid melting methods that are available. The different mechanisms that drive the polarisation transfer in dynamic nuclear polarisation (DNP) will also be presented. Finally, the importance of the radical and the glassing agent will be explained.

## 3.2 Hyper-polarisation Methods

Hyper-polarisation is the term given to the technique of creating a spin system that has a level of polarisation higher than that predicted by the Boltzmann equation, where the population differences are greater than the expected thermal equilibrium level. There are many ways in which non-thermal polarisation can be generated, some of which will be explained here.

### 3.2.1   Spin Exchange Optical Pumping

Spin exchange optical pumping (SEOP) is a commonly used technique to produce hyper-polarised noble gas which can be used to image porous media, where the contrast arises from nuclear dependent relaxation properties. This can be used to investigate problems ranging from the interactions between molecules in vapour form, to diagnosing different stages of Emphysema (45).

SEOP involves polarising Rubidium ($^{87}Rb$) nuclei, using circularly polarised laser light which is applied parallel to the magnetic field, in order to transfer angular momentum to the electron spin. Spin exchange occurs from the Rubidium to a noble gas such as Xenon via Fermi contact collisions with the Rubidium (46). The unpaired electron in the outer shell can be optically excited on its $D_1$ transition using either positively or negatively circularly polarised laser light. This then has multiple relaxation pathways which it can follow due to the hyperfine splitting caused by the interaction of the electron with the $\frac{3}{2}$ nuclear spin (47). This builds up polarisation on the nuclear spin which is transferred to the noble gas via collisions.

### 3.2.2   Brute Force Polarisation

The main concept behind brute force polarisation is to cool a sample down to very low temperatures (e.g. 50 $mK$) at very high magnetic field strength (14 Tesla). Under these conditions a high level of polarisation is established according to the Boltzmann distribution of the populations.

After some polarisation time, which has to be much greater than the solid state nuclear $T_1$, the sample is then rapidly heated up via dissolution, and the enhanced liquid state NMR data can be collected. The dissolution has to be fast compared to the nuclear $T_1$ in the liquid state or the signal decays before the measurement takes place.

An experimental set-up such as this potentially allows many samples to be polarised at once, achieving polarisation enhancements in the liquid state on the order of 1500, where detection is carried out at 1 Tesla (48). However, this enhancement factor is significantly reduced when measurements are carried out at higher fields. The system also lends itself to the transportation of samples to different locations, provided there is no radical required to aid the relaxation (49). The disadvantage of the brute force polarisation approach is that at low temperatures and high magnetic fields the nuclear $T_1$ of many nuclei is extremely long. This means that the time taken for the magnetisation to build up is often on the order of days. For polarisation of nuclei that have typically long build up times, it is beneficial and more time efficient to also carry out cross polarisation from the protons to the nuclei of choice while in the solid state, as the proton $T_1$ is usually much shorter than for other, low gamma nuclei (50; 51).
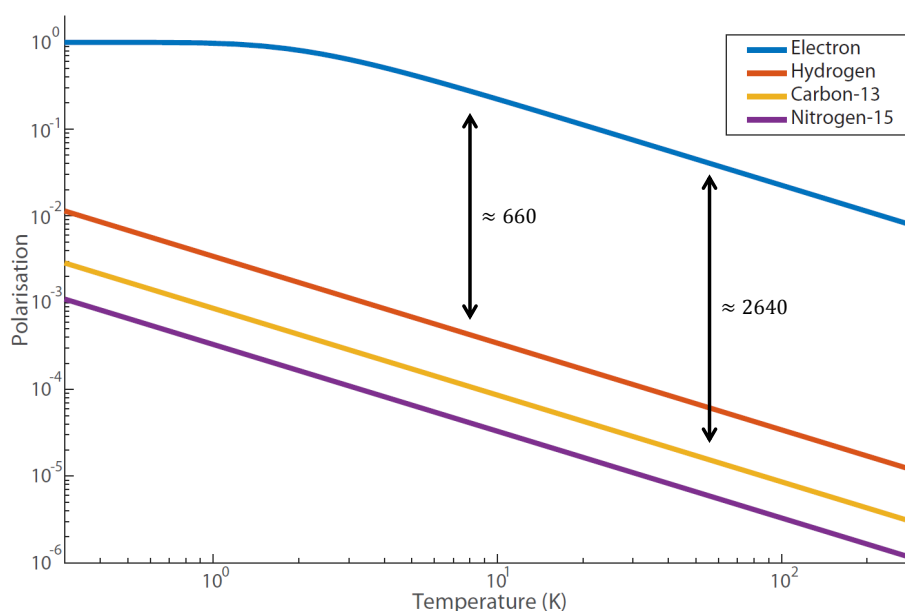
Figure 3.1: A log-log plot showing how the polarisation of the spin changes with temperature for three different spin species at a field strength of 3.35T.

### 3.2.3 Dynamic Nuclear Polarisation

The main focus of this chapter will be DNP and the mechanisms that drive the polarisation transfer. A very simplistic model will be presented before examining the intricacies of the different mechanisms and sample preparation.

DNP is essentially a method for increasing the population differences in the nuclear spin state by transferring polarisation from the electrons to the protons or other low gamma nuclei. This is advantageous as the electron's gyromagnetic ratio is much larger than that of any nuclear spin. The maximum theoretical enhancement achievable by transferring polarisation from the electron to the nuclear spin of protons is given by Equation 3.1.

$$\varepsilon = \frac{\gamma_e}{\gamma_n} \simeq 658.$$

(3.1)

Due to the gyromagnetic ratio of $^{13}C$ being a quarter of that of the proton, the achievable enhancement is 4 times larger, as shown in Figure 3.1.

In high field DNP the frequencies at which the transitions that drive polarisation transfer take place are in the microwave regime of the electromagnetic spectrum. The time that describes the polarisation increase is known as the build up time and this is loosely related to the $T_1$ of the nucleus being polarised. However, depending on the mechanism of polarisation transfer, other factors can affect this.

Figure 3.1 shows that in order to get the best enhancement from the polari-

sation transfer, it is beneficial to go to low temperatures, as at approximately 1.8 K the electron Boltzmann polarisation is very close to unity (at a field strength of $3.35T$) (52). The transfer from the electron to the nuclear spin is mediated by the pseudo-secular part of the hyperfine interaction. To obtain a sample in the liquid state a rapid temperature jump is performed. Frequently, the sample is transferred to a different field. The overall enhancement after sample transfer can be estimated by:

$$\varepsilon^* = \frac{\gamma_e}{\gamma_n} \frac{T_{liquid}}{T_{DNP}} \frac{B_{DNP}}{B_{liquid}} \times exp\left(\frac{-t}{T_1}\right).$$

(3.2)

Here $T_{liquid}$ is the temperature of the sample during the liquid state measurement, $T_{DNP}$ is the cryogenic temperature at which the solid state DNP experiment was carried out. This ration of the temperatures accounts for the Boltzmann factor that contributes to the overall enhancement. $B_{DNP}$ is the field strength of the magnet used for the hyper-polarisation and $B_{liquid}$ is the field strength at which the liquid state signal is acquired.

It is vital that the temperature jump is fast in comparison to the $T_1$ relaxation time of the nucleus of interest. Otherwise the hyper-polarised signal will decay before any liquid state measurement has been carried out. Several methods for how the rapid temperature jump may be carried out have been proposed and explored:

1. Laser heating

2. Hot gas

3. Microwave heating

4. Rapid dissolution

**Laser Heating**

This method has been explored to reasonable effect by Griffin *et al.* by using a 10.6 $\mu m$ infra-red laser and has shown promise at relatively high temperatures ($> 40$K) (53). This system is advantageous if small sample volumes are desirable (Griffin's experiment uses $9\mu L$ in a $2.5mm$ tube) where multiple experiments on the same sample need to be carried out. The benefit of the laser melting system is that the sample can then be refrozen and another experiment carried out. since it does not rely on the sample being highly soluble, it lends itself to studies of complex proteins and polymers that are expensive to buy in large quantities and poorly soluble (53; 54). The enhancement factor for the temperature jump experiment described by Griffin *et al.* is given by

$$\varepsilon_{TJ} = \varepsilon \times \frac{T_{liquid}}{T_{\mu wave}},$$

(3.3)

where $T_{\mu wave}$ is the temperature arising from the microwave irradiation. The room temperature enhancements achieved by this system when heating the sample from $90K$ are between $120$ and $400$ depending on the experiment (53).

**Hot Gas**

The use of hot (usually nitrogen) gas has been employed in rapid temperature jump systems for varying sample sizes and starting temperatures. This technique has been developed and built by van Bentum *et al.* In this system small sample volumes, on the order of nL, have been hyper-polarised at liquid nitrogen temperatures (55). Using DNP, the sample is polarised, after which the entire capillary containing the sample is shifted up through a sliding seal where the sample melting zone is located. At this point, hot nitrogen gas ($70^oC$) is passed across the capillary to melt the sample. A second shuttling stage moves the capillary into the detection zone, where a strip-line resonator is located. This, like the laser heating, works best for small sample volumes as otherwise the time required to melt larger samples becomes too long compared to the nuclear $T_1$. The enhancements achieved using this experimental set up are on the order of 400, where the polarisation and the liquid state measurement are both carried out within a single isocentre at a field strength of $3.4T$ (56).

**Microwave Heating**

Yoon *et. al.* (57) have used the microwave source that drives the DNP as a means to also melt the sample. The polarisation and liquid state measurements are done in situ on a $50\mu L$ sample. The microwaves generated at 0.5 W by a 260 GHz gyrotron are used for polarisation. To melt the sample the microwave power is ramped up to 100 W and applied for 1.5 seconds in a typical $^{13}C$ experiment (it is reduced for protons, as is the sample size). Typical enhancements for $^1H$ and $^{13}C$ are shown to be on the order of 40 and 550 respectively. The limitation of this system is that the high microwave power causes boil off of the sample during melting making repetition of the experiment unreliable (57; 58).

**Dissolution**

Dissolution of the hyper-polarised sample is currently the most common method for converting a solid state sample into the liquid state, with enhancement factors of $> 10000$ being achieved in some experimental set-ups (7). It is this type of method that the Dissolution-DNP system presented in this thesis is based upon.

Initially Ardenkjaer-Larsen discovered that it is possible to retain the higher than thermal solid state spin polarisation during a phase transition into the liquid state if the melting process is on a time-scale much less than $T_1$ (7).

The process is carried out by injecting a hot solvent at the frozen sample which dissolves it and then transferring the liquid sample into the detection area. This has been developed for both NMR and MRI in the form of the Oxford instruments HyperSense for NMR and preclinical MRI and the GE SpinLab for clinical applications which can achieve a liquid state polarisation on the order of $\geq 40$ percent (59). In a typical *in vivo* experiment, a hyper-polarised solution is created which can be injected into a patient in order to study (for example) metabolism of tumours.

The typical metabolites used in metabolism and cancer studies are required to have long longitudinal relaxation times and therefore do not suffer significantly from the comparatively slow time between dissolution and measurement. For spectroscopy however, the disadvantage of a stand-alone polariser is that the sample shuttling times to a high field magnet are long (on the order of 2 - 10 seconds) (60; 52) which make it difficult to observe fast relaxing molecules.

Dissolution DNP has been employed to great effect by Frydman *et. al.* in the analysis of metabolism of cancer cells (61). Here a Hypersense system was used to create hyper-polarised samples of $^{13}C_1$-pyruvate, which was then injected below a cell culture inside an 11.7 T measurement magnet. Under these conditions it is possible to observe how the pyruvate is converted to lactate within cancerous cells. Other systems, developed by Hilty *et. al.* have been designed in order to measure chemical reaction such as ligand binding (62). In this system a rapid dissolution is carried out where the liquid state sample is held at high pressure to ensure a short transfer time and to limit the effect of micro-bubbles in the sample (63). The system also employs an elegant rotary valve system to allow sample mixing.

Metabolic experiments *In Vivo* have been pioneered by Brindle *et. al.* where hyper-polarised pyruvate is injected into rats and both spectroscopy and imaging is carried out to assess the size of tumours as well as the stage of the cancer (64; 65). These experiments were carried out using the Hypersense and helped to push forward the development of the SpinLab for clinical use (66; 67). Recently the Cunningham *et. al.* showed that the technique can be used to study metabolism of the heart in animals and healthy volunteers in order to understand heart failure (68).

These types of *in vivo* study rely on the long longitudinal relaxation time of the metabolite to ensure that enough polarisation is retained during the sample transfer process. To overcome the problem of long sample transfer times a dual iso-centre magnet is used at Nottingham (69). The dual iso-centre system can deliver a liquid state in 300 ms and the dissolution procedure will be explained in detail in chapter 4 (69).

The drawback of using any dissolution system is that each experiment is a single shot process in which each sample can only be used once. This is because the sample is diluted by the hot solvent in the temperature jump process. Therefore minimizing the time taken to dissolve and transfer the sample and then measure the signal is of great importance in order to maximize the amount of information that can be extracted from one experiment.

## 3.3  DNP Mechanisms

There are several mechanisms by which polarisation can be transferred from electrons to nuclei. Each of which depends on slightly different experimental conditions. Experimental parameters such as the microwave irradiation frequency, the number of participating electrons and the ESR linewidth play a role defining which of the different DNP mechanisms will dominate the polarisation transfer. Here the different mechanisms of DNP will be examined and explained.

### 3.3.1  Overhauser Effect DNP

The first DNP pathway was proposed by Overhauser in 1953 (6) and then verified experimentally in the early 1960's by Carver and Slichter in NMR experiments on metallic elements dissolved liquid ammonia (70). The first experiment showing polarisation transfer in the liquid state, was carried out by Abragam and Goldman (71). Recently, Can *et. al.*(72) have shown that Overhauser DNP can also occur in insulating solids.

The Overhauser Effect is driven by saturating the electron transitions ($W_{EPR}$). Cross relaxation driven by the time dependent modulation of the hyperfine interaction causes a higher than thermal distribution of the populations. Fluctuations of the hyperfine interaction are on a time scale comparable to the electron Larmor frequency. In metals this modulation occurs due to the electron mobility, whereas in liquids it is due to molecular tumbling (72).

The energy level diagram in Figure 3.2 shows a spin system for a coupled electron and nuclear spin. The lowest energy state is given by $|\beta\alpha\rangle$ because the gyromagnetic ratio of the electron has the opposite sign to that of the nuclear spin. The rates for the single, zero and double quantum transitions are defined as $W_{EPR,NMR}$, $W_0$ and $W_2$ respectively. They define the probability for transitions. To drive polarisation transfer microwaves are applied to the $W_{EPR}$ transition, which equalises the populations of the electron spin. Relaxation then takes place along the different pathways at the given jump rates, causing the saturated electrons to return to the thermal equilibrium value, while leading to a build up of polarisation for the nuclear spin due to $W_{0,2}$.

The maximum enhancement achievable from polarisation transfer between electrons and protons is $\simeq \gamma_S / 2\gamma_I \sim 330$ if only dipolar relaxation occurs (73). The enhancement factor, the fractional increase in the intensity of $\langle I_z \rangle$ when $S$ is saturated compared with the thermal equilibrium $I_0$ is given by

$$\varepsilon = \frac{\langle I_z \rangle}{I_0} = 1 - \rho f s \frac{|\gamma_S|}{\gamma_I}, \tag{3.4}$$

where $\rho$ is the coupling factor, $f$ is the leakage factor and $s$ the saturation factor. The saturation factor describes the portion of the electron spins that are saturated by the microwave, which is defined as,

$$s = \frac{\langle S_0 \rangle - \langle S_z \rangle}{\langle S_0 \rangle}. \tag{3.5}$$

This gives a result between 0 and 1 depending on the level of electron saturation, where a value of 1 represents a fully saturated system (58; 74). The coupling factor is given by,

$$\rho = \frac{W_2 - W_0}{2W_1 + W_0 + W_2} \qquad \in [-1, 0.5], \tag{3.6}$$

where $W_2$, $W_0$ and $W_1$ correspond to the double, zero and single quantum transitions shown in Figure 3.2. $\rho$ is 0.5 if the coupling is purely dipolar and tends towards -1 as the coupling becomes dominated by the scalar interaction.

The leakage factor $f$ describes the amount of relaxation the nuclear spin experiences that is not due to the presence of the electron spin. This is verified experimentally by observation of the nuclear $T_1$ with and without the presence of the paramagnetic agent. The equation for the leakage factor is given by

$$f = 1 - \frac{T_1^{+e}}{T_1^{-e}}, \tag{3.7}$$

where $T_1^{+e}$ is the longitudinal relaxation time constant of the nuclear spin in the presence on the electron and $T_1^{-e}$ is the relaxation time constant without electrons. In the ideal case the leakage factor is 1, which occurs when the relaxation does not depend on the electron (75).

Due to the distance dependent nature of the dipole-dipole interaction, the Overhauser effect is often used for characterisation of molecules by measuring distances between nuclei based on the amount of polarisation transfer (73).
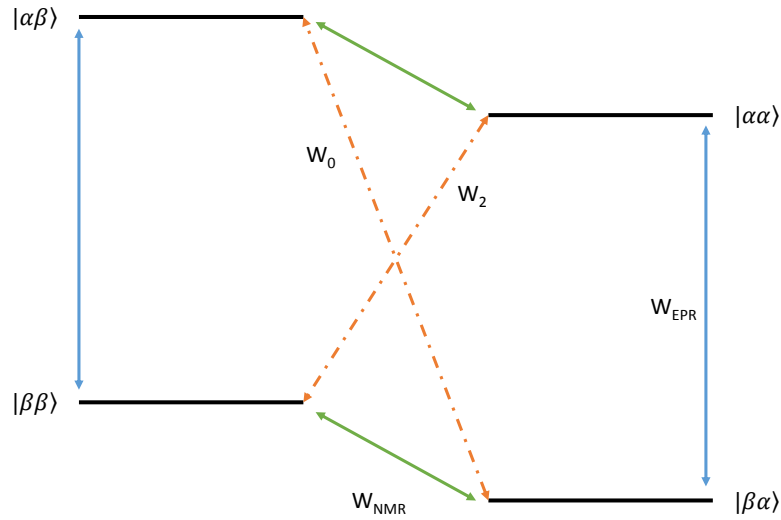
Figure 3.2: Diagram of the energy level transitions for an electron-nuclear spin system. $W_{EPR}$ and $W_{NMR}$ are the single quantum transitions that pertain to the electron and nuclear respectively. $W_0$ and $W_2$ are the zero and double quantum transitions.

### 3.3.2 Solid Effect

The solid effect (SE) only requires consideration of the interaction between one electron and one nuclear spin. It becomes the dominant polarisation transfer mechanism when the EPR linewidth of the electron spins in the solid state is smaller than the nuclear Larmor frequency (76).

Unlike the Overhauser Effect, the solid effect, as the name suggests, is a mechanism that only works in the solid state. Polarisation transfer is driven by exciting the 'forbidden' $W_0$ or $W_2$ transitions (see Figure 3.2), which at high field correspond to the microwave frequency range of the EM spectrum (77).

In the solid state the pseudo-secular part of the hyperfine interaction causes off-diagonal terms in the Hamiltonian, which lead to state mixing. The hyperfine Hamiltonian is expressed as:

$$\hat{H}_{hfi} = A\hat{S}_z\hat{I}_z + \frac{1}{2}\left(B_+\hat{S}_z\hat{I}_+ + B_-\hat{S}_z\hat{I}_-\right), \tag{3.8}$$

where $\hat{I}_{\pm}$ are the raising and lowering operators. $A$ represents the coupling constant for the secular part of the hyperfine interaction and $B_{\pm}$ represent the pseudo-secular coupling constants. In the liquid state these pseudo-secular terms are averaged out due to molecular motion. However, in the solid state the terms remain. This means that the pure electron-nuclear states shown in Figure 3.2 become mixed by the $S_zI_+$ and $S_zI_-$ terms of the Hamiltonian. The Hamiltonian, including the Zeeman interaction terms is given by:
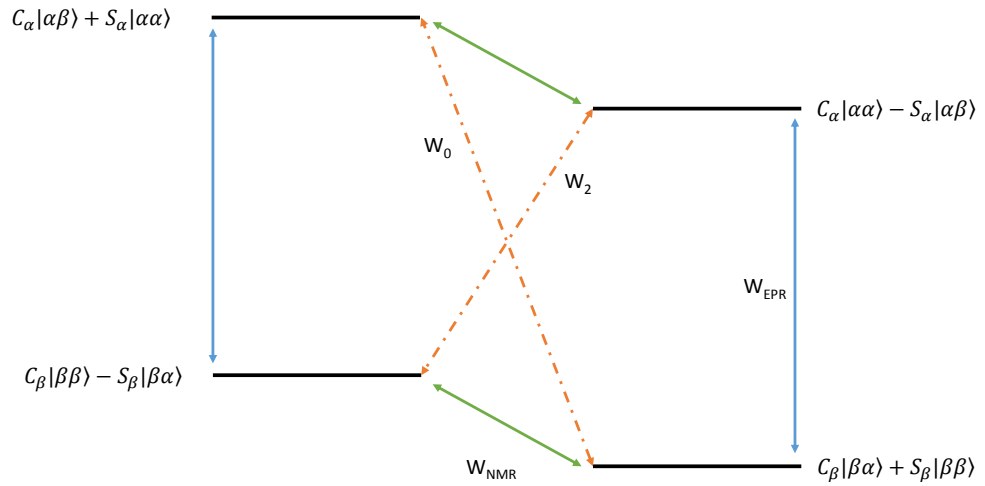
Figure 3.3: SE energy level diagram showing the single, zero and double quantum transitions along with the state mixing that drives SE DNP.

$$\hat{H} = \omega_e \hat{S}_z + \omega_n \hat{I}_z + A\hat{S}_z \hat{I}_z + \frac{1}{2}\left(B_+ \hat{S}_z \hat{I}_+ + B_- \hat{S}_z \hat{I}_-\right). \qquad (3.9)$$

In Equation 3.9 the first two terms represent the Zeeman interaction, the third term $(A\hat{S}_z \hat{I}_z)$ represents the secular part of the hyperfine interaction, which causes splitting of the energy levels (78). The final term determines the pseudo-secular part of the hyperfine interaction. The Hamiltonian can be represented in matrix form as,

$$\begin{pmatrix} +\frac{\omega_e}{2} + \frac{\omega_n}{2} + \frac{A}{4} & +\frac{B}{4} & 0 & 0 \\ +\frac{B}{4} & +\frac{\omega_e}{2} - \frac{\omega_n}{2} - \frac{A}{4} & 0 & 0 \\ 0 & 0 & -\frac{\omega_e}{2} + \frac{\omega_n}{2} - \frac{A}{4} & -\frac{B}{4} \\ 0 & 0 & -\frac{B}{4} & -\frac{\omega_e}{2} + \frac{\omega_n}{2} + \frac{A}{4} \end{pmatrix}. \qquad (3.10)$$

By diagonalising the Hamiltonian shown in Equation 3.10, carried out using Wolfram Mathematica (Wolfram, Oxford), the eigenvalues can be calculated to determine the energy levels. The off diagonal terms in the Hamiltonian cause the state mixing of the energy states which are now given as ($|\lambda_1'\rangle$ represents the lowest energy level and the prime denotes that there is state mixing)

$$|\lambda_1'\rangle = C_\beta|\beta_e\alpha_n\rangle + S_\beta|\beta_e\beta_n\rangle$$
$$|\lambda_2'\rangle = C_\beta|\beta_e\beta_n\rangle - S_\beta|\beta_e\alpha_n\rangle$$
$$|\lambda_3'\rangle = C_\alpha|\alpha_e\alpha_n\rangle - S_\alpha|\alpha_e\beta_n\rangle$$
$$|\lambda_4'\rangle = C_\alpha|\alpha_e\beta_n\rangle + S_\alpha|\alpha_e\alpha_n\rangle$$

$$(3.11)$$

The previously forbidden transitions between levels $|\lambda_1\rangle$ and $|\lambda_4\rangle$, along with $|\lambda_2\rangle$ to $|\lambda_3\rangle$ now have a finite probability due to the state mixing as demonstrated by Equation 3.11.

The constants that determine the level of state mixing, $C_{\alpha,\beta}$ and $S_{\alpha,\beta}$, are defined by the hyperfine coupling constants, where $C_{\alpha,\beta} = \cos\left(\frac{\eta_{\alpha,\beta}}{2}\right)$, $S_{\alpha,\beta} = \sin\left(\frac{\eta_{\alpha,\beta}}{2}\right)$ and $\eta_{\alpha,\beta} = \arctan\left(\frac{-B}{A\pm2\omega_I}\right)$. This can be rewritten in terms of a coupling coefficient $q$ which relates the initial states to the coupled states (e.g. $|1'\rangle = |1\rangle + q|2\rangle$), this is given as

$$q = \frac{3}{4}\frac{\gamma_S\gamma_I}{\omega_{0,I}}\frac{1}{r^3}\sin\theta\cos\theta\exp^{-i\phi}, \qquad (3.12)$$

where $q$ is the level of state mixing determined from first order perturbation theory (71). $\gamma_{I,S}$ are the nuclear and electron gyromagnetic ratios respectively, the terms $r, \theta$ and $\phi$ are the polar coordinates describing the electron-nuclear vector and $\omega_{0,I}$ is the nuclear Larmor frequency. The probability of a double-quantum or zero-quantum transition is calculated from these mixed states using second order perturbation theory which results in the probability being proportional to $4q^2$ (79; 80). The jump rate for the double and zero quantum transitions therefore becomes proportional to $\omega_I^{-2}$ (81; 78).

The microwave frequency required to drive these transitions is given by

$$\omega_{MW} = \omega_e \pm \omega_n, \qquad (3.13)$$

corresponding to an irradiation of either the $W_0$ or $W_2$ transitions. The effect of irradiating at the $\omega_e \pm \omega_n$ frequency for a narrow linewidth radical such as Trityl is shown in Figure 3.5.

The effect of the off resonant microwave irradiation of the electron on the nuclear polarisation is to equalise the populations of levels $|\lambda_1'\rangle$ and $|\lambda_4'\rangle$ or $|\lambda_2'\rangle$ and $|\lambda_3'\rangle$, depending on the microwave frequency. The population differences are increased further by the system attempting to retain a Boltzmann distribution by relaxation along the single quantum transitions ($W_1$) by $T_1$ relaxation. Due to the electron $T_1$ being much faster than the nuclear $T_1$
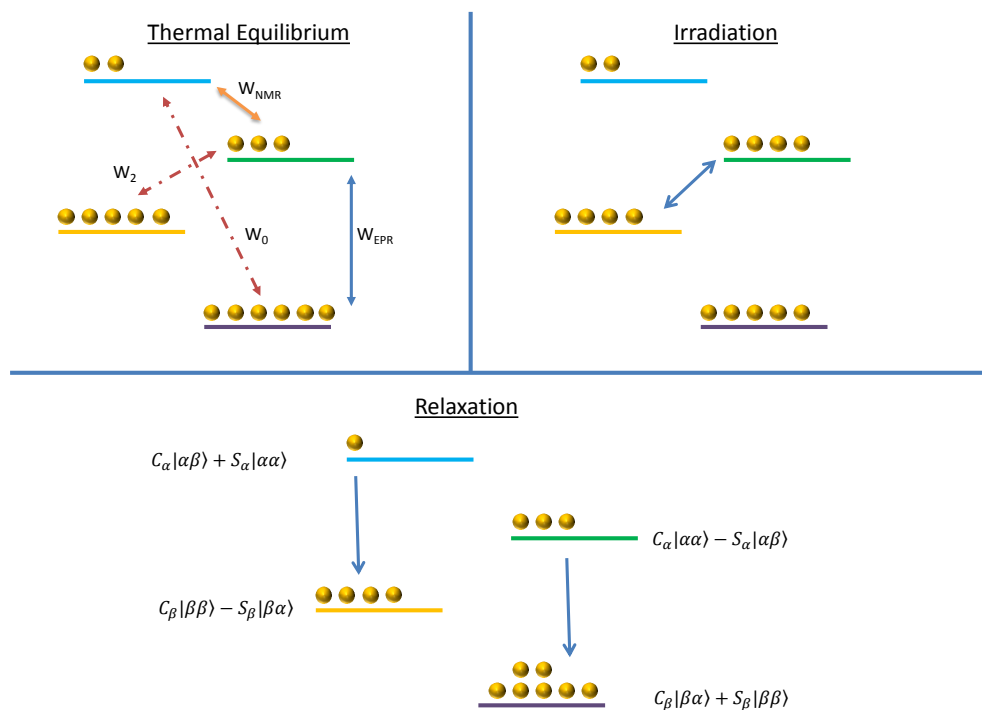
Figure 3.4: SE energy level diagram showing effect of irradiation of the double quantum transition and how the relaxation via the single quantum transitions adds to the population differences.

the polarisation can be built up analogous to a pumping effect. This process is highlighted in Figure 3.4.

Polarisation is transferred to the bulk nuclei from nuclei local to the electron via the dipole-dipole interaction in a process known as spin diffusion, which acts through coupled spin flip-flops (16; 82).

Due to the proportionality between the transition rates and the magnetic field strength, the solid effect becomes less efficient at higher fields. As the field is increased the energy difference between the levels also increases, therefore there is a higher energy gap to cross at higher fields. The field dependence required polarisation experiments to be carried out at lower fields than the observation. This has become less of a problem since the introduction of high power microwave sources at very high frequencies (83; 84; 85).

### 3.3.3 Cross Effect

The cross effect (CE) is a mechanism of polarisation transfer that involves one nuclear spin and two coupled electron spins as shown on the left hand side of Figure 3.6. The two coupled electrons must have different Larmor frequencies in order to meet the criteria for polarisation transfer (86).

The presence of the second coupled electron spin causes, under certain condi-
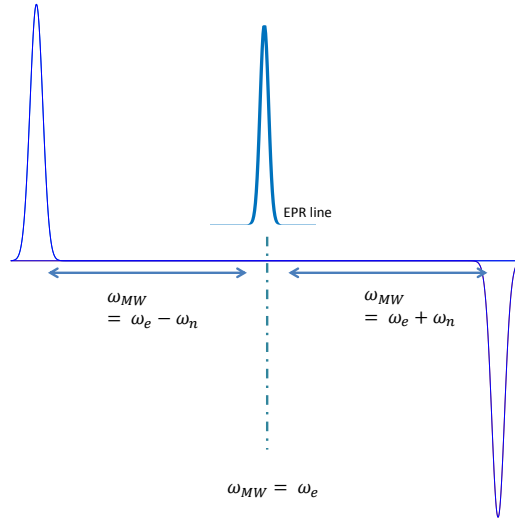
Figure 3.5: Schematic of a DNP sweep curve and EPR line of the electron in a two spin system that is strongly obeying the Solid Effect condition.

tions, degeneracy of the energy levels. Therefore, transitions between $|\beta\alpha\beta\rangle$ and $|\alpha\beta\alpha\rangle$ become allowed (87) where the spin states are given in the form of $|e_1, e_2, N\rangle$ ($e_{1,2}$ are the electron spins and $N$ is the nuclear spin). The degeneracy means that the cross effect is driven by irradiation of the electron along allowed transitions (). Three spin flip-flops between the degenerate states mediate the polarisation transfer from the electron to the nuclear spin and are caused by the dipolar fluctuations (88; 89). This can be visualised in the energy level diagram shown in Figure 3.7. The condition that allows this to occur is given by Equation 3.14, where polarisation transfer occurs when the difference between the Larmor frequencies of the two electrons is equal to the nuclear Larmor frequency (90; 91)

$$\omega_I = |\omega_{S1} - \omega_{S2}|. \tag{3.14}$$

When the inhomogeneous broadening of the electron linewidth is larger than the nuclear Larmor frequency, the CE matching condition is met (89; 92). This inhomogeneous broadening is caused by separate electron resonances arising from electrons having a strong g-anisotropic interaction.

An on resonant single quantum transition, where microwave irradiation of one electron mediates as a double or zero quantum transition of the second electron and the nuclear spin. As with the solid effect case, $T_1$ relaxation of the electron towards a Boltzmann distribution of the populations increases the nuclear population differences further. The achievable enhancement is directly proportional to the difference in the polarisation of the two electrons (94). This is expressed as

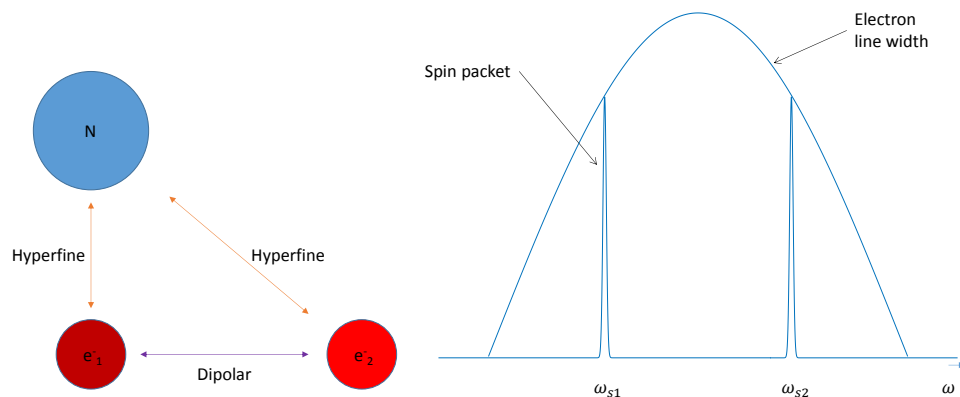$$P_n = \frac{P_a - P_b}{1 - P_a P_b}. \tag{3.15}$$

56

Figure 3.6: Left: Diagram of interactions between electron and nuclear spins for the cross effect. Right: Inhomogeneous line broadening of the EPR spectrum due to the two electrons.
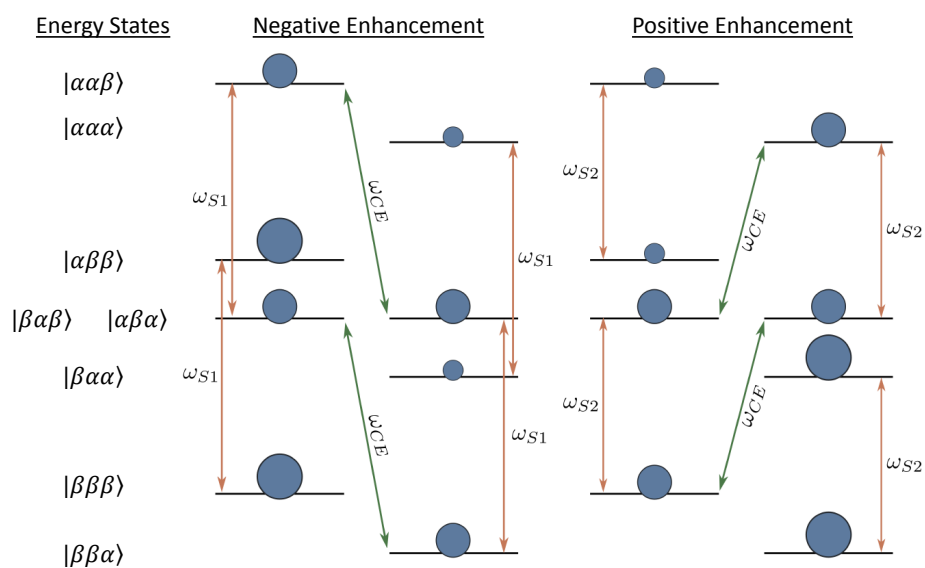


Figure 3.7: Energy level diagram for a 3 spin system, showing the positive $(\Delta\omega_S = +\omega_I)$ and negative $(\Delta\omega_S = -\omega_I)$ enhancement due to cross effect transitions. The relative population is represented by the size of the circle. The spin states are given in the form of $|e_1, e_2, N\rangle$ Polarisation is built up due to the flip-flops across degenerate levels between the $|\beta\alpha\beta\rangle$ and the $|\alpha\beta\alpha\rangle$ states and relaxation of the electron. Recreated from (93).

Figure 3.8: Spin temperature diagram for 4 quantum states (solid lines) with equally spaced energy levels. (a.) Thermal equilibrium where populations follow Boltzmann distribution. (b.) Spin temperature is zero giving unity polarisation. (c.) populations are evenly distributed, therefore the spin temp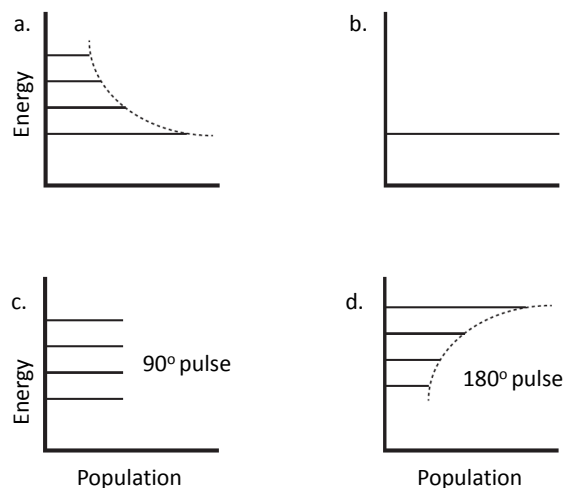erature is $\inf$ - equivalent to a perfect $90^o$ pulse. (d.) Populations are inverted where $T_s = -T_{eq}$ - equivalent to a perfect $180^o$ pulse.

Where $P_n$ is the nuclear spin polarisation and $P_{a,b}$ is the polarisation of the two electron spins. The equation holds for electron Larmor frequencies $\omega_a > \omega_b$ (94). As the polarisation transfer is dependent on allowed transitions and the difference between the electron Larmor frequencies, the efficiency of the enhancement scales with the Zeeman splitting $(B^{-1})$ , as opposed to the SE enhancement which scales with $B^{-2}$ (79). This makes the cross effect more effective for polarisation transfer at high magnetic fields.

## 3.3.4   Thermal Mixing

Thermal Mixing (TM) describes polarisation transfer in a system of many electron spins coupled to many nuclear spins. The model uses the high temperature approximation, shown in Equation 2.18, to relate polarisation to the concept of spin temperature $(T_s)$ (95). Therefore, a non-thermal polarisation is represented by an apparent temperature given the measured polarisation level. Visualisation of how energy level populations and spin temperature relate is in Figure 3.8.

TM is the dominant DNP mechanism when the EPR linewidth is greater than the nuclear Larmor frequency and when the EPR line broadening is homogeneous (although it can also occur with some inhomogeneous broadening (96; 86)), this means that the microwave irradiation at a frequency close to $\omega_S$ will saturate the entire EPR line.

In order to describe the TM process it is usual to divide the Hamiltonian into three thermal reservoirs, the electron-Zeeman reservoir (EZR), the nuclear-
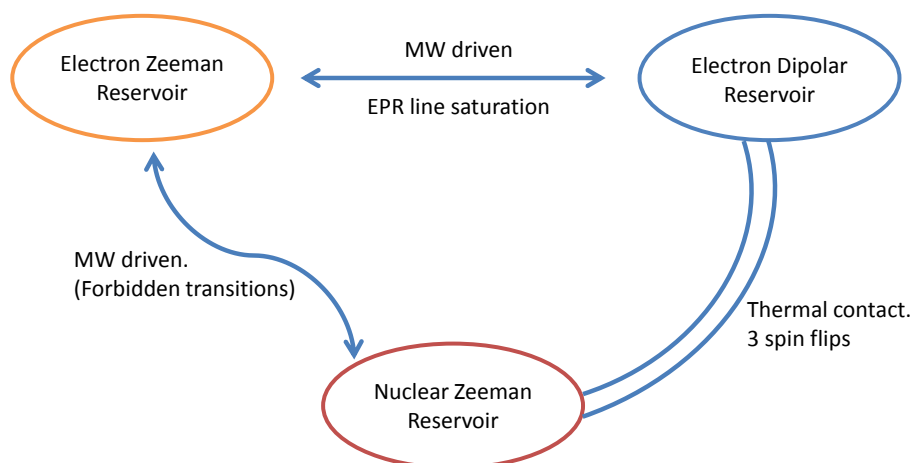
Figure 3.9: Off resonant irradiation reduces the spin temperature of the dipolar reservoir. The NZR is cooled by a three spin flip (between two electrons and one nuclear spin) due to thermal contact with the EDR. Irradiation of forbidden transitions (equivalent to solid effect transitions) also results in a cooling of the NZR.

Zeeman reservoir (NZR) and the electron dipole-dipole reservoir (EDR). In the rotating frame of the electron-Zeeman interaction, the electron and nuclear-Zeeman reservoirs are in contact, which means the off resonant microwave drives allowed transitions, cooling the NZR (97).

The EPR line saturating field ensures strong contact between the EZR and the EDR. Thermal contact between the EDR and the NZR causes three spin flips, providing a further cooling of the NZR (96; 98). The role of the microwaves and the EDR in cooling the NZR is demonstrated in Figure 3.9 (97).

The typical radicals and the radical concentrations used in the experiments presented in this document means that it is unlikely (but not impossible, see (99; 96)) that TM plays a large role in the polarisation transfer given the typical EPR line widths and radical concentrations used in the experiments presented in the subsequent chapters.

## 3.4   Radical

DNP requires unpaired electrons to be present that act as a source of polarisation for the surrounding nuclei. Therefore, it is usual that the sample is doped with a radical compound during preparation. The position of the electron carrying nuclei in the radical is important for the DNP mechanism as a well shielded electron, far away from any magnetically active nuclei, will have a narrow EPR linewidth (100).

For SE-DNP a mono-radical that have a well shielded electron giving them a narrow EPR linewidth, such as Trityl or BDPA is used (101). For CE-DNP a

high concentration of a mono-radical such as TEMPO or a specially designed bi-radical like TOTAPOL is preferable, as these have much larger EPR line widths, due to the strong g-anisotropy and the strong hyperfine interaction between the electron and the nitrogen nuclei. Examples of EPR spectra of some of these radicals are shown in Figure 3.10 (101; 86; 102).
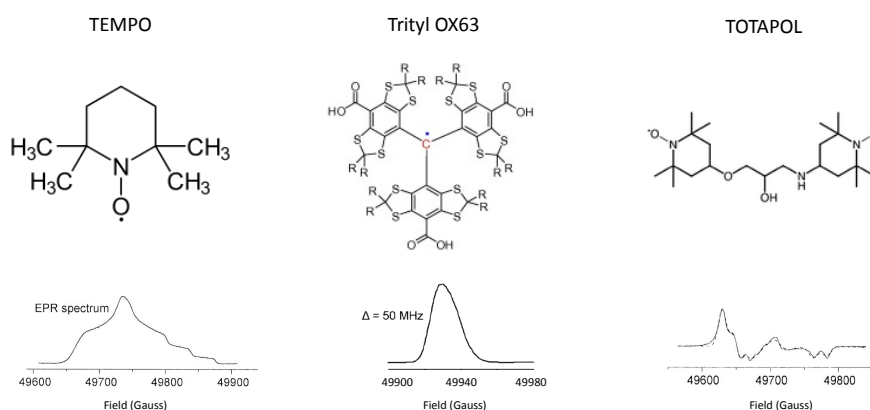


Figure 3.10: Radicals for DNP and their typical EPR lines at 140 GHz. Left shows the poorly shielded mono-radical tempo. The central radical is Trityl and has a narrow linewidth due to the electron being shielded at the centre of the molecule from magnetically active nuclei. Right shows a typical bi-radical (TOTAPOL) where there are two electrons that are not well shielded, leading to large ESR lines. (93; 86)

The concentration of the radical in the sample will affect the polarisation process as the paramagnetic agent will also cause an increase in the nuclear longitudinal relaxation rate. Another consideration to take into account is that as the concentration is increased, the proximity of the radicals in the sample also increases. This changes the line-shape of the EPR spectrum and, it is possible to activate the TM and CE-DNP mechanisms with a high concentration ($> 30\ mM$) of a narrow linewidth radical like Trityl (103; 99; 96). Typically the concentration of this radical for SE DNP (at 3.34 T and $< 4k$) is 15 mM (102).

## 3.4.1 Radical Removal

Even though the concentration of the radical is low (¡ 1 mM) in the final dissolved sample, for preclinical and clinical uses, such as monitoring metabolic processes within tumours (66), it may be important to remove it as it may be harmful and also has a negative effect on the liquid state nuclear $T_1$. It is also beneficial for polarisation storage as at low temperatures the strong dipolar interaction with the paramagnetic centre causes rapid $T_1$ relaxation in low fields (104; 105; 49). Removing the radical for clinical and preclinical uses means that it cannot harm the patient or animal into which the hyper-polarised solution is being injected, it also means that the $T_1$ of

the hyper-polarised nuclei can be preserved in both solid and liquid state (106).

A further possibility that has been presented by A. Comment *et al.*, and is currently under investigation by J. Ardenkjaer Larsen *et al.*, is the use of UV light induced free radicals in samples such as pyruvic acid (107; 108). Pyruvic acid undergoes a photodecarboxylation when exposed to UV irradiation at low temperatures. This process is capable of producing free electrons on the $2^{nd}$ carbon site in the molecule, at the concentrations required for DNP (109). The radical can be easily removed by a "thermalisation process" which involves warming the sample to bring the free electron back into a bound energy state. This temperature increase does not need to melt the sample, which means that long $T_1$ of the hyper-polarised nuclear spin in the solid state can be utilised. This has potential applications for storing hyper-polarised samples for long periods of time allowing them to be distributed to scanners that are not located close to a polariser (107; 109).

## 3.5   Glassing Agents

A glassing agent is often added to the sample in conjunction with the radical to create an amorphous solid that prevents the sample becoming a crystal structure when subjected to cryogenic temperatures. The glassing agent can also act as a cryo-protectant for biological samples (110).

In order to allow for an even distribution of the radical and to allow the necessary interaction between the radical and the nuclei it is important that the sample does not form a crystal structure. A typical DNP glassing agent used by Griffin *et al.*, colloquially referred to in the DNP community as 'DNP juice', is $d_8$-glycerol/$D_2O$/$H_2O$ with ratios of 60/30/10 (83). This is used as it provides a flexible, partially deuterated sample that forms an amorphous solid at cryogenic temperatures. Griffin used a partially deuterated sample in order to retain a good level of spin diffusion while also increasing the nuclear $T_1$. However, there is some debate as to the necessity of the deuterium in the glassing matrix (113). Although initially relevant to the topic of solid state MAS DNP, the effect of deuteration is still relevant in D-DNP as it will have a profound effect on the final achievable polarisation.

### 3.5.1   Glassing Solvent Deuteration

It has been shown that full deuteration of the glassing solvent leads to a increase in the $^{13}C$ signal enhancement when radicals with wide EPR line-widths are used. However, when a narrow linewidth radical, such as Trityl is used the presence of the deuterium has an adverse effect on the polarisation (101), as shown in Figure 3.11.

This effect is explained by examining the TM picture in a heteronuclear system by associating each different nucleus with a Zeeman energy reservoir. These have thermal contact with the electron dipolar reservoir of which the strength is determined by an associated heat capacity ($C_z^n$) where $C_z^n \simeq N\omega_n^2$ and $N$ is the number of spins. Given this picture, it is clear that $C_z^{1H} > C_z^{2H}$ and as such, when the EDR is in contact with both of these baths it will preferentially cool the $^1H$-NZR. Therefore removal of the protons from the system allows preferential cooling of the $^{13}C$ NZR. For radicals with a narrow EPR line, the $^1H$-NZR is no longer strongly coupled to the EDR. This means that it is no longer preferentially cooled and that increasing the number of deuterium spins in the system will cause the $^2H$-NZR to act as a heat sink, thus reducing the cooling power to the $^{13}C$-NZR (101; 111; 113). This is demonstrated in the schematic shown in Figure 3.12.

Some organic solvents of interest are known to be self-glassing, therefore the addition of a glassing agent is not required. This is especially useful for samples that are for in-vivo clinical studies as the glassing agent may well have negative effects on subject. One such self-glassing molecule is the free pyruvic acid (113). This is highly popular as it can be used as a bio-marker for determining the metabolising pathways of a tumour.
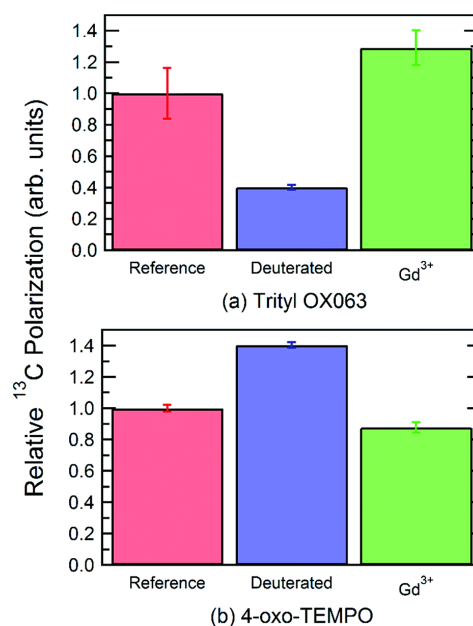


Figure 3.11: Result of deuteration of the glassing matrix for Trityl and TEMPO radicals as published by Long *et al.* in (111; 112). For the narrow linewidth radical Trityl, presence of deuterium inhibits the polarisation. However for TEMPO where the line is broad, the opposite is true. The $Gd^{3+}$ does not effect the linewidth of the electron but is thought to improve the enhancement by reducing the electron Zeeman relaxation time. The sample followed Griffin's typical DNP juice recipe (83).

$$C_z^{2H} < C_z^{13C} < C_z^{1H}$$
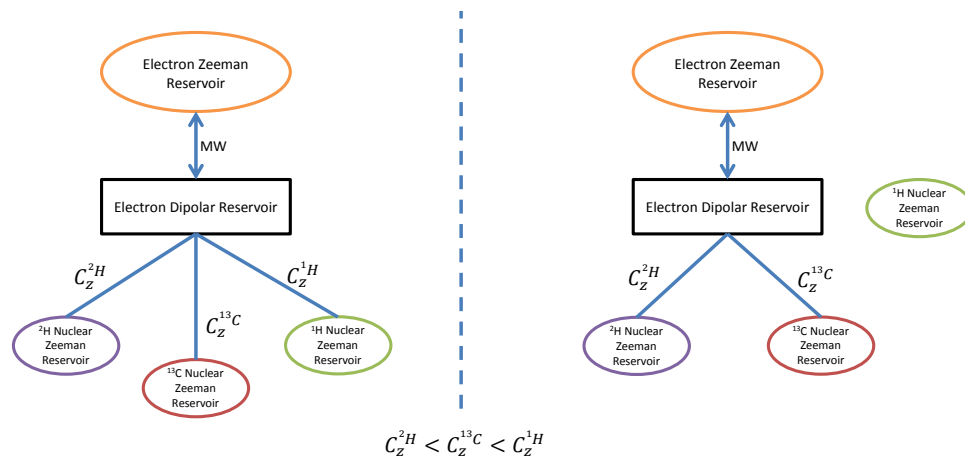
Figure 3.12: Diagram showing how the thermal contact causes the $^1H$-NZR to act as a heat sink for the EDR, preventing efficient cooling of the $^{13}C$-NZR when the EPR line is wide (left). The $^2H$-NZR acts as a heat sink when the EPR line is narrow and no longer covers the proton frequency, meaning that there is no thermal contact with the $^1H$-NZR (right). (111).

## 3.6 Summary

This chapter has presented the principal mechanisms driving DNP along with a brief overview of some of the techniques used to create a hyper-polarised spin system. The chapter has alluded to some of the hardware and sample related challenges that are encountered when using DNP. This gave the reader an insight into the complexity of working with DNP.

# Chapter 4

# Dissolution DNP: Experimental Set-up and Results

## 4.1 Introduction

Nuclei with short $T_1$ relaxation time constants are very difficult to measure with standard dissolution DNP systems as often, for a stand alone polariser, there is a long transfer time between the polariser and the magnet used to acquire the NMR signal (60). However with the use of the dual iso-centre system presented in this chapter it is possible to measure hyper polarised signal from molecules that process a $T_1$ relaxation time on the order of 0.5 s by limiting the transfer time and for nuclei with longer time constants more polarisation is retained.

This chapter presents the hardware aspects behind carrying out D-DNP in a dual iso-centre magnet as well as some of the challenges faced in finding a experimental set-up that provides consistent levels of polarisation enhancement.

Experiments are described using several biologically relevant molecules to determine the level of enhancement and relaxation times. A hardware characterisation is carried out using [1-$^{13}$C] sodium acetate and then the achievable enhancement and relaxation times of the hyper polarised signal for glucose, pyruvic acid and aspartic acid are summarised. These model compounds were used to demonstrate the advantage of the rapid dissolution achieved by the dual iso-centre magnet. The results also provide a way of assessing the limit of detection due to the average enhancement achieved in a single experiment.
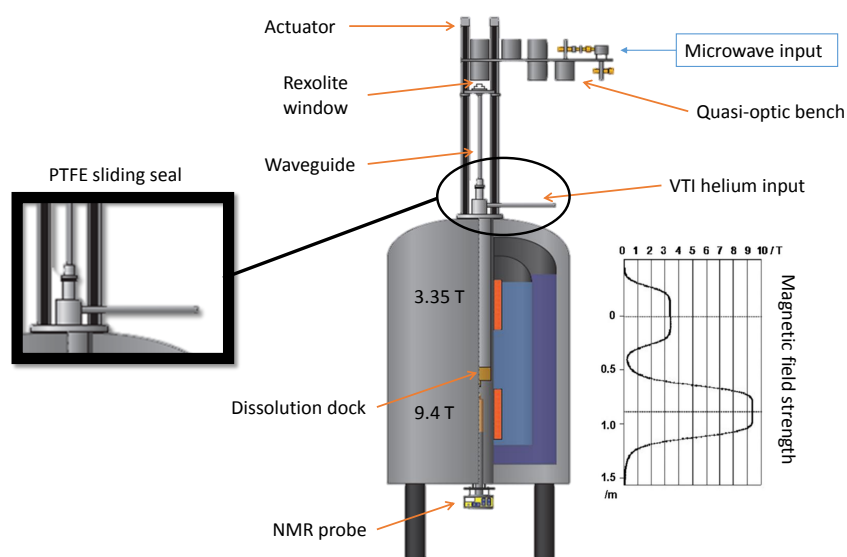
Figure 4.1: D-DNP experimental set-up using the dual iso-centre magnet. The schematic shows the field strength distribution across the height of the wide bore magnet. The microwaves are passed though the quasi optic-bench before being delivered to the sample by the actuator mounted wave guide. A PTFE sliding seal provides a vacuum tight seal at the top of the cryostat whereas the bottom is sealed by the dissolution dock. Figure reproduced with permission from the author (114).

## 4.2 Dual Iso-centre System

The purpose of the dual iso-centre magnet is to achieve high levels of polarisation enhancement while being able to minimise the time between polarisation, dissolution and measurement stages. The dual iso-centre magnet consists of two magnets contained in a traditional magnet casing. The polarising field of 3.35 T is directly above the measurement field of 9.4 T. A schematic of the dual iso-centre DNP magnet is shown in Figure 4.1 where the field strength across the length of the magnet is also plotted (8). The sample never experiences a magnetic field strength less than (approximately) 0.5 T during the shuttling and dissolution process. The vacuum is maintained during the shuttling through a PTFE sliding seal. Microwaves are delivered to the sample through a Rexolite window at the top of the wave guide.

### 4.2.1 Microwave Hardware

A 20 $\mu$L sample is initially contained in a small Rexolite cup (shown in Figure 4.2) situated at the end of the 1.96 m long stainless steel corrugated wave guide which is moved by an actuator. The Rexolite cup allows microwave to pass through while being able to maintain its strength at both low and high temperatures and the open bottom allows the solid state sample to be flushed out easily in the dissolution process. A copper ring is added to
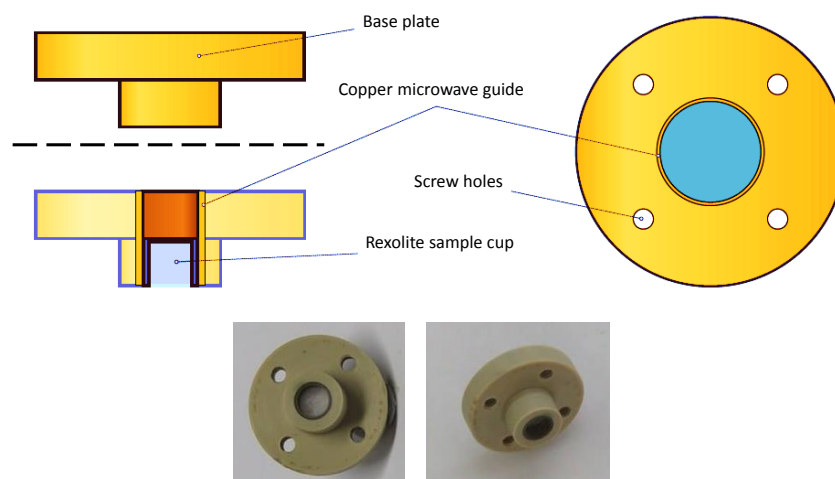
Figure 4.2: The sample cup is an open bottom Rexolite cup that is inset into a PEEK base in order to allow it to be mounted to the end of the wave guide. There is a copper ring around the Rexolite cup to guide the microwaves. the cup is attached to the end of the wave guide with 4 brass screws.Figure reproduced from (114).

the dissolution cup with the aim of restricting the loss of microwave power outside the sample space. The ring and Rexolite cup are secured in a PEEK base plate to allow the sample to be attached to the wave guide.

Two different microwave sources have been used in conjunction with the experimental set-up presented in this chapter. The original source (Virginia diodes - Charlottesville, VA, USA) outputs a frequency of 11.75 GHz with a power of 180 mW and the source is tunable to $\pm0.1$ GHz of this frequency. The microwaves were fed through three frequency doublers which achieve a final frequency of 94.0$\pm$0.8 GHz. The system also requires a separate microwave counter to lock the source to the correct frequency and a voltage controlled attenuator. All of the characterisation experiments presented in this chapter were carried out with this microwave source.

Current experiments are carried out with a simplified system that does not require the use of a microwave frequency counter or any frequency multipliers. The microwave source is an ELVA VCOM-10 (ELVA-1 - Furulund, Sweden) which operates at a central frequency of 94.0$\pm$0.5 GHz with an output power of up to 200 mW. In both cases a Gaussian horn is used to feed the microwaves into the quasi-optic (QO) bench. The role of the QO-bench is to allow through air transmission of the Gaussian microwave beam into the top of the wave guide. The reason for this is to enable the wave guide to be free to move and not require a physical connection to the microwave source. A Rexolite window allows the vacuum within the cryostat to be maintained while providing a transparent path for the microwaves to enter the wave guide.

Figure 4.3 shows how the power of the microwaves changes with frequency for
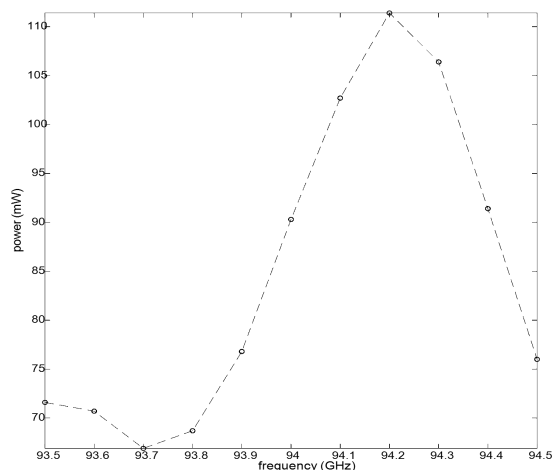
Figure 4.3: Graph showing the frequency dependence of the microwave power produced by the Virginia diodes microwave source. The peak power is 111 mW, which is 69 mW less than the stated maximum power.

the Virginia diodes microwave source, whereas no such frequency dependence on power dependence has been measured for the ELVA source. The power of the microwaves when set to the positive enhancement peak is a maximum of 73 mW measured from the reflected power using a zero bias detector. This means that in reality there is likely to be significantly higher microwave power delivered to the sample than that which is measured as the loss of the microwave optics and wave guide is reported to be approximately 9 dB attenuation (8).

## 4.2.2 Variable Temperature Insert

The sample is cooled in a variable temperature insert (VTI) produced by IceOxford (Abingdon, UK) which allows the sample to be cooled to temperatures less than 2 K. The cryostat is designed with an open bore to allow movement of the sample for dissolution. This differs from typical cryostats used by (115) where there is a bath of liquid He that cools the sample. This means that in the open bore VTI the sample is cooled by the continuous expansion of a small flow of liquid He.

A steel disk at the lower end of the cryostat provides a sturdy base to support the outer shield and the sample space wall. This produces a tight vacuum seal between these two walls which forms the outer vacuum jacket, which is maintained though the use of an Indium seal. The top of the cryostat uses a rubber O-ring seal between the outer wall and the head of the cryostat. The reason for this is to allow for the contraction of the VTI during cooling. As the cryostat cools the inside will contract much more than the outer shields due to the large temperature gradient, therefore the rubber seal is used to
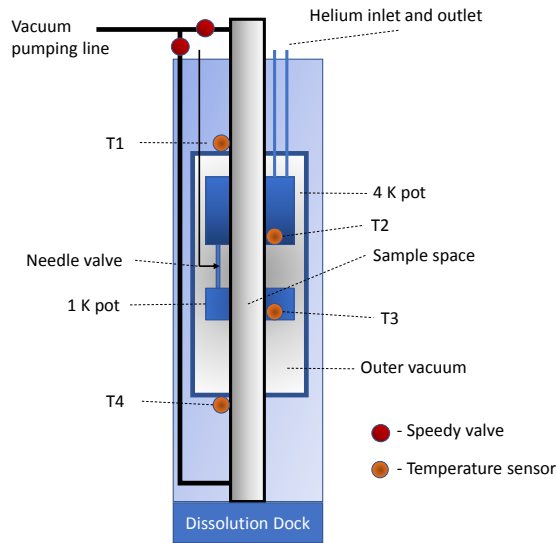
Figure 4.4: Schematic of the VTI. Pumping lines that allow pumping on both the top and bottom of the cryostat are shown and the position of the temperature sensors is shown.

allow some vertical movement of the outer wall, reducing internal stresses. This contraction in fact causes the top of the airlock to become miss-aligned with the wave guide and applies unwanted lateral force to the wave guide which can compromise the PTFE sliding seal. The VTI is supported by a stainless steel flange welded to the top of the outer shield of the cryostat which has six holes to allow guiding pins to keep it secured to the top of the magnet. A PTFE spacer at is attached to the bottom of the cryostat to ensure a snug fit with the bore of the magnet. This has to be replaced after a number of experiments as it becomes stretched with the expansion and contraction of the VTI.

The liquid He is delivered to the sample from a separate He dewar via the inlet shown in Figure 4.1. An intermediate stage called the 4 K pot acts as an internal reservoir of liquid He. During the initial cooling period only a small flow of cold He gas is allowed though the VTI as the 4 K pot is filled and the temperature of the entire VTI is brought down. A needle valve is used to regulate the He flow between the 4 K pot and the sample space.

Two pumps (Pfeiffer DUO 65 M - Asslar, Germany and Leybold RUVAC - Cologne, Germany) are used to provide the vacuum required to allow the Joule-Kelvin expansion of the He required for cooling. Speedy valves control the pumping lines directed to the top or bottom of the open bore cryostat which allows even pumping on the sample space.

Multiple carbon ceramic temperature sensors are used to monitor the progress of the cooling in conjunction with return He flow meters for the bore and transfer line. Observation of the pressure and flow are vital in achieving the lowest and most stable temperatures. The temperature sensors require a constant current source of $10\ \mu$A and a temperature dependent voltage is measured by a Labview program using a voltage/temperature calibration

Table 4.1: Temperature sensor labels and the position they monitor in the cryostat

| Sensor | Position |
|--------|----------|
| T1 | 50 K heat shield (top) |
| T2 | 4 K pot |
| T3 | sample space[1] |
| T4 | 50 K heat shield (bottom) |
| T5 | Room temperature resistor[2] |

curve. The five sensors are labelled from T1 to T5 and the positions are given in Table 4.1 and are visualised in the schematic of the cryostat shown in Figure 4.4.

In the initial cooling stage the VTI is kept between 200-800 mbar by applying a slight vacuum to the bottom pumping port of the cryostat, using only one of the two pumps. This draws a small flow of cold He gas through the VTI and allows an even cooling of the entire cryostat. Once 15 - 30 K is reached on T3, the pressure is reduced and the He flow is also reduced to lower the temperature further.

Once the temperature falls below 4 K the needle valve is adjusted to reduce the flow of He to the sample space and lower the temperature to approximately 1.7 k. Finally the second pump can be introduced to reach the minimum temperature. The lowest temperature that has been achieved is 1.4 K. However, it is preferable to maintain a higher temperature of (for example) 1.6 K for polarising to reduce the chances of sudden temperature fluctuations.

### 4.2.3   Sample insertion

The sample is introduced when the temperature of the cryostat (T3) falls below 100 K. The sample, fixed to the end of the wave guide, is frozen in a bath of liquid nitrogen outside of the VTI. An airlock is over-pressured with He gas while the actuator is moved down and a sliding seal secures the vacuum at the top of the airlock.

The actuator is torque rated to avoid damaging the inside of the cryostat in the event of a build up of ice. In the early stages of the development of the system the sample was rapidly shuttled between locations at 1000 mm/s which caused many problems with the cryostat and wave guide. In the current experimental configuration the shuttling process is carried out at 50 mm/s to avoid damage to the system.

---

[1]Temperature close to the sample, not the actual sample temperature.

[2]This is required to ensure the accuracy of the other sensor measurements by providing electrical continuity.

The sample is positioned at the centre of the polarising field where the microwave table is then rolled along a rail into position above the wave guide to allow the DNP experiment to be carried out. During this stage a "press" is carried out periodically as a precaution to ensure that the wave guide is not freezing in position. This is a very small movement downwards with a low torque rating that ensures no ice has built up. After polarisation the sample is moved to the dissolution dock (approximately 1 m).

### 4.2.4 Dissolution

Upon firing of the dissolution process the vacuum is released and the bore of the cryostat filled with an overpressure of He to prevent dissolution solvent escaping into the sample space of the cryostat. The sample cup, shown in Figure 4.2 is designed to form a seal with the dissolution dock to create a small mixing chamber where the hot solvent is stored before being pushed though to the waiting NMR tube.

Figure 4.5 shows the main components involved in the dissolution process. The solvent is injected into the pressurising tube via a manual three way port, typically between 5 and 10 ml of solvent is injected at this stage, although the amount that is used for the dissolution is significantly less.

The solvent is passed into a coaxial tube whereby it is heated with hot silicon oil pumped through the outer compartment. The oil is heated in an oil bath that maintains a temperature of 99 degrees in the bath, with the oil in the coaxial measuring between 85 to 95 degrees.

The progression of the solvent to the dissolution dock and then on to the NMR tube is controlled by two pneumatically driven Takasago valves (Takasago Fluidic Systems - Nagoya, Japan) before and after the dock. The pressurised air is supplied to the Takasago valves through solenoid valves away from the magnet which are controlled by the Labview program. The timing of the firing of the valves determines the final volume of the dissolution solvent in the NMR tube.

A slight vacuum can be applied to the NMR tube in order to ensure the solvent fills the tube without any air gaps. The vacuum also helps to improve the settling time as micro bubbles post dissolution settle quicker (8; 116).

The total time taken to transfer the hyper polarised solid state sample into the liquid state is 300 ms. However, as shown by Figure 4.6, there is a period of turbulence within the sample which causes line broadening in the NMR spectrum. The data was collected by observing the proton linewidth of 600 $\mu$L of water when it is flushed through the dissolution system. The experiment was carried out at room temperature and no sample was dissolved, The magnet was pre shimmed before the experiment using a 600 $\mu$L water sample. This indicates that an extra delay of at least 300 ms is required to allow for the sample settling.
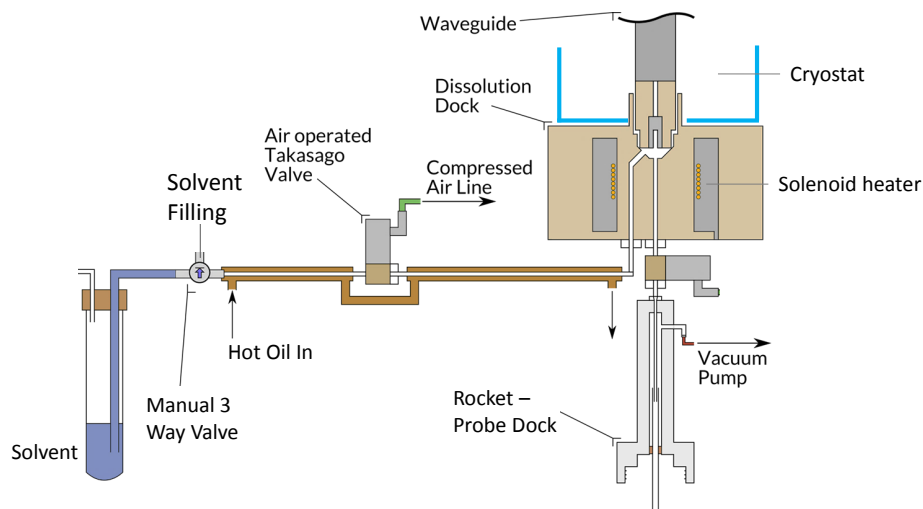
Figure 4.5: Schematic showing the experimental set-up of the dissolution system. the solvent is supplied to the system through a manual 3-way valve, it is pressurised with 5 psi of nitrogen gas and heated by being passed though the centre of a coaxial tube containing hot oil. Pneumatically controlled valves (Takasago) are used to allow the solvent to move to the sample space and then on to the waiting NMR tube.
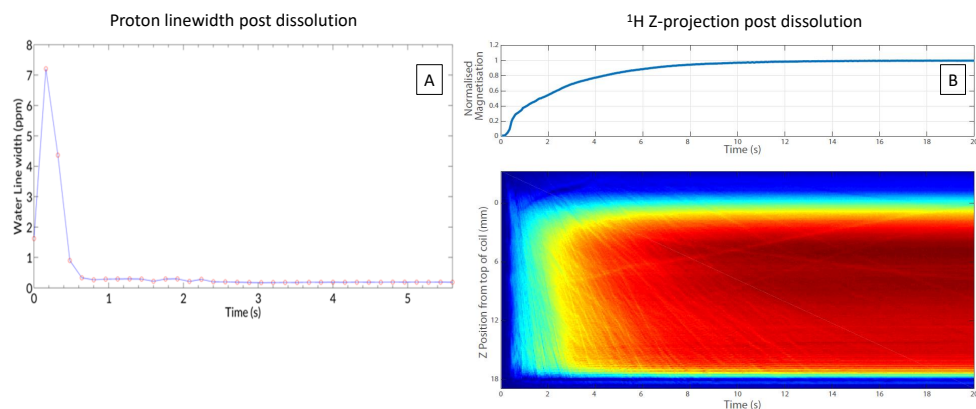


Figure 4.6: A: Graph showing the change in $^1$H linewidth as a function of time. The linewidth is measured as the full width half maximum of the water peak. The sample volume was 600 $\mu$L and the experiments were carried out at room temperature without a solute. The linewidth changes due to the settling of the turbulent system. B: Z-projection of protons during and post dissolution with no hyperpolarised sample present. The experiment was carried out with a series of small flip angle pulses and the solvent was at room temperature. The figure shows magnetization increasing as the solvent smends more time in the high magnetic field. Bubbles and agregates can be seen to move out of the sample. Data collected by A. Gaunt and B. McGeorge Henderson, the figure has been reproduced from (114).

Figure 4.7: The Figure shows how long it takes the system to cool down before and after a dissolution is carried out. The arrow d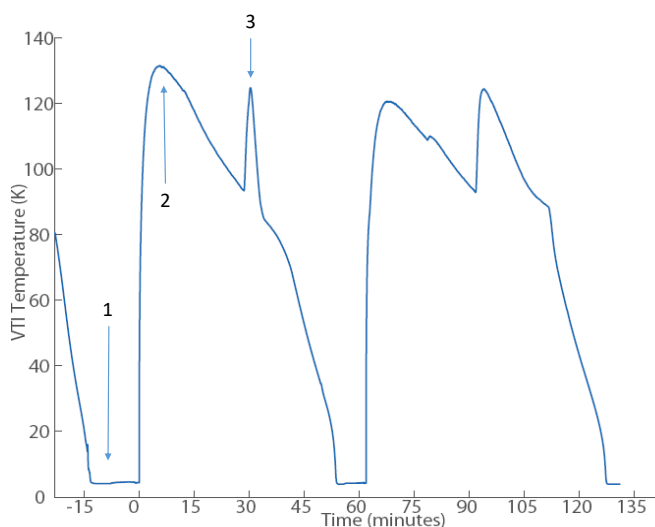enoting position (1) shows the stable period which would be used for polarising, the temperature is typically 1.8 k at this point. Position (2) is the point of dissolution, the need to overpressure the cryostat causes rapid heating. Position (3) shows the point at which the sample and wave guide are inserted.

The system is capable of doing multiple D-DNP experiments in one day due to the relatively rapid recycle time, as demonstrated by Figure 4.7. The figure shows how the temperature can be lowered fast enough to mean that the a dissolution can be carried out and a new sample is ready to be polarised within 60 minutes.

## 4.3  DNP experiments

Both solid state and liquid state experiments are presented in order to assess the capabilities of the dual iso-centre magnet. Biologically relevant molecules have also been tested to characterise potential metabolites for future imaging experiments.

### 4.3.1  Solid state experiments

Before considering different metabolites the DNP system itself must be tested. Initially, many of the experiments to test the repeatability of the D-DNP system were carried out on $[1-^{13}C]$ sodium acetate due to the fact that at 9.4 T the carbonyl $^{13}C$ has a liquid state $T_1$ of $22\pm2$ s. Solid state microwave sweeps and build up experiments were carried out to assess the required microwave frequency and duration for polarisation of $^{13}C$.

The results of the build up experiments are shown in Figure 4.8, where a microwave frequency sweep is also shown. This demonstrates that the
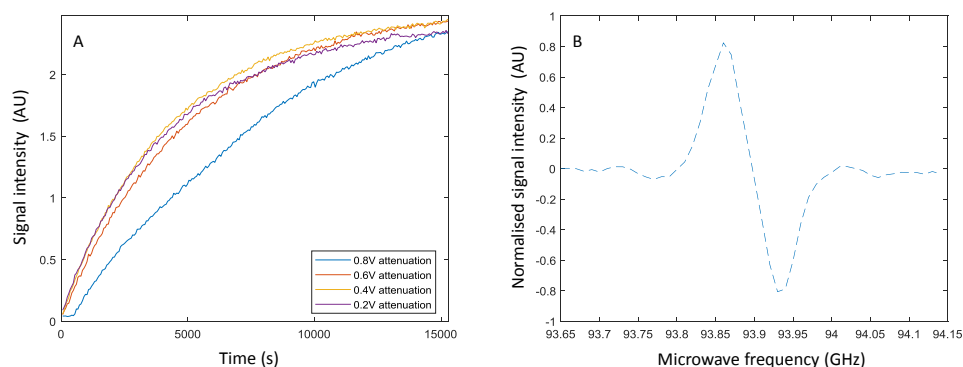
Figure 4.8: Solid state polarisation experiments using [1-$^{13}$C] sodium acetate. (A) Polarisation build-up curve of $^{13}$C labelled [1-$^{13}$C] sodium acetate for varying levels of attenuation. A higher voltage equates to a bigger attenuation. The curve shows that the fastest build-ups are achieved for the lower attenuation however the highest final polarisation is achieved for the 0.4 V and 0.6 V attenuation. This may well be partly due to microwave heating. (B) Microwave sweep for [1-$^{13}$C] sodium acetate. The double quantum transition gives the positive enhancement peak at 93.86 GHz and the zero quantum transition give the negative enhancement at 93.935 GHz. This data was collected by A. Gaunt and B. McGeorge Henderson and is also presented in (114).

Table 4.2: Solid state [1-$^{13}$C] sodium acetate build up times for varying levels of microwave attenuation.

| Attenuation (V) | Attenuation (dB) | Build up time (min) |
|:---:|:---:|:---:|
| 0.2 | 3 | 64 |
| 0.4 | 6 | 66 |
| 0.6 | 9 | 80 |
| 0.8 | 12 | 197 |

optimum frequency for the microwaves, to achieve a positive enhancement, is at 93.86 GHz. The build-up curves were carried out at different microwave powers in order to assess the effect on the build-up times. It was found that the optimum build-up time, while retaining a high level of $^{13}$C polarisation was achieved for an attenuation between 0.2 V and 0.6 V (approximately -3 and -9 dB). Table 4.2 shows the various build up times for each of the attenuation voltages. As a consequence of the solid state experiments, the dissolution experiments presented are all carried out with 0.2 V attenuation for the fastest build-up.

## 4.3.2  Dissolution Experiments

After the dissolution, longitudinal relaxation is typically measured with a train of small flip angle pulses and the $T_1$ of the resonance line is extracted by fitting an exponential. The equation that is used to fit the decay of the hyper polarised signal in order to extract $T_1$ is given by

$$S(t) = S_0 \exp\left(\frac{-t}{T_1}\right) \cos(\theta)^{(n-1)}, \qquad (4.1)$$

where $S_0$ is the initial signal, $\theta$ is the flip angle of the applied pulse and $T_1$ is the longitudinal relaxation rate constant (117). The equation takes into account the loss of longitudinal magnetisation due to the application of RF pulses. For small flip angles ($\sim 1^o$) and small values of $n$ this factor becomes close to 1 and therefore can be neglected so that only the exponential term remains.

The enhancement is calculated by comparison of the first spectrum after dissolution with an equivalent spectrum scan of the sample at thermal equilibrium. It is important to consider the effect of the addition of noise if multiple scans are required to obtain a thermally polarised spectrum. The enhancement when comparing SNR is given by

$$\varepsilon_{\mathrm{SNR}} = \frac{\mathrm{SNR}_{\mathrm{DNP}}}{\mathrm{SNR}_{\mathrm{therm}}\big/\sqrt{n}}, \qquad (4.2)$$

where $n$ is the number of averages used for the thermal acquisition.

### 1-$^{13}$C Sodium Acetate

Sodium acetate plays an important role in controlling uptake of liquids in the body as well as affecting metabolism and may be of interest in the future for monitoring biological processes (118). It has a simple molecular structure, good levels of polarisation enhancement and long $T_1$ relaxation times (118; 119).

Dissolution experiments were carried out on [1-$^{13}$C] sodium acetate to test the achievable enhancement. 20 $\mu$L of 1 M [1-$^{13}$C] sodium acetate in 50:50 water/glycerol solution, with 15 mM trityl was polarised for 90 minutes with a microwave attenuation of 0.2 V. This is, according to the build up curve, approximately 80 percent of the achievable polarisation enhancement in the solid state. The recorded spectrum and the relaxation curve is shown in Figure 4.9. The spectral width is not wide enough to observe the methyl group of the [1-$^{13}$C] sodium acetate or the peaks that arise due to the natural abundance $^{13}$C in glycerol.
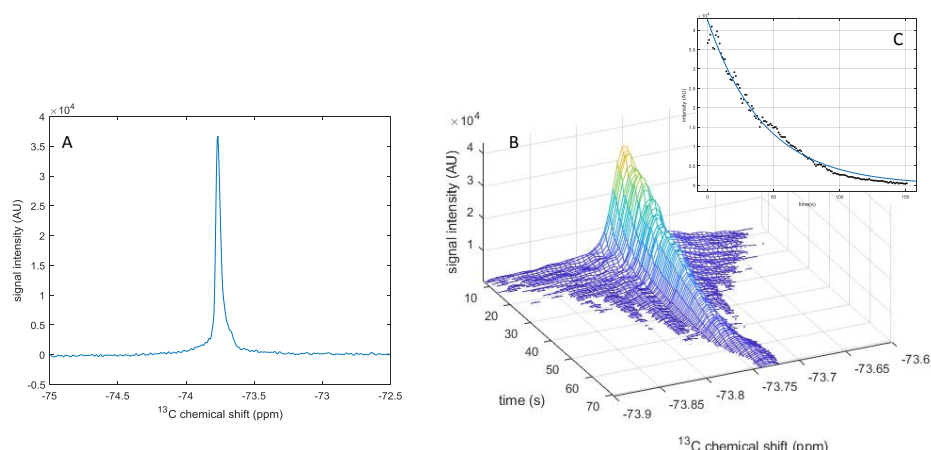
Figure 4.9: Dissolution DNP data for [1-$^{13}$C] sodium acetate. (A) First peak in the DNP decay curve. (B) Relaxation curve for [1-$^{13}$C] sodium acetate polarised for 90 minutes. (C) The inset figure shows the fitting of the decay curve to extract the $T_1$ relaxation time.

Table 4.3: Table showing the maximum measured enhancement for various relevant molecules as well as the $T_1$ measured in the liquid state.

| molecule | Maximum enhancement | $T_1$ (s) |
|---|---|---|
| [1-$^{13}$C] sodium acetate | 4700 | 22±2 |
| Glucose ($^2$H) | 5000 | 22±1 |
| Aspartic acid | 5500 | 4.9±0.5 |
| [1$^{13}$C] pyruvic acid | 7000 | 70±2 |

The measured $T_1$ and polarisation enhancement is given in Table 4.3 along with other biologically relevant molecules that have been tested.

The average enhancement achieved using the dual iso-centre system to polarise the carbonyl peak of labelled [1-$^{13}$C] sodium acetate is 4700 with a standard deviation of 400. The variation is observed over 8 different experiments however there are many factors affecting the error in the measurement, such as temperature, concentration and solvent volume. The results show that high levels of polarisation are achieved consistently and that $T_1$ information can be efficiently extracted from the data which was measured to be 22 (at 9.4 T) at the post dissolution sample temperature.

**Glucose**

Glucose is a mono carbohydrate molecule that is made up of a chain of 6 carbon atoms and is present in many metabolic processes (120; 121). It is readily transported across cell membranes by the GLUT1 and GLUT4 transporters which can be expressed in cells such as the Xenopus oocyte (122; 123). Therefore, in terms of characterising potential metabolites for

Table 4.4: Table showing the measured T1 of both deuterated and non-deuterated $^{13}$C labelled glucose.

| Peak number | Glucose $T_1$ (s) | |
| --- | --- | --- |
| | Non-Deuterated | Deuterated (s) |
| 1 | 0.70±0.05 | 22.2±0.2 |
| 2 | 0.80 | 21.0 |
| 3,4 | 0.80 | 18.1 |
| 5 | 0.90 | 16.2 |
| 6,7,8 | 1.10 | 20.6 |
| 9 | 0.80 | 20.1 |
| 10 | 0.40 | 15.1 |

imaging of molecular transport and metabolism it is of great interest.

Two samples were made containing 1 M of both fully protonated and fully deuterated glucose dissolved in a 50:50 water/glycerol solution. The samples were polarised for approximately 60 minutes at 3±1 K due to unusual fluctuations in the temperature of the VTI. This was due to the OVC seal being broken during maintenance to the cryostat prior to the experiments, resulting in the vacuum being too weak to allow sub 2 K temperatures. As a consequence the measured enhancement is lower than expected.

The spectra for the two experiments is presented in Figure 4.10 where the position of nuclear spin in the molecule and the associated peak position is given. The molecule is $^{13}$C labelled on all carbon sites in both cases. Due to the very short $T_1$ relaxation time of the non-deuterated glucose only a single acquisition with a 90$^o$ pulse was acquired.

The $T_1$ relaxation time constant was measured for each of the peaks and presented in Table 4.4. The $T_1$ of the fully deuterated molecule was extracted from the DNP decay curve shown in Figure 4.10 and calculated by fitting Equation 4.1, whereas the $T_1$ of the non-deuterated glucose was measured using an inversion recovery experiment on the thermally polarised sample.

The enhancement achieved on the peak with the longest relaxation time for the fully deuterated glucose molecule is 5000. However, it is important to remember that the polarisation was not optimised due to the build up time being unknown and the temperature of the VTI being higher than normal. The enhancement achieved for the non-dueterated glucose was not measured. However it is promising that single excitation acquisition of a molecule with such short $T_1$ can be achieved and the result demonstrates the power and capability of the dual iso-centre magnet system.

The high level of polarisation achieved for the deuterated glucose despite sub-optimal conditions makes it an acceptable candidate for metabolism and
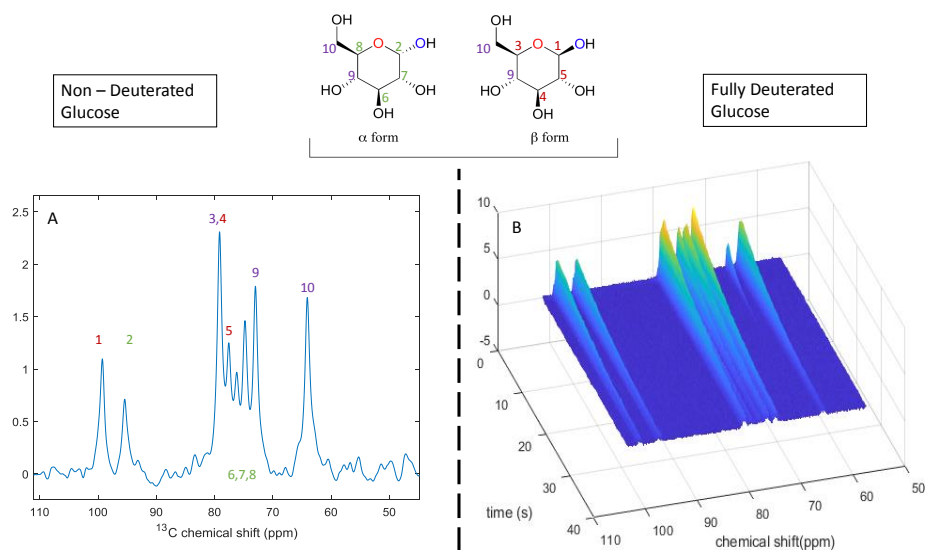
Figure 4.10: D-DNP NMR results for deuterated and non-deuterated glucose. (A) Single excitation acquisition of non-deuterated, fully $^{13}$C labelled glucose. The numbers relate to the position of the carbon spin in the molecule shown at the top of the figure. Green numbers are peaks from the $\alpha$ anomer of glucose, red numbers are from the $\beta$ anomer of glucose and purple numbers are peaks common to both anomers. (B) Relaxation decay for deuterated glucose acquired with multiple small flip angle pulses in order to extract the $T_1$.

molecular transport experiments in biological systems (124).

## Pyruvic acid

Pyruvic acid is a common metabolite in biological systems and is the molecule of choice for in vivo hyper polarisation experiments (125). It has a favourable long liquid state $T_1$ and well a shielded carbonyl group that is relatively relaxation insensitive to field strength changes (126; 127). This means that in the liquid state, it retains the polarisation even when moved though very low fields . Pyruvic acid is preferentially taken up and metabolised by cancerous cells in an anaerobic pathway to lactate. This makes the molecule iontersting for cancer diagnostics. It is the primary choice for use with the standalone clinical polariser system, the GE SpinLab, designed for in vivo human experiments (128; 129).

Pyruvic acid is transported across the cell membrane by the MCT (Monocarboxylate) transporter (130). This could provide a potential model for observation of molecular transport as the pyruvic acid molecule has a long $T_1$ without the need for deuteration.

An experiment was carried out to measure the enhancement and $T_1$ relaxation time of the pyruvic acid in the dual iso-centre magnet system. The DNP relaxation decay curves were collected using the same pulse sequence as that for the glucose and [1-$^{13}$C] sodium acetate and the results are shown in
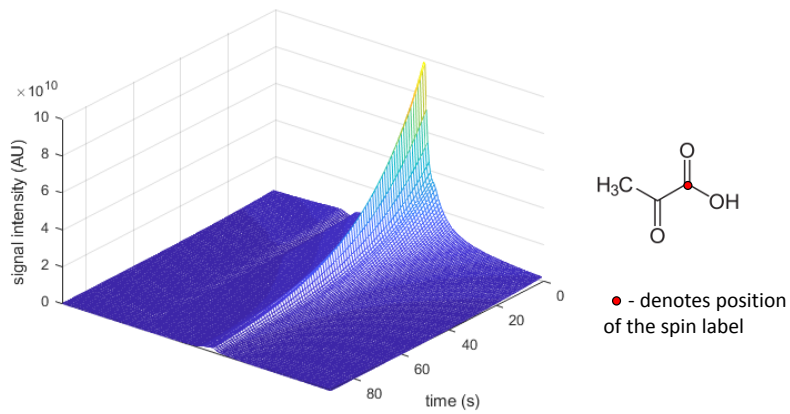
Figure 4.11: Dissolution DNP decay curve for pyruvic acid measured with a train of $< 1^o$ pulses. The schematic on the right shows the position of the spin label in the pyruvic acid molecule. The $T_1$ was measured from the decay curve to be 70 s.
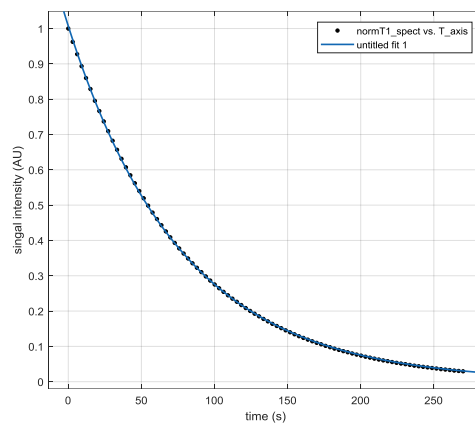


Figure 4.12: Fit of the $T_1$ decay of hyper polarised pyruvic acid.

Figure 4.11. The peak shows the hyper polarised signal from the [1-$^{13}$C] pyruvic acid where the position of the label is shown by the red dot.

The sample was pure pyruvic acid and 15 mM of the trityl radical. No glassing agent was required as pyruvic acid is self glassing (131; 111). This is a further reason as to why it has become the main focus of in vivo experiments as there is no concern over the effect of the glassing agent on the subject. The polarisation was carried out at approximately 1.6 k however small fluctuations in the temperature meant that it was as low as 1.4 k at points. The total polarisation time was 150 minutes at low temperature, however the microwaves were activated as soon as the sample was in the polarising position (from approximately 100 K).

The fit of the exponential decay to calculate the $T_1$ is shown in Figure 4.12 and was calculated to be 69 s.

The long $T_1$ of pyruvic acid means that it is ideal for imaging metabolic processes. However, the T1 observed in the above experiment is for pyruvic acid where there are very few paramagnetic relaxation agents present. When placed in oxygenated blood Marco-Rius *et al.* (127) have observed $T_1$'s on the order of 45 seconds. Therefore it can be expected that the $T_1$ of the pyruvic acid would likely fall to levels comparable to that shown in (127) when taken up by a small biological object such as the Xenopus oocyte.

**N-Acetyl-L-Aspartic Acid**

N-Acetyl-L-Aspartic acid (NAA) is the second most abundant, naturally occurring molecule in the human brain and acts as a neuronal osmolyte (132). It is key to aiding diffusion of liquid and controlling fluid balance in the brain and also plays a part in myelin synthesis. The levels of NAA in the brain have been measured by MRI and are shown to vary due to the effect of diseases such as Alzheimer's and brain injuries or strokes. The molecule has six carbon sites and therefore gives interesting structure to the spectra to allow assessment of the enhancement (133; 134; 135).

For a D-DNP NMR experiment a sample containing 1 M NAA in a 50:50 water/glycerol solution was used and 15 mM of trityl radical was added to this. The sample was polarised at 1.7 k for 150 minutes and this was done on the assumption that the $^{13}$C build up is similar to that of [1-$^{13}$C] sodium acetate. The temperature of the cryostat remained stable for the duration of the polarisation (within $\pm 1^o$). After the dissolution the NAA concentration in the dissolved sample was 3 mM and the glycerol concentration is estimated to be 10 mM. Only natural abundance $^{13}$C was detected in this experiment.

The experiment consisted of a single $90^o$ pulse and the full amount of hyper polarised signal was collected in a single shot. Proton decoupling in the form of a Waltz-16 decoupling sequence was applied. The data was acquired with

Table 4.5: SNR, polarisation enhancement and $T_1$ values for each of the NAA peaks shown in Figure 4.13. The highest enhancement is not attributed to the longest $T_1$ and the smallest enhancement is not related to the shortest $T_1$.

| Peak | SNR | enhancement | $T_1$ (s) |
|---|---|---|---|
| 1,2 | $9.44 \times 10^4$ | 5500 | 4.9 |
| 3 | $2.35 \times 10^4$ | 2000 | 5.1 |
| 4 | $3.43 \times 10^4$ | 3000 | 0.8 |
| 5 | $3.05 \times 10^4$ | 2800 | 0.5 |
| 6 | $0.16 \times 10^4$ | 200 | 2.2 |
| Glycerol (peak 2) | $61.73 \times 10^4$ | 12000 | - |
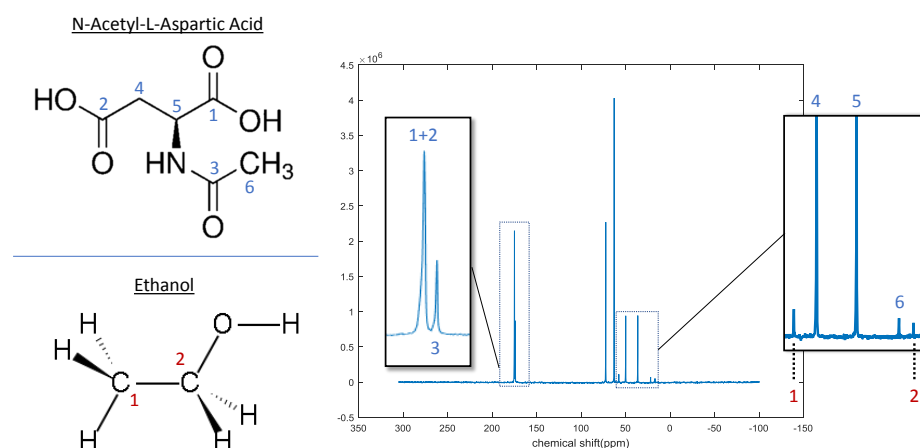


Figure 4.13: Single shot ($90^o$ pulse) acquisition of N-acetyl-L-aspartic acid (NAA). The peaks pertaining to the NAA are labelled with blue numbers. The unnumbered peaks arise form natural abundance $^{13}$C glycerol and the peaks numbered in red are from the trace amounts of ethanol that were present due to contamination. The data was collected by A. Gaunt and B. McGeorge Henderson.

a Bruker-BBO probe on the broadband channel rather than the specific $^{13}$C channel due to the proximity of the broadband coil to the sample in order ensure maximum sensitivity. The acquired natural abundance $^{13}$C spectrum is shown in Figure 4.13.

The spectrum shown in Figure 4.13 shows the hyper polarised signal from NAA and glycerol. There are two further peaks present which were initially unaccounted for, however it was realised that these peaks are due to trace amounts of ethanol deposited while cleaning the syringe used to insert the sample into the sample cup. It is estimated from the spectrum that the concentration of the ethanol is approximately 0.7 mM in the dissolved solution.

A comparison between the hyper-polarised spectrum and a thermally po-

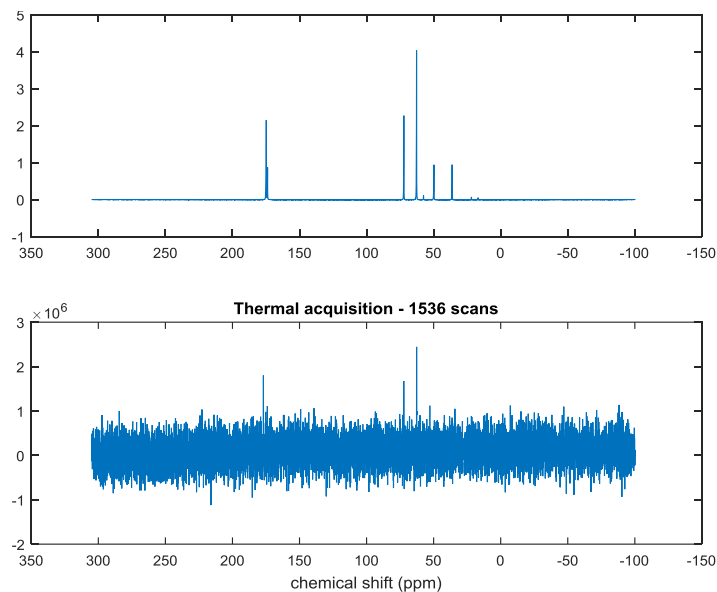Figure 4.14: Comparison between single shot hyper polarised NAA and thermally polarised acquisition. Both were acquired using 90 degree pulses. After 1536 averages only one of the NAA peaks and the glycerol peaks are visible with the glycerol showing an SNR of 300.

Table 4.6: The number of spins in the system for the spectrum shown in Figure 4.13 and the average SNR achieved due to hyper polarisation.

| Molecule | N-spins | $\bar{\text{SNR}}$ |
|---|---|---|
| NAA | $1.3 \times 10^{16}$ | $3.68 \times 10^4$ |
| Glycerol | $3.9 \times 10^{16}$ | $8.42 \times 10^4$ |
| Ethanol | $0.3 \times 10^{16}$ | $0.17 \times 10^4$ |

larised signal is shown in Figure 4.14. The thermal acquisition consisted of 1536 averages and the pulse sequence parameters used are the same as those used to acquire the hyper polarised spectrum. The repetition time between averages was 50 s in order to ensure the spins system had fully returned to equilibrium. The enhancement for each of the peaks was calculated, where the maximum enhancement for the NAA was found to be 5500. The full list of enhancements is given, along the the $T_1$ values, in Table 4.5. The $T_1$ was measured by an inversion recovery experiment on a high concentration sample of NAA, it is assumed that the dilution factor of approximately 30 means the relaxation effect of the trityl is negligible (136; 137). It is clear from the table that there is no linear relationship between $T_1$ of the nuclear spin and the achieved enhancement.

The relationship between the number of spins being measured and the average SNR achieved for each of the three molecules in the hyper-polarised spectrum is plotted in Figure 4.15 and the data is presented numerically in Table 4.6. The average SNR was calculated by finding the SNR for each
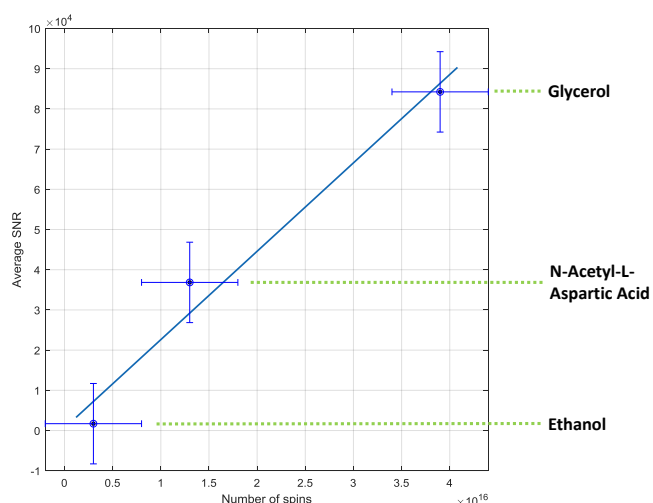
Figure 4.15: The Average SNR for the NAA, Glycerol and Ethanol plotted against the predicted number of natural abundance $^{13}$C spins in the dissolved sample. The linear fit gives a gradient of $2.2 \times 10^{-12}$ has an R-square value of 0.97.

of the peaks and taking an average. There is a linear relationship between the average SNR and the number of spins, which in a thermally polarised system is to be expected. However, in a hyper-polarised system the amount of enhancement achieved for a given molecule is highly dependent upon the local environment and structure.

The gradient of the linear fit shown in Figure 4.15 gives the SNR per number of spins, which is shown to be $2.2 \times 10^{-12}$. Given that in order to distinguish signal from noise an SNR of three is required as a minimum, this value can be used to estimate the limit of detection given the presented level of polarisation. To achieve an SNR of three, $1.3 \times 10^{12}$ spins are required given the enhancement achieved. This equates to a concentration in the 600 $\mu$L post dissolution sample of 0.35 $\mu$M of $^{13}$C-NAA.

## 4.4 Discussion

The initial experiments carried out with [1-$^{13}$C] sodium acetate in the solid state to measure the DNP frequency sweep and the build up curve display an interesting characteristic that occurs when the microwave power is adjusted. It appears that the maximum polarisation is achieved, and with an equally fast (if not marginally faster) build up time when the microwave is not operating at full power. The cause of this effect could be related to the sample itself as the build up time and total polarisation is dependent on the sample forming an amorphous solid when it is flash frozen before insertion into the VTI (113).

It is clear that the power of the microwaves has an affect on the system

however, it is not proven as to wether the polarisation transfer is affected as a direct consequence of the microwave power or if it is affected due to heating caused by the microwaves. Batel *et al.* (138) have demonstrated that when a resonant cavity is used the temperature of the cavity increases by 0.2 K for a microwave power increase of 160 mW (from 20 mW to 180 mW) (138). In a stand alone polariser this heating may be more efficiently reduced as often a container (oversized cavity) is sat in a bath of liquid He. Whereas in an open bore, flow cryostat the small amounts of liquid He used may be less effective in dissipating the heat energy (139).

It is not clear in these experiments or in those presented in (138) weather the sample is heated by the microwave directly or if there is a heating effect on the surrounding metal (the copper ring in the sample cup) which raises the sample temperature. At the very low temperatures used here it is not known what the dielectric properties of the sample are and therefore it is difficult to predict the microwave penetration and absorption by the sample lattice. A reflection measurement of the microwaves during the polarisation showed that the reflected power was less than 40 percent of the input power at 180 mW, therefore the sample is absorbing or transmitting at least 60 percent of the microwaves that arrive at its surface. The very fact that a polarisation enhancement is measured when the microwaves shine on the sample suggests that the microwaves must penetrate and interact with the sample lattice. The fact that levels of polarisation enhancement do not match those presented by Ardenkjaer-Larsen *et al.* (140) shows that the system is not as efficient as those which incorporate a microwave container and shows the strong temperature dependence of the DNP process in this critical regime.

The liquid state experiments showed that [1-$^{13}$C] sodium acetate, deuterated glucose and pyruvic acid all display good enhancement and a long enough $T_1$ relaxation time to be used as markers (for micro-NMR/MRI) in a biological system such as an oocte. However the $T_1$ for non-deuterated glucose and aspartic acid means the polarisation decays too rapidly to be used in monitoring of metabolism. The fact that deuteration is required to provide the long lifetime of glucose could compromise the natural uptake, however this kind of experiment has been tested by Jeong *et al.*(124) and shown to provide promising insight into glucose metabolism.

The quoted polarisation enhancement for all molecules except NAA is achieved after only approximately 80% of the build up time, therefore it is likely that slightly higher values can be achieved through polarising for longer. Higher polarisation could also be achieved through introduction of a cavity (instead of the copper ring) to contain the microwaves in the VTI. Batel *et al.*(138) have demonstrated that a "resonant microwave structure", where oversized multi-mode cavities are used, allows for a more efficient polarisation through concentration of the magnetic field of the microwaves in the sample volume.

## 4.5 Conclusions

This chapter explained the experimental set-up based on a Dual iso-centre dissolution DNP magnet and shows some possible reasons as to why the enhancement achieved may not match the values found by other, standalone, polarisers. The pitfalls involved in using a shuttling system and an open bore cryostat are discussed and the dissolution process is described in detail.

Data from both solid and liquid state DNP experiments is presented on [1-$^{13}$C] sodium acetate, which was collected to assess the performance of the DNP experiment. Further experiments were carried out on glucose, aspartic acid and pyruvic acid. It was found that the $T_1$ of the non-deuterated glucose and the NAA were both to short to be considered for use in monitoring biological systems. However, the short relaxation times demonstrated the advantages of using the dual iso-centre system. In a stand-alone polariser system the measured liquid state enhancement on these molecules would negligible due to the time required to transfer the liquid sample between magnets. The results also suggest that deuterated glucose or pyruvic acid would be suitable molecules to polarise for monitoring biological processes.

# Chapter 5

# Rapid Acquisition for MR Microscopy

## 5.1 Introduction

Hyper polarised signals have a lifetime limited by their $T_1$ relaxation time constant. Therefore it is imperative that the signal be acquired in the shortest time frame possible to maximise the observed signal enhancement. Some common techniques for accelerating MRI acquisition beyond the Nyquist limit are discussed in this chapter. One current method for accelerated image acquisition in MRI, to allow the artefact free, under-sampling of $k$-space is Sensitivity Encoding (or SENSE) (141). The flexibility and versatility of SENSE will be explained and demonstrated. Work that allowed important decisions to be made relating to the direction of the design of the micro-imaging probe-head will be presented, along with results from simulations of under-sampling and reconstruction to verify the validity of the technique for micro imaging.

It is also important to understand the limitations on achievable resolution due to the capabilities of the spectrometer along with the limitations imposed by the properties of a typical sample to be imaged. This is an important consideration as if the resolution limits due to the gradient strength of the sample properties are higher than the desired resolution, further development of an imaging probe-head is rendered meaningless. The effect of the coil sensitivity on and the limit of detection on the resolution are not considered at this point, only the final resolution limit is considered to ensure that imaging with a micron scale resolution is possible.

The aim of this chapter is to show that micro-imaging will work with rapid acquisition techniques and to allow decisions to be made on appropriate coil array configurations in order to achieve micro-imaging of small hyper-polarised samples.

## 5.2  Rapid Acquisition Methods

Due to the nature of collecting images in magnetic resonance, each frequency encoding line of $k$-space requires a given amount of time in order to allow the magnetisation to evolve in the presence of a gradient. If imaging is to be applied effectively to hyper-polarised samples with a limited lifetime, then the amount of lines of $k$-space required needs to be minimized. By sampling fewer lines of k-space it is possible to accelerate the acquisition of the data with a small cost to the final SNR (10), which should be offset by the signal enhancement from DNP (7). With specific hardware in place (i.e. a coil array) it is possible to reconstruct artefact free images from an under-sampled $k$-space.

Rapid acquisition techniques have been implemented on macro scale image acquisition sequences in both clinical and preclinical setting for many years (142; 143). Currently Compress Sensing is being implemented, sometimes in conjunction with SENSE or Grappa as these are routine for clinical scanners, in order to obtain rapid image acquisition of hyper-polarised pyruvate metabolism in prostate cancer (144; 145). As explained by Webb *et. al.* parallel imaging is typically carried out at field strengths found in clinical scanners (146). This is partly due to the patient lead nature of the research and partly due to the complexity involved with decoupling multiple coils at high frequency. Webb showed how a linear array of volume coils can be used to collect micro-scale images of the entire length of a rat tail at 14 T, using multiple coils to allow reduced imaging time and increased sensitivity (146). It is hoped that similar principles can be built upon to optimise the rapid image acquisition of hyper polarised samples on a micro-scale.

In this section, a brief review of possible schemes for accelerated or parallel MR image acquisition are presented before a detailed description of SENSE is given.

### 5.2.1  PILS

Partially Parallel Imaging with Localised Sensitivities (PILS) is one of the original forms of under-sampled image acquisition (147). It is based upon using the well defined sensitivity of a linear receiver array, placed along the phase encoding direction, to allow under-sampled images to be reconstructed. The caveat of this method is that the under-sampling must be also along the phase encoding direction. The technique can be applied to most pulse sequences but the reconstruction will only work when the direction of under-sampling is in the same direction as the coil array.

Image reconstruction is carried out by direct comparison of the coil sensitivities with the reconstructed image. Due to the under-sampling along the phase encoding direction, there are periodically repeating "sub-images"

(repetitions or segments of the true image due to not reaching the Nyquist sampling rate (148)) formed when the whole Field of View (FOV) is reconstructed (147). If the condition that states that the FOV must be larger than the finite sensitivity region of each of the individual coils, is met then the sub-images are separated from each other and do not overlap (4). The information of the true position of the sub-images is not retained in the initial reconstruction of the under-sampled $k$-space, so the position of the individual receiver coils is used to provide the missing spatial encoding and recombine the sub-images.

Due to the need for separated sensitivity profiles of each of the coils, combined with the fact that PILS is only applicable for specific FOV sizes and when the phase encoding is aligned along the direction of the coil array (4; 147). PILS is restricted in its imaging capabilities and also limits the shape of the receiver array. Therefore, due to the many limitations and constraints placed upon the design of a receiver array for the dual iso-centre magnet, it is not versatile or flexible enough to be considered for use.

### 5.2.2 Compress Sensing

Compress Sensing (CS) was originally employed as a way of compressing images for data storage (149) and is not a technique that affects the hardware particularly. However, it is worth mentioning in this chapter as it is a burgeoning technique in the world of rapid MR-image acquisition. Unlike many other rapid acquisition methods, CS does not rely on any extra spatial encoding step to reconstruct under-sampled images, but in fact uses the inherent sparsity of images to allow under-sampling with artefact free reconstruction (150).

The requirement for a good reconstruction using CS is that the data is not uniformly under-sampled as this makes it impossible to distinguish between signal and noise (151). By under-sampling randomly, it is possible to avoid the aliasing and spatial information is retained, as shown in Figure 5.1. By (pseudo) randomly under-sampling, the problem of reconstruction is converted from an ill-conditioned problem (as is the case for parallel imaging) into a sparse signal de-noising problem. The assumption is that in a given transform space, such as the image domain, Fourier space or discreet wavelet space, any MR image data will be a sparse matrix (143).

It is possible that this method could be combined with another, rapid acquisition technique, such as sensitivity encoding (152), to further reduce the scan time. This has been demonstrated by Gong *et al* in their implementation of PROMISE, an acquisition scheme to combine parallel imaging with CS (153).
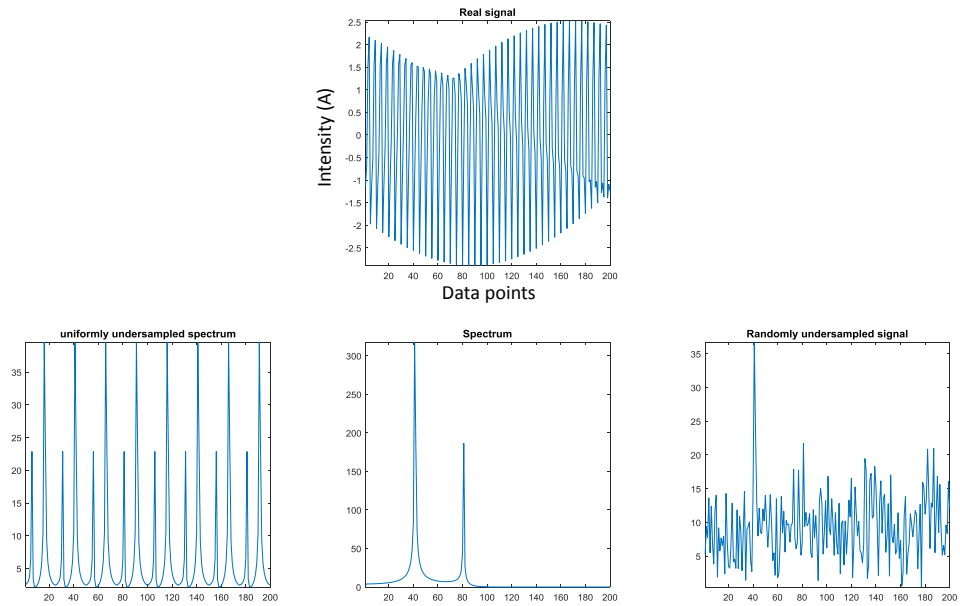
Figure 5.1: The top of the figure shows a simulated, fully encoded FID signal (with a very long decay constant) with the fully encoded spectrum directly below. Bottom left shows how a uniform under-sampling requires further spatial information for reconstruction of the correct spectral positions. Bottom right shows how spatial information is still retained with random under-sampling. (143)

## 5.2.3   Sensitivity Encoding (SENSE)

Sensitivity Encoding or SENSE was developed by Pruessmann *et al.* (141) in order to reduce the time that a patient was kept in an MRI scanner, as lengthy scans can become uncomfortable (10). It also opened up an opportunity to image regions of interest with a periodic motion, such as the heart. As the rapid acquisition can be gated to trigger between heart beats (154; 155).

SENSE works in a similar way to PILS, however, it has more flexibility in terms of the position of the receiver coils and the direction of the under-sampling (4). This need for flexibility can be somewhat overlooked when designing hardware for macroscopic imaging and working at fields used for clinical MRI because the receivers are large and easy to work. Large receiver coils are more forgiving when inserting decoupling elements due to the physical dimensions of the receivers and the operational frequencies involved. For microscopy, small detectors are required which limits the design and shape of the array coil.

SENSE allows an acceleration factor as high as the number of separate receiver coils, where acceleration factor ($R$) is defined as the number of consecutive lines of $k$-space missed between acquired lines. If $R$ is greater than the number of receivers ($N_c$) the Nyquist sampling condition is not met and the image will not have sufficient spatial encoding to be reconstructed artefact free (141).
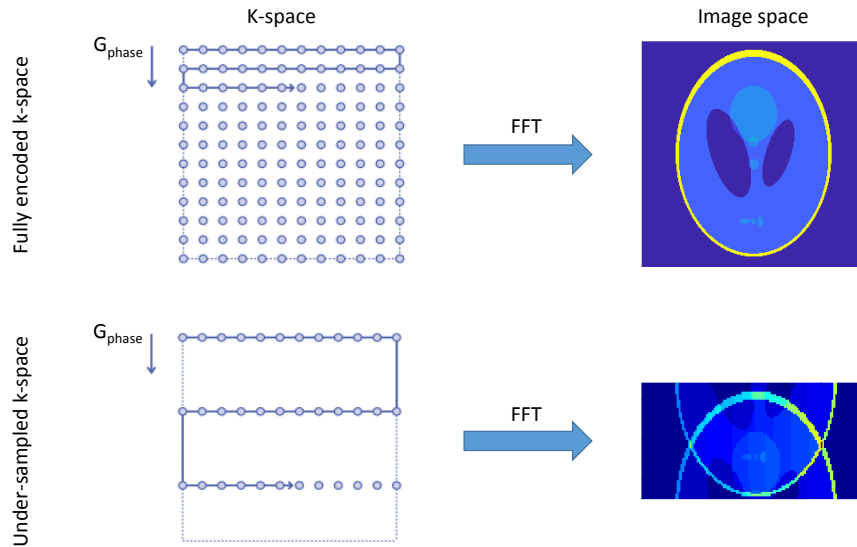
Figure 5.2: Top:Fully phase encoded $k$-space $(top)$ with its Fourier transform to an artefact free image. Bottom: A partially encoded image $(bottom)$ leads to overlapping of the signal in the Fourier transformed image space.



Figure 5.3: SENSE reconstruction with four receiver coils $(N_1$ to $N_4)$ and an acceleration factor of $R = 4$. This demonstrates how the folded pixel vector is constructed and how the reconstruction is carried out by using the multiple receivers to solve a set of simultaneous equations.

**Coil 1 Sensitivity Map**

PIXEL POSITION 1

OVERLAPPED
POSITION - PIXEL
POSITION 1+R

**Coil 2 Sensitivity Map**

PIXEL POSITION 1

OVERLAPPED
POSITION - PIXEL
POSITION 1+R

Build sensitivity matrix

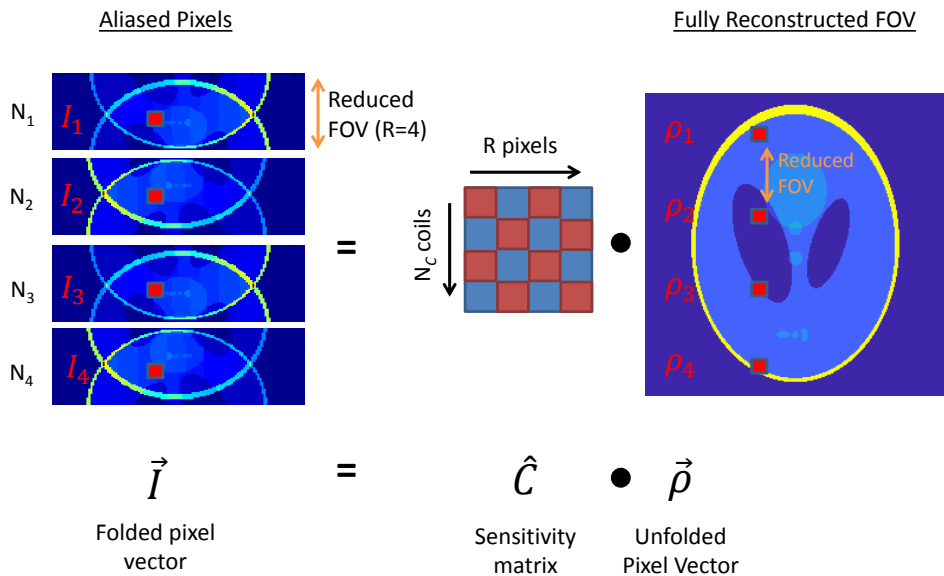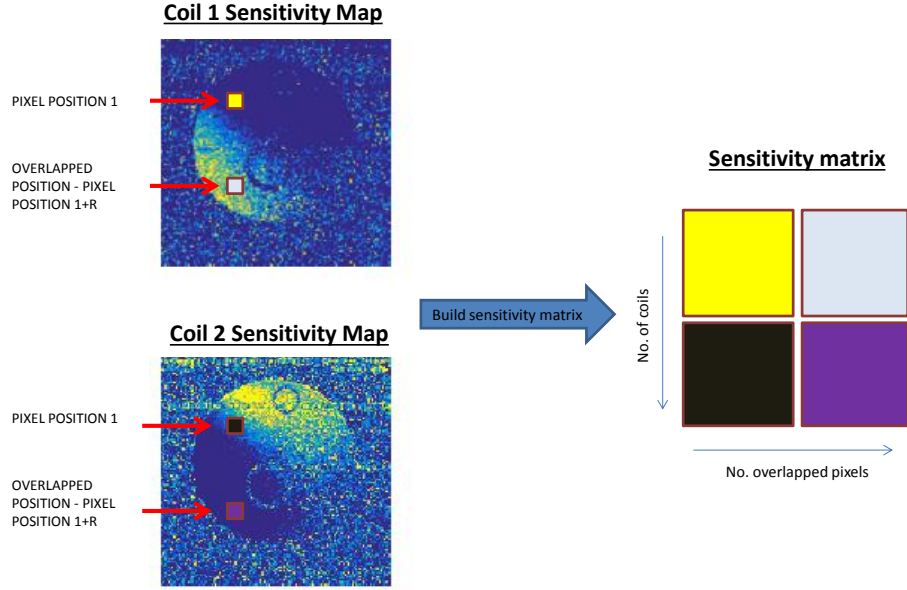**Sensitivity matrix**

No. of coils

No. overlapped pixels

Figure 5.4: Figure showing how the sensitivity matrix for unfolding the pixel at position $x$ in an image (denoted as position one in the figure) is constructed from the sensitivity maps for each of the coils in the array. The example is based on a 2 coil array with an acceleration factor of 2.

The SENSE reconstruction, which is illustrated in Figure 5.3, requires prior knowledge of the coil sensitivities in the form of a sensitivity map for each of the coils which allows the construction of an unfolding matrix $(U)$,

$$U = (C^H \psi^{-1} C)^{-1} C^H \psi^{-1}, \tag{5.1}$$

where $\psi$ is the noise correlation matrix and $C$ is the sensitivity matrix, $H$ denotes the conjugate transpose. $C$ is a $N_c \times R$ ($N_c$ being the number of coils) matrix corresponding to the coil sensitivity for each receiver $(k)$ at a given pixel position.

As an example, suppose that the acceleration factor is two and there are two coils. In order to unfold a given pixel at position $x$ the sensitivity matrix must be built by taking the value from a sensitivity map for each of the receiver coils at that pixel position and also the value at the corresponding overlap position $\Delta x$ (determined by $R$). The sensitivity matrix can be written as

$$C_{k,l} = s_k(\mathbf{r}_l), \tag{5.2}$$

where $k$ is the reviver and $l$ goes from 1 to $R$. The right had side of the equation represents the spatial sensitivity of coil $k$ at a given position for both

the original and overlapped pixel positions (given by $\mathbf{r}_l$). The construction of the sensitivity matrix is explained visually within Figure 5.4. Here an example of a sensitivity matrix required for unfolding an overlapped pixel in an image with an $R = 2$ acceleration is given. The example assumes that the receiver array consisting of two separate coils.

In an imaging experiment where under-sampling is carried out along the $y$ direction, and the sensitivity maps of the coils are known, the received signal $I$ at image location $(x, y)$ from the $k^{th}$ receiver coil (for $R = 2$) is given by

$$I_{\mathsf{k}}(x, y) = C_{\mathsf{k}}(x, y_1)\rho(x, y_1) + C_{\mathsf{k}}(x, y + \Delta y)\rho(x, y + \Delta y), \qquad (5.3)$$

where $\rho$ is the unfolded pixel value. For an entire image Equation 5.3 can be generalised to cater for any value of $R$, which is written as

$$I_k = \Sigma_{l=1}^{R} C_k \rho_l. \qquad (5.4)$$

The number of unknowns in the above equation means that the problem is still ill-posed and therefore a further generalisation is carried out to include the contributions from all of the $(N_c)$ receiver coil, and the linear equations can be combined in matrix form to give the SENSE equation:

$$\vec{I} = \hat{C} \cdot \vec{\rho}, \qquad (5.5)$$

where $\vec{I}$ is the a vector containing the overlapped pixel value from each of the receiver coils. $\hat{C}$ is the sensitivity matrix containing the sensitivity value of each coil at the specified superimposed position and $\vec{\rho}$ is a vector that contains the unfolded pixel values (141). To generate an artefact free image, the inverse of the sensitivity matrix must be applied to $\vec{I}$ for each pixel in the image:

$$\vec{\rho} = (C^H \Psi^{-1} C)^{-1} C^H \Psi^{-1} \cdot \vec{I}, \qquad (5.6)$$

where $\Psi$ is an $N_c \times N_c$ noise correlation matrix which describes the noise level on each of the receivers and the crosstalk between them. If the coils are coupled through mutual inductance there will be a high level of noise correlation which then needs to be accounted for in order to limit SNR loss in the reconstruction. For simplicity this can be set to the identity matrix at a slight cost to the final SNR (141). For the purposes of simulations there is no crosstalk between the coils and the receivers are noise free so there is no detrimental effect from negating $\Psi$. The inverse of the sensitivity and the noise correlation matrix shown in Equation 5.6 can be simplified into the unfolding matrix $U$ and the equation can now be expressed as

$$\vec{\rho} = U \cdot \vec{I}, \qquad\qquad (5.7)$$

where $U$ is the unfolding matrix presented in Equation 5.1. The unfolding process and the construction of the vectors is demonstrated schematically in Figure 5.3.

There are two different methods that are often used to build the sensitivity matrix. The first and simplest is to collect low resolution images that are fully encoded for each coil (141; 4). Using low resolution images means that the imaging time is short due to only the low frequency regions of $k$-space being needed. These images can be combined, typically using a sum of the squares reconstruction, to produce an image that is equivalent to one using a single "body" coil. Each of the individual coil images is divided by this "sum of the squares image" to generate the sensitivity map for each coil. The sensitivity maps is then used to construct the sensitivity matrix $C$ as demonstrated by Figure 5.4. On clinical MRI scanners there is often a "body" coil available so this may be used instead of a sum of the squares image (10).

A more elegant, although slightly more complicated method, involves collecting some consecutive lines of the central $k$-space region during the accelerated acquisition (147). This is then used to generate the low resolution images which then can be combined to generate the sensitivity maps. This method can be advantageous for reducing the effect of motion artefacts, however, it requires more lines of $k$-space so acquisition time is longer. It also can lead to a poor reconstruction if the resolution of images is very low (147; 156).

## 5.3   SENSE simulations

It is important to understand how the coil array and the direction of under-sampling will effect the image reconstruction. Therefore, simulations have been constructed to understand better the reconstruction process and to aid with the development of a probe-head that is capable of micro-imaging with a hyper-polarised sample.

Under-sampled images of the Shepp-Logan head phantom (Mathworks) are generated for a given number of receivers that have a sensitivity weighting based on a specified coil size and position, relative to the centre of the FOV. An under-sampled image is generated for each receiver in the simulation and then the under-sampled image is given a weighting based on the sensitive profile that a surface coil would have if it was placed at the edge of the FOV. Multiple dimensions and position of receiver were tested and the field maps were created using a Biot Savart simulation in Matlab. Sensitivity maps for each of the receivers are constructed through applying the same weighting to the original full FOV images which are then applied within the
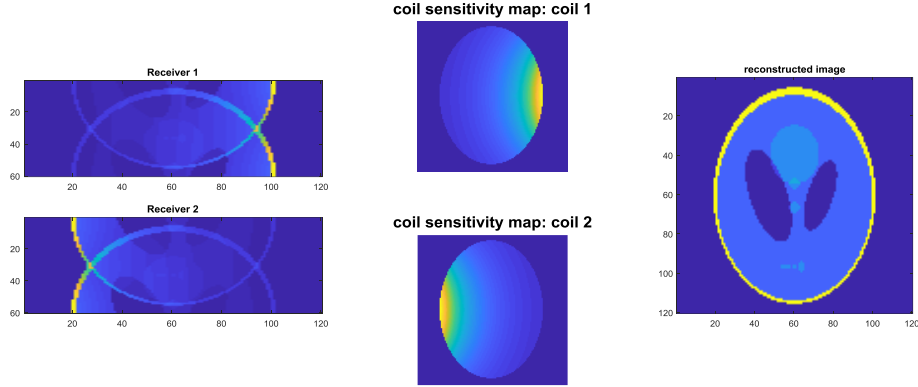
Figure 5.5: Left: under-sampled image from two receiver coils with an acceleration factor of 2. Middle: Sensitivity maps for each of the two coils in the array. Right: The artefact free, fully reconstructed image of the modified Shepp-Logan phantom (Mathworks Co.).

SENSE algorithm as shown in Equation 5.5 to separate the overlapped pixels. Figure 5.5 shows how aliased images are reconstructed into an artefact free, fully encoded image.

The sensitivity maps are generated using the Biot-Savart law to determine the field map of each of the coils in the array. This is equivalent to the sensitivity of the coil as the sensitivity in NMR is directly proportional to the field produced by the receiver coil.

### 5.3.1 Geometry Factor

In order to assess the array coils propensity for spatial encoding and reconstruction a measure of how well the image is reconstructed is required. The SENSE reconstruction matrix is rarely unitary as is the case for the matrix representation of the FFT used in fully encoded reconstruction, therefore in SENSE the noise will vary across the pixels with noise correlation between the pixels that is partly based on the noise correlation between the coils. A measure of the goodness of reconstruction is called the g-factor ($g$), known as such due to the relation to the geometry of the array coil (157; 158). The g-factor is described by

$$g = \sqrt{\left[(C^H \Psi^{-1} C)^{-1}\right] (C^H \Psi^{-1} C)} \geq 1. \qquad (5.8)$$

$\Psi$ is an $N_c$ x $N_c$ receiver noise matrix, which has been set as the identity matrix as it is assumed there is a good level of decoupling between the receivers. In a physical system the noise correlation matrix would not be identity. The diagonal terms represent the noise variance of a single array element and the off diagonal terms pertain to cross-correlated noise between
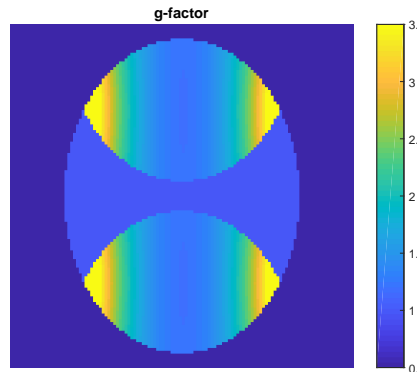
Figure 5.6: g-factor map for the two coil reconstruction shown in Figure 5.5, where R is equal to 2.

array elements (141). The g-factor is always greater than one and is a quantification of the noise magnification and goodness of spatial reconstruction (141; 10; 156).

g-factor is a better representation of noise and reconstruction power than SNR as it shows how well each pixel in the image has been reproduced and sheds light on the number of aliased replicates at each pixel position given the associated coil sensitivities (hence why the sensitivity matrix is required). Therefore in a real world system the g-factor depends on coil loading, the position and number of coils in the array, the direction of under-sampling as well as the plane of imaging and finally the location of the pixel in the image. In order to assess how well a coil configuration operates, the reconstructed image and the g-factor will be examined.

### 5.3.2  SNR in SENSE

The SNR achievable is governed by the acceleration applied to the imaging sequence and the g-factor, with a better level of spatial encoding leading to a better final SNR. The SNR from a sensitivity encoded image is given by the SNR of a fully encoded image divided by the g-factor and the square root of the acceleration factor (141),

$$\mathrm{SNR}_{\mathsf{SENSE}} = \frac{\mathrm{SNR}_{\mathsf{Full}}}{g\sqrt{R}}.$$ (5.9)

However, for the purposes of examining the goodness of the reconstruction in terms of an optimum coil array, it is more convenient to consider g-factor maps such as the one shown in Figure 5.6. This allows easy comparisons between coil array configurations.
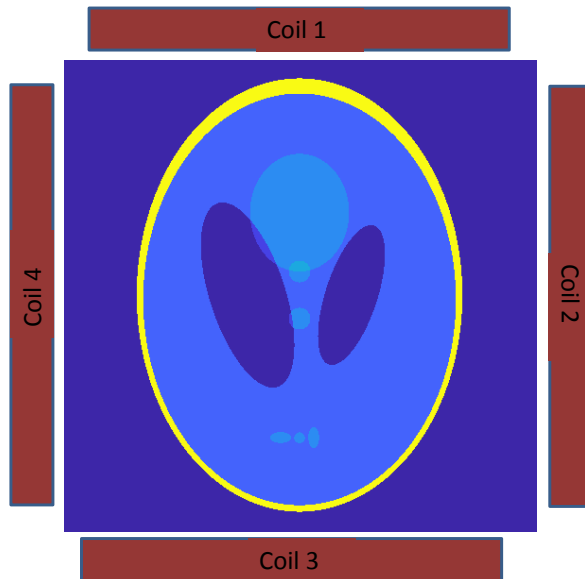
Figure 5.7: Schematic of the positions of the four orthogonal coils about the FOV. The FOV is a 1.1 mm square, with four 0.6 mm OD coils placed around the edges (shown as red blocks). The distance between the coil and the centre of the FOV is 0.7 mm.

### 5.3.3  Results

The effect of increasing the acceleration factor on a 4 channel receiver array, demonstrated in Figure 5.7 where the coils are positioned at $90^o$ intervals around the FOV, is shown in g-factor maps in Figure 5.8. The receiver coil diameter is 600 $\mu$m, the FOV is a 1.1 mm square and the distance between the coil centre to the centre of the FOV is 700 $\mu$m. These dimensions were chosen to match the approximate dimensions of a system designed for imaging large biological single cells such as that developed by Webb *et al.* for imaging of the Xenopus *Laevis* Oocyte (159).

Table 5.1: Mean and variance of the g-factor over the region of interest in the FOV for different acceleration factors. The reconstruction for SENSE factor of 5 contained artefacts.

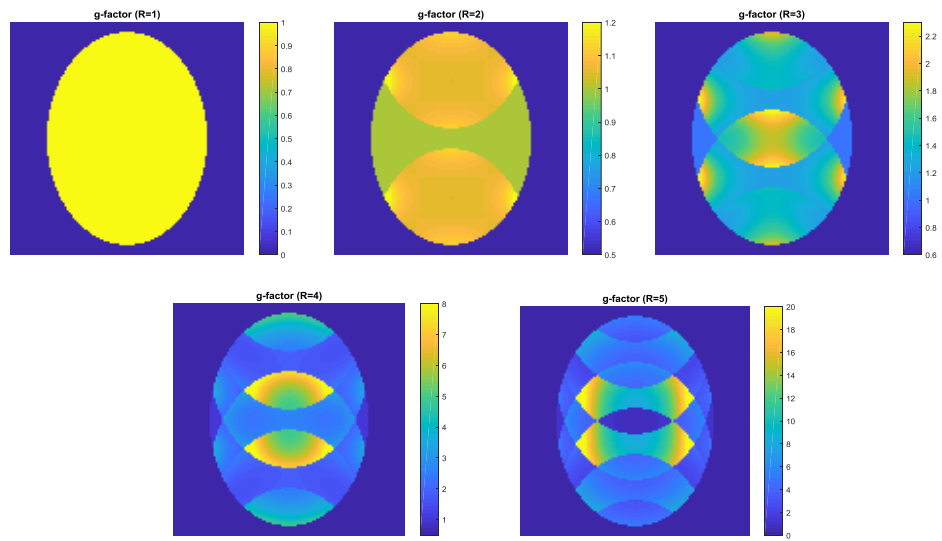| SENSE Factor | Mean g-factor | g-factor variance |
| --- | --- | --- |
| 1 | 1.00 | 0.000 |
| 2 | 1.05 | 0.002 |
| 3 | 1.45 | 0.067 |
| 4 | 3.13 | 3.021 |
| 5 | 6.70 | 19.265 |

Figure 5.8: g-factor maps for varying acceleration factors from 4 orthogonal receivers. acceleration factors vary from R= 1 in the top left of the figure to R= 5, in the lower right corner. The image for R= 5 was reconstructed with artefacts as the acceleration factor is higher than the number of coils.
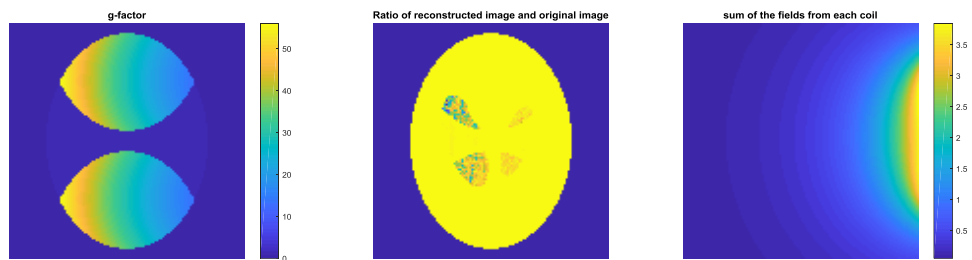


Figure 5.9: Effect of having a 2-coil linear array with coil OD of $600\mu m$, FOV length is 1.1 mm and the radius from the centre of the FOV to the centre of the coils is $700\mu m$. Left: g-factor map for reconstruction with linear array. Middle: Ratio of the original image and the reconstruction showing the netter reconstruction on the side of the coil array. Right: Sum of the field maps for each of the elements in the coil array.

From examination of Figure 5.8 and Table 5.1 it is clear that as the rate of under-sampling increases, the g-factor also increases; increasing dramatically once the number of coils matches the rate of under-sampling. Typically a g-factor variance is a good indicator as to the goodness of the reconstruction as a large change in g-factor will indicate a region of poor quality reconstruction in the image. A g-factor variance less than 10 will usually indicate that the reconstruction is acceptable and less than 1 is that there are minimal areas of poor reconstruction.

In contrast to an array of coils placed around the sample (155), if a linear array is used with overlapping coils, as is often the case in many MRI studies of the spine, it is clear that for a 2 element coil array with an acceleration factor of 2, the reconstruction is limited by the coils separate sensitive regions (158; 160). This is evident when considering that the average g-factor is 23

with a variance of 260 in the g-factor map for the linear array (where the $B_1$ fields from each of the coils significantly overlap and have a similar receiver phase), shown in Figure 5.9.

The reconstruction is dramatically affected by the over-encoding of one side of the image. In a non-ideal, real world system, the reconstruction is also susceptible to artefacts from cross talk noise between the array elements which would be increased in the linear array due to the angle and proximity of receiver elements (161). The g-factor map for the linear array in Figure 5.9 shows how only one side of the image is being spatially encoded to a reasonable degree of accuracy. Counter intuitively the g-factor is not only high (although not as high) on the side of the FOV where no receivers are placed but also on the side of the receiver. This is due to the fact that it is difficult to distinguish between the individual sensitivity maps due to the close proximity of the receivers. This is demonstrated by the plot of the summed magnetic fields (shown on the right hand side of Figure 5.9). A good and reliable reconstruction requires that the coils in the array have well defined, separate sensitive regions, that do not overlap significantly (141; 4; 155).

By considering a 2-element array in a similar manner to the original investigation into SENSE carried out by Pruessmann *et al.* (141) and changing the angle between array elements, it is possible to see how the reconstruction is affected. Figure 5.10 shows how changing this angle affects the ability of the individual elements to encode the image, with g-factor maps and sensitivity maps highlighting how the image is encoded by the position of the coils shown in Figure 5.11. The optimum configuration, for two coils with an acceleration direction along the y axis, is to place the coils in an orthogonal configuration about the FOV. Figure 5.10 shows how the g-factor varies with angle between two coil. The minima in the data occur at the points where the angle between the two array elements is $90^o$.

The effect on the reconstruction due to the direction of under-sampling relative to the position of the receivers is shown in Figure 5.11. Two receiver coils positioned parallel to each other about the FOV are used. The results (in combination with the results presented in Figure 5.10) suggest that the direction of under-sampling (for a Cartesian sampling of the $k$-space) plays an important role in the quality of the reconstruction when the coils are placed opposite each other and appears not to have an effect when the array elements are arranged orthogonally. The reconstruction achieves the same g-factor values as orthogonally placed coil array elements only when the direction of under-sampling is $90^o$ to the parallel coils.

The direction of under-sampling has such a pronounced effect for two parallel coils placed about the FOV when the direction of under-sampling is in line with the coils because the central lines of $k$-space have little difference in sensitivity in each of the individual coil images. In contrast, when the under-sampling is orthogonal to the coils, every sampled line in $k$-space will bisect some part of the high sensitivity regions from each coil array element. In

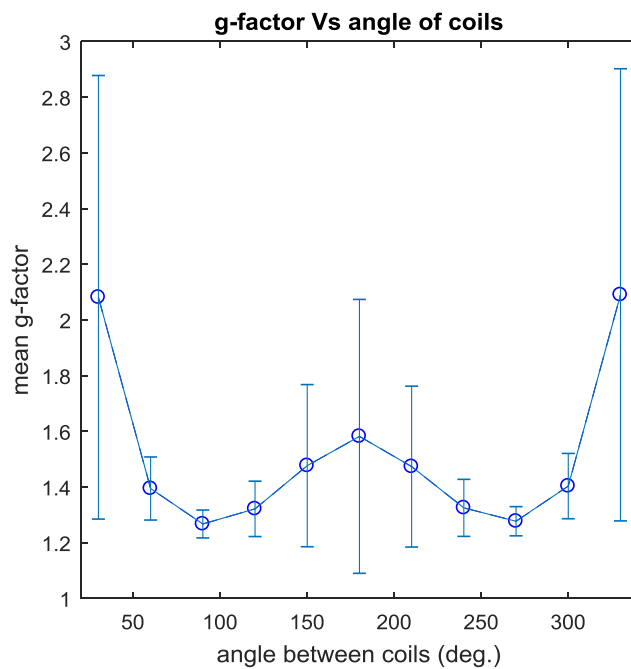Figure 5.10: g-factor as a function of angle between the two coils in the array. The errorbars represent the variance across the ROI. Minima occur when the coils are place orthogonally to each other about the FOV.
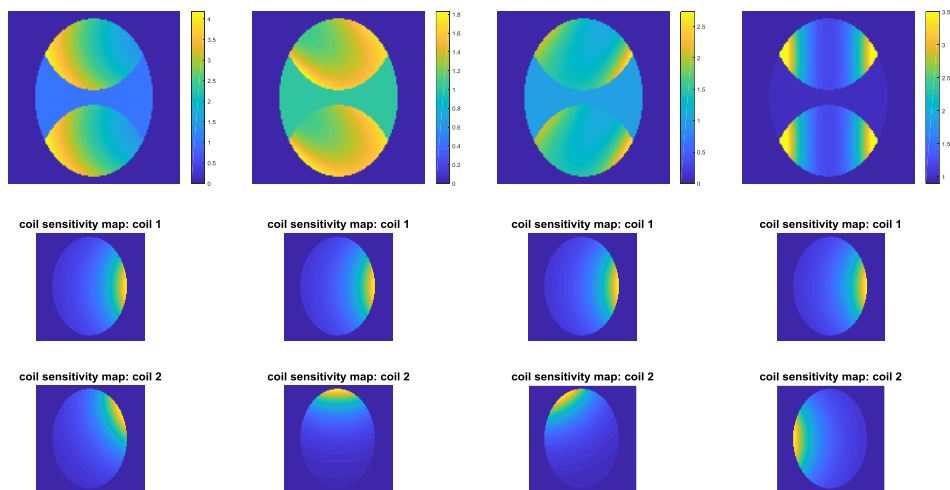


Figure 5.11: g-factor maps for varying angles between coils (top line) and the corresponding sensitivity maps for the coils below. The figure demonstrates how coil position affects the image reconstruction.
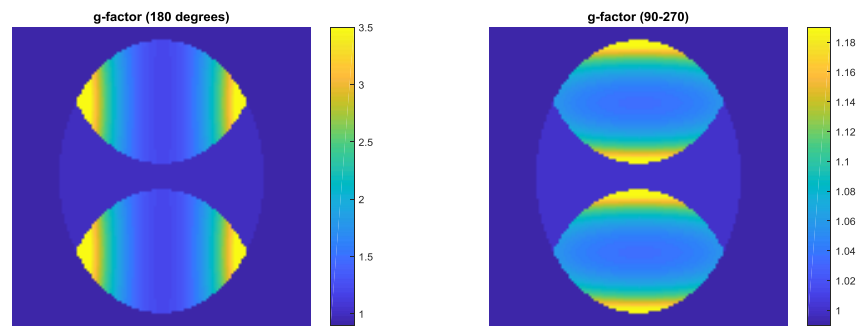
Figure 5.12: g-factor maps for reconstructed images where coils $180^o$ apart were place parallel and orthogonal to the direction of under-sampling. The average g-factor is approximately 3 times larger when the under-sampling is in line with the coils.

this case the achievable reconstruction is comparable to the orthogonal coil arrangement as shown in Figure 5.11. However for the purposes of defining an efficient probe-head design, 2 orthogonal coils are more flexible and have favourable electronic properties.

## 5.4 Discussion and Conclusions

PILS does not provide the versatility required for micro imaging, as the separation between the coils needed means that it increases the smallest possible FOV size. PILS provides fewer challenges electronically compared to SENSE, however it is limited with the direction of under-sampling (with respect to the receiver) as it requires a linear coil array. Therefore it is considered to be less effective for rapid micro-imaging than the more flexible SENSE.

SENSE, like most other under-sampling techniques is limited in its acceleration factor by the number of elements in the coil array and the final SNR is determined partly by this. Motion of the sample has a negative effect on the reconstruction as this not only makes the localisation difficult, but can also have an effect on the sensitivity of the coils. Motion artefacts in MR microscopy may be caused by either diffusive processes or vibration due to rapid switching of large gradients. However, these effects also cause artefacts in fully encoded images. It is possible to reduce the effect of such artefacts by using auto-calibration methods.

The results of the simulations show that the SENSE technique is suitable for micro-imaging as images with millimetre scale FOV's can be reconstructed. This is improved with coils that are smaller than the FOV placed around its edges. Therefore, limiting physically the amount the sensitive region of each detector overlaps. The data also shows that the optimum configuration for a coil array is 4 elements (that are smaller than the FOV width) placed at $90^o$

intervals around the FOV, this provides the best reconstruction. However, limitations on space and number of spectrometer channels available means that this is not possible if there is to be a separate transmit channel. Therefore it was determined that the next best situation is to have two coils placed orthogonally to each other. This may result in some darker patches towards one corner of the image, however it allows the best quality reconstruction, as seen from the g-factor maps.

Parallel coils provide a good image overall and are nearly as good as orthogonal ones as long as the direction of under-sampling is not parallel to the coils. For this reason, it is better for imaging flexibility to have orthogonal coils.

What is not clear from the simulations or even considered at this point is how the phase change due to diffusion in the presence of the gradient, as given by Equation 2.57 will limit the reconstruction, as the received signal phase contributes to the reconstruction.

In conclusion it has been shown that the SENSE reconstruction will work effectively with only 2 coils in the receiver array. It has been shown that for a good reconstruction the coils need to be smaller than the FOV in order to limit the overlap between the sensitive regions of the receiver coils. It was also demonstrated that SENSE will allow images to be reconstructed that have an FOV size on the order of 1 mm. Finally, the results support the idea that the most flexible and achievable compromise for a coil array to be used with the dual iso-centre magnet is to have two coils that are placed $90^o$ apart about the FOV.

# Chapter 6

# 2 Channel Proton
# Probe-Head

## 6.1  Introduction

The design and building of novel hardware for NMR microscopy poses many challenges, especially when it is necessary to perform sub Nyquist sampling of the data. Aspects involved in the construction of any NMR probe along with complications faced when constructing an array of small coils are presented in this chapter.

In this chapter the first generation of the micro imaging probe-head for SENSE imaging is presented along with the problems that have been overcome to allow the high level of sensitivity required for each of the coils. This has been designed to allow rapid acquisition of millimetre scale FOV sizes and pixel resolution of tens of microns. The overall goal is to be able to image large single cells, such as the Xenopus Oocyte and eventually use hyper-polarised metabolites to image active transport without the need for bulky green fluorescing proteins attached to the metabolite in question. The Oocytes are large compared to normal single cells however are still small enough to pose a significant challenge for MRI as they are approximately $1mm$ in diameter. In order do distinguish features such as the animal and vegital hemisphere and the cell nucleus, pixel sizes on the order of 10's of $\mu$m will be required.

In section 6.2 the principles behind the sensitivity of a receiver coil in NMR is presented along with how the coil resistance is affected by frequency and how this affects the performance. section 6.3 explains the importance of the quality factor and how tuning and matching networks are used to achieve the most efficient power transfer from the spin system to the spectrometer, via the tuned and matched receiver. section 6.4 deals with the electronic difficulties faced when constructing an array of multiple transmitters and receivers. The effect of coupling is discussed and possible ways to eliminate

this are presented. Bench-top experiments to determine the appropriate coil configuration are summarised before a detailed overview of the materials and methods used to construct the 2 channel micro-imaging probe-head is given in section 6.5. section 6.6 shows the performance of the probe-head in terms of the tuning and matching, achievable SNR in a single scan and the $B_1$ field it produces. Imaging with the probe head in order to demonstrate that parallel acquisition is a suitable tool for NMR microscopy is carried out and the results are presented in section 6.8.

The aim of this chapter is to demonstrate the design philosophy and principles underpinning the hardware and to show that the probe-head is fit for purpose as a micro-imaging device with accelerated acquisition capabilities.

Reconstructed under-sampled images are generated using the SENSE algorithm in order to show the versatility of the constructed probe.

## 6.2   Coil design considerations

When constructing a probe-head for NMR there are many considerations to be taken into account such as maximising the sensitivity of the probe, which is paramount for micro-imaging in order to obtain the required SNR. The factors affecting the sensitivity, the noise and hardware related methods, to improve the achievable SNR are explained in this section.

### 6.2.1   Sensitivity and Noise

One of the main factors affecting the SNR is the ability of the detector to couple to the entirety of the magnetisation. Due to the principle of reciprocity, originally demonstrated by Hoult (17), we see that the signal observed at a given point in space is proportional to the magnetic field at that point produced by the detection coil when a unit current is passed through it,

$$S = - \left( \frac{\delta}{\delta t} \right) \int_V \left( \frac{B_1}{i} \right) \cdot M dV, \qquad (6.1)$$

where $S$ is the received signal amplitude, $B_1/i$ is the field per unit current applied to the coil and $M$ is the magnetization at a given point in the sample (25; 14; 22). It has been shown that the amplitude of the received signal will vary spatially if the $B_1$ field is not homogeneous across the sample. Therefore it is important when considering the detector design to also consider the size and shape of the detector and the sample.

The sensitivity of the NMR experiment for small samples is given by (18; 162; 163):

$$\text{Sensitivity} = \frac{\text{Signal}}{\text{RMS noise}} = \frac{S}{\sigma_{\text{noise}}}, \tag{6.2}$$

where $\sigma_{\text{noise}}$ is the Johnson or thermal noise. Thermal noise for a given bandwidth ($\Delta f$) is then (164),

$$\sigma_{\text{noise}} = \sqrt{4K_B T_c \Delta f R}. \tag{6.3}$$

Equation 6.3 shows that the noise in the final spectrum is dependent on the temperature of the coil ($T_c$), the receiver bandwidth ($\Delta f$) and the total effective resistance of the coil ($R$) (165; 166). Care has to be taken when considering the receiver bandwidth as this affects the spectral width and the noise. The sample temperature affected the final SNR, however this is taken into account when considering the total magnetisation (see Chapter 1). When building an NMR probe the resistance is an important factor to consider as this is usually intrinsic to the device and determines the limit on the minimum level of the noise contribution from the coil.

## 6.2.2 Coil Resistance

The total resistance of the coil depends on a combination of several factors, as demonstrated by

$$R_{\text{Tot}} = R_\Omega + R_{\text{sample}} + R_{\text{ac}}, \tag{6.4}$$

where $R_\Omega$ is the DC resistance and is conditional upon the physical properties of the material used for the receiver coil (165). The term $R_{sample}$ describes the effect of eddy currents and mutual impedance due to the presence of a sample near the receiver coil which gives rise to radiation damping (167). For small coils the interaction between the coil and the sample is minimal so this term can be neglected for many micro-NMR experiments. $R_{ac}$ is the resistance that is encountered due to alternating current. $R_{\text{ac}}$ is given by,

$$R_{\text{ac}} \approx \frac{l\rho}{\pi \left( D - \delta \right) \delta}, \tag{6.5}$$

where $l$ is the total length of the conductor, $D$ is its diameter, $\rho$ is the resistivity (14). $\delta$ is the depth at which the current density is 37 percent of the value at the surface of the conductor due to alternating current, known as the skin depth.

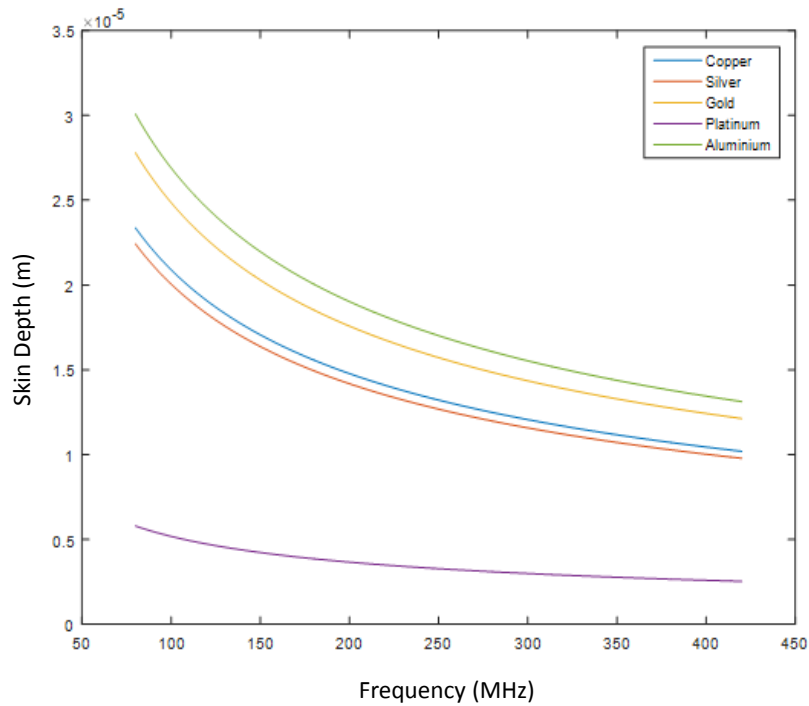The skin depth ($\delta$) is given by,

Figure 6.1: Graph showing simulated skin depth as a function of frequency for metals with varying conductivities. The graph was produced in Matlab using Equation 6.6.

$$\delta = \sqrt{\frac{\rho}{\mu_0 \mu_r \pi f}}. \tag{6.6}$$

$\mu_0$ and $\mu_r$ are the permittivity of free space and relative permittivity for the conductor respectively. $\rho$ is the resistivity of the conductor and $f$ is the working frequency. As the frequency ($f$) increases the current carrying area of the conductor reduces and therefore the resistance ($R_{\mathrm{ac}}$) increases (168; 159). The effect of the frequency on the skin depth for some of the conducting materials used for MR-applications is shown in Figure 6.1.

From Equation 6.5 it follows that by minimizing the ratio of conductor length to cross sectional area (within the skin depth limits) the resistance of the coil can be minimised, thereby reducing the noise.

### 6.2.3 Filling Factor

Minimising the length of the conductor in the probe has the advantage of reducing the volume of the resonator and therefore the proximity of the coil to the sample. Having a coil that is as close to the sample as possible is important as the the principle of reciprocity shows that the signal received from a given point is proportional to the strength of the magnetic field produced by the coil at that same position (169). Therefore, given that the

104

RF field strength is proportional to the distance from the resonator it is vital that the coil size is suited to the volume of the region of interest. The term relating the volume of the sample to the volume of the coil is known as the filling factor ($\eta_c$), described for a solenoid as,

$$\eta_c \simeq \frac{V_s}{2V_c},\qquad(6.7)$$

where $V_s$ is the sample volume and $V_c$ is the coil volume (159). This term is harder to quantify for surface coils and it is simple perhaps to just consider coil sensitivity maps within the sample and the principle of reciprocity.
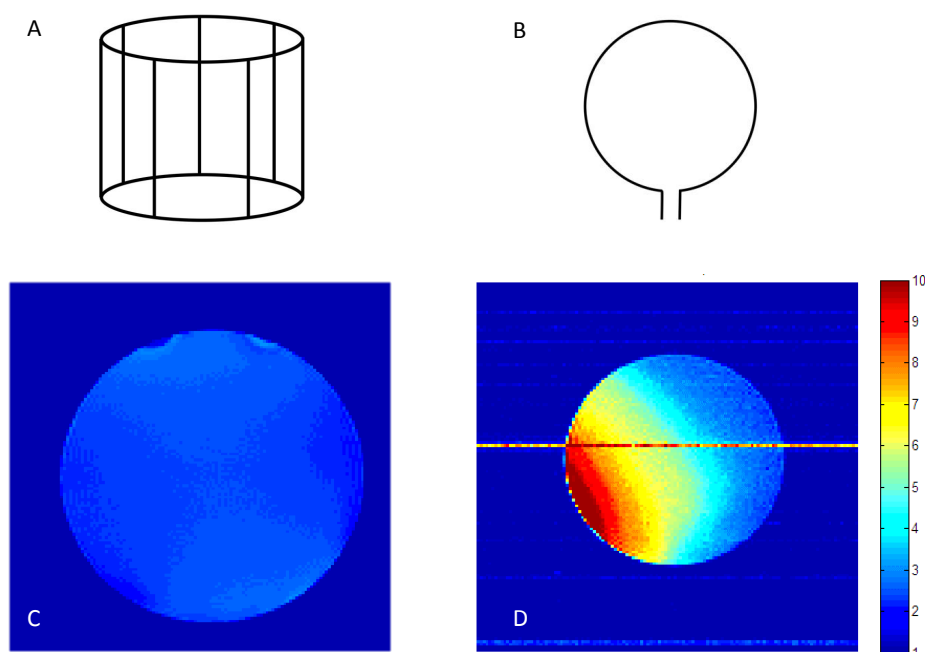


Figure 6.2: Diagram of a 30 mm (ID) birdcage coil (A) and a 1.6 mm (ID) surface coil (B) with their corresponding field maps, (C) and (D) respectively. The field maps are displayed in units of $\mu$T and the color axis of the the birdcage coil map is set to the same as that of the surface coil in order to highlight the difference. The artefact in the surface coil field map is due to external noise. The field of view in (C) is 50 mm where as the field of view in (D) is 5 mm.

Since sensitivity is improved by increasing the filling factor and considering that the aim of the project is to carry out micro-imaging on small sample, it is clear that the coil needs to be as close to the sample as possible. The optimum SNR per unit volume is achieved by using surface coils as the coil can be placed directly at the point of interest (170).

The difference in the $B_1$ field due to proximity of the coil is shown in Figure 6.2. A commercial birdcage coil (30 mm ID, Bruker) , tuned to proton frequency is compared with a home built 2 turn surface coil wound from 0.7 mm enamelled copper wire. The specifications of the two coils and the maximum measured $B_1$ values are presented in Table 6.1.

105

The FOV is $128 \times 128$ pixels with the sample a 10 mM $CuSO_4$ water solution. The colour map scale in Figure 6.2 has been kept the same for both images to highlight the difference between the coils. Artefacts that appear in the phase encoding direction of the image occur due to spurious echoes caused by poor homogeneity of the $B_1$ field and external noise being received by the transmission line (171). The field produced by the surface coil is greater across the sample than that of the birdcage coil however the strength of the field decays with distance, according to the Biot-Savart law. It is clear from the images in Figure 6.2 that over a small volume the performance of the surface coil is much better. Following the principle of reciprocity, the surface coil's $B_1$ field equates to a much higher SNR per unit volume compared to the volume coil. However, the volume coil produces a much more homogeneous field map, allowing homogeneous excitation across the sample.

Table 6.1: Table showing the specifications of the birdcage and surface coil. The sample is water and 10 mM $CuSO_4$.

|  | Birdcage Coil | Surface Coil |
|---|---|---|
| Coil ID | 30 mm | 1.6 mm |
| FOV | 50 mm | 5.0 mm |
| sample width | 30 mm | 2.6 mm |
| Max $B_1$ | 3.8 $\mu$T | 11.4 $\mu$T |

## 6.3   Resonant Circuits

In order to effectively detect the minuscule voltages that form the NMR signal, it is important to efficiently couple the detector to the sample magnetisation. This is achieved by using passive components in a given arrangement to create a resonant circuit, so that the small oscillations that occur due to the precession of the spin system are able to produce large amplitude oscillating voltages in the receiver circuit.

A resonant circuit is traditionally consists of three types of passive components, a resistor ($R$), and inductor ($L$) and a capacitor ($C$). Other, more exotic resonators using transmission lines or dielectrics have also been proposed, however they are not relevant for the scope of this discussion (172; 173; 174; 175; 176).

Figure 6.3 shows three different types of resonant circuit based on passive components (165). The resistance of these components, for the purpose of the diagram is assumed to be negligible, however, as the coils get very small or very big the resistances become difficult to work with. The NMR coil is represented by the inductor. The resonant circuit (A) associated with inductor L1, is known as as parallel tuned - series matched circuit, where as
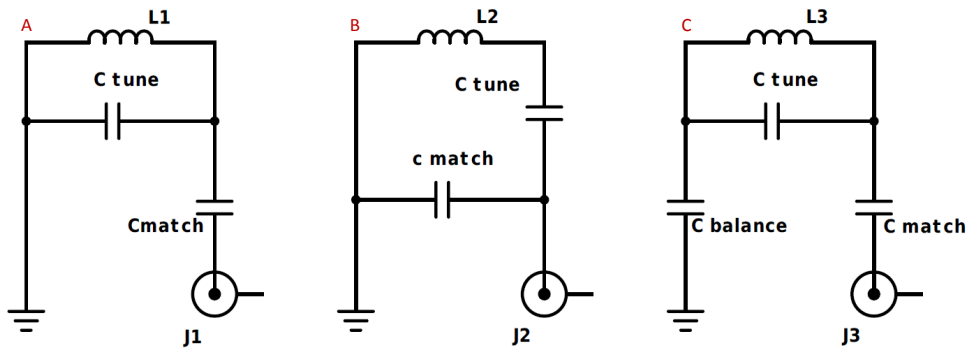
Figure 6.3: Three types of tuned and matched resonant circuit, series tuned - parallel matched (A), parallel tune - series matched (B) and parallel tuned - balanced matched (C) (165).

the circuit (B) associated with L2 is a series tuned - parallel matched circuit. This means that the coil is tuned to resonate by a capacitor in series with an inductor and then matched to the appropriate impedance by a second capacitor, in parallel. (C) is known as a balanced matched circuit and is described in detail in subsection 6.3.3.

Considering only a circuit with a capacitor $C$ and inductor $L$ in series, where the reactive component of the impedance for a capacitor is $X_c = \frac{1}{C\omega}$ and for an inductor is given by $X_L = L\omega$, it is shown from Equation 6.8 how the impedance of the circuit is affected by the inductor and capacitor

$$Z = R + j(L\omega + \frac{1}{C\omega}),\qquad(6.8)$$

where $L$ and $C$ are the inductance and capacitance respectively. Resonance occurs when the reactive terms in Equation 6.8 cancel so that $Z(\omega) = Re\{Z\}$. This means that the current is maximum and in-phase with the voltage. An $LC$ tank circuit is resonant when

$$L\omega_0 = \frac{1}{C\omega_0}.\qquad(6.9)$$

Therefore the resonance condition for tuning of the RF coil is given by (166)

$$\omega_0 = \frac{1}{\sqrt{LC}}.\qquad(6.10)$$

107

It is Equation 6.10 that is used to estimate the required capacitance value when building an NMR probe head (165).

## 6.3.1 Quality Factor

The ability of the resonant circuit to store energy is given by the $Q$-factor. This is related to the bandwidth ($\Delta f$) and the frequency to which the circuit is tuned (165). The $Q$-factor is given by

$$Q = \frac{\omega_0}{\Delta \omega} = \frac{\omega_0 L}{R},$$ (6.11)

where $\Delta \omega$ is the bandwidth expressed in angular frequency units. Equation 6.11 shows that the resonator stores energy more easily at high frequencies and is limited by the resistance of the circuit. The time constant determining the rate of decay of energy, known as the ring down time ($\tau$) is given by

$$\tau = \frac{2Q}{\omega_0},$$ (6.12)

which shows how the energy storage is damped by the resistance of the resonator (165). It is important for receiving the signal that the Q-factor is as high as possible, however it is also vital that the transmitted RF pulse is not still "ringing" when the receiver gate is open. Therefore in some high Q resonators, designed for transmit and receive, a damping circuit activated by gated diodes or veractors can be incorporated (177; 178).

## 6.3.2 Matching Networks

Matching the probe head to the spectrometer input is vital when attempting to maximise the SNR from the detected signal. A typical matching network, shown in Figure 6.3, will contain a capacitor ($C_M$) to convert the output impedance of the tuned resonator to the required input impedance (179). Typically this is $50\Omega$ due to the fact that the characteristic impedance of standard transmission lines are also $50\Omega$. As a consequence most spectrometers will have their components, such as the pre-amplifiers and the power amplifiers matched to this impedance figure (180). The role of the matching network is explained in a general sense by Figure 6.4, where it is shown how the matching network transforms the impedance to match the characteristic impedance in order to achieve the most efficient power transfer. If the probe-head is poorly matched then power is reflected. The quality of the match between output and characteristic impedance is determined by the real and imaginary components of the reflection coefficient, as represented by a Smith chart.
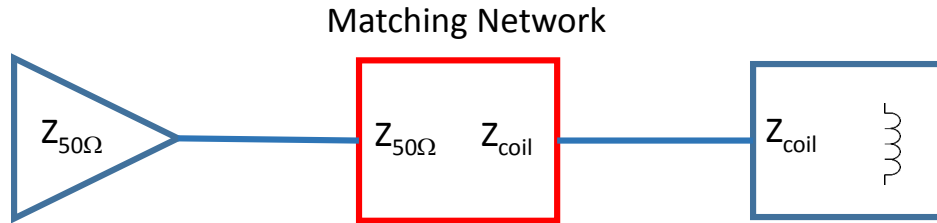
Figure 6.4: The schematic shows how a matching network is integrated into the circuit between the resonator and the pre-amplifier in order to allow the optimum power transfer between the two.

An example of a Smith chart is shown in Figure 6.5. The Smith chart is a polar plot that considers the reflection coefficient ($\Gamma$) for a given characteristic impedance ($Z_0$) and allows relatively easy visualisation of the required components to achieve a good match. At the centre of the chart is the point of perfect matching where $\Gamma = 0$. The right hand side represents an infinite impedance or an open circuit, and the left hand side represents a short circuit with an impedance of zero. The reflection coefficient is given by,

$$\Gamma = \frac{Z - Z_0}{Z + Z_0},$$ (6.13)

where $Z$ is the impedance of the load (i.e. the resonant $LC$ circuit) and $Z_0$ is the characteristic impedance, usually $50\Omega$. By considering the effect of a parallel and a series capacitor on an inductor (as demonstrated in Figure 6.3 it is possible to understand how matching works. When a capacitor is placed in series it changes the impedance of the circuit by moving its position to a different point along a circle of constant resistance. Conversely, the parallel capacitor has the effect of changing the impedance as though it is moving along a line of constant reactance (165).

The effect of the tuning and matching capacitors on a series tuned parallel, matched resonant circuit is shown for a series $LC$ circuit to be,

$$\frac{1}{C_T\omega} = L\omega - \sqrt{r(Z_0 - r)},$$ (6.14)

and for a parallel $LC$ circuit,

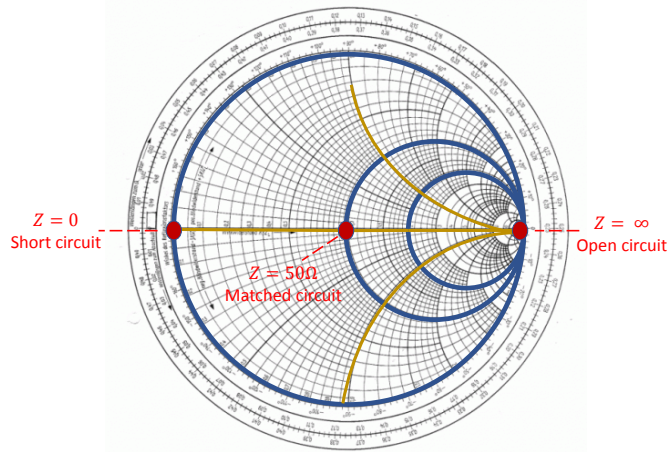$$\frac{1}{C_M\omega} = Z_0\sqrt{\frac{r}{Z_0 - r}},$$ (6.15)

109

Figure 6.5: Example of a smith chart. The blue circles represent lines of constant resistance and the yellow lines are lines of constant reactance. The centre of the smith chart is set to the matching resistance which is typically $50\Omega$. The upper hemisphere relates to an inductive circuit and the lower relates to a capacitive circuit.

where $r$ is a purely resistive impedance. When using a series tuning capacitor this kind of circuit is preferable when the inductor has a low DC resistance. Conversely the parallel tune-series matched circuit makes a large impedance across the inductor requiring a conjugate series matching to cancel the inductive impedance. Parallel tuned resonators usually provide a less lossy circuit than a series tuned circuit because in parallel tuned circuits, only the tuning capacitor resistance (ideally) contributes to the losses.

### 6.3.3 Balancing

The circuit in Figure 6.3 (C) shows a balanced probe head, where the matching capacitor is split into two and placed one either side of the tank circuit. Due to the addition of capacitors in series the value has to be double that of the single matching capacitor. The value for the balanced matching capacitor ($C_B$) is given by,

$$C_B = 2C_M. \tag{6.16}$$

Splitting the capacitors has the effect of creating an equal voltage across the terminals of the tank circuit, with opposing phase and generating a virtual ground positioned at the centre of the inductor (181; 182). This reduces the the E-field between any point and ground (not within the coil itself. Therefore this can help to reduces the coupling to other elements in the circuit and the sample. This plays an integral role in helping to remove

110

common mode effects in the transmission lines which are highly deleterious to the coil array.

Sensitivity is often reduced due to an increased coupling of the E-field to the sample as the electric field induces currents in the conducting sample which can cause a heating of the coil and an increase in resistance. These induced eddy currents in the the sample can couple to the coil and reduce the Q-factor (as described in subsection 6.3.1) and also increase the mutual coupling between elements of a receiver array. Coupling to the sample causes a shift in the tuned frequency as the mutual impedance affects the resonance. Placing a virtual ground at the centre of the probe splits the voltage across the coil terminals and therefore the E-field is halved (183). The reduction in E-field reduces the coupling to the sample and so eliminates some of the shift from the tuned frequency that this causes in the coil. This shift is reduced by a factor of approximately $\sqrt{2}$ (165).

The antenna effect is caused by far field, electric field losses in the transmission lines of the probe (184). This may have a drastic negative effect on the sensitivity and in a coil array will cause coupling between the transmission lines and other components in the probe. The minimisation of the coupling between receiver array elements is discussed in subsection 6.4.1.

## 6.4   The Coil Array

The small surface coil provides a much higher SNR per unit volume than a much larger volume resonator (or "body" coil). However the drawback of using small coils is that the volume over which signal can be detected is also small. The sensitive depth of a surface coil is approximately the radius of the coil. If the desired FOV size is larger than that of the surface coil, this will cause sensitivity artefacts in the form of dark areas in the image. To counteract this the NMR phased array was proposed by Roemer *et al* in the 1990 seminal paper. Roemer presented a method for constructing a receiver that consisted of an array of surface coils, with the intention of expanding the working volume of the receive from the single surface coil. It was shown that an array of small coils provides a better SNR than a single receiver covering the entire sample (161).

The main requirement for the coil array is that each element in the array has an individual receiver channel in order for the elements' signal to be distinguished and separated.

### 6.4.1   Coupling

When two resonant circuits are placed close two each other (especially when there is a sample present) they will have some level of cross talk or coupling.
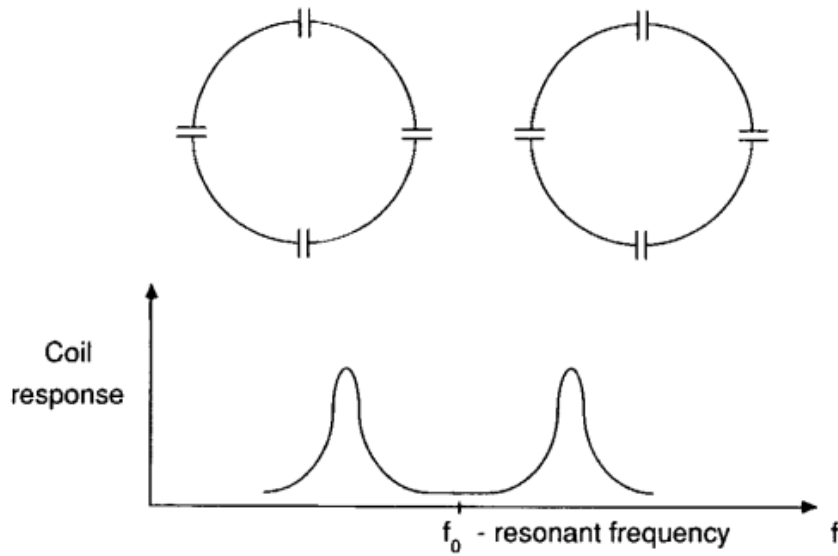
Figure 6.6: Schematic demonstration of how two coils in close proximity cause a splitting of the tuned frequency as presented by Roemer (161). Top shows two coils that are tuned to the same frequency placed in the same place in close proximity. Bottom shows the schematic representation of the effect of the proximity of the two tuned coils on the resonance.

This has the negative effect of reducing the sensitivity of both of the receiver circuits and causing a splitting of the tuned frequency, as demonstrated by Figure 6.6 (161; 182). The cross talk between the two coils means that there is a shared SNR, leading to the introduction of correlated noise between the receiver elements. This is especially damaging if the array is to be used for accelerated acquisition as it reduces the uniqueness of each receiver element and hamper the ability of the receiver to spatially encode the under-sampled signal. Therefore it is important when constructing a coil array that there is an understanding of how the coupling works and how to best minimise it (185).

The effect of coupling between two tuned circuits is represented in the circuit diagrams shown in Figure 6.7 and 6.8, where the coupling is shown in terms of lumped elements (resistance, capacitance and inductance) in the latter.

The mutual resistance between two array elements ($i$ and $j$) occurs due to eddy currents and thermal noise in the dielectric sample, which in turn produce a current in the inductors (22). The mutual resistance is given by

$$R_{ij} = \omega^2 \sigma \int \mathbf{A}_i \cdot \mathbf{A}_j d^3 v, \tag{6.17}$$

where $\sigma$ is the RMS noise and $\mathbf{A}$ represents the vector potential for each of the coils which is written as,
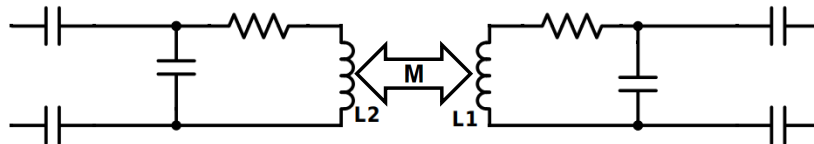
112

Figure 6.7: Two tuned coils placed in close proximity to each other exhibit a mutual inductance. L1 and L2 represent the individual inductances and M is the shared inductance between the coils.
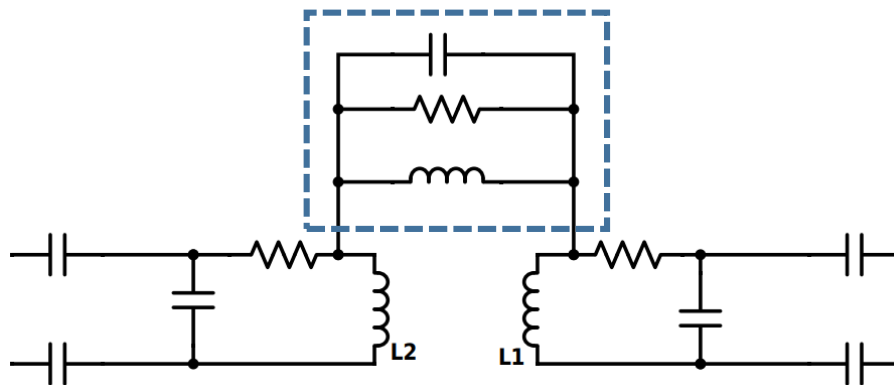


Figure 6.8: Circuit diagram for two coupled coils. The components situated in the dashed blue box represent the mutual inductance, capacitance and resistance between the coils. These contribute to the impedance and the resonance in a parasitic accumulation.

$$\mathbf{A} = \frac{\mu_0 I}{4\pi} \int \frac{\mathbf{ds}}{|\mathbf{r} - \mathbf{r'}|}. \tag{6.18}$$

$I$ is the current, $\mathbf{ds}$ is a vector that is tangential to the centre line of the coil and has a magnitude equal to the total distance around the coil and $|\mathbf{r\text{-}r'}|$ is the vector distance between the coil and the measurement position (161). Equation 6.17 and 6.18 show how the mutual resistance is affected by the current in the coils as well as the geometry of the coils in the array. However whenever there is a conducting sample the resistive noise will always contribute to the total noise in the received signal.

The effect of mutual capacitance between two coils is caused by electric fields due to charges on the two coils and is exacerbated by going to higher frequencies, usually at NMR frequencies this has a less prominent effect than coupling caused by the magnetic field (165).

Mutual inductance $M_{ij}$ is caused by the magnetic fields from two coils coupling which drives currents in the opposing coil. Unlike the previously described couplings, mutual inductance is not dependent on the current in the coil, but is determined purely by the geometry of the coils. This is demonstrated by Equation 6.19, known as the Neumann Equation,

$$M_{ij} = \frac{\mu_0}{4\pi} \int \int \frac{\mathbf{ds}_i \mathbf{ds}_j}{|\mathbf{r}_{ij}|}. \tag{6.19}$$

Where $\mathbf{r}_{ij}$ is the vector describing the distance between a point on coil $i$ and a point on coil $j$ of the coil, when the coil is broken up into elements, $\mathbf{ds}_{i,j}$ (161; 186). The mutual inductance is dependent on the inductance of the two coils that are in proximity to each other and can also be determined experimentally given,

$$M_{ij} = k\sqrt{L_i L_j}, \tag{6.20}$$

where $k$ is a coupling coefficient equal to,

$$k = \frac{Al}{2\pi d^3}. \tag{6.21}$$

$A$ is the area of the coil, $l$ is the conductor length and $d$ is distance between the coil centres (165). To retain good sensitivity on each of the receivers it is necessary to minimise the coupling.

## 6.4.2 Geometric Decoupling

Due to the mutual inductance ($M_{ij}$, defined in Equation 6.19) being purely related to the geometry of the coils and their relative positions, it is possible
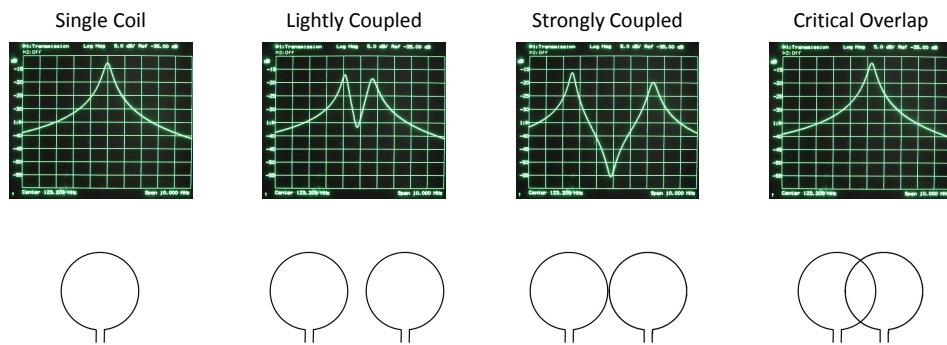
Figure 6.9: Frequency response of a tuned coil and the effect on introducing a second coil tuned to the same frequency. At a critical overlap point the mutual inductance cancels to reduce the splitting.

to reduce the coupling by overlapping the coils. The overlap, when at the critical point, generates a current that is in opposition to the current from the non-overlapped part of the coil and cancels the signal that is shared. This has the effect of removing the frequency splitting, shown in Figure 6.6, that is caused by the coil coupling (161; 187).

The critical overlap is demonstrated by Figure 6.9, where the effect on the resonance response of a tuned coil is shown and how the resonance response changes as a second coil, tuned to the same frequency is introduced. As the coils couple the resonance response displays the characteristic splitting shown in Figure 6.6 and then the splitting is removed due to overlapping of the two tuned coils to a critical point. As a rule of thumb to determine how much overlap is required, the distance between the coil centres for circular coils should be approximately 0.75 times the diameter. For a square coil this goes up to 0.9 times the diameter (161).

However, as was shown in the previous chapter, overlapping of the receiver coils is detrimental to reconstruction of under-sampled images, as the sensitivity profiles are no longer well defined (155; 188). This is one reason why clinical coil arrays require so many elements to guarantee a good and reliable reconstruction with up to 128 individual receiver elements (189).

**Bench Test of Geometric Decoupling**

A bench top experiment was carried out using two tuned circuits to examine the level of coupling between two coils. Two small coils made from 0.5 mm (OD) enamelled copper wire with 2 turns were tuned to 400 MHz. The coils were placed on etched circuit board in parallel tuned, series matched circuits. The angular and distance dependence on the coupling was measured using an network analyser (Agilent). The results were then compared to the theoretical models for distance and angular dependence on the coupling from Equation 6.21 and 6.19.
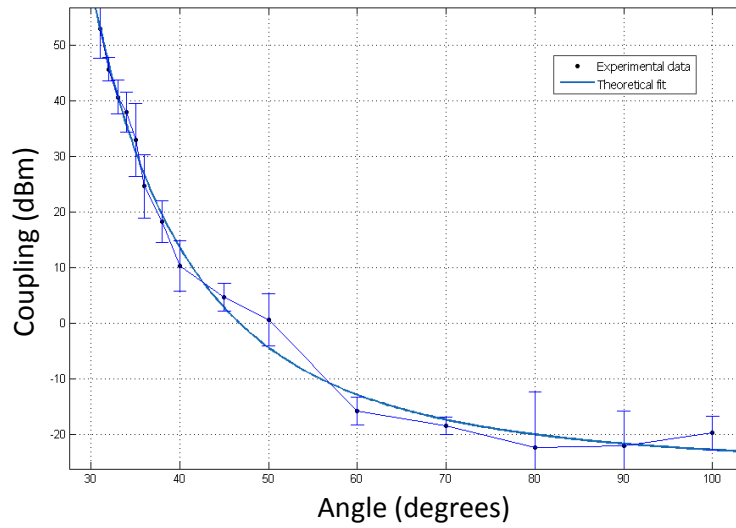
Figure 6.10: Top: Experimental set up for measuring the coupling between two tuned coils. Bottom: plot showing coupling fitted to Equation 6.21.
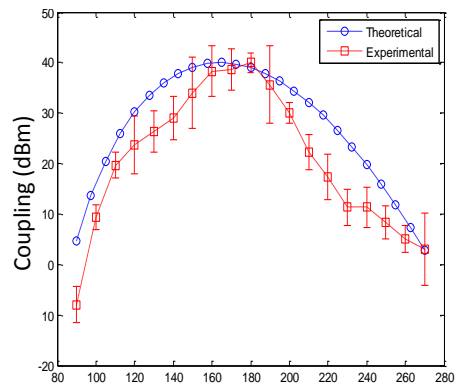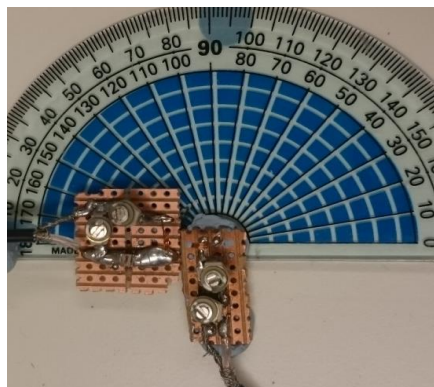




Figure 6.11: Left: Image of the set-up used to collect the data. Right: plot of the coupling and the mutual inductance calculated using Equation 6.19.

Figure 6.10 shows that the coupling between two coils scales as predicted by Equation 6.21 and also demonstrates that the level of coupling between the two parallel coils does not reach a satisfactory level until they are positioned at least 50 mm apart. This is not acceptable for a micro imaging array, due to the necessity to position the coils as close to the sample as possible, combined with the size of a typical sample being on the order of 1 mm.

Similarly, Figure 6.11 demonstrates the angular dependence on the mutual inductance and that a minimum in the coupling is achieved when the coils are placed at $90^o$ to each other. This is also advantageous as it was shown in previous chapters that the best SENSE reconstruction is achieved for coils that are orthogonal with well defined sensitive regions.

Discrepancies between the theoretical model and the experimentally collected data can be attributed to slight changes in distance, coupling between other elements in the circuit and capacitive coupling having a conjugate reactance and acting as a decoupling effect (190).

## 6.5   Probe Head Construction

Based on the simulations carried out on SENSE reconstruction in chapter 5 and the preliminary experiments to observe coupling between small coils, a 2 channel probe has been constructed that should be capable of collecting micro-scale proton images in a single scan, with an in-plane pixel resolution of $\sim 30 \mu$m easily achievable.

The methods and materials used to construct the probe-head along with some of the obstacles that had to be overcome to optimize the sensitivity of the coils are presented in this section.

### 6.5.1   Materials

In order to carry out accelerated acquisition, it is a minimum requirement for the probe-head to have two individual receiver channels. Restrictions on the probe dimensions are imposed by the dimensions of the gradient set.

The imaging gradients that are in place have a bore diameter of approximately 40 mm (there is some change down the inside of the bore) so this determines the outer diameter of the body of the probe, which is set to 39 mm. The length of the shaft is 600 mm to reach the iso-centre of the magnet with the probe-head itself adding a further 40 mm. The shaft is constructed from hard nylon tubing, as it is important to avoid materials that distort the magnetic field or are susceptible to induced eddy currents during the application of magnetic field gradients. The designs for the completed probe-head are shown in Figure 6.12.
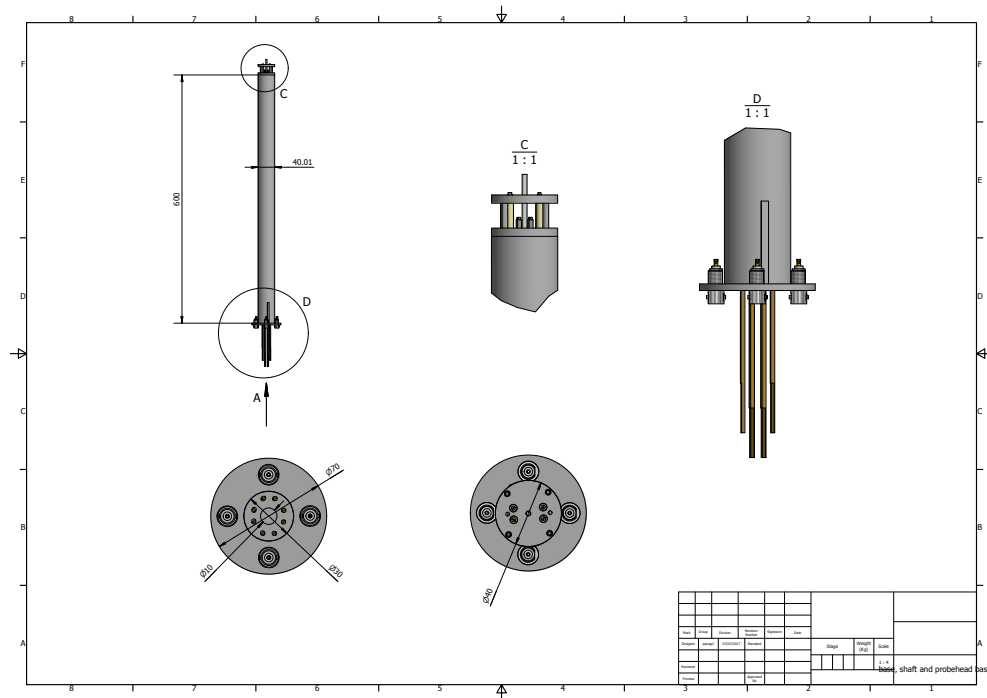
Figure 6.12: CAD drawing of the two channel proton imaging probe-head highlighting the important dimensions of the probe. The probe was designed to accommodate channels in 4 different positions for flexibility.

In order to maximise the sensitivity and limit parasitic inductance and capacitance due to unnecessary wiring, it is important to keep the tuning and matching circuit as close to the coils as possible (182; 183; 191; 192). This also means that the resistive losses between the matching circuit and the coil are kept to a minimum (180). However, placing two sets of circuits that can be tuned from outside the magnet in the top of the probe poses its own challenges as it is important to be able to adjust the tuning and matching of the probe-head once it is placed inside the magnet. Tuning rods are used to adjust the variable capacitors and these are held in place by the probe shaft and are spring loaded to keep them in contact with the variable capacitor. The rods are made from fibreglass with brass flat head screwdriver tips glued into the ends with epoxy resin. The tip of a tuning rod is visible in Figure 6.13 along with two tuned circuits.

**Tuning and Matching**

As demonstrated in subsection 6.4.1, the proximity of components and their orientation to one another, affects how they interact due to the nature of electric and magnetic fields. For this reason the probe-head was split across two levels to increase the distance between the circuits which reduces the electric field effect between the capacitors in the circuit.

The tuning and matching circuit used for both the coils in the array is a

**¹H SENSE probe-head**
(initial configuration)

CuSO₄ water sample

Semi rigid coaxial cable
RG405\U

Unused tuning rod

Coil 2 platform
(upper coil)

Johanson trimmer
capacitor (0.6-6 pF)

Coil 1 (lower coil) – PTFE
coated silver wire
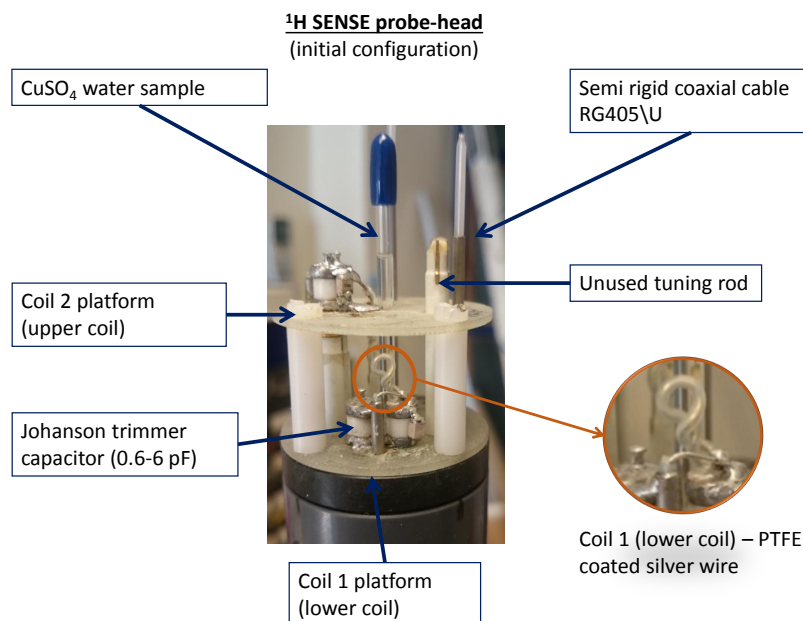
Coil 1 platform
(lower coil)

Figure 6.13: Image of the probe-head with a water and copper sulphate sample in place. The sample is contained in a 3mm OD NMR tube. The tuning circuits are placed on different levels to create space and improve the isolation of the array elements.

parallel tuned/series balanced-matched circuit. Variable capacitors were used for the tuning and one side of the balanced matching. The other balance matching capacitor was a Piconics ceramic chip capacitor. The capacitors are 0.8-6 pF Johanson non-magnetic trimmer capacitors with a 5.6 pF non-magnetic chip capacitor (Piconics Inc.) placed in parallel with the tuning capacitor to tune the coil to 400 MHz. Two 2 pF capacitors were placed in series with the coil and the variable matching capacitor to balance-match the circuit.

## Coil Construction

The coils were wound around a 1.6 mm diameter brass rod to ensure that they were all of a similar shape and size. Two different wires were tested while constructing the probe. Originally the coils were made from 1.5 turns of uncoated German Silver wire (seen in Figure 6.13), which was used for its favourable electrical properties. However, because the wire was not insulated it was necessary to cover the coil using PTFE tubing, thus meaning the spacings between the wires were large. Along with increasing the inner diameter of the coil, this created unfavourable $B_1$ fields and reduced the filling factor making it difficult to achieve a reasonable sensitivity.

In the final configuration of the probe-head two turns of 0.7 mm enamelled copper wire were used. Due to the enamel coating the turns can be placed much closer together and the inner diameter is 1.6 mm. The legs of the coils were wound tightly together as it was found that this improved the
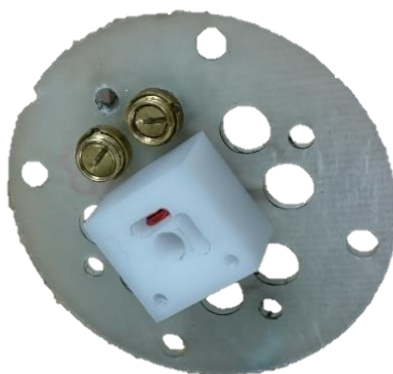
Figure 6.14: The underside of the top plate of the NMR probe-head showing the coil support that also acts as a sample holder. This keeps the coils perfectly aligned and close to the sample and reduces vibration of the sample. The underside of the trimmer capacitors are also visible.

isolation between the elements. It is thought that the field from the straight legs was able to interact with the other elements in the probe-head. This is cancelled, or at least reduced when the legs are wound around each other. The trade-off for this isolation is a slight increase in the self capacitance of the coils, bringing the self-resonance closer to the tuned resonance (193). The tuned circuits were attached to the spectrometer via RG405 semi-rigid coaxial cable (FC Lane - Horsham, England) connected to BNC connector at the bottom end of the probe.

## 6.5.2   Coil Performance

The coil performance was initially measured using a network analyser and showed a frequency response at 400 MHz of between -10 to -20 dB. In an ideal case a response of -30 dB would be achieved by both coils. When examined individually, both of the tuned circuits showed, unloaded responses of <-30 dB and a Q-factor of 60. However when placed inside the probe-head assembly the response was significantly decreased due to coupling between circuits and the sample. When a sample is added to the system, known as loading the coils, the frequency response and the Q-factor are affected due to the electric field effects in the sample (194).

The coupling between the two coils was measured on the bench-top, again using the network analyser, to be -1 dB. This was also tested inside the magnet with an aqueous copper sulphate solution, where the coupling was measure to be -11dB, with the difference being attributed to the presence of other conducting elements affecting the mutual inductance (195). Images collected from this configuration of the probe show a poor sensitivity and a resulting low SNR due to the coupling (Figure 6.15).

Previous bench-top experiments, as presented in subsection 6.4.1, showed
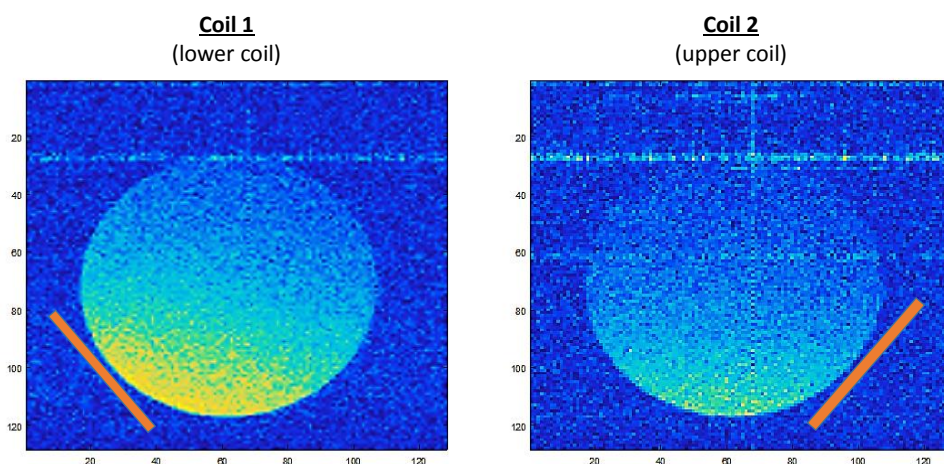
**Coil 1**
(lower coil)

**Coil 2**
(upper coil)

Figure 6.15: 128 by 128 pixel, gradient echo images from both the elements in the coil array with significant coupling. There is a 4 mm isotropic field of view and the slice thickness is 0.5 mm. The images show how the coils are sharing the signal and the separate sensitive regions are not distinguishable. The coils were place $90^o$ to each other about the sample, roughly highlighted by the orange squares. The sensitive regions in the images should correspond to the position of the coils for a well decoupled system. The line of noise towards the top of the image is due to poor shielding.

that the position of the coils is optimum for magnetic decoupling, therefore it is evident that other aspects of the probe cause the excess of cross-talk. This coupling is caused by several interactions between various elements of the probe-head, such as interactions between the "legs" of the coils, common mode currents in the transmission line, grounding issues and stray mutual impedance between the two circuits (in some cases exacerbated by the presence of the sample) (165; 196). In order to minimize this several methods have been implemented.

### 6.5.3   Removing Common Mode Effects

Common mode currents occur when the length of the transmission line is comparable to a single wavelength or more and are created by the signal being carried on the inner conductor of a coaxial line, inducing a current of the outer shield (see Figure 6.16) (197). This problem is especially disruptive in an array coil as there are multiple transmission lines and the common mode currents cause other currents to be generated on nearby elements of the array, which increase the noise in the image due to an increased level of cross talk. The common mode effects can be detected trough the presence of the antenna effect, whereby touching the shaft of the probe will cause a shift in the resonance response of the coil. This effect adds noise as well as parasitic impedance which reduces the sensitivity of the coil (165).

Traditionally a current trap or ferrite balun is added to a circuit displaying common mode, or antenna effects. This is an inductor wound around a
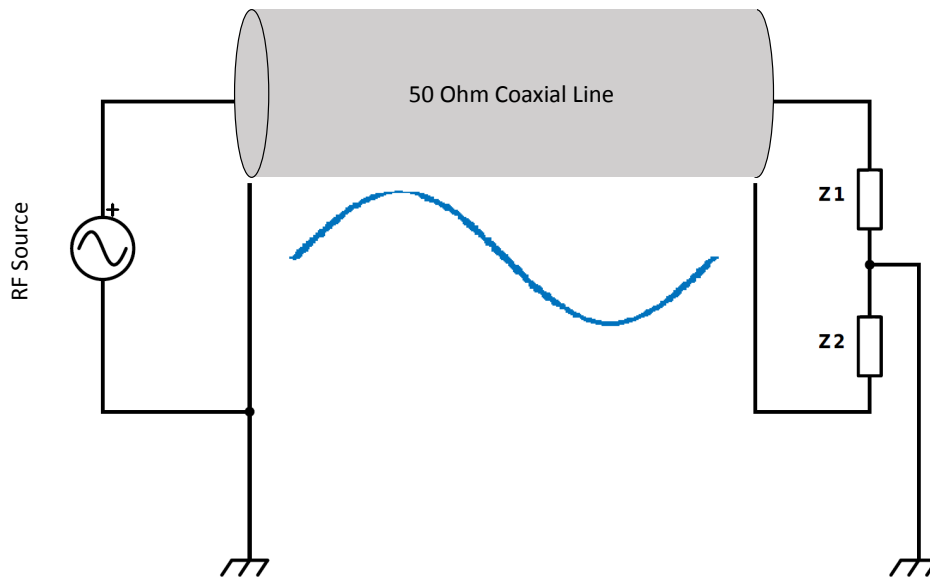
Figure 6.16: Formation of common mode currents in the outer shield of the coaxial cable due to the oscillating voltage on the inner coaxial conductor. The impedance of the outer shield, as by the inner conductor adds parasitically to the system.

toroidal ferrite material in order to filter out the unwanted current by posing a high impedance, and the ferrite core limits the far field effects of the inductor. However, in a system to be used inside a strong magnetic field, a ferrite core balun is not feasible. To reduce the effect a Bazooka (or sleeve) balun is added to the coaxial cable at node current points (184; 197).

The Bazooka balun is a length of cylindrical conductor that fits around the outer jacket of the transmission line with a dielectric between them. It is shorted at one end and open at the other. The length and diameter of the balun is determined by the materials being used and the frequency of operation. It is important, in order for there to be as close to infinite impedance as possible, that the electrical length is close to $\lambda/4$, and that the ratio of the balun sleeve and the inner diameter of the dielectric (the coaxial cable's shield outer diameter) be as large as possible, however there is little improvement to be had for a ratio greater than 3. The length of the balun can differ from the wavelength in the transmission line, however the balun must then be tuned to the correct electrical length with the addition of capacitors at the shorted end (184).

The balun used is shown in Figure 6.17 where it is also shown how the RF choke is situated in the probe. Two chokes were used for each transmission line as it has been shown in the literature that placing a choke at every node point is more effective for common mode rejection than only using one (197; 184). Due to the need for multiple baluns, the ratio of the inner and outer diameter is marginally sub-optimal at 2.7, however, good improvement in the reflection coefficient was measured.

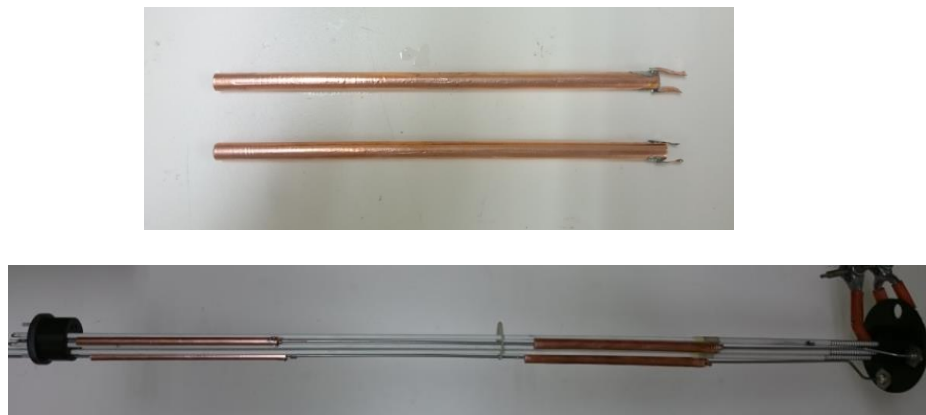As an added measure, extra PCB discs have also been added to the probe

Figure 6.17: Top: Two RF chokes with a OD of 5.75 mm and length of 15cm. Bottom: The inside of the probe, with the transmission lines and the tuning rods visible. The RF chokes are attached at node current points on the transmission line. The lines are also grounded every $\lambda/15$ cm along the line.

at intervals along the shaft. These allow all the internal parts to be held in place and also act to ground the probe, which helps to break down the common mode effects as the current is sent to ground and is prevented from forming a standing wave along the transmission line shield. To ensure that the grounding prevents common mode currents this has to be realised every $\lambda/20$, however $\lambda/10$ is sufficient to have a limiting effect (197).

The reflection coefficient is measured by calculating the voltage standing wave ratio (VSWR) for the coaxial cable. This was done using a homebuilt current probe to determine the position of current peaks along the shield of the coax. Before the introduction of the ballun and multiple grounds, common mode currents caused a reflection coefficient 0.53, which is equal to a reflected power of -6.35 dB (approximately 48% of the power is reflected). Compounding this problem coupling between elements was measured to be on the order of 10's of dB (depending on the tuning and matching of the circuits). When the RF chokes are applied and grounding points are introduced, the reflection coefficient is better than -40 dB and the coupling between two elements is measured as approximately -17 dB (this is still somewhat dependent on the tuning and matching capacitor positions).

As a result of the decoupling, balun and extra grounding, the coil frequency response was measured to be better than -20 dB at 400 MHz for both coils and the level of cross talk was limited to acceptable levels, thus ensuring that the coils were collecting individual image. The extra measures also saw the elimination of the antenna effect (i.e. the shift in frequency response due to touching of the probe shaft. Figure 6.18 demonstrates the benefit to the overall probe, where the imaging sequence is the same as that shown in Figure 6.15, the same $CuSO_4$ water sample was used. The sensitive regions of the individual coil elements are now visible and distinct due to the removal of the cross talk and reduction of the parasitic impedance.
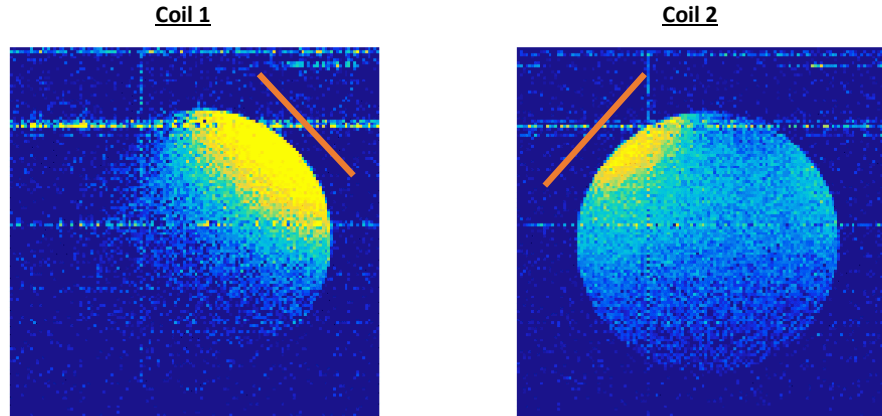
Figure 6.18: 128 by 128 pixel gradient echo images of copper sulphate showing two separate sensitive regions for the coils. Therefore, demonstrating that cross talk between the two coils is reduced by decoupling the elements of the array coil though the addition of balluns and grounding. The orange lines give a guide as to the position of the coils relative to the sample.

## 6.6 Probe-head Characterisation

The performance of the probe is often measured by the Q-factor which is calculated using Equation 6.11. Due to the parasitic impedance effect of the sample, the Q-factor changes depending on the sample loading. Therefore, it is important to express the loaded and unloaded Q-factor to give a full picture of the coil's performance. The Q-factors for the probe are shown in Table 6.2, where a water and copper sulphate sample was used for measuring the loaded Q. The Q-factor was measured by recording the central frequency and the bandwidth of the frequency response on the network analyser and the bandwidth was taken from the $-3$ dB mark at the frequency response. The bandwidth of the receiver is proportional to the resistance of the coil, $R$,

$$R = L\Delta\omega, \tag{6.22}$$

where $L$ is the inductance and $\Delta\omega$ is the bandwidth (159). Given that the sample contributes a mutual resistance to the coil, it is possible to work out from the loaded and unloaded Q-factors, exactly the contribution of the coil to the resistive noise, when compared with the total noise, as demonstrated by

$$\frac{\sigma_{\text{coil}}}{\sigma_{\text{total}}} = \frac{\sqrt{r_{\text{coil}} + r_{\text{sample}}} - \sqrt{r_{\text{sample}}}}{\sqrt{r_{\text{coil}} + r_{\text{sample}}}}. \tag{6.23}$$

$\sigma_{\text{coil}}$ is the noise due to the coil's resistance, and $\sigma_{\text{total}}$ is the total noise in the

loaded system. Since the resistance determines how well energy is stored in the resonant circuit is is possible to use the Q-factors to simplify the above equation:

$$\frac{\sigma_{\text{coil}}}{\sigma_{\text{total}}} = 1 - \sqrt{1 - Q_{\text{loaded}}/Q_{\text{unloaded}}}. \tag{6.24}$$

This shows that the majority of the noise in the system is due to the coils (180; 198), however there was still a change in the Q-factor as well as a frequency shift upon loading the device which indicates that the coil is coupled to the sample. This is explained by the results presented in Table 6.2.

Table 6.2: The table shows how Q-factor, bandwidth, shift of the tuned frequency due to loading and the coil noise as a percentage of the total noise. Due to the size of the coils, within the error of the measurements, all of the noise is due to the coils, meaning there is little parasitic resistance between the sample and the coil.

|  | Coil 1 (lower coil) | Coil 2 (upper coil) |
| --- | --- | --- |
| $Q_{loaded}$ | 53.76 | 44.15 |
| $Q_{unloaded}$ | 53.51 | 44.80 |
| loaded resonance response (dB) | $-58$ | $-60$ |
| unloaded resonance response (dB) | $-54$ | $-52$ |
| loading shift (MHz) | 0.6 | 0.5 |
| Bandwidth unloaded/loaded (MHz) | 7.48/7.44 | 9.13/9.06 |
| coil noise percentage | 100 | 100 |

Table 6.2 shows that there is a considerable shift in the resonance response upon loading, which suggests that there are parasitic effects taking place. This is not observed when considering the measured loaded and unloaded Q-factors. However it is possible that the coupling between the coils means that the effect is shared and so appears to have less of an effect on the Q-factor.

Coil one has a resonance response when loaded of $-58$ dB ($\pm 6$ dB) and when unloaded this drops to $-54$ dB. The response of coil two is $-60$ dB which drops to $-52$ dB when a sample is introduced. This is a more than acceptable frequency response for achieving a good SNR in an imaging experiments.

## 6.6.1  Signal to Noise Ratio

A 10 mM copper sulphate and water phantom was constructed with two capillaries placed inside to give contrast to the images and allow assessment of the effect of the coils and their positions. A schematic of the sample is shown in Figure 6.19 where the approximate positions of the coils are
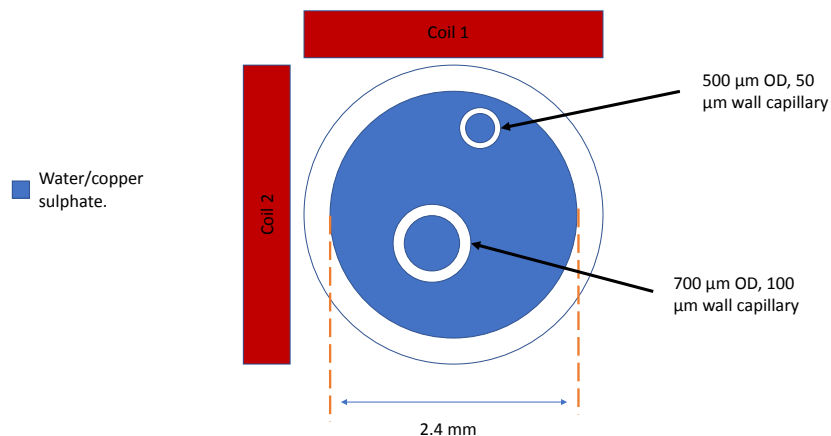
Figure 6.19: A schematic of the sample used to give contrast and ensure correct spatial representation of the sensitivity of the coils. The sample is a 10 mM $CuSO_4/H_2O$ solution. It is contained in a 3/2.4 mm OD/ID NMR tube with a 0.7/0.5 mm OD/ID capillary and a 0.5/0.4 mm OD/ID capillary.

indicated relative to the capillaries. This sample is used later in this chapter as it serves as a good test of the ability of the sense algorithm to properly reconstruct under-sampled images.

By creating a map of the SNR it is possible to see where the limit of detection lies. Figure 6.20 shows how the SNR varies across the FOV for each of the coils in the probe-head. The images were collected using a gradient echo sequence with a 4mm FOV on a 128 x 128 grid and a slice thickness of 0.5 mm. The flip angle is not known due to the spatially varying $B_1$ field and only a single scan was required.

The SNR maps show that close to the coils there is high SNR, given the small sample volume, however they also show that the depth of detection is poor. This is highlighted further by the plots in Figure 6.21, where the SNR in an axial direction from the central position of each of the coils is plotted against distance.

Given that the diameter of the coils is approximately 1.6 mm, Figure 6.20 and 6.21 provide evidence for the rule that the sensitive region of a surface coil receiver is approximately equal to its diameter, given that the coils are positioned just at the edge of the FOV (165). The sudden drop off in SNR in the profile for coil 1 in Figure 6.21 is due to the edge of the quartz capillary where there is no NMR signal, highlighted by the green arrow. Whereas the peaks highlighted by the red arrows that are seen at 0.2 mm and 0.9 mm for coil 2 is due to external noise.

Coil 2 has a lower performance and a greater antenna effect contribution, despite both coils being well shielded at the probe-head. This suggests that
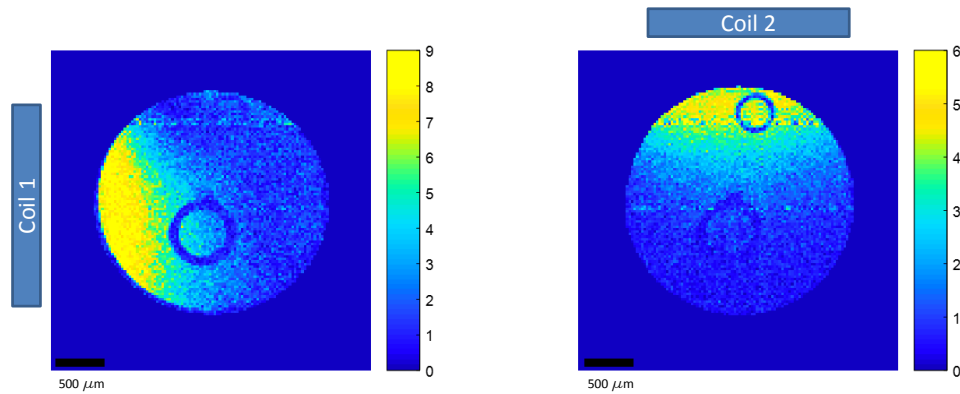
Figure 6.20: SNR map for the two coil elements (coil 1 is on the left and coil 2 is on the right) in the probe-head. 128 x 128 images of $CuSO_4/H_2O$ with two quartz capillaries to allow accurate determination of the position of the coils. The slice thickness was 0.5 mm, the FOV was 4 mm and the nominal resolution was $31.3 \times 31.3$ $\mu$m. The images were acquired with a single scan.
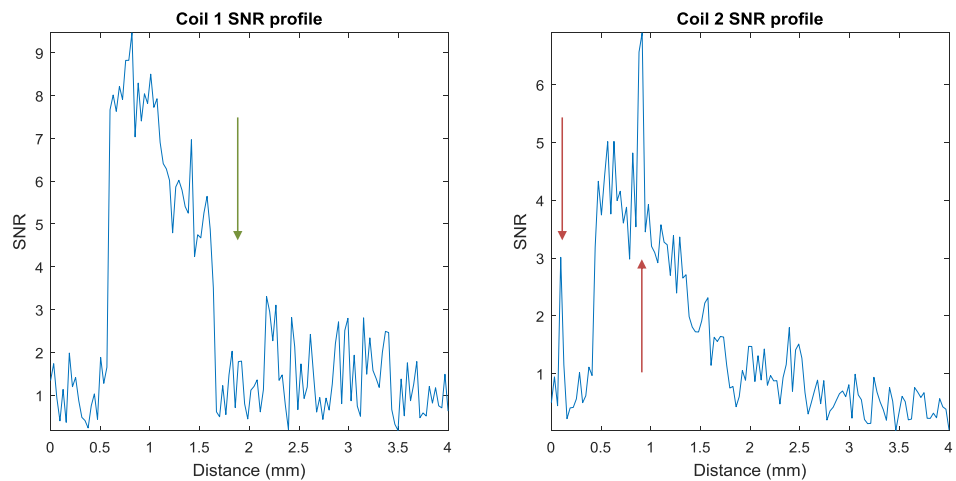


Figure 6.21: Plots for both of the elements in the probe-head showing how the SNR depends on the distance from the coil. The FOV starts at the approximate position of the coil and the distance is given along a line through the coil centre orthogonal to the face of the coil. The green arrow determines highlights the position of the large capillary and the red arrows indicate the position of external noise acquired during the acquisition.

127

the common mode problems still exist which impede the signal being trans-
mitted, increasing the noise in the received signal.

The SNR map allows limitations to be placed on the imaging capabilities,
and allows assumptions to be made about the limit of detection. Given that
the coils can not be placed any closer to the sample, there is little point in
decreasing the field of view and therefore it is the slice thickness that limits
the detection. Given that the peak SNR is 9, close to the coil, the slice
thickness could be reduced by a factor of 3 before the SNR would be too
low to distinguish the signal from the noise. However this would mean that
only the area very close to the coil would be visible, so a more realistic slice
thickness limit is a reduction factor of 2 or less in order to be able to resolve
central parts of the FOV.

## 6.6.2   B$_1$ Field Mapping

As alluded to in the SNR maps shown in Figure 6.20, and demonstrated by
the principle of reciprocity, the $B_1$ field strength is directly proportional to
the received signal (9). Therefore, to fully assess the performance of a given
coil it is useful to have a map showing the amplitude of the $B_1$ field.

There are several methods for collecting a map of the field distribution that
have been developed. Methods such as $B_1$ mapping by Bloch-Siegert shift
or the double angle method (199; 200; 201), where two images are collected
with flip angles $\alpha$ and $2\alpha$, the ratios of the two images (assuming that they
have been collected on a shorter time scale than $T_1$) give the flip angle,
shown by,

$$\alpha = \cos^{-1}\left(S_2/2S_1\right),\qquad(6.25)$$

where $S_1$ is the signal due to the smaller flip angle and $S_2$ is the signal due
to the larger flip angle. However, this method is susceptible to relaxation
artefacts and not suited to high resolution.

In order to get an accurate representation of the change in $B_1$ across the
field of view a series of images are collected with varying pulse length. As the
pulse length changes the signal strength follows a sinusoid given by,

$$S = \sin\left(\omega_1 t\right),\qquad(6.26)$$

where $\omega_1 = \gamma B_1$. $B_1$ is the strength of the RF field and $t$ is the duration the
RF pulse (202). The Fourier transform of the modulating signal displays the
frequency at which the sinusoid oscillates, and from this the $B_1$ information
can be extracted.

Multiple flip angle $B_1$ maps are presented in Figure 6.22 where the maximum
$B_1$ field produced by the coils is $11 \times 10^{-3}$ Tesla for coil 1 and $7.5 \times 10^{-3}$

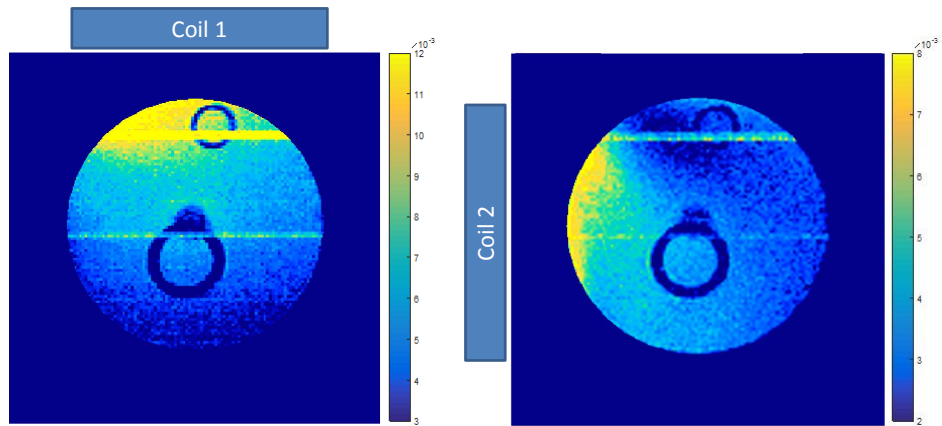Figure 6.22: Multiple flip angle $B_1$ maps for both coils (Left: coil 1, Right: coil 2) showing the distribution of the field in units of mT. The band across the top of the image is an artefact due to external noise.
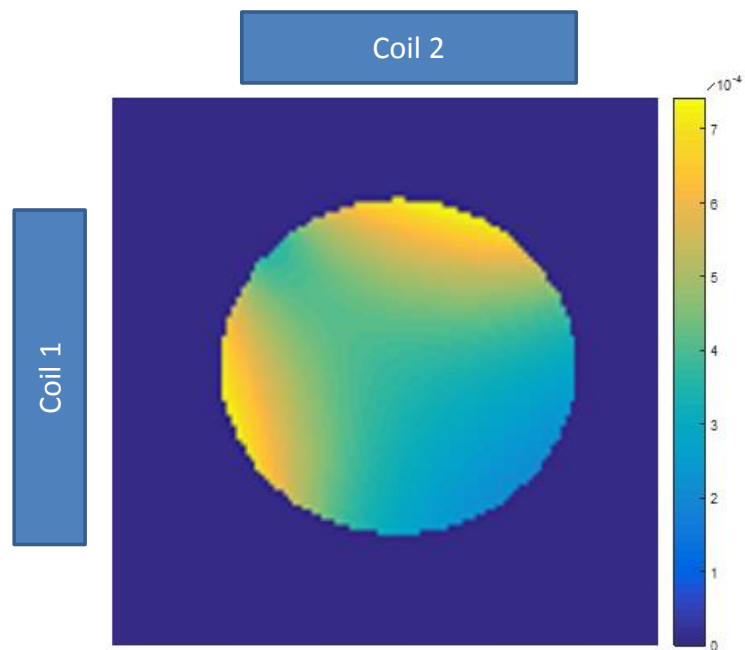


Figure 6.23: Sum of the simulated $B_1$ fields for both coils. The coils are 2 mm outer diameter and positioned 2 mm from the centre of the FOV. The maximum $B_1$ field is $7.5 \times 10^{-4}$ T.
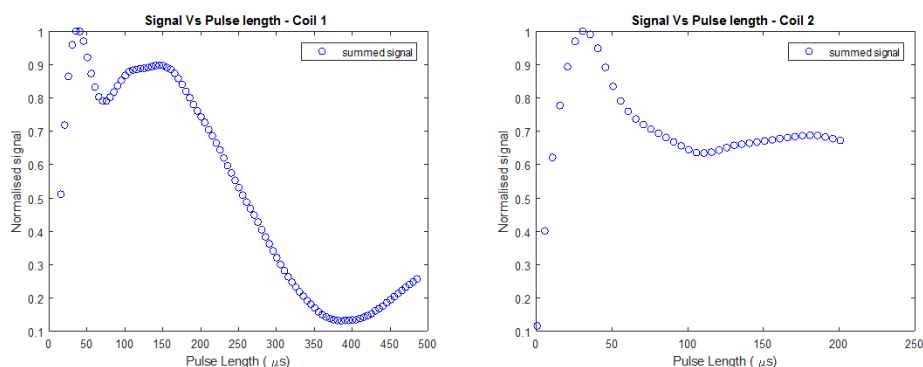
Figure 6.24: Power optimisation experiments for each of the coils in the array. The normalised integral of the signal is plotted against the pulse duration in order to establish the maxima and minima. The fact that a minimum does not occur at twice the maximum shows that there is significant $B_1$ inhomogeneity.

Tesla for coil 2, which equates to a nutation frequency on the order of 300 KHz for protons. Observation of the image from coil 2 in Figure 6.22, shows that the coil is not perfectly aligned with the sample, as the field appears to radiate at an angle through the sample. There is also a low intensity region near to where the coil 1 is positioned, at the point where the two coils are closest, this could be due to coupling effects between the coil elements.

Figure 6.23 shows the simulated $B_1$ field for two orthogonal coils with an OD of 2 mm. The coils are positioned 2 mm from the centre of the FOV, parallel to the left hand side of the FOV and the top of the FOV. The position of the sample is estimated by overlaying a mask from the experimental data. The FOV is 4 x 4 mm and a 128 pixel square matrix is used, with the region of interest equating to a 2.4 mm circle.

The maximum field produced in the simulated field maps is $7 \times 10^{-4}$T which is an order of magnitude less than that of the experimental set-up and corresponds to a nutation frequency of 30 KHz. This may be due to differences in the size, shape and position of the coils in relation to the sample. However, it is clear that the combination of the fields causes a similar low intensity region at the point where the two coils are closest and that the fields do not appear to act perfectly in line with the axis going through the centre of each of the coils.

The inhomogeneous $B_1$ field is useful for adding an extra level of spatial encoding, however it makes excitation of the entire sample difficult. This is shown by the results from power optimisation experiments for each of the coils in the probe-head which can be found in Figure 6.24. The experiment is carried out by incrementing the pulse length after each scan and recording the received spectrum. A transmitter coil producing a homogeneous $B_1$ field displays a sinusoidal signal intensity response, however this is not the case for a planar coil as the $B_1$ field is highly non-uniform.

The problem with a non-uniform excitation is that the signal intensity varies across the sample and it is difficult to perform spin echo pulse sequences as refocussing pulses are long. Also the stronger $B_1$ field close to the coil causes the spins in that region to have a much higher nutation frequency than the spins furthest from the coil. This can lead to spurious echoes being generated when multiple refocussing pulses are applied (171).

## 6.7 Imaging of Oocytes

Given that it has been shown in the the previous section that there is good SNR available using the surface coils for pixel sizes of tens of microns it was decided that the probe should be used to image some Xenopus Oocytes. This poses more of a challenge than the phantom sample as the bound water means shorter relaxation times.

The imaging was carried out with a spin echo sequence where the FOV is a 4 mm square with $128 \times 128$ pixels and the slice thickness was set to 0.4 mm. The image was acquired with only one of the two coils available with ten averages and took approximately 30 minutes due to a long TR.
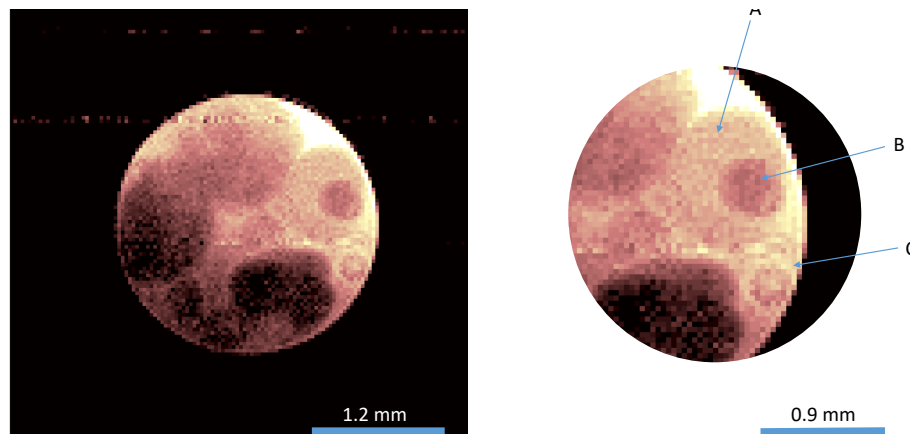


Figure 6.25: MR-image of a collection of Xenopus Oocytes. The imaging was carried out with a spin echo sequence where the FOV is a 4 mm square with $128 \times 128$ pixels and the slice thickness was set to 0.4 mm. The arrows in the cutaway highlight interesting features of the image. A) Cytoplasm area in a well developed Oocyte. B) Nucleus or geminal vesicle of the Oocyte, this usually takes up approximately a third of the volume of the Oocyte and is located in the animal hemisphere. A diagram of the constituent parts of a Xenopus Oocyte can be found in Figure 7.5. C) a much less developed Oocyte where the constituent parts are still distinguishable.

The Images demonstrate that with the current set-up and little optimisation it is feasible to distinguish features within a single Oocyte when imaging a cluster. In order to improve the images it would be necessary to implement imaging on the second coil as this would allow a more even sensitivity profile across the image to better distinguish the features.

# 6.8　SENSE Imaging

SENSE allows accelerated acquisition of the k-space and achieves sub-Nyquist sampling rates while allowing artefact free reconstruction, this means that the acquisition time can be halved.

To show that the simulations presented in chapter 5 are a true representation of the experimental system, and to show that SENSE is a valid technique for accelerating microscopic MR images with an orthogonal coil array, it is important to see that images can be reconstructed.

In order to demonstrate this, two gradient echo based images have been collected, one from each of the coil elements in the probe-head array, with an acceleration factor of 2. The FOV is 4 mm and the $CuSO_4$ water sample shown in Figure 6.19 has been used. The under-sampled images are shown in Figure 6.26 where the alternate missing lines of $k$-space have caused uniform overlapping in the reconstructed image.

Sensitivity maps (Figure 6.27) were constructed by taking two fully encoded images and then combining them using the sum of the squares method (10). The coil sensitivities are calculated by dividing each individual coil image by the sum of the squares image.

These show similar results to the $B_1$ maps presented in Figure 6.22, as they are a normalised measure of each of the individual coils sensitive regions. There is a shared section of the images, in the lower left hand side of the region of interest, that has very low SNR due to the fact that neither coil has a well defined field in this area of the sample (highlighted in the figure by the red arrow).

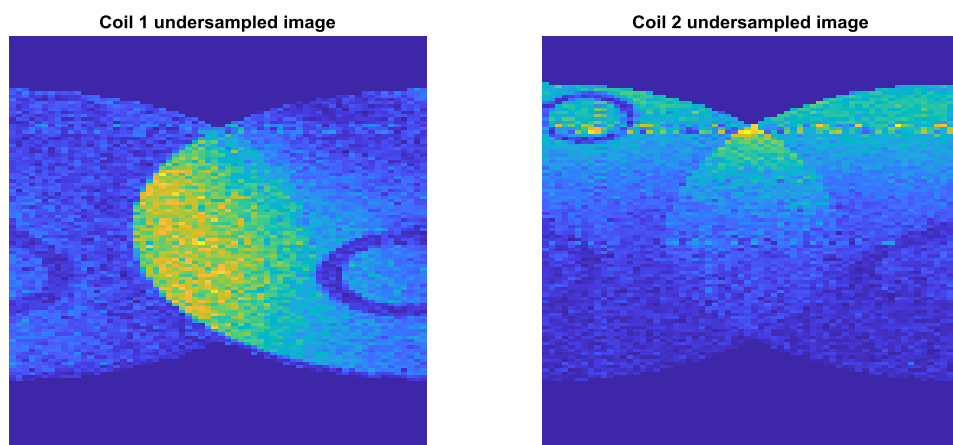The under-sampled images and the sensitivity maps, shown in Figure 6.27,



Figure 6.26: Left: Coil 1 under-sampled image. Right: Coil 2 under-sampled image. Both images are 64 by 128 pixels. The acceleration factor is 2 and the FOV is a 4 mm square. The images were collected using a gradient echo sequence with a slice thickness of 0.5 mm.

are passed into the reconstruction algorithm (presented in the earlier chapter) written as a Matlab function and the fully encoded images are reconstructed. The resulting reconstructed image is presented in Figure 6.28.

To assess the quality of the reconstruction a g-factor map has also been produced, shown in Figure 6.29, which gives an average g-factor of 2.3, a variance across the ROI of 4 and a standard deviation of 2. Low g-factor values indicates a high reconstruction quality. The higher values occur in the area of the image that has low $B_1$ field. This makes it harder for the reconstruction algorithm to accurately separate out the overlapped pixels.

The average g-factor for the reconstruction is within tolerable limits (less than 5 average value) to suggest that the reconstruction is of good quality. Figure 6.30 shows the reconstructed under-sampled image, the sum of the squares image and the difference between the reconstruction and the sum of the squares, which serves to bolster this assertion. On inspection of these images it is clear that there is a reduction by a factor approximately equal to the acceleration factor in the signal level, which is expected as the amount of signal collected in the under-sampled images is half that of the fully encoded images. It is clear that there are no artefacts and that the geometry of the image has not been altered due to the under-sampling and reconstruction process, only the SNR has been effected by the under sampling. This just echoes what is shown in the g-factor map, that the reconstruction is of an acceptable level to mean that the final image has the correct spacial positioning of the pixels and there are no artefacts generated due to the under-sampling.

Therefore the data presented shows that the two channel proton coil array is suitable for micro imaging and allows SENSE to be employed to collect accelerated micro scale images with an artefact free reconstruction of fine detail within the image.
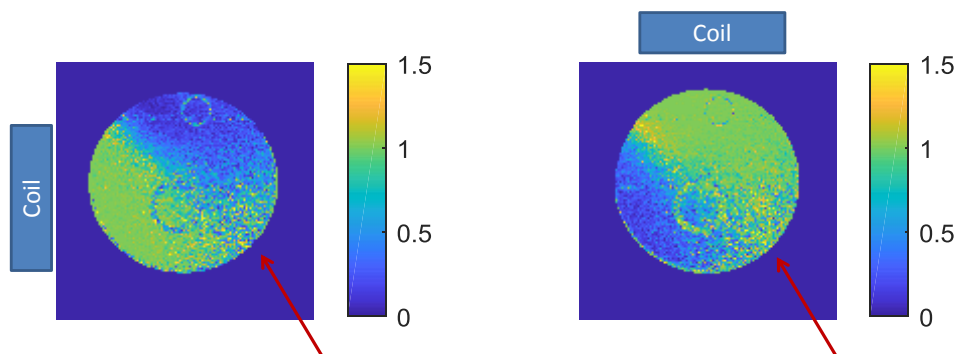


Figure 6.27: Sensitivity maps for coil 1 (left) and coil 2 (right). The red arrow highlights the shared region of low sensitivity for the two coils in the array. The approximate position of he two coils is also marked outside the FOV.
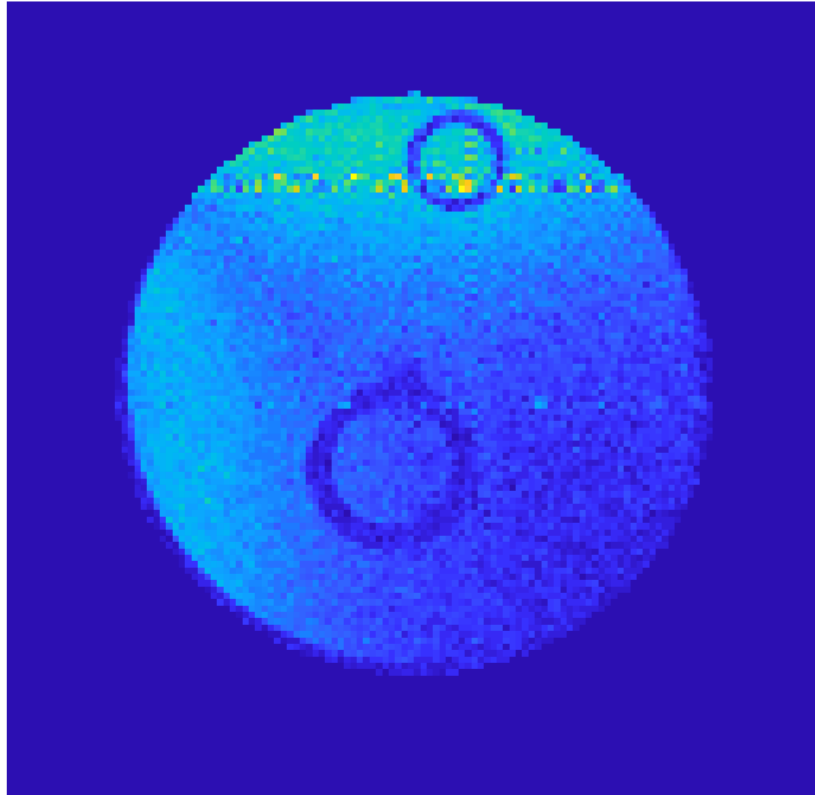
Figure 6.28: Image reconstructed with the SENSE algorithm. the images were acquired with two seperate receivers with an acceleration factor of $R = 2$.

## 6.9   Discussion

At the beginning of this chapter the benefits of using surface coils were presented, and it is clear that if any accelerated image acquisition technique is to be employed (other than compressed sensing), surface coils will be crucial to the success of the image reconstruction. The main attraction of the surface coil being that the field produced has a well defined spatially varying $B_1$ field. As a further consequence, the shape and size of surface coils means that the sample can be placed in very close proximity to the coil, which means that it experiences the maximum possible $B_1$ field, therefore, further increasing the SNR per unit volume.

This improvement in signal intensity per unit volume is the reason why arrays of surface coils have replaced traditional coils in clinical MRI scanners (203). By reducing the size of the coil the $B_1/i$ is inherently improved, allowing, due to reciprocity, a greater signal level to be collected. This means that for a small sample the amount of time required to collect the signal can be drastically reduced by making the coil smaller, as the acquisition time is proportional to the signal squared. This was originally shown by Mansfield and Morris (204), who derived an equation for the acquisition time for a given volume, without prejudice towards a specific pulse sequence. This is demonstrated by
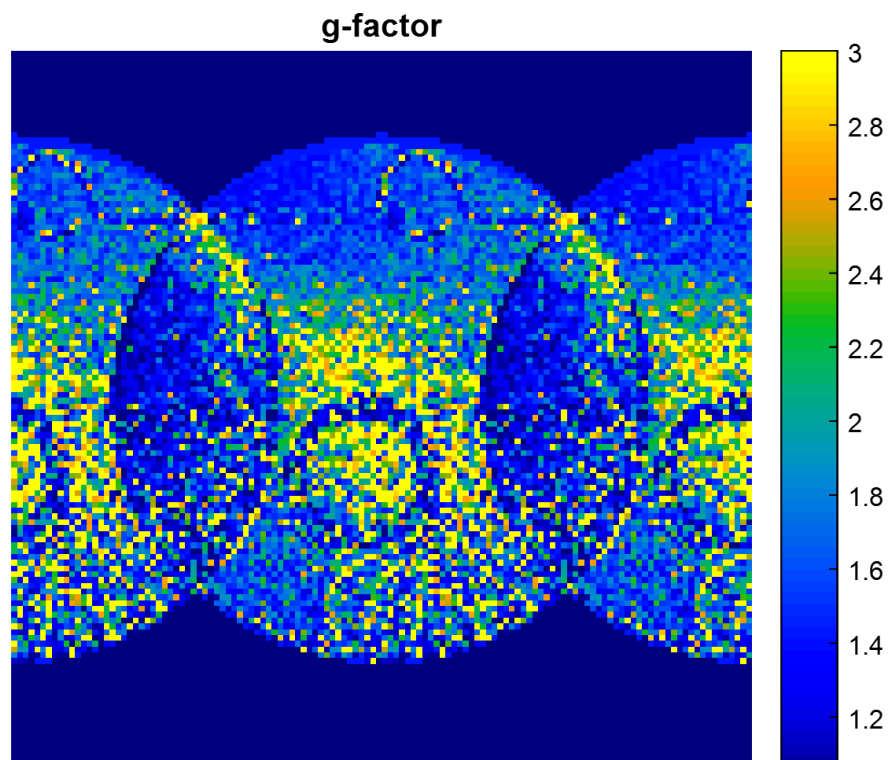
**g-factor**

Figure 6.29: The g-factor map for the SENSE reconstruction shown in Figure 6.28. The g-factor shows that there was excellent reconstruction in the areas close to each of the coils and reconstruction was harder in the shared area of low signal (the area highlighted in Figure 6.27). The g-factor is still within acceptable levels at this point.
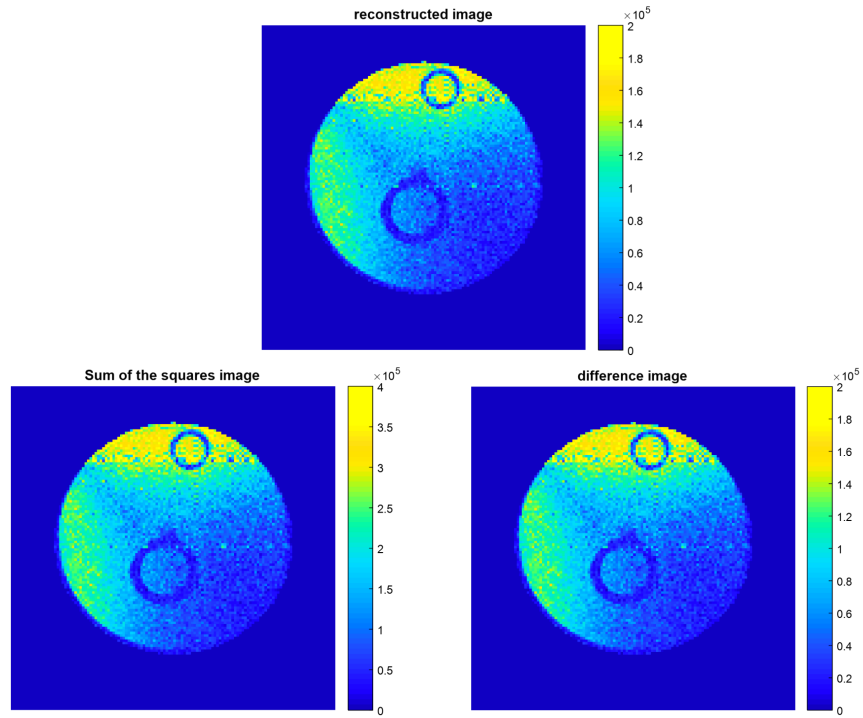
Figure 6.30: Top: Reconstructed under-sampled image. Left: Sum of the squares image. Right: difference image between sum of the squares and reconstructed image. There is a factor of 2 difference in the signal intensity (as shown by the difference image) due to the under-sampling.

$$t = \text{SNR}^2 \times a^2 \left(\frac{T_1}{T_2}\right) \frac{2.8 \times 10^{15}}{f^{7/2}} \left(\frac{1}{\Delta x}\right)^6. \qquad (6.27)$$

Where $a$ is the radius of the RF coil, $T_1$ is the longitudinal relaxation time, $T_2$ is the transverse relaxation time and $\Delta x^3$ is the volume of the sample. However, the benefit of using a single surface coil is only realised when the sample volume is comparable to the coil volume (204). If the sample volume remains large, then the SNR over the entire sample will be poor due to the spatially varying $B_1$ field of the surface coil.

The sensitive depth of a surface coil is approximately equal to its diameter which means if the sample is larger than this, an array of coils is preferable and the improvement in SNR over larger volumes can be shown. However, for very small samples, where only a small number of nuclear spins are being detected, it is always preferable to improve the sensitivity (i.e. the $B_1/i$), in order to reduce the amount of time required to image a given number of spins.

It has also been shown that due to the nature of the $B_1$ field, surface coils are not ideal for use as transmitters. This is because it is difficult to excite the entire spin system and hard to produce a homogeneous refocussing pulse. Adiabatic pulses are $B_1$ invariant and therefore may provide a way of

homogeneously exciting the sample with a planar coil. The disadvantage of using adiabatic pulses is that they are much longer than standard pulses and potentially more power intensive (205).

The surface coils constructed are not capable of producing a uniform refocussing pulse, and therefore typical methods used to describe the inhomogeneity are not applicable. For instance, the homogeneity is often measured by the ratio of the signal form a $90^o$ pulse and a $5 \times 90^o$ or $7 \times 90^o$. However, for the aqueous copper sulphate solution used a pulse duration on the order of ms begins to become comparable to the relaxation times.

The inhomogeneity of the pulse can cause issues in the final images such as repeating lines along the phase encoding direction. This is explained by Zur and Stoker in their 1987 paper on the benefits of phase cycling (171). Repeating lines in the phase encoding direction can be caused by spurious echoes being generated before or after the principle echo, which is the effect of having an incomplete re-phasing of the magnetisation, instead different components of the net magnetisation re-phase at different times. A further problem that can arise due to the non-uniform excitation of the magnetisation is a mirroring artefact, however this has been less prominent in the images collected with the probe-head described above. It is caused, again, by only partial refocussing of the magnetisation during the echo train. However, in this case, some portion of it is stored along the z-axis until the next RF pulse, after which, the magnetisation is transferred back into the transverse plane with the same phase, which causes a mirror image effect. The mirroring effect is less prominent as it is difficult to produce a refocussing pulse. It is possible that the problem of artefacts due to field inhomogeneity is exacerbated further due to the presence of the second coil as this clearly distorts the $B_1$ field, demonstrated by Figure 6.23 and 6.22.

A further cause of the major artefact present in some of the images, such as the one shown in the $B_1$ field maps is due to a frequency spike from an external source that is oscillating close to 400 MHz. Given that the probe-head is well shielded, it is likely that the signal is being detected due to an antenna effect on the coaxial line, this is more prominent in images on coil 2, which supports the idea that the common mode effects have not been fully eliminated and are worse for the second coil. These effects still exist, even though the probe-head itself is balance-matched because the length of the coaxial cable is greater than a wavelength of the signal being transmitted. Therefore, the shield will experience node and anti-node points from the wave travelling along the inner conductor. This should be eliminated by the combination of grounding and RF chokes on the coaxial cable, however it may be the case that the level of grounding was not sufficient. It was not possible to fit an optimal sized balun inside the probe assembly, and therefore they are less effective at providing an impedance to the common mode currents. In industrially produced probes the ground plane is provided by an all metal casing, whereas the probe in question is made from nylon tubing. The idea of using a metal shaft to support the probe was initially quashed as it was

thought the eddy currents along it due to gradient switching would cause problems.

The probe performance is seen to be more than satisfactory for carrying out micro-imaging with a single scan resolution of 31.25 $\mu$m square pixel size, for a 500 $\mu$m slice easily achievable. this resolution is not limited by the gradient performance but by the limit of detection of the probe, this is determined by the probe sensitivity.

In order to improve the sensitivity of each of the elements in the probe-head the Q-factor of the receiver coil must be increased. The Q-factor is determined by the inductance and the resistance, if there is a mutual impedance between the coil and the sample (or between the coil elements) the Q factor will be effected. Due to the resistance of the coil being very high relative to the sample for small coils, the mutual resistance is usually negligible for coils smaller than 3 mm in diameter, which is supported by the measurements shown in Table 6.2 (206). The frequency shift due to loading suggests that there still is some coupling between the sample and the coils. Due to the fact that the frequency is shifted down it is likely that the sample is providing a mutual capacitance. These results were collected using a water and copper sulphate solution sample, if a different sample with significantly different dielectric properties were used then it may provide different results.

## 6.10   Conclusions

The initial results for coil coupling showed that the optimum geometry for decoupling two coils is to place them orthogonally, which matches the optimum g-factor arrangement shown in chapter 5, thus making a two coil array attractive and feasible.

The probe-head has been constructed to achieve the highest sensitivity possible, thus allowing single scan micro-scale imaging, with a 31.25 $\mu$m in-plane resolution and a sub millimetre slice thickness. It has been shown that the limit on the resolution is the achievable SNR and not the gradient performance, as predicted in the previous chapter.

The $B_1$ field maps show that the individual coil array elements have distinct and well defined sensitive regions that are ideal for employing accelerated image acquisition techniques. The artefacts present are due to unavoidable detection of external RF signals which are detected due to poor shielding of the cables.

The reconstruction of the under-sampled images prove that the simulations presented in chapter 5 are a valid representation of what is achievable experimentally as the reconstructed image shown in Figure 6.28 is artefact free, where a reduction in the signal intensity is the only clear penalty due

to under-sampling. The g-factor map shows that the reconstruction of the image is good, however there is a section of the FOV which is harder to reconstruct due to the lower intensity of the $B_1$ field. This was highlighted by the field maps and the sensitivity maps.

In order to achieve higher resolution or to detect nuclei with lower gyromagnetic ratio the sensitivity will need to be increased further, it is clear that smaller coils can provide this. Smaller coils will also allow the FOV to be reduced for the accelerated acquisition to work. There needs to be a clear distinction between the sensitive regions of each of the coils inside the region of interest to achieve the extra level of spatial encoding. This is not achievable when the FOV is considerably smaller than the coils.

# Chapter 7

# NMR Microscopy and Micro-coil Fabrication

## 7.1 Introduction

To monitor the distribution of $^{13}$C labelled molecules in an NMR microscopy experiment, suitable hardware must be in place to optimize the data acquisition. A schematic of the ideal set-up is shown in Figure 7.1. The multiple channels of the spectrometer are utilised to realise parallel acquisition of signal arising from hyper-polarised small molecules. One step towards this goal is to place the detector as close to the sample as possible. If multiple detectors are used then the possibility of single shot, hyper-polarised images becomes a reality.

The purpose of this chapter is to demonstrate the need for and the benefits that arise when using micro-coils for NMR and MRI of small samples. Section 7.2 explains how SNR can be improved though the use of smaller detectors. A brief review of different receivers that are used in NMR microscopy is presented in section 7.3 and a case is made for the use of planar coils. The difficulties that occur when using coils made via standard fabrication techniques, such as the need for a bonding wire, or the effect of the substrate on the magnetic field are discussed in section 7.6.

Details of how the novel, flexible micro coil array was conceptualised, fabricated and implemented in order to collect nL scale NMR measurements of $^{1}$H and $^{13}$C at 9.4 T are summarised in section 7.4. The process behind the development of a flexible micro coil array will be demonstrated along with problems that were encountered during the design and fabrication, and how these problems were overcome.
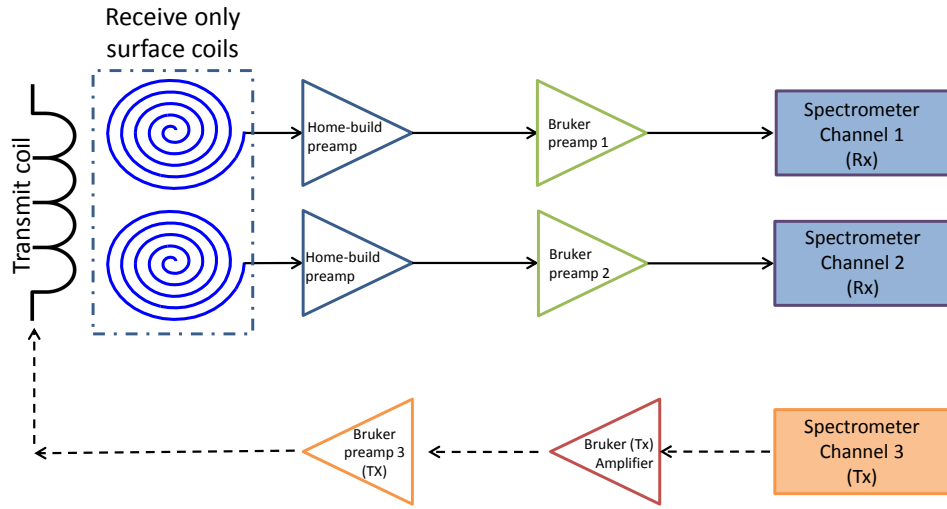
Figure 7.1: Experimental set-up for two receiver coils and a single transmitter coil using the dual isocentre spectrometer at the University of Nottingham. Home built pre amplifiers are to be introduced to reduce the losses between the receiver and the Bruker pre amplifiers.

## 7.2 SNR in NMR Microscopy

As shown in chapter 6, the principal of reciprocity means that the strength of the field produced by the coil is directly proportional to the signal received (9). Therefore, in order to detect small volumes and very small numbers of spins it is important to place the receiver as close to the sample as possible.

The SNR in NMR is given by

$$\mathrm{SNR} \propto [\gamma B_0] \left[ \frac{N\gamma^2 \hbar^2 B_0}{16\pi^2 KT} \right] \left[ \frac{B_1}{i} \right] \left[ \frac{1}{V_n} \right], \qquad (7.1)$$

where the term in the first square brackets is the Larmor precession frequency, the term in the second square brackets is the thermal equilibrium magnetization, the third square brackets represents the $B_1$ field per unit current and the final square brackets is the voltage noise as given by Equation 6.3. The third and fourth square brackets relate to the detector as the $B_1/i$ is dependent on the size of the coil. When the coil length is reduced this value increases and therefore, due to reciprocity, the signal received also increases.

The increased SNR is spatially dependent as a surface coil has a limit to the sensitive depth approximately equal to the coil diameter. This means that for a sample volume larger than the coil the total SNR is worse than using a volume coil. However, (161) showed that using a combination of surface coils around a sample will produce a higher SNR across the entire volume than using a single coil (161). Therefore in order to measure hyper-polarised signal in small objects such as the Xenopus oocyte two or more micro coils
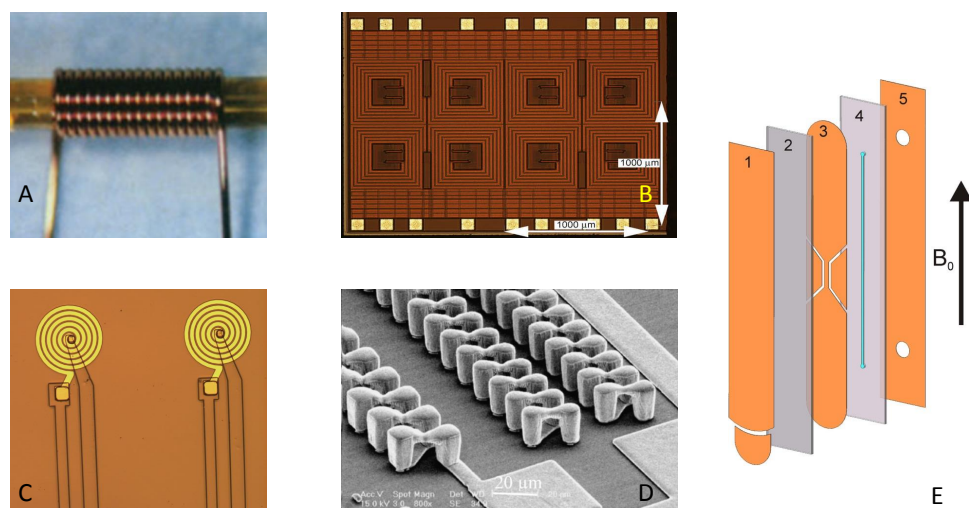
Figure 7.2: Hand wound 500 $\mu$m solenoid coil (210)(**A**). Array of 500 $\mu$m planar micro coils on a silicon substrate with on-chip pre-amplifier (211) (**B**). 500 $\mu$m flexible planar micro coils fabricated on a polyimide substrate (**C**). SEM images of microfabricated 3D solenoid (212). Schematic of a strip line resonator and flow path (213) (**E**), where the strip line resonator itself is situated at position 3.

need to be employed. This will also provide the option to use parallel imaging techniques such as SENSE.

## 7.3   Detectors for micro-NMR

Many variations of detector have been proposed for micro scale NMR of small samples, such as strip line resonators (207), solenoids (208) and planar micro coils (209). Examples of some of the possible detector configurations are shown in Figure 7.2. Each type of detector is suited to a different experimental set-up and often has to be manufactured bespoke for the application.

Strip-line resonators are often used in micro-fluidic NMR systems due to the nature of the shape of the sensitive region and have also been employed in a temperature jump DNP system in order to collect hyper-polarised signal from samples on the order or 10's of nL (214; 213; 215; 56). These have a high sensitivity over a very small space due to the geometry of a single tuned strip. However, the large metal planes suffer from eddy currents during gradient switching and cause inhomogeneity in the polarizing field.

For micro-fluidic devices it is common for the micro-fluidic channel to be integrated into the detector fabrication in some way as it is the case for Massin *et al* (216; 217). However for a static system, where flow is not required, this kind of detection method is less desirable, as the flexibility of the system is reduced.

Traditionally solenoid probes were considered the best strategy for achieving the optimum spin sensitivity as they will produce a strong, homogeneous magnetic field and their relatively high self inductances allows good tuning and matching at many field strengths. Microscopic solenoids have been fabricated and used in NMR microscopy experiments (212; 218), some examples of which are shown in Table 7.1. However, they are difficult to fill and often require a flow path to be fabricated in conjunction with them. This can spoil the filling factor and reduce the quality factor of the coil due to capacitive effects. Therefore it is usual for solenoids to be used when the sample is on the order of 0.1 - 10 mm at which point they are large enough to be wound rather than microfabricated, making them more robust (219; 220). The nature of the solenoid and the direction of the field it produces means that it has to be positioned perpendicular to the polarising magnetic field. This incurs a large penalty as it increase the effect any susceptibility mismatched elements of the sample or detector have on the magnetic field, requiring a highly complex experimental set-up (210).

Planar coils have become a standard for NMR microscopy given the relative ease of fabrication and good electrical properties to allow tuning and matching of the coil. The planar coil also offers an ease of sample handling and placement that is not achieved with a solenoid or strip line resonator. However, as surface coils are reduced in size the spatial dependence of the field becomes problematic for samples that are larger than the diameter of the coil. Massin *et al.* showed how planar micro coils could be fabricated using the photo-resist SU8 and copper electroplating on a glass substrate (221). Coils such as these have been used successfully for detecting samples containing as few as $10^{12}$ spins due to their high Q-factor and proximity to the sample (222). The planar coil also offers a better Q-factor and lower AC resistance than the solenoid when the experiment is carried out at very high fields. This is due to the increased skin and proximity effect as demonstrated in Figure 7.3 (218). Possibly the most promising of the recent work on NMR-microscopy of cells has been carried out by Gobel *et. al.* (223). Here multiple coils are wound to interleave each other and placed in a hexagonal pattern. This means that there is a 1 mm diameter planar sample area and the coils can be geometrically decoupled to allow accelerated acquisition. The Drawback of this is that the sensitivity is not optimal as the coils are not truly planar and the typical imaging time for an image with $25 \times 25 \times 100$ $\mu$m pixel volume is on the order of 11 hours. It is hoped that with hyper-polarised samples in slightly larger cells this time will be significantly reduced.

Table 7.1 shows some examples of typical detectors, the sample volume that the detector has been used to examine and the NMR linewidth that was achieved in the experiment. The table also shows the magnetic field strengths at which the experiments were carried out and the nuclear species that have been detected with the micro probe. It is clear from the table that as the volume is reduced it becomes difficult to maintain a high frequency resolution in the spectrum. The linewidth is especially affected as the experiments move
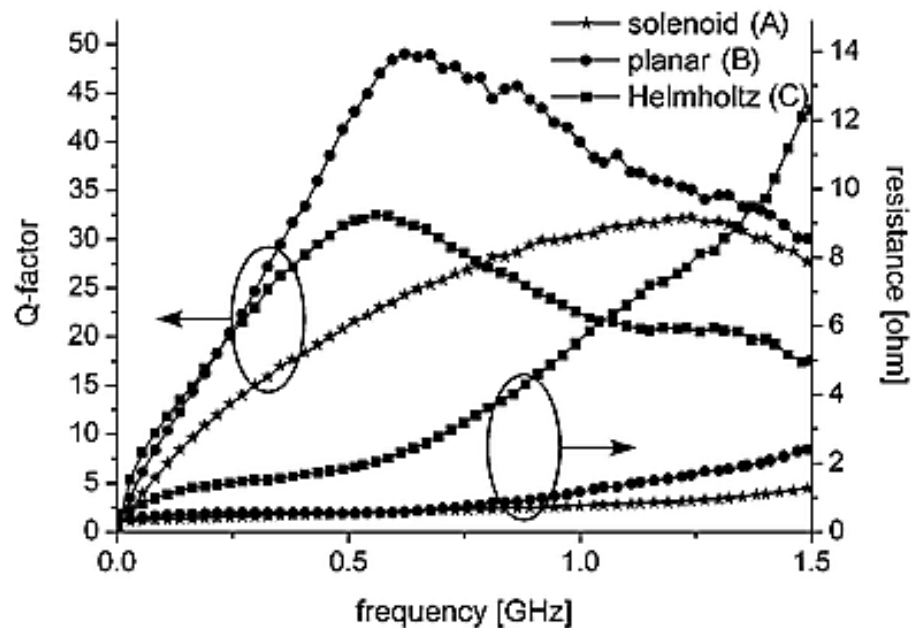
Figure 7.3: Graph first published by (218), showing how Q-factor and AC resistance changes with frequency for a solenoid coil of $200 \times 85\mu$m ID (**A**), a planar coil with an ID of $160\mu$m (**B**) and a Helmholtz pair with an ID of $400\mu$m (**C**).

to high field strengths.

To achieve high resolution spectroscopy it may be beneficial to go to lower field strengths and use hyper-polarised samples (224). The susceptibility mismatching effects which cause the short $T_2^*$ times that are responsible for poor spectroscopic resolution in MR microscopy experiments are reduced at lower fields, although chemical shift resolution is also reduced and therefore can make it impossible to distinguish peaks. However, this is somewhat limited by the ability to tune and match the detector to the low frequencies required and the fact that a reduction in linewidth is potentially be offset by the reduction in chemical shift resolution and polarisation.

Table 7.1: Table showing the achieved line width of various detector configurations for different sample volumes and field strengths. The type of nuclei that the detectors were tested on is also shown. Nuclei highlighted in bold correspond to the measured linewidth.

| Detector Type | Sample Volume (nL) | Line width (Hz) | Field Strength (T) | Observable Nuclei |
| --- | --- | --- | --- | --- |
| Helmholtz (225) | 3000 | 0.5 | 0.6 | $^1$**H** |
| Strip line (207) | 2000 | 1.73 | 7 | $^1$**H** |
| Planar coil (216) | 470 | 30 | 7 | $^1$**H** |
| Solenoid[1] (208) | 400 | 3.6 | 11.2 | $^1$**H**\$^2$H |
| Solenoid[2] (209) | 100 | 30 | 7 | $^1$**H**\$^{11}$B\$^{19}$F\$^{23}$Na |
| Planar array (211) | 12 | 195 | 7 | $^1$**H** |
| Planar coil (226) | 1 | 70 | 7 | $^1$**H** |
| Planar coil(209) | 0.13 | 30000 [3] | 7 | $^1$**H**\$^{19}$F |
| Planar coil (on polyimide) | $\leq$35[4] | 430 | 9.4 | $^1$H \ $^{13}$**C** |

[1]Susceptibility matched plugs and Flourinert are used to improve the linewidth

[2]The coil is inserted into a tube filled with $D_2O$ for susceptibility matching

[3]An exponential filter with a time constant of 100 $\mu$s was applied to the FID.

[4]The sample volume is calculated based on the assumption that the entire sample is excited and detected. In reality it is likely that only half the sample plays a real contribution to the measured signal.

### 7.3.1 Quality Factor

One disadvantage when using planar micro-coils is that they often posses a low Q-factor which is caused by their small inductance and high resistance due to their specific geometry. It is difficult to retain a high Q-factor for a micro coil as the inductance is determined by the geometry of the coil and the the resistance is increased by reducing the height and diameter of the wires.

A low Q-factor makes it difficult to tune and match the coil. This is the reason why solenoids have been so popular in the past due to their high inductance. The Q-factor and other electrical properties of the coil are also effected by the substrate upon which it is fabricated.

### 7.3.2 Typical Substrates

A convenient substrate for any microfabricated coil is silicon as it is commonly used in many microfabrication processes and many common resists, etchant and developers have been engineered to be used with semiconductor based devices (227; 228). The use of semiconductor as a substrate also opens up the potential for lab on a chip (LoC) applications as presented by Grisi *et al*, where the pre-amplifier and even the entire spectrometer is integrated into the micro-fabricated device (211; 209; 226).

This has deleterious effects however when considering the electrical performance of the coils since at high frequencies there is a capacitive effect from the substrate due to the eddy currents in the semiconductor. These eddy currents are exacerbated when gradient switching is introduced and significantly limit the attainable Q-factor of the coils. This has been shown by Woytasic *et al.* comparing the frequency dependence of the Q-factor for a 1 mm planar coil fabricated on Kapton (DuPont Ltd. - Stevenage,England) and on silicon (see Figure 7.4) (212). The insulating Kapton substrate increases the maximum achievable Q by a factor of 5.

Another solution is to fabricate the coil on glass or Pyrex which provide a strong and chemically resistant surface to which the inductor and can be easily bonded. This has been demonstrated by Massin *et al.* where 500 $\mu$m and 1000 $\mu$m (ID[5]) inductors were fabricated on a glass substrate above a flow cell. Using this substrate Q-factors on the order of 17-20 were achieved for varying coil sizes at 300 MHz. Glass has the drawback of being difficult to scribe (the separation of the multiple devices on the wafer) and is easily broken, coupled with the often poorly matched susceptibility of glass causing a shortening of $T_2^*$ (216; 221).

---

[5]The outer diameter of the coils is not described in the paper. The figures suggest that the outer diameter is significantly larger than the inner diameter and also larger than the coils fabricated as part of this project. This means that it is difficult to make a direct comparison between electronic characteristics.
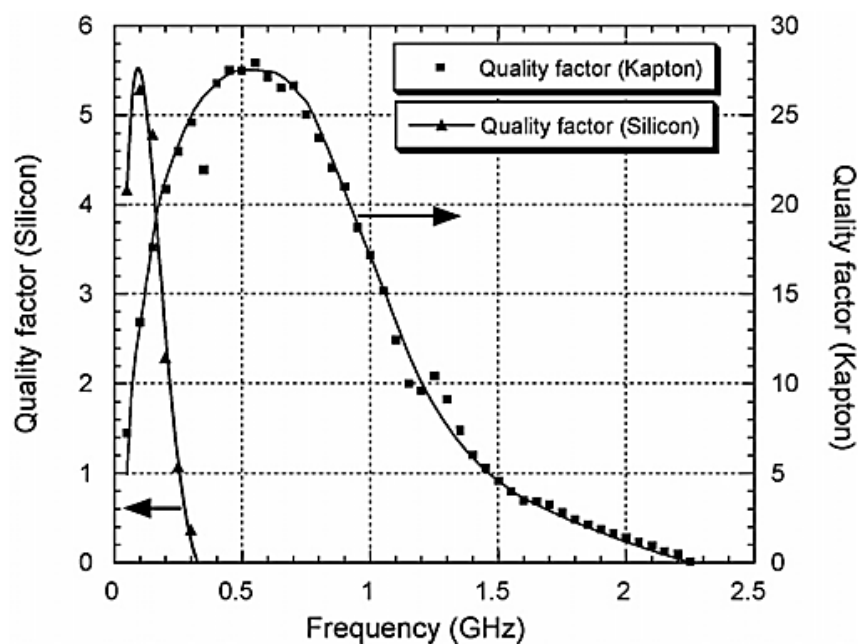
Figure 7.4: The graph, originally published in (212), shows how the Q-factor varies as a function of frequency for a 1 mm OD planar coil on a silicon and a Kapton (DuPont Ltd. - Stevenage,England) substrate.

Both semiconductor based and glass type substrates have the drawback of being rigid which makes positioning multiple receivers around a spherical or cylindrical sample difficult. The rigid edges of the substrate also increase the field inhomogeneity, which reduces the achievable resolution and overall sensitivity of the detectors. Therefore, it is beneficial to consider utilising a substrate that matches the susceptibility of the sample and that can be shaped to reduce the edge field distortions caused by rectangular or straight edges.

The magnetic susceptibility of some relevant materials is shown in Table 7.2, where the susceptibility relative to water is also shown. It is clear from the table that substrates such as glass and silicon will have a much greater effect on the field than a material like polyimide.

Using a polymer based substrate such as PDMS/PEEK or polyimide not only has the advantage of being well matched to water, it allows more favourable shapes to be used to support the coils, as films of these polymers are often highly flexible while maintaining strength (232; 233). Therefore by using a flexible substrate the coils can be made to sit on a cylinder which reduces the field inhomogeneity within it.

Table 7.2: List of Materials with their magnetic susceptibility and susceptibility relative to water (229; 230; 231).

| Material | $\chi_v$ (ppm) | $\chi_v - \chi_{H_2O}$ (ppm) |
|---|---|---|
| Water | -9.032 | 0.000 |
| Air | 0.360 | 9.392 |
| Polyimide | -8.915 | 0.117 |
| PEEK | -9.332 | -0.300 |
| PDMS | -7.8 | 1.232 |
| Araldite | -9.694 | -0.662 |
| SU8 | -9.732 | -0.700 |
| Glass | -14.40...-6.342 | -5.37...2.96 |
| Silicon | -3.73 | 5.302 |
| copper | -9.63 | -0.60 |
| Silver | -23.80 | -14.77 |
| Gold | -34.40 | -25.37 |
| Alumina | -464.00 | -454.97 |

### 7.3.3 Flexible Substrates

Examples of flexible fabricated devices have been presented in the literature, the first example of note was carried out by (234) for the production of bolometers on a Kapton sheet (234). This work was then continued by (212) for the production of two and three dimensional coils on both Kapton and PEEK substrates in order to create a flexible magnetic field sensor with a high inductance (212; 235; 236).

It was shown that for multiple stages fabrication processes, Kapton film looses adhesion with the donor substrate. Therefore spin-on polyimide was used for several devices, with a silicon wafer as a donor substrate from which the polyimide can be removed at the end of the fabrication process (237; 238; 217).

It is clear that a planar device that can be shaped to suite the surface of the intended sample while limiting the effects it has on field inhomogeneity is highly desirable (233; 235). Therefore it was decided to explore the possibility of fabricating a multilayer device on a flexible polyimide substrate.

## 7.4 Flexible Coil Fabrication

### 7.4.1 Design Concept

It has been shown in previous chapters that to utilise parallel imaging in order to reduce the acquisition time, multiple receivers are required. With
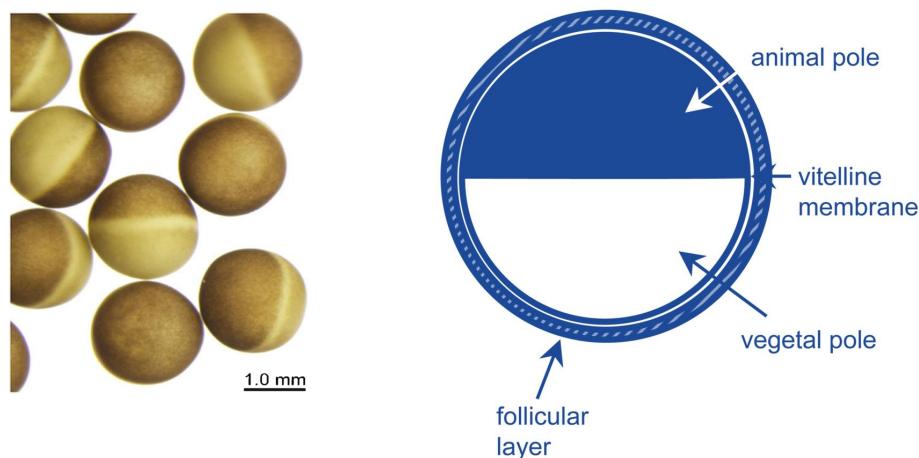
Figure 7.5: Xenopus Laevis Oocyte, one of the largest naturally occurring single cells and a schematic of the Oocyte showing that it has two separate hemispheres (239).

this knowledge, coupled with the fact that a planar receiver coil has an optimum signal to noise per unit volume, it makes sense that any system designed to eventually image hyper-polarised small molecules in very small objects such as cells must have multiple planar RF coils positioned around the sample. Therefore, in order to design a system that will work efficiently, knowledge of a typical sample is important.

One such system is the Xenopus Laevis oocyte (shown in Figure 7.5) which is one of the largest naturally occurring single cells, with a diameter of approximately 1.3 mm. It is a standard model system for biological experiments investigate active transport of metabolites (239). The objective of this project is to develop a suitable experimental set-up to monitor molecules via their hyper-polarised NMR signal within the oocytes.

The initial design constraints placed upon the system are that there must be multiple receivers to allow accelerated acquisition and the substrate upon which the coil sits must be well matched to the sample susceptibility and must not degrade the resonators Q-factor. Finally it is important to be able to get the detector as close to the sample as possible. Therefore, the device is fabricated on polyimide as it has favourable susceptibility values and is strong, chemically resistant yet flexible to allow the surface coils to match the topology of the object of interest. Two detector coils are placed on each individual device and are positioned so that they are approximately orthogonal to each other when wrapped around a 1.3 mm sample. Figure 7.6 shows the basic concept of the design flow where wires are first laid down on the substrate, then another layer of polyimide is applied and finally the coils are placed on the top. The figure shows the wires in what is termed the horizontal configuration as it is imagined that the wires will be placed horizontal to the polarising field in the final system.
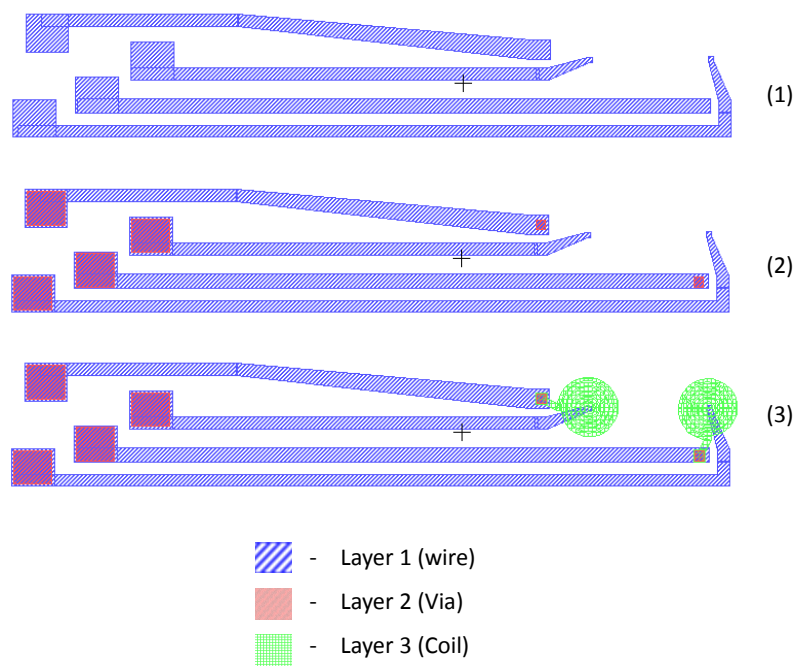
Figure 7.6: Schematic showing the layout of one of the variations of coil design on the mask, made in LEdit (Mentor - Düsseldorf, Germany). (1) The "legs" or wires on the 1st layer. (2) The position of the holes to create a via between layers. (3) The coils on the top layer. Some of the via holes are not shown in the figure due to the scale of the image.

Table 7.3: Table showing the various coil designs used on the mask design for the micro-fabrication process. The diameter (D) of the coils effects the strength of the $B_1$ and the range of detection, and the number of turns (N) and the width (W) of the wires effects the inductance and the resistance of the coil. S is the spacing between the wires of the coil.

| D $\mu$m | W $\mu$m | S $\mu$m | W/S | N |
|---|---|---|---|---|
| 450 | 30.0 | 10.5 | 2.9 | 5.75 |
| 600 | 34.0 | 12.0 | 2.8 | 6.0 |
| 600 | 36.0 | 19.0 | 1.9 | 5.0 |
| 700 | 34.0 | 15.5 | 2.2 | 6.5 |
| 1000 | 30.0 | 12.5 | 2.4 | 11.0 |

To allow flexibility and as a way of anticipating changes to the system a range of coil sizes were fabricated, with both horizontal and vertical wires. The outer diameter (OD) of the coils range from 450 $\mu$m to 1000 $\mu$m and the wire widths and spacings were determined by results from Matlab simulations to predict the resistance, inductance and maximum $B_1$ field for a given coil geometry. The different coil dimensions that were used are shown in Table 7.3. A comparison of the predicted and measured values of R, L and Q is made in section 7.5 and summarised in Table 7.6.

## 7.4.2 Process Flow

Figure 7.7 shows a schematic of the main processing steps in the fabrication of the devices. First a silicon nitride ($S_iN_4$) layer of approximately 200 nm was applied to the silicon wafer, the benefits of which will be discussed further in subsection 7.4.5. Four small rectangles of self adhesive Kapton tape where then attached symmetrical around the edges of the wafer in order to aid the final peel off stage, this can be seen in Figure 7.9. This step was devised to limit the number of polyimide resists required and is used instead of creating a sacreficial layer (which can also be used as a stress buffer), as demonstrated in the fabrication process used by (240). A small amount of adhesion promoter VM652 (Dupont) was applied to the wafer only around the edge of the wafer to prevent the polyimide from detaching during the fabrication stages[6].

The initial polyimide layer, is applied in a multi-stage process in order to achieve the required thickness of 35 $\mu$m. The resist PI5878G (Dupont) was applied in 5 stages via spin coating at 2000 RPM to achieve a thickness of 7.5 $\mu$m, between each spin coat a soft bake stage was used to drive out the

---

[6]Adhesion promoter applied to the entire wafer caused the polyimide to be impossible to remove or to rip in a unpredictable manner as it was peeled from the wafer. No adhesion promoter resulted in premature peel of or bubbling of the polyimide during the fabrication steps.
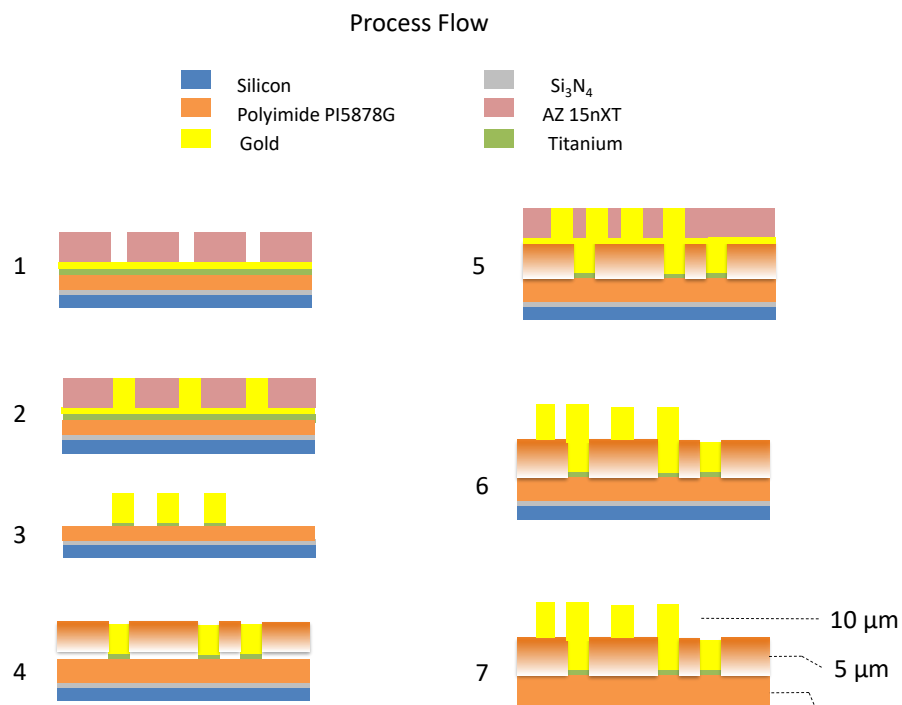
Figure 7.7: Process flow for production of flexible micro coils. (1) spin on polyimide PI5878G (Dupont) is applied to the donor substrate in a multi-stage process, Ti and Au are evaporated onto the polyimide and the photo resist AZ15NXT (micro chemicals) is applied and patterned. (2) The wires are plated to approximately 2 $\mu$m. (3) The resist is stripped and seed layers are etched away. (4) Planarisation with PI5878G and windows are opened to allow contact to the top layer. (5) Another seed layer of Ti and Au is applied with plating resist and the coils are plated to approximately 12 $\mu$m. (6) Plating resist and seed layers are removed. (7) polyimide wafer is peeled from silicon donor wafer.

Table 7.4: Table of chemicals, uses and the suppliers for the products required for fabrication of the novel, flexible micro coils.

| Chemical | Purpose | Supplier |
|---|---|---|
| PI5878G | Spin-on polyimide | Dupont Ltd. |
| VM652/VM651 | Adhesion promoter | Dupont Ltd. |
| SX AR-P 5000/82.7 | Photo-definable polyimide | AllResist |
| AR 300-26 | polyimide developer | AllResist |
| AZ 15nXT | Plating photo-resist | MicroChemicals |
| TechniStrip NI555 | Resist stripper | MicroChemicals |
| AZ4533 | Thick photo-resist | MicroChemicals |
| AZ 726(MIF) | Developer | MicroChemicals |
| NB SEMIPLATE AU 100 | Gold plating solution | MicroChemicals |
| Potassium iodide solution | Gold Etching | Prepared in house |

solvent. The final measured thickness of the polyimide after the cure (or hard bake) was $30 \pm 3$ $\mu$m.

Care must be taken in way the polyimide is cured as the maximum temperature and duration of curing determines how much of the polyimide becomes cross-linked. When curing after any metallisation further care must be taken to alleviate stresses between the metal and polymer which could compromise the adhesion. This is achieved by ramping the temperature at a rate no quicker than $5^o$ per minute so that the relative thermal expansion and contraction that occurs is small. At $250^oC$ 80 % of the polyimide is cross linked. In order to achieve a fully cross-linked substrate the polyimide was held at $300^o$ for 3 hours. The timing diagram of the temperature sequence used to cure the polyimide is shown in Figure 7.8.

The glass transition temperature of PI5878G polyimide resist is $450^o$ meaning that a stress buffer as a base layer could be beneficial. A stress buffer constitutes a polyimide resist with a much lower glass transition temperature which allows movement of the layer above while maintaining adhesion during the curing process.

In order to be able to plate the wires, a seed layer of Titanium (Ti) and Gold (Au) and a final layer of Ti were evaporated onto the polyimide. The photo-definable plating resist (AZ15NXT) was spun on and patterned with the first mask as shown in Figure 7.6.

After the wires were plated there is a planarisation stage, shown in part (4) of Figure 7.7 in order to electrically isolate the wires on the lower layer from the coils on the top layer. Initially it was hoped that a photo definable polyimide could be used for this task however budget restrictions prevented the ideal chemical from being used. A replacement was sourced and tested however it was found that it was too thin to achieve the required thickness to effectively planarise the wires.

153
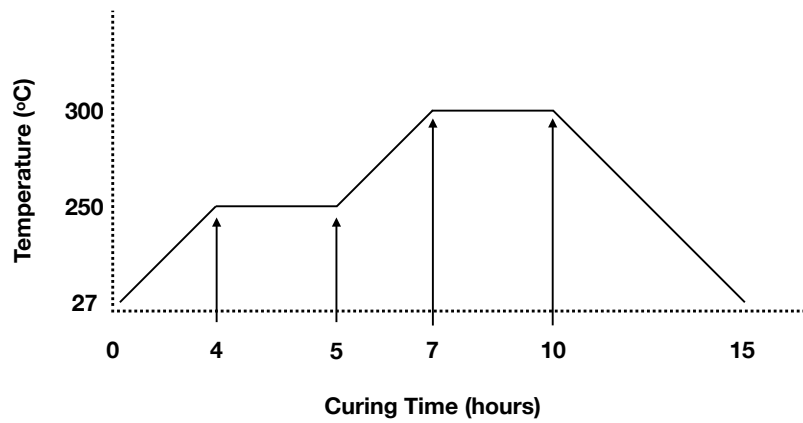
Figure 7.8: Schematic of the temperature profile that the programmable oven carried out in order to cure the polyimide. Slow curing is necessary in order to limit thermal expansion and contraction as this can cause de-lamination of the layers.



Kapton tape

Figure 7.9: A wafer in the process of being spin coated with polyimide. The spread of the resist was affected by the manner in which is it was dispensed and consequently starting the application from the wafer edge resulted in a smooth layer and starting from the middle of the wafer resulted in what is shown in the figure. The strips of Kapton tape to aid the final peel off are highlighted.

Figure 7.10: (A) shows a ×10 magnification optical microscope image of a 600 $\mu$m OD coil. The step down to the layer below is visible with a cle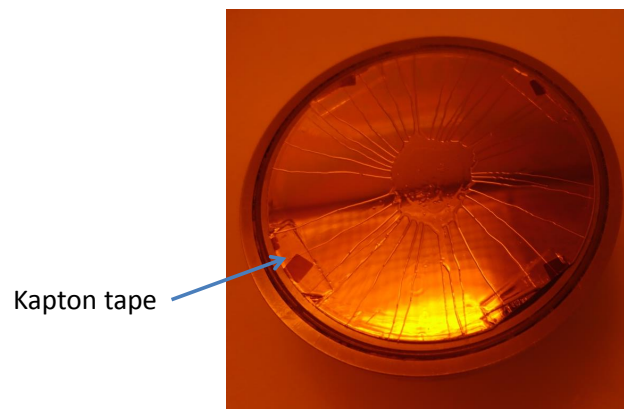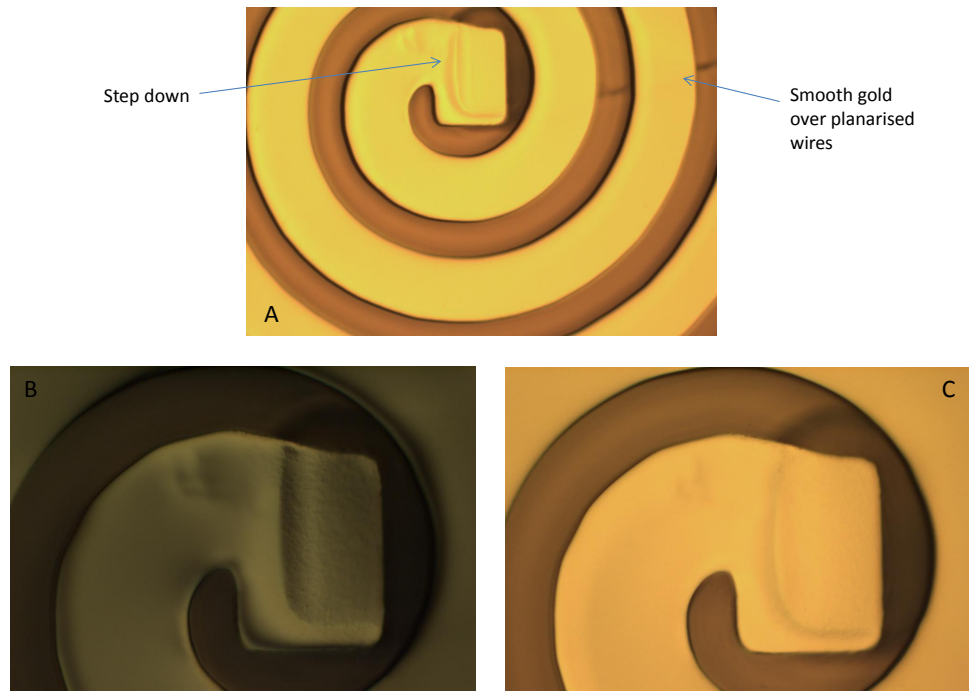ar metallic connection. The smoothness of the metal over the planarised wires is also visible. (B) The centre of the coil with polarising filters to show roughness (×20 magnifications). (C) ×20 magnification optical image of the centre of the coil with no polarising filter.

The planarisation was eventually carried out using a single application of PI5878G (6$\mu$m thick), then vias are opened up to allow electrical connections at the ends of each of the wires. One end allows connection to the macroscopic electronics and the other provides the path between layers to connect the coil. This was done by spin coating a layer of AZ4533 positive tone photo resist and allowing the developer to etch through the planarising polyimide. The polyimide is sufficiently thick to cover the first layer with only a variation in the surface topology of approximately 5 $\mu$m, this variation was smoothed out to a negligible level during the final plating process. It is important for formation of a good electrical connection between layers that there is no undercut due to the etching process. The connection at the centre of the coil (the step down) and the smooth surface of the coil across the planarised wires are shown in Figure 7.10.

Before patterning and electroplating the coil itself, another seed layer was applied and a 15 $\mu$m layer of the plating resist was patterned in order for the coils to be plated to a height of approximately 10-12 $\mu$m. After plating and once the seed layer is removed the final stage in the process was to remove the silicon wafer and release the flexible polyimide based device, the result of which is shown in Figure 7.18.
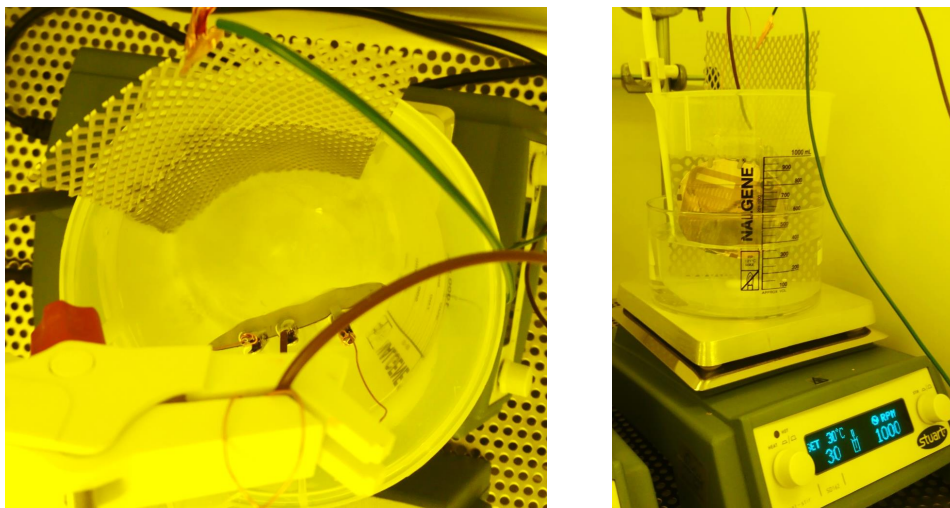
Figure 7.11: Plating set-up. The temperature needs to be carefully maintained for consistent plating therefore a water bath with a thermocouple is used. The side of the wafer to be plated is placed facing away from the anode in order to make the charged solution diffuse around the plating area. The colour tint in the image is due to the plating being carried out in a yellow room environment.

### 7.4.3   Gold Electroplating

The system used for gold plating is shown in Figure 7.11. The plating bath was SEMIPLATE AU 100 plating solution (Microchemicals) which is a cyanide free solution. The wires were plated initially for 45 minutes with a pulsed forward voltage (the upper pulse sequence shown in Figure 7.12). The total forward duration was 1.0 ms, the on duration was 0.1 ms and the off time 0.9 ms. This resulted in a plated height of approximately 2 $\mu$m however there were artefacts and imperfections across the wafer due to an effect known as current crowding.

For the final wafer the plating scheme was adapted to incorporate a reverse plating duration, with the intention of reducing the current crowding effects and to improve the homogeneity across the wafer. This plating scheme is shown in the lower half of Figure 7.12. Scanning Electron Microscopy (SEM) was used to asses the quality of the plating and to ensure that the topology of the coils is consistent. The images presented in Figure 7.14 and Figure 7.13 show clean side walls of the coils and minimal residual seed metal in the tracks of the coil. The images also show that the centre via has plated well to form a good electrical connection between the coil and the wires on the layer below.

### 7.4.4   Current Crowding

Current crowding causes the characteristic 'bunny ears' seen in Figure 7.17 and Figure 7.15. It is due to the current flux lines being concentrated at
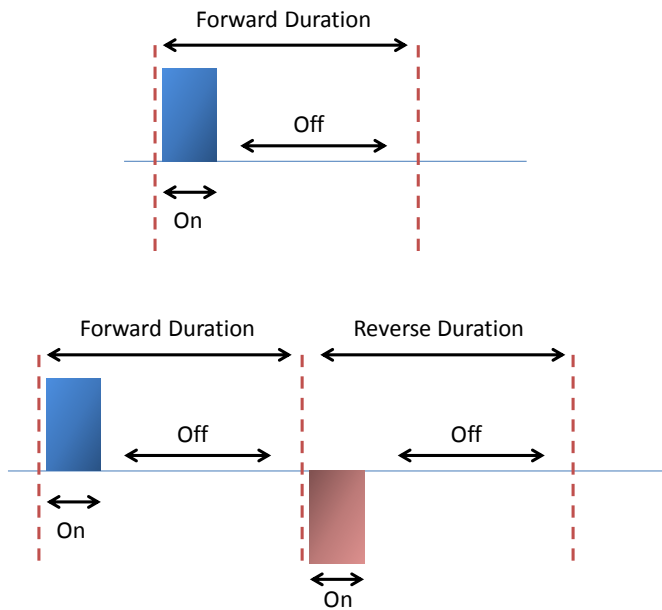
Figure 7.12: Top: A forward voltage only plating scheme as used initially to plate the wires of the micro coils. Bottom: Forward and reverse plating pulse sequence in order to improve the quality of the plating and reduce inhomogeneity across the wafer. The timings used are displayed in Table 7.5. For the reverse plating the forward duration is applied multiple times (e.g. 100) for every reverse duration.
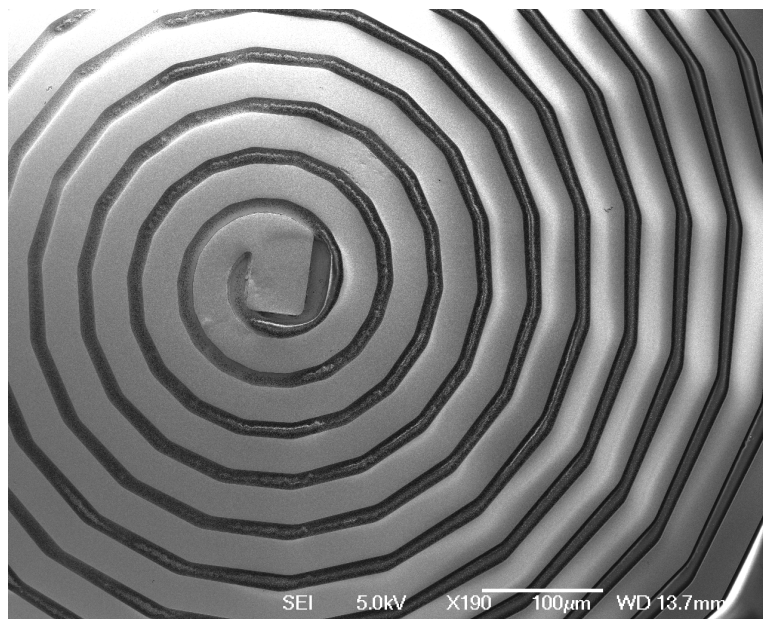


Figure 7.13: SEM images of the 1000 $\mu$m coil.
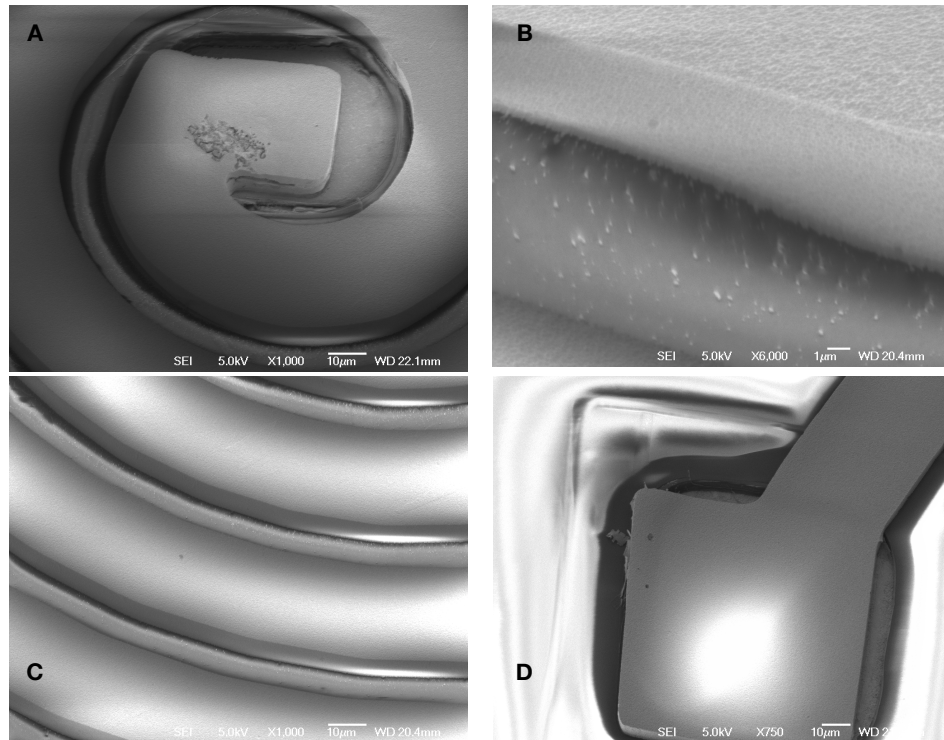
Figure 7.14: SEM images of the microfabricated devices. (A) ×1000 magnification of the central contact pad of a 450 $\mu$m coil showing that the plating has formed a good electrical connection across the via step. Some cracking and debris is also visible (B) ×6000 magnification of the plated wall and polyimide planarising layer. Small amounts of debris are visible however these are not big enough to compromise the coil. (C) ×1000 magnification of the 450 $\mu$m OD coil tracks. The top of the coil, the wall and the base of the tracks are all visible showing a smooth topology and a high aspect ration of the plated gold. The polyimide in the tracks shows up as white due to charging. (D) Outer contact pad of the 450 $\mu$m coil showing a good connection across the via. The polyimide is white due to charging.
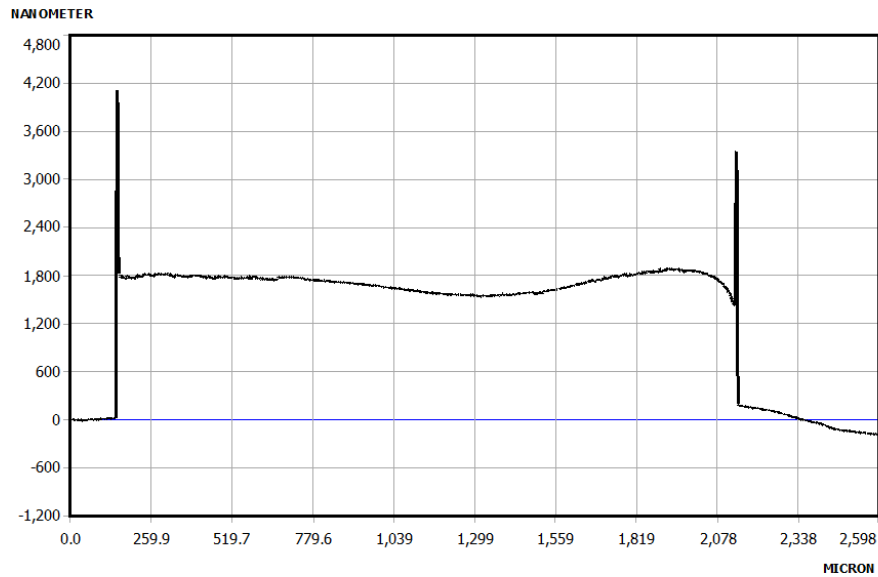
Figure 7.15: Stylus profiler plot across one of the larger square features on the wafer post plating where only forward plating was used. The spikes at the edges (often referred to as bunny ears) and the dip in the middle are due to current crowding during the electroplating process.

points where there are perpendicular surfaces (241; 242).

Figure 7.16 shows how the current flux lines increase around the edges of the larger micro-structures and cause a faster plating effect at these points.

The current crowding effects are reduced by applying the reverse plating scheme shown in Figure 7.12 and by allowing sufficient space between the anode and the cathode. The side of the wafer to be plated was placed facing away from the anode in order to increase the distance the ions have to travel and create a more homogeneous system.

By reverse plating, the edges that are preferentially plated during the forward voltage period are preferentially reverse plated during the reverse voltage period resulting in a more uniform plate overall. The plating scheme that was used to plate the coils is shown in Table 7.5.

Figure 7.17 shows stylus profiler data for gold plated devices with and without the use of reverse plating. It is clear from the figure that the homogeneity is greatly improved and the effect of current crowding are significantly reduced through the use of a reverse plating stage in the pulse sequence.

## 7.4.5 Peel Off

Several methods for removing the polyimide from the silicon wafer have been proposed and tested in the literature with varying levels of complexity and

159
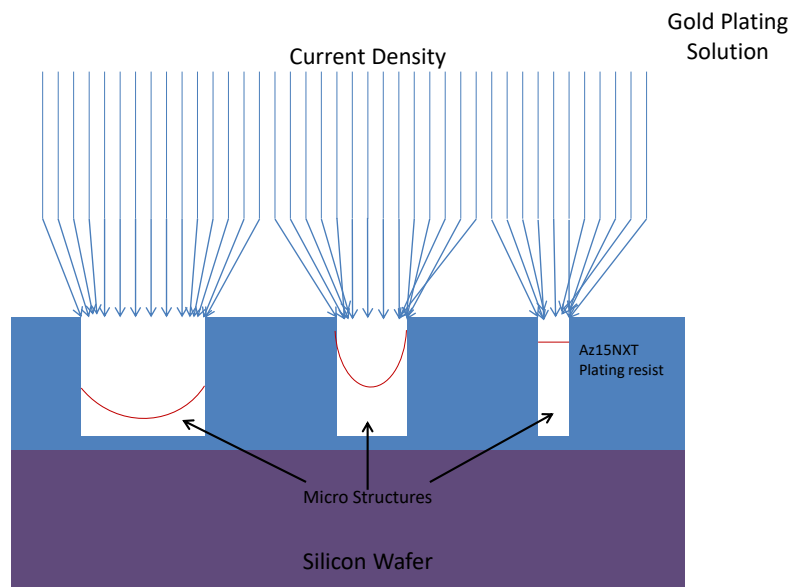
Figure 7.16: Current crowding is caused by the current flux density being increased at the edges of features in a micro-structure. The size of the feature will determine how large the 'bunny ears' are and if there are varying sizes across a wafer the plating rate may vary significantly (241).

Table 7.5: Plating timing parameters for both forward and reverse plating. This plating scheme was used to plate the final fabricated coils with a voltage of 0.09 V and current of 0.0018 A. For the final wafer there are 100 forward plating steps to every reverse plating step.

| Parameter | Duration (ms) |
| --- | --- |
| Forward Duration | 99.99 |
| Forward On | 0.10 |
| Forward Off | 99.89 |
| Reverse duration | 1.00 |
| Reverse On | 0.10 |
| Reverse Off | 0.90 |
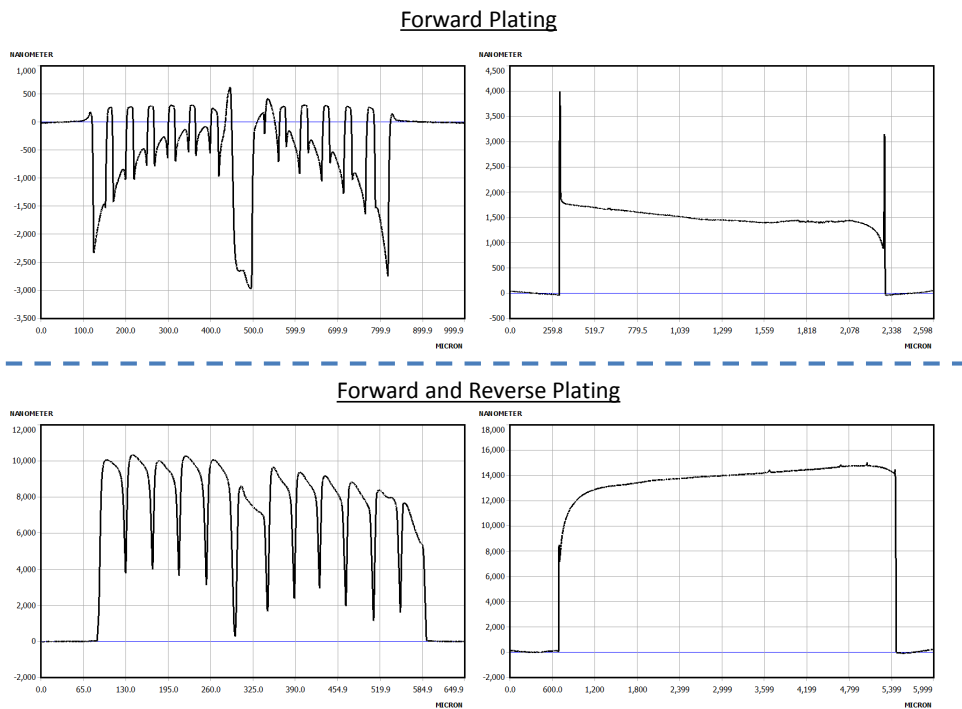
Figure 7.17: Stylus profiler plots across coils (left) and a large square feature on the mask (right) showing the 'bunny ears' effect (spikes at the edges of features) due to current crowding during plating (top). The plots below show how utilising a reverse plating stage in the pulse sequence can reduce the current crowding effects.

success. Initially (243) used super glue and Kapton sheets which could then be pulled gently from the donor substrate after the processing steps were completed (233). However, this technique reulted in a poor surface topology after multiple processing stages. Therefore, Mahmood (235) implemented a flexible device on spin-on polyimide to avoid surface wrinkling and improve adhesion between the polyimide and the donor wafer (232; 235; 237). To release the polyimide they scratched away the edge with a scalpel, peeled it off manually and did not use any adhesion promoters. The poor adhesion between wafer and polyimide meant that surface bubbling during processing was still a problem.

Other works cited the use of anodic dissolution where a sacrificial layer of metal is removed, however this adds unnecessary levels of complexity to the fabrication process and risked leaving a layer of Chromium on the underside of the polyimide which would be detrimental to the device performance (232).

In order to utilise a water activate separation of the polyimide from the donor wafer, a 200 nm thick layer of silicon nitride was applied to the donor before the polyimide. Polyimide is hydrophilic and the silicon nitride is hydrophobic meaning that when water is placed between the two surfaces the polyimide is gently removed from the silicon wafer. This was tested and worked well when no adhesion promoter was applied. However, this resulted in surface bulbing

161
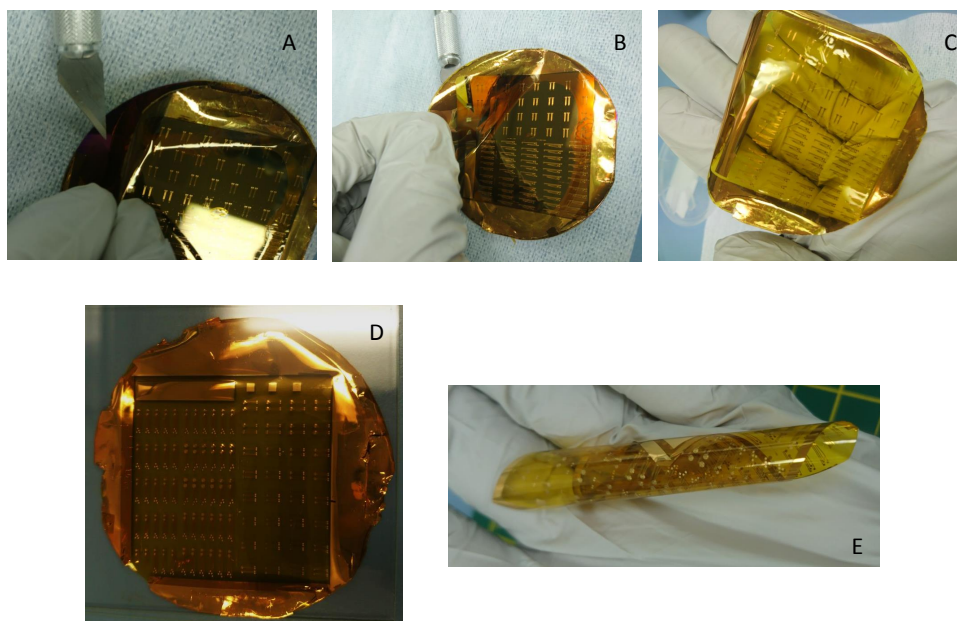
Figure 7.18: The top row (A to C) shows the peeling process, where the polyimide is carefully removed from the donor wafer with a scalpel blade under the Kapton tape. (D) Fully peeled off polyimide based set off devices. (E) demonstrating the flexibility of the polyimide and the devices.

during the other fabrication steps. Application of the adhesion promoter nullified the possibility of a water activated peel off (240; 234).

To test the peel off varying amounts of adhesion promoter VM652 (Dupont) were used and the ability to remove an intact disk of polyimide was observed. It was determined that covering the entire wafer resulted in the polyimide ripping during peel off and if the adhesion promoter is soft baked then the polyimide is impossible to peel from the wafer. In this situation it was removed with Piranha etch.

To achieve a balance between the necessary adhesion while still being able to remove the polyimide, a ring of adhesion promoter was spin coated around the edge of the wafer and soft baked. The polyimide could then be easily removed in the manner shown in Figure 7.18.

## 7.5 Electronic Characteristics

The resistance and inductance of the micro-coils were measured using a four point measurement system (244) and the results compared with simulated values which were calculated Matlab using equations presented by (216). The results are shown in Table 7.6 where they are also compared with the

Table 7.6: The table shows the measured and predicted resistance (R), inductance (L) and Q-factor for the 450 $\mu$m coil. These are also compared with a commercial micro coil (Piconics).

| | Measured | Predicted | Commercial [7] |
|---|---|---|---|
| R $\Omega$ | 5.2 $\pm$0.8 | 0.41 | $^{10.0}/_{1.5}$ |
| L $nH$ | 3.8 $\pm$0.2 | 5.5 | 7.7 |
| Q ($^{100}/_{400}$ MHz) $\pm$0.5 | $^{2.2}/_{4.3}$ | $^{8.4}/_{33.6}$ | $^{3.2}/_{12.6}$ |
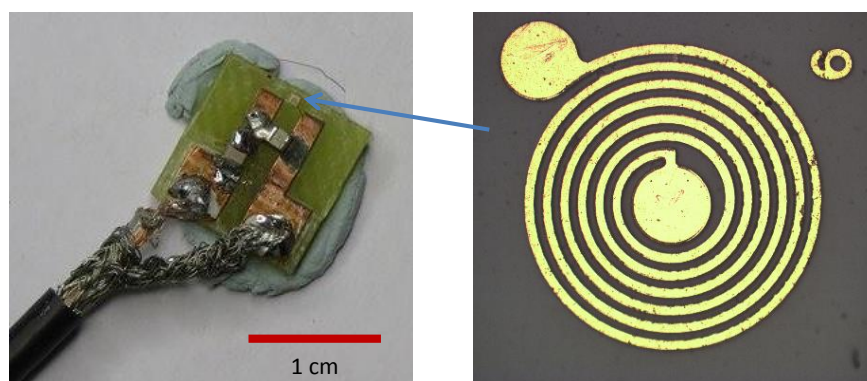


Figure 7.19: Tuned and matched commercial micro coil mounted on PCB. The 6.5 turn, 520 $\mu$m OD coil is shown where the contact pads in order to form an electrical connection are seen in the top left and at the centre of the coil.

values from commercially manufactured micro coils of the same size as shown in Figure 7.19.

The commercial coils are 520 $\mu$m OD with 6.5 turns of 6 $\mu$m high plated gold on a Alumina substrate (Piconics - Tyngsboro, Massachusetts). They are fabricated as a single layer so require a bonding wire bridging from the centre of the coil to make an electrical connection to the macroscopic system which increases the distance to the sample. One advantage of the fabricated flexible micro coils is that the wires occupy the layer below the coils and are therefore kept out of the way and do not limit the distance between the coil and sample.

Table 7.7 summarises how the largest and the smallest of the flexible coils that were fabricated compare in terms of the way in which they tune to the relevant working NMR frequencies. The coils were tuned to both 100 MHz and 400 MHz ($^{13}$C and $^{1}$H Larmor frequencies at 9.4 T) and matched to 50 Ohms. The resonance, bandwidth and Q-factor were measured using a network analyser. The table also shows how the commercially made coil compares when tuned to 100 MHz.

---

[7]Both measured and manufacturer stated values for resistance and are given in the form measured/stated. The value for inductance is that stated by the manufacture

Table 7.7: The table shows the difference between the smallest and largest fabricated coils in terms of the tuning and Q factor. It shows how the larger coil clearly has a larger inductance making it easier to tune and match. The results are compared to the commercially produced coil (as shown in Figure 7.19) which fairs badly in comparison due to the small inductance and high resistance.

| | 100 MHz | | 400 MHz | | 100 MHz |
| Coil Diameter | 450 $\mu$m | 1000 $\mu$m | 450 $\mu$m | 1000 $\mu$m | Commercial |
| --- | --- | --- | --- | --- | --- |
| Cap$_{tune}$ pf | 330 | 27 | 3.5-8.9 | 0.6-6 | 180 |
| Cap$_{match}$ pf | NA | 0.5-11 | 15.6-21.0 | 3.9-9.3 | NA |
| Loss (dB) | -25 | -60 | -30 | -33 | -9 |
| Band Width (MHz) | 80 | 40 | 95 | 59 | 140 |
| Q-factor | 2.2 | 2.8 | 4.3 | 7.2 | 1.0 |



5 mm
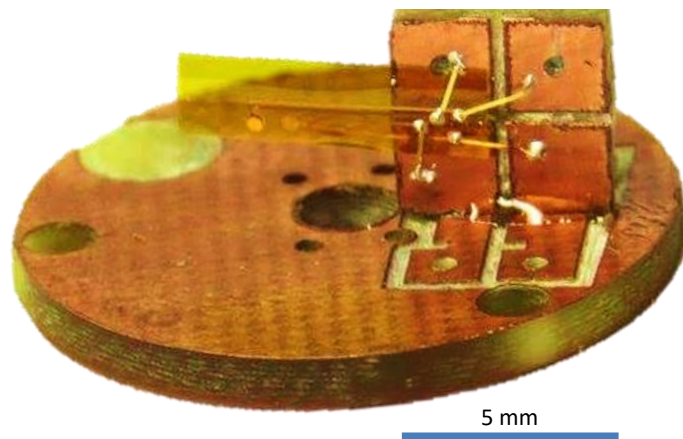
Figure 7.20: Horizontal coil mounted on PCB with gold bonding wires to form an electrical connection between the device and the PCB. The PCB is through plated to allow electrical connection to the opposite side. Tuning and matching is done on either side of the circular PCB.

The coupling between the two coils on the device when tuned to 100 MHz was measured using the network analyser. This was done for both the 450 $\mu$m and 1000 $\mu$m OD coils where it was found that for the smallest coils the coupling was >-20 dB when regardless of coil orientation or sample loading. However the largest coils showed -12$\pm$2 dB isolation when the coils were in a parallel configuration and -18$\pm$2 dB when the coils were placed orthogonally about a sample tube, which is an acceptable level of coupling, based on work presented in chapter 6.
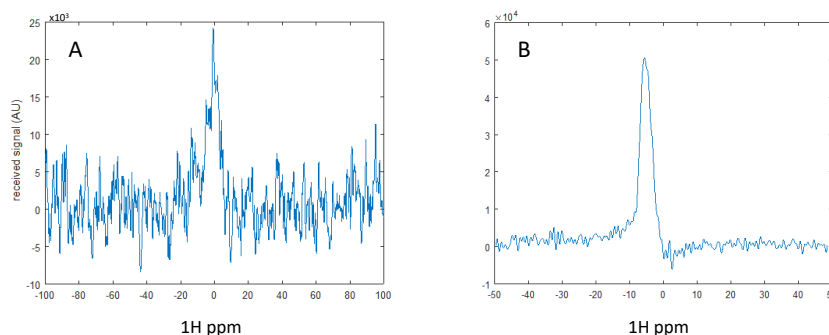
Figure 7.21: (A) $^1$H signal collected from the commercially produced coil in Tx/Rx mode. The sample was held in a 0.5 mm ID capillary with a wall thickness of 100 $\mu$m. (B)$^1$H signal collected from the commercially produced coil in Rx only mode with the same sample as shown in (A).

## 7.6  $^1$H NMR

In order to detect NMR signal, the coils are mounted on a through plated circular PCB, with appropriate dimensions so it could be used in conjunction with the Bruker Micro5 gradient set, Figure 7.20. The coils were initially mounted with epoxy resin on a square PCB that is milled and through plated and gold ribbon was affixed to the contact pads of the flexible coils and the PCBs. This was then attached, again with epoxy resin, to the circular PCB and an electrical connection is formed by soldering the PCBs together. This means that the tuning and matching capacitors can be kept at a distance from the coils and each other. The commercial coils were also mounted on PCB and used to acquire $^1$H NMR signal to allow comparison to the performance of the flexible devices. The mounted commercial coils are shown in Figure 7.19.

Figure 7.21 shows the $^1$H spectra obtained from the commercial coils (A and B),using two different experimental set-ups. The first spectra was collected using the micro-coil as both transmitter and receiver (shown in A) and the second case the micro-coil used a separate transmitter coil used for excitation of the entire sample (B). The sample is contained in a 0.5 mm ID capillary with a 100 $\mu$m wall thickness. The line broadening is reduced and the SNR increased due to the presence of the volume transmitter as the spins closest to the coil are no longer preferentially excited. No shims were applied during the acquisition of these spectra therefore for a reference Figure 7.22 shows the un-shimmed line width attained using the two channel proton probe presented in the previous chapter. Here the FWHM is measured to be 2700 Hz, which is caused by the poor homogeneity of the un-shimmed dual iso-centre magnet and the misalignment with the bore of the magnet due to
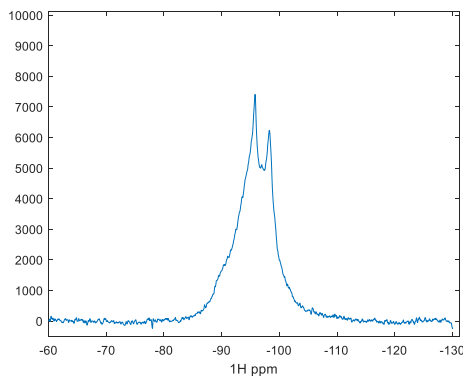
Figure 7.22: The figure shows the un-shimmed linewidth achieved by the two channel proton probe presented in the chapter 6. The sample is orders of magnitude larger than in the spectra shown in Figure 7.21 and 7.23 with sample held in a 3mm OD NMR tube. The FWHM of the peak is 2700 Hz with a 10 Hz line broadening filter applied to the raw signal. After shimming the linewidth can be reduced to approximately 100 Hz, and the splitting is removed.

the standard spacers being incompatible with this probe and the incumbent dissolution pipes. After shimming this can be reduced to the order of 100 Hz therefore there is a significant field inhomogeneity to deal with when the shims are not in use. Using a well constructed BBO Bruker probe with a 5 mm NMR tube, the un-shimmed linewidth is still on the order of 800 Hz which can be reduced to approximately 20 Hz with the application of the shims.

Due to the volume of the samples being considered in Figure 7.21 and 7.23, it is incredibly difficult to make any significant improvement with the built in shim set. It may be useful to use the Bruker micro-imaging gradient set as a shim set in the future.

The flexible coils were used as a transmitter and receiver in both of the spectra presented in Figure 7.23, however spectrum (C) used the same 100 $\mu$m wall capillary as the spectra in Figure 7.21, whereas spectrum (D) uses a capillary that has a 10 $\mu$m wall thickness in order to get the sample as close to the coil as possible. The achieved SNR from a single scan from each of the experiments as well as the linewidth achieved is shown in Table 7.8.

It is clear from examination of the SNR that the microfabricated flexible coils are significantly superior to the commercial coils. This is for several reasons: i) The improved electronic characteristics allowing a better resonant circuit to be created. ii) The flexible coils can be placed directly on the sample. The linewidth for all the spectra shown is large but is improved by the use of the flex-coils when considering the distance between the coil and the sample.
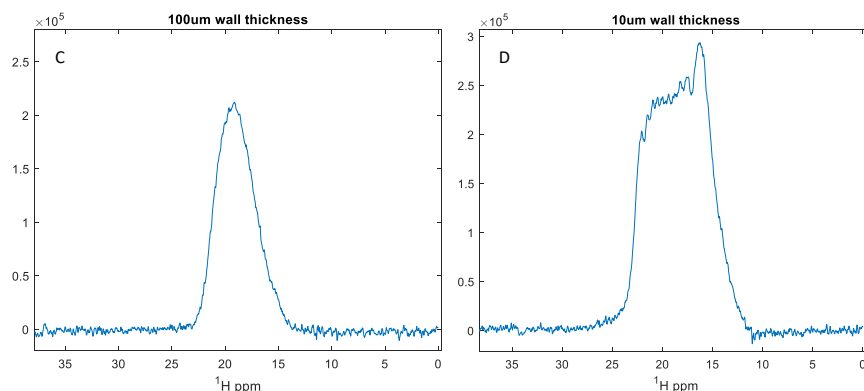
Figure 7.23: (C) $^1$H signal from the flexible coil placed against the capillary wall used in Tx/Rx mode. (D) $^1$H signal from the flexible coil with a 10 $\mu$m wall capillary. The coil is wrapped around the capillary and glued in place. The broad line of the peaks is due to there being no shimming and no centring of the probe inside the magnet. Spectrum (D) broadened more due to the susceptibility mismatches caused by placing the coil closer to the sample and $B_1$ inhomogeneity of the micro coil.

Table 7.8: SNR, linewidth and and peak signal intensity for $^1$H spectra of free water collected using both the commercial coils and the equivalently sized microfabricated flexible coils. The commercial coils were used as both a receive (Rx) only coil and a transmit/receive (Tx/Rx) system, whereas the flex-coils were used only in a Tx/Rx set-up. the change in linewidth shows how the susceptibility is effected by the proximity and how the $B_1$ field effects the received signal.

| Coil | SNR | linewidth (Hz) | peak signal (AU) | Figure 7.23 |
|------|-----|----------------|------------------|-------------|
| Commercial (Tx/Rx) | 5 | 2900 | $24\times10^3$ | A |
| Commercial (Rx only) | 11 | 2450 | $6.8\times10^4$ | B |
| flex-coil (100 $\mu$m wall) | 87 | 1700 | $2.1\times10^5$ | C |
| flex-coil (10 $\mu$m wall) | 202 | 3000 | $3.0\times10^5$ | D |

Table 7.9: The table shows the un-shimmed line widths and the effect of shimming on the acquired $^1$H spectra. The table demonstrates how poor the field homogeneity is without shims and also shows how difficult it is to shim small sample volumes.

| Probe | un-shimmed (Hz) | shimmed (Hz) | Volume |
|-------|-----------------|--------------|--------|
| BBO (Bruker) | 840 | 28 | 600 $\mu$L |
| 2 channel SENSE probe | 2700 | 100 | 10 $\mu$L |
| $\mu$-coil (100 $\mu$m wall) | 1700 | 1700 | 35 $n$L |
| $\mu$-coil (10 $\mu$m wall) | 3000 | 3000 | 35 $n$L |

167

Table 7.9 shows how the shimming affects the linewidth measured for some of the probes that were used in the acquisition of data in this thesis. The un-shimmed linewidth for all probes is very large due to the big field inhomogeneity. It is clear that for small samples the shims are not affective. It was also considered that the large linewidth shown in the flexible coil spectra could be partly due to background signal, however this does not appear to be the case as after 10 scans without a sample present no measurable signal was recorded for protons.

## 7.6.1 Susceptibility

The change in linewidth obtained from the use of the flexible coils compared with the commercial coil (as well as the effect of varying the distance of the coil from the sample) can be somewhat accounted for by the large effect on the magnetic field the coil itself has. This is demonstrated by the results from field perturbation simulations shown in Figure 7.25, where the field perturbation maps in plane and orthogonal to the coil is shown. The basis of the simulation was developed by Bowtell *et. al.* (245) and carry out a Fourier space multiplication of the geometry with a dipole to generate the field perturbation maps. Such simulations have been verified by modelling venous systems, as demonstrated by Ziener *et. al.* and Sedlacik *et. al.* (246; 247). The geometry of the simulated system is given in Figure 7.24 and Table 7.2 shows the susceptibility values used in the simulation. Figure 7.25 shows how the variation in the field within the sample is greatest close to the coil, where the field perturbation oscillates due to the windings of the receiver. Further from the coil there is still a field offset, however this is a homogeneous shift in the field from $B_0$ rather than a gradient.

The results of the simulation shown in Figure 7.25 are used to plot a histogram of the field perturbation within the sample volume, this is compared to the NMR spectrum and is shown in Figure 7.27. The simulations do not take into account the effect of external field variation that are down to poor shimming or misaligned probes. Some of the broadening shown in the spectrum (B) is also apparent in the histogram however the peaks of the histogram are not evenly weighted. This is because the histogram has no weighting of the frequency distribution in order to take into account any effects due to the $B_1$ inhomogeneity.

The same simulation was used to asses the effect of the coil and substrate on the field within the sample given a copper coil rather than gold. The histogram of the field perturbation within the sample for both the copper and gold coils are shown in Figure 7.28.

It is evident from the histograms that it is likely some broadening would still be observed given a copper coil, due to the proximity of the coil to the sample, however the bandwidth over which the field perturbation occurs is significantly reduced for a copper coil (histogram B) suggesting that a
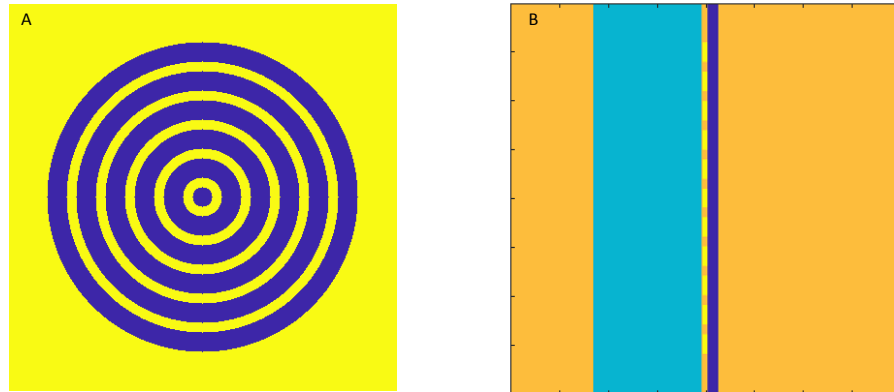
Figure 7.24: The geometry of the system simulated to determine the level of the field perturbation. (A) the coil geometry, placed in the centre of the array. The height of the coils is 10 $\mu$m and the widths of the wires and spacing matches the 600 $\mu$m coil shown in Table 7.3. (B) side on view of the central slice thought the simulated geometry. The orange is air, light blue is sample, dark blue is polyimide and yellow is the gold coil.
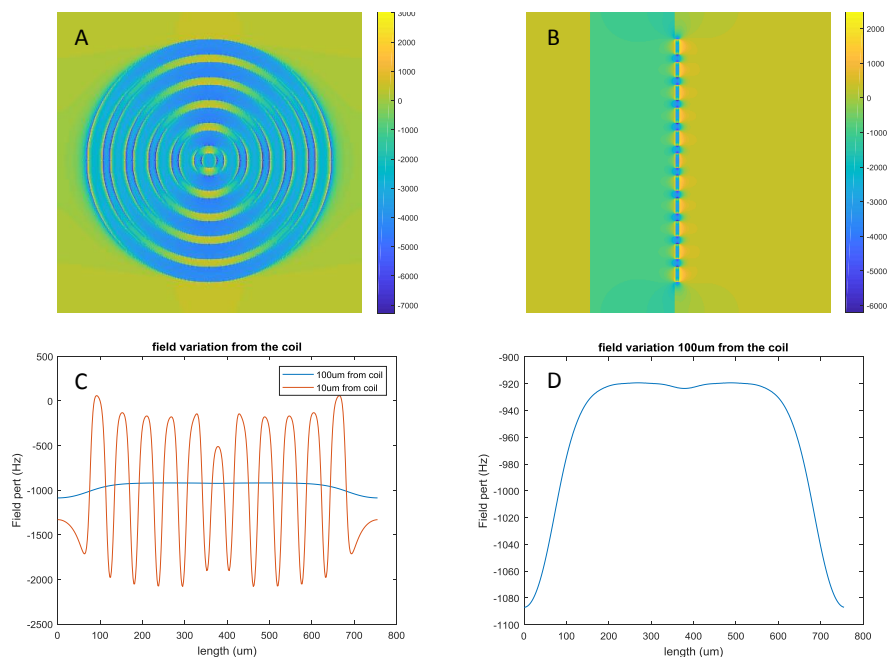


Figure 7.25: Simulated susceptibility maps for protons at 9.4 T of a 600 $\mu$m gold coil with a polyimide substrate and a water sample. (A) Field perturbation map across the coil at the coil surface. (B) Field perturbation map orthogonal to the coil, through the centre of the coil and the sample. (C) The variation in field perturbation inside the sample 10 $\mu$m (orange line) from the coil surface and 100 $\mu$m from the coil surface (blue line). (D) field variation inside the sample 100 $\mu$m from the coil surface.
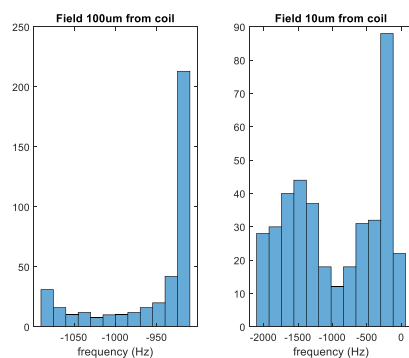
Figure 7.26: Histogram of the frequency perturbation 100 $\mu$m and 10 $\mu$m from the coil within the sample. In reality there is a weighting to give the spins closest to the coil a higher sensitivity meaning that the line will appear broader than the simulations suggest.
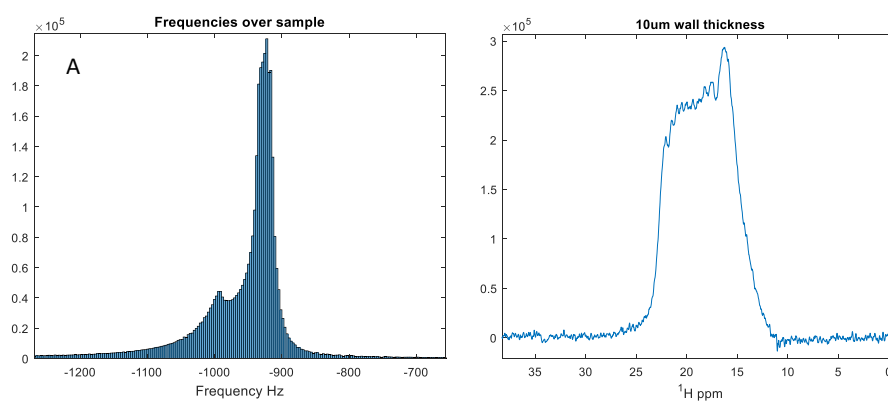


Figure 7.27: (A) Histogram of the field perturbation frequencies within the entire sample due to the presence of the detector at 9.4 T. (B) $^1$H spectrum with the coil place 10 $\mu$m from the sample. A 30 Hz line broadening filter was applied to the FID. Some of the broadening caused by placing the sample closer to the coil appears to be an affectation of the susceptibility mismatches.
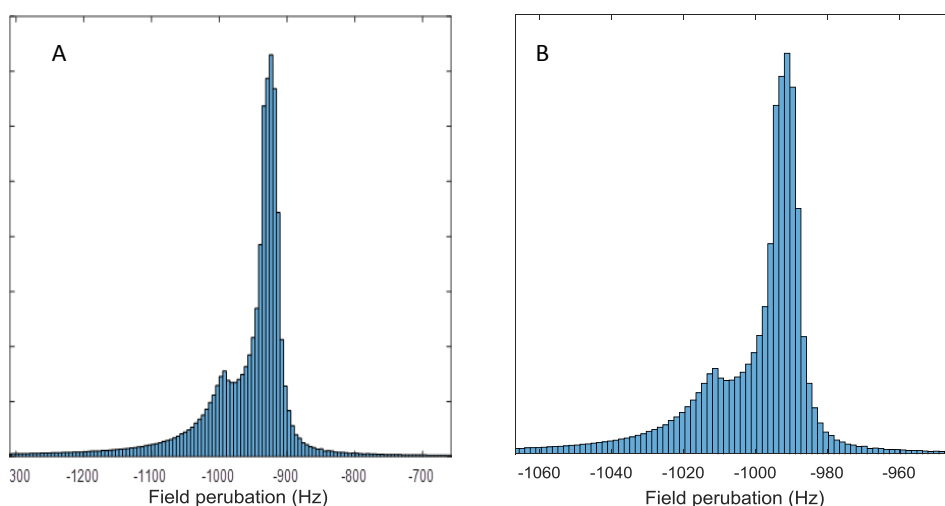


Figure 7.28: Histograms showing the field perturbation within the water sample for a copper coil (A) and a gold coil (B). The copper coil creates a much narrower spread of frequencies due to the smaller mismatch in susceptibility.
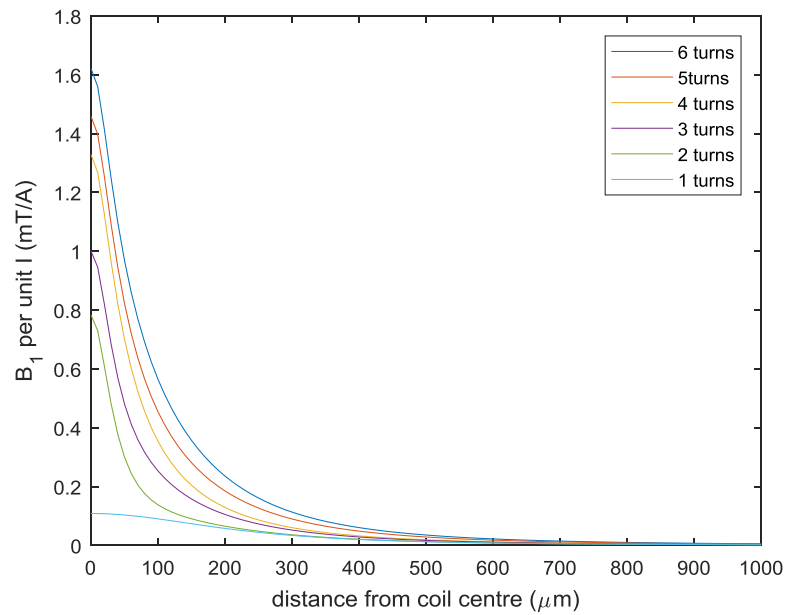
Figure 7.29: Graph showing simulated $B_1$ field as a function of distance from the coil for coils with increasing number of turns (216).

much better line width is achievable. This is due to the better matched susceptibility of copper to the water sample.

## 7.6.2 $B_1$ Field Inhomogeneity

A further factor potentially affecting the quality of the spectra is the homogeneity of the RF field across the sample. It is clear from the tests with the commercial coils shown in Figure 7.23 that the use of a separate transmitter to excite the entire spin system improves the linewidth and the SNR. The separate transmitter coil provides uniform excitation of the sample so there is no longer a weighting towards exciting the spins closest to the coil. However, for use on a single channel system it may be necessary to use the flexible coils as both transmitter and receiver. The field produced by a given coil geometry as a function of distance from the coil is shown in Figure 7.29. The plot was produced using a Matlab simulation based on the equations presented in (216). It is shown that for the 6 turn coil, at 100 $\mu$m from the coil the intensity of the $B_1$ field has reduced by more than half. This is why there is such a drastic improvement between the commercial coil and the flex-coil when used in Tx/Rx mode. This also explains why the use of the thinner walled capillary improves the SNR further for the flex-coil.

To demonstrate the inhomogeneity of the flex-coil a pulse length optimisation experiment is carried out on protons. This is shown in Figure 7.30, where the maximum signal can be seen to be collected for a pulse length of 25 $\mu$s. However, no $180^o$ pulse is found due to the field inhomogeneity.

Through examination of the effect distance to the sample on the SNR it is
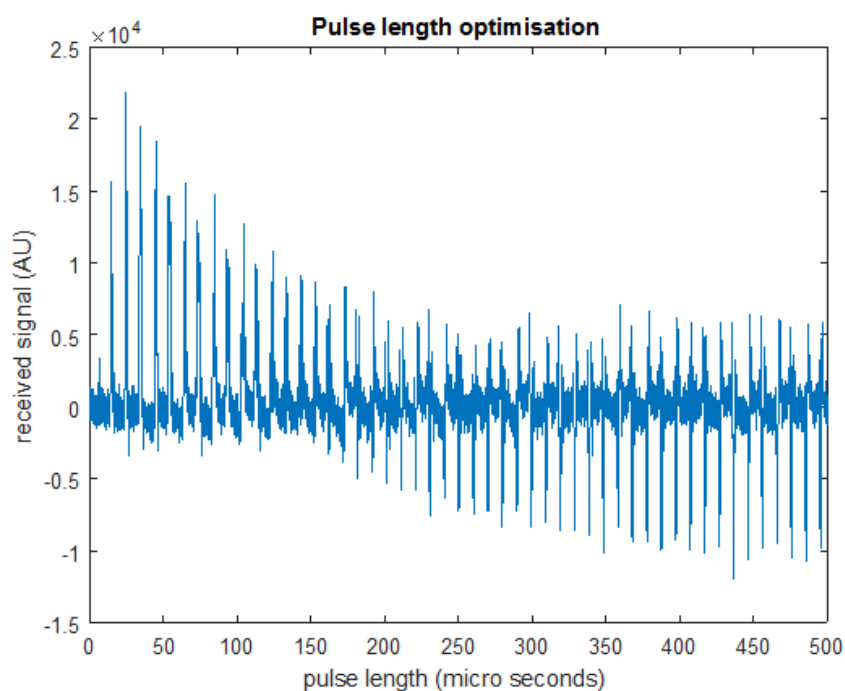
Figure 7.30: Pulse length optimisation for the 450 $\mu$m coil tuned to protons at 9.4 T. The inhomogeneity of the $B_1$ field means that there is no clearly defined $180^o$ pulse.

possible to estimate the homogeneity of the sensitivity of the coils. There is a 43 percent difference when comparing the SNR achieved at 10 and 100 $\mu$m sample distance. Taking difference in the predicted $B_1$ field for a 6 turn coil shown in Figure 7.29 for the same distance values one calculates a difference of 40 percent. Therefore there is good agreement between the theoretical and measured value and the profile is likely to correctly represent the change in $B_1$ across the sample.

## 7.7 $^{13}$C NMR

To show that the coils are suitable for use in observing hyper-polarised $^{13}$C nuclei in small metabolites, the coils were tuned and matched to 100.6 MHz. Two different experimental set-ups were tested. One used the micro coil for both transmit and receive and another used a separate transmitter is used in an attempt to excite the sample homogeneously.

Figure 7.31 shows the 3 mm OD saddle coil used to excite the sample which gives a $90^o$ excitation pulse for a pulse power of 30 W and duration of 59 $\mu$s. The sample is a 1 mm OD capillary filled with a 4 M sodium acetate solution, where the sodium acetate is labelled with a single $^{13}$C on the carbonyl. This was chosen as it is a molecule that occurs in biological processes and one that is routinely used in D-DNP experiments on the dual iso-centre magnet.

172
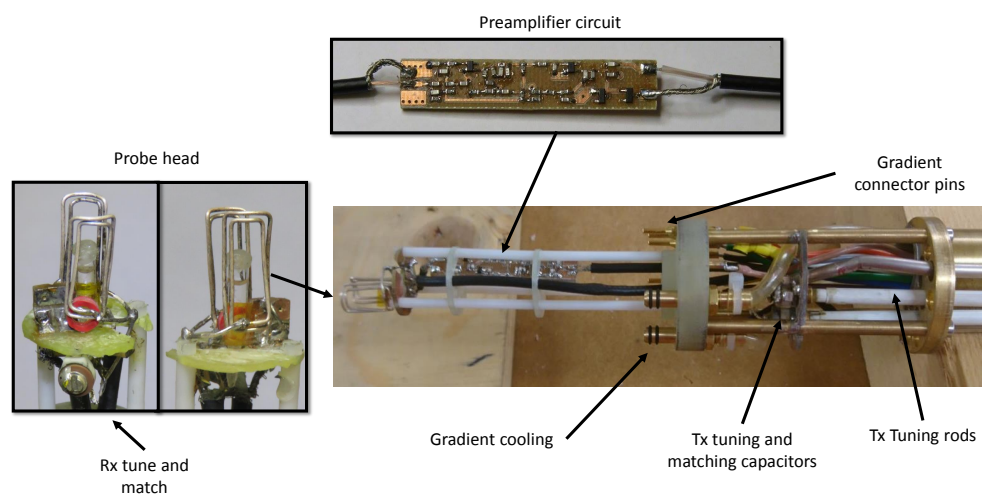
Figure 7.31: Probe head for $^{13}$C NMR microscopy. The transmitter coil is shown and the polyimide substrate can be seen wrapped around the sample. The receiver coils are not visible in the image. The pre-amplifier and its position in the probe head is shown along with the gradient connectors and cooling. The transmitter coil is tuned remotely to alleviate space at the top of the probe head.
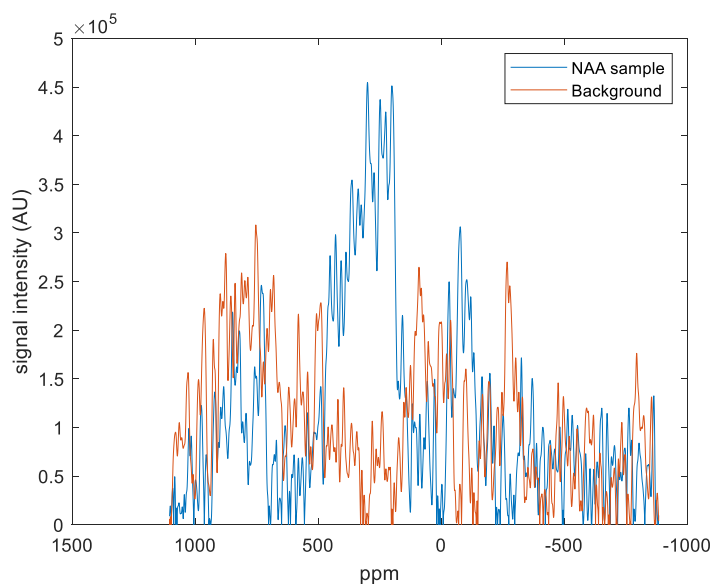


Figure 7.32: $^{13}C$ sodium acetate signal received from the flex-coil tuned to 100 MHz while in Tx/Rx mode. The blue line is the signal collected with the sample present and the orange line is the signal acquired without the sample. The broad lines are likely due to a combination of background signal, coil ringing and field inhomogeneity.
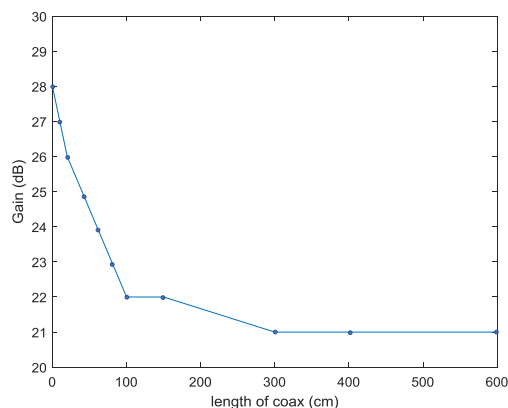
Figure 7.33: Plot of the received signal gain as a function of cable length between the signal source (the coil) and the input of the pre-amplifier.

Figure 7.32 shows the signal that is received from 5000 scans using the flex-coil as a transmitter and receiver and only the Bruker pre-amplifiers. The spectrum is significantly wider than is expected for a liquid state sample. However there is a solid state background signal from the polyimide itself as well as potentially the epoxy resin that is used to secure the sample in place, the effects of coil ringing may also be problematic however it is unlikely that the ring down time of a coil with such low Q-factor is the only cause of the signal. The spectrum demonstrates that it is possible to acquire $^{13}C$ signal with the novel detectors.

To maximise the signal received pre-amplifiers were constructed that are designed specifically to fit the dimensions of the probe head to reduce the losses that occur from long cables between receiver and pre-amplifier. This effect is demonstrated in Figure 7.33 where increasing lengths of coaxial cable were placed between the pre-amplifier and the frequency source.

The home built pre-amplifier is a two stage amplifier that has a total gain at 100 MHz of 28±3 dB and each of the FETs are driven by an initial input of 10V which is delivered through the transmission line, a method known as phantom power. The circuit diagram for the pre-amplifier is shown in Figure 7.34. A potential divider supplies the desired gate voltage of 0.47 V to each of the FETs, while the amplifiers are protected from high power transmitter pulses through the use of crossed diodes going to ground on the front end. The noise figure of the home built pre-amplifier has been measured during bench top testing using a spectrum analyser, and was found to be less than 1.0 dB. However, this is for a perfectly matched system (purely 50 $\Omega$ coax) and the true value was measured with a loaded coil attached to the front end of the pre-amplifier to be at least 2.7 dB. The noise figure and gain values are comparable to that of the commercial pre-amplifiers (Bruker

174
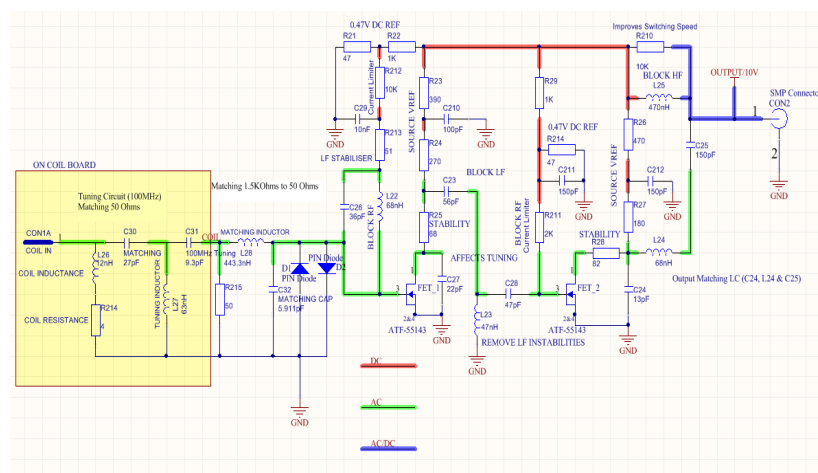
Figure 7.34: Circuit diagram showing the routing of the DC (red), AC (green) and shared (blue) lines on the amplifier. The values shown for the tuning of the coil are different from the capacitor and inductor values used in the final assembly.

Table 7.10: The SNR, linewidth and approximate sample volumes for different experimental set-ups used to detect $^{13}$C signal. The mass related SNR is highest for the transmitter coil as the sample volumes are estimates and given the shape of the sample and the small coils it is likely that the volume of the sample detected by the surface coils is overestimated and the total volume of sample inside the transmitter is under estimated.

| Coil | V (nL) | N.spins | SNR | $\mathrm{SNR}/n\mathrm{L}$ | Line width (Hz) |
|---|---|---|---|---|---|
| $\mu$-coil ($^{\mathrm{Tx}}/\mathrm{Rx}$) | 35 | $2.1\times10^{16}$ | 11.00 | 0.31 | 23000 |
| $\mu$-coil(Rx and preamp) | 35 | $2.1\times10^{16}$ | 10.14 | 0.29 | 431 |
| $\mu$-coil(Rx only) | 35 | $2.1\times10^{16}$ | 4.53 | 0.13 | 530 |
| Tx coil | 600 | $3.8\times10^{17}$ | 276.34 | 0.46 | 512 |

Ltd. - Coventry, England) supplied with the spectrometer.

Figure 7.35 shows multiple spectra collected using a separate transmitter and the micro coils are used only for receiving. The background signal, acquired when the coils were glued to an empty NMR tube is shown here also. There is some background on the transmitter channel but no background on the receiver.

The introduction of the pre-amplifier to the the receiver channel results in a much clearer carbon peak with significantly better SNR, this can be seen in Figure 7.36. A comparison is drawn between all the data in Table 7.10.

Figure 7.36 and 7.35 highlight the differences between the signal acquired with and without the use of the pre-amplifier. It shows that there is not only an increase in the SNR but also a slight reduction in the linewidth and an overall smoothing effect on the spectrum when the pre-amplifier is
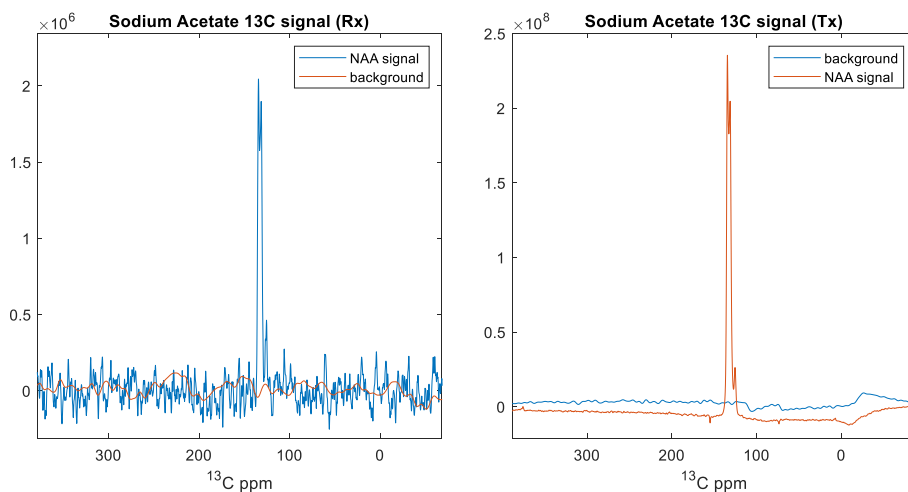
Figure 7.35: $^{13}C$ sodium acetate signal from 5000 averages with a $75^o$ flip angle. Right: Spectrum from the transmitter coil detecting a volume of approximately 600 nL . Left: Received signal from flex-coil as a receiver only with the homebuilt pre-amplifier in place. The receiver coil was detecting a maximum volume of 35 nL. No reference compound was used and therefore the chemical shift axis is there as a guide to the linewidth of the peaks only and 100 Hz line broadening was applied to the FID.
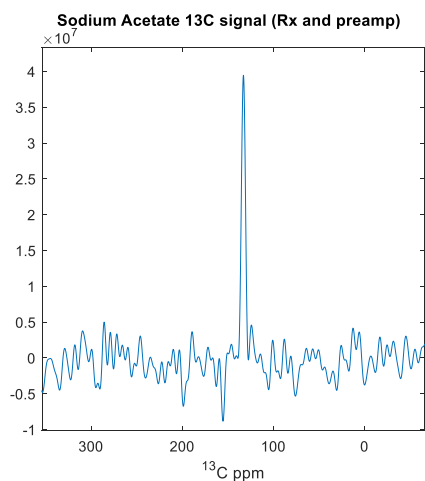


Figure 7.36: $^{13}C$ sodium acetate signal from 5000 averages with a $75^o$ flip angle. The receiver coil was detecting a maximum volume of 35 nL. The spectrum shows the receive only flex-coil signal with the pre-amplifier integrated into the line. 100 Hz line broadening was applied to the FID. No reference compound was used and therefore the chemical shift axis is there as a guide to the linewidth of the peaks only.

used. The SNR, line widths and maximum sample volume for each of the experiments are displayed in Table 7.10. The figure also highlights the benefit of employing a separate transmitter channel, especially when considered as a comparison with the spectrum shown in Figure 7.32.

## 7.8   Discussion

The difference between various micro NMR detector configurations are considered, however, for the purposes of this project it was decided to pursue a planar micro coil geometry. The use of a micro-solenoid was easily ruled out due to the inability to build an array of detectors linked with difficult experimental set-up to achieve an acceptable linewidth. From Table 7.1 it is clear that each of the different devices has its advantages and disadvantages depending on the intended sample volume and geometry. However, the most important factor is that the detector must be designed appropriately for the intended sample.

To achieve accelerated image acquisition of hyper-polarised samples multiple detectors are required and therefore the bulky strip line resonator is not suitable. The Helmholtz pair used by Goloshevsky *et. al.* (225) also shows promising results for the analysis of small samples at low field due to its high inductance. However, this is not suitable for use in a multi-receiver system as the coupling between the coils is difficult to manage. Therefore, given the size of the anticipated sample (approximately 1 mm) the most versatile option is a set of planar micro coils. Gobel *et. al.* demonstrated that you can build an array of wound coils that are decoupled using geometric overlapping and achieve good enough field homogeneity to image diseased skin cells (223).

Initial trials with commercially produced coils showed that there is good versatility when using micro surface coils. However, the commercial coils required extra wires that limit the distance between the sample and the receiver. The substrate also caused large field perturbations due to the huge mismatch in the susceptibility of alumina. Both of these problems were overcome in the designing of the novel, flexible micro coils as the central wire is built into the fabrication process and the substrate (polyimide) is well matched to the susceptibility of water. The positive effect of these changes are seen in the increase in signal and reduction in linewidth when the novel flex-coils are used, shown in Figure 7.21 and 7.23.

### 7.8.1   Novel fabrication process

To realise a versatile coil array that is capable of image acquisition of volumes less than 1000 nL (a typical Oocyte volume) a novel fabrication process was engineered whereby a flexible substrate is used to allow coils to be positioned

in an optimal configuration for parallel imaging and susceptibility matching. Polyimide is used as the flexible substrate as it is strong and chemically resistant, with the added advantage of it being available in liquid form to allow spin coating.

Simulations of electronic characteristics for various coil configurations determined several possible coil dimensions, with a 600 $\mu$m (OD) coil being most applicable to imaging of a $\leq$1 mm diameter sample due to the penetration depth of the sensitive region compared to the size of the sample. The use of gold coils gave significantly better electronic characteristics than other examples of micro coils presented in the literature (see Table 7.1) due to a low resistance (248; 211; 207; 213; 226). Other factors such as the inert nature of gold and the presence of an already well established gold plating system made it the first choice of coil material.

Initially it was thought that the substrate would play a larger role in the susceptibility effects than the coil itself, which is certainly true for the commercially produced coils. However, once the substrate was matched it was found that the coil itself becomes the main issue. This is reduced to an acceptable level when the sample is 100 $\mu$m from the coil as seen in Figure 7.23. It can be argued that for observation of very small samples (nL scale) a copper plated coil would be more appropriate, as copper is more closely matched to the susceptibility of water than gold. However, this would reignite the problem of the coil's resistance being too high to allow a tuned and matched circuit at the Larmor frequency of low gamma nuclei such as $^{13}$C.

The gold plating itself was significantly better than expected with smooth topology and a shiny finish being produced. The etch rate of the plated gold was found to be relatively comparable to that of evaporated gold (within a factor of 3) which suggests that the plated gold is of a similar harness to that of the evaporated gold. This may be due to the specific plating solution used, but is also likely to arise from the small plating currents used, since the plated gold was built up slowly. The plating rate was marginally reduced by the implementation of the reverse plating as the current in the forward direction was increased, which was applied to improve homogeneity across the wafer and remove bunny ears.

## 7.8.2 nL Scale NMR

The fact that the coils are close to the sample means that volumes on the order of 10's of nano litres or smaller can be detected in a single scan (for protons) and retain a good SNR. This is a smaller sample volume than all but three of the literature examples presented in Table 7.1. However the proximity of the coils to the sample comes at a cost of larger field inhomogeneity due to the susceptibility mismatch between the gold coil, air and the sample itself. The $^1$H NMR data has shown a good correlation between the spectra and the simulated field perturbations suggesting that

the splitting observed in the flexible coil spectra, when placed only 10 $\mu$m from the sample, is due to the proximity of the coil to the sample. This is further backed up by observation of the $^1$H spectrum from a thick walled capillary (so as to move the coil further away from the sample) where the linewidth is reduced and no splitting is observed. At this distance from the coil inside the sample the field perturbation simulations show a constant shift in the field strength rather than the rapidly fluctuation field (across the length of the coil) observed at the shorter distances.

The difference between the experimental data and the simulated field perturbation data is most likely due to inaccuracies in the modelling of the geometry, as the sample is not contained in an infinite cylinder but a tapered capillary with epoxy resin at each end. The sample is also unlikely to be perfectly aligned with the field, which is the assumption in the simulation. Finally the other components, such as the transmitter coil, the probe shaft, the gradient set or the dissolution pipes, which all occupy space in the bore of the magnet are not taken into account. The effect of these can be somewhat quantified by considering that a standard Bruker probe, with a 5 mm NMR tube will give a linewidth in the un-shimmed magnet of 650-850 Hz (depending on the volume of sample).

Given the magnitude of the field variations over such a small sample volume it is not conceivable that a standard shim system is capable of reducing the inhomogeneity. It is also unclear as to weather a susceptibility matching substance will improve the linewidth in this case. Fluorinert and susceptibility matching plugs have been employed to match the sample to the surroundings and reduce field variation (249), although this adds a further level of complexity to the probe head design.

Similar effects are observed for $^{13}$C NMR of similar sample size. The number of scans increases significantly as the sensitivity of the $^{13}$C is lower than that of protons coupled with there being fewer spins in the region of the detection (sodium acetate solution is 4 M where as hydrogen in water is 110 M).

It is unusual for a planar coil to be used to detect such low gamma nuclei (as shown by Table 7.1), This demonstrates how the novel flexible coil is highly versatile thanks to its favourable electrical properties.

The NMR signal presented is drastically different for spectra collected via a separate transmitter to spectra collected when using the coil for both transmit and receive. This is most likely due to the polyimide substrate and the difference in the $B_1$ homogeneity between the two set-ups. The high powers used in the transmitter coil mean that it is easy to excite the entire spectral width, whereas such powers would potentially destroy the micro coil.

## 7.9 Conclusion

A novel fabrication process has been used to realise a flexible micro coil array, consisting of two receiver coils and one transmitter coil. The devices have been shown to function well at multiple NMR frequencies and are unusual in the fact that they can be used to detect nL size samples of $13$C labelled molecules. Signal has been detected in a single acquisition for protons at 9.4 T with a SNR of 50 and also detected from spin labelled $^{13}$C using multiple averages. The need for averaging would be negated by the signal enhancement achieved with dissolution DNP.

The devices are a significant step towards the realisation of a micro imaging system suitable for imaging hyper-polarised small molecules moving across membranes of small objects such as oocyte cells.

# Chapter 8

# Outlook and Further Work

It is hoped that the use of hyper-polarised molecules may be able to remove the need for Green Fluorescing Proteins that are commonly used in the study of molecular transportation in biological systems (1).

With the aim of micro imaging of metabolic processes and uptake of molecules through transporter pathways in mind, it has been important to be able to characterise possible metabolites and small, biologically relevant molecules in terms of their DNP enhancement and $T_1$. Given a favourable $T_1$ relaxation time, it is thought that a hyper-polarised small molecule could be used to observe biological process. The removal of the necessity for GFP's means that any observed transportation becomes a true representation of the biological process.

Experiments on glucose, pyruvic acid, sodium acetate and aspartic acid were presented in chapter 4 and it was shown that it is possible to capture hyper-polarised $^{13}$C signal of fast relaxing molecules with the use of the dual iso-centre magnet DNP system. These experiments also demonstrated that deuterated glucose, sodium acetate and pyruvic acid all display ideal hyper-polarisation characteristics for imaging experiments. The experiments carried out on aspartic acid was used to determine the limit of detection for a single experiment, which was found to be $1.3 \times 10^{12}$ spins to achieve an SNR of 3 for the enhancement achieved. The workings of the dual iso-centre magnet system and discussion as to why the achieved enhancement is less than that stated in other literature sources was also given.

In order to decide upon an appropriate receiver array geometry for micro-imaging of hyper-polarised $^3$C signal with SENSE, simulations were carried out and presented in chapter 5. These showed that the optimum coil configuration, when using two receiver coils, is to place them orthogonally about the FOV. This was determined by analysis of the geometry factor maps produced from the reconstruction. The results from the simulations where used in chapter 6 in order to build a fully functioning orthogonal 2 coil micro-imaging array. The results show that an in plane resolution of 32 $\mu$m can

be achieved with a single scan on both coils. Field maps show that the sensitivity of the coils is significantly improved on what is possible when using a volume resonator. Finally SENSE reconstruction shows that it is possible to under-sample micro-scale images and achieve an artefact free reconstruction.

In order to efficiently detect signal from even smaller samples it was proven that smaller coils are required. The process of designing and fabricating the novel, flexible micro-coils is presented in chapter 7. The coils are built on a susceptibility matched substrate in order to improve upon the experiments carried out with commercially available coils. The novel design removes the need for a bonding wire, which allows the coils to be placed close to the sample. the flexible substrate not only matches the susceptibility, but also allows the coils to be positioned around the topology of any given sample, which improves the filling factor. Experiments on $^1$H with both commercial and home built coils show the advantages in terms of SNR and linewidth. Finally experiments carried out on $^{13}$C demonstrate the favourable electrical properties of the coil and show their suitability for combination with D-DNP and imaging.

## 8.1   Future work

In order to develop the system further is necessary to conduct field maps for the receiver coils (carried out at proton frequencies), this way it is possible to calculate the exact working volume and form an estimate on the limit of detection. From this it is possible to calculate the level of polarisation enhancement required to achieve a reasonable SNR for a given FOV and resolution.

NMR spectroscopy experiments on collections of oocytes expressed with the necessary transporters need to be conducted to determine that the process is measurable. After which imaging experiments can then be devised and carried out.

It may also be useful to tune the flexible micro-coils to other low gamma frequencies as they are highly versatile and would allow detection of low concentrations or small samples of nuclei such as nitrogen, fluorine or xenon.

Improvement to the DNP set-up itself, such as assessing the affect of the shuttling on the spin system and incorporating a solid state coil for cross polarisation into the dissolution cup may help to improve the achievable liquid state enhancement and reduce the polarisation time. More experiments need to be carried out to determine how the microwave power affects the heating of the sample and whether the system would benefit from a microwave cavity.

# Bibliography

[1] P. Casey, D. P. McIntosh, A. M. Dvorak, J. Liu, and P. Oh, "Protein lipidation in cell signaling," *Science*, vol. 268, pp. 221–225, 1995.

[2] S. Bowen and C. Hilty, "Rapid sample injection for hyperpolarized NMR spectroscopy," *Physical Chemistry Chemical Physics*, vol. 12, no. 22, p. 5766, 2010.

[3] A. Gaunt, R. Morris, and M. Newton, "Magnetic Resonance Imaging: A Tool for Pork Pie Development," *Foods*, vol. 2, no. 3, pp. 393–400, 2013.

[4] M. Blaimer, F. Breuer, M. Mueller, R. M. Heidemann, M. a. Griswold, and P. M. Jakob, "Smash, Sense, Pils, Grappa," *Topics in Magnetic Resonance Imaging*, vol. 15, pp. 223–236, 2004.

[5] J. V. Frangioni, "New technologies for human cancer imaging," 2008.

[6] A. W. Overhauser, "Polarization of nuclei in metals," *Physical Review*, vol. 92, no. 2, pp. 411–415, 1953.

[7] J. H. Ardenkjaer-Larsen, B. Fridlund, A. Gram, G. Hansson, L. Hansson, M. H. Lerche, R. Servin, M. Thaning, and K. Golman, "Increase in signal-to-noise ratio of $> 10,000$ times in liquid-state NMR," *Proceedings of the National Academy of Sciences*, vol. 100, no. 18, pp. 10158–10163, 2003.

[8] J. Leggett, R. Hunter, J. Granwehr, R. Panek, A. J. Perez-Linde, A. J. Horsewill, J. McMaster, G. Smith, and W. Köckenberger, "A dedicated spectrometer for dissolution DNP NMR spectroscopy," *Physical Chemistry Chemical Physics*, vol. 12, no. 22, p. 5883, 2010.

[9] D. I. Hoult, "The Principle of Reciprocity," 2011.

[10] K. P. Pruessmann, M. Weiger, and P. Boesiger, "Sensitivity-Encoded MRI," no. November, pp. 10–16, 2000.

[11] W. Gerlach and O. Stern, "Das magnetische Moment des Silberatoms," *Zeitschrift Physik*, vol. 9, pp. 353–355, 1922.

[12] M. H. Levitt, "Spin dynamics : basics of nuclear magnetic resonance," 2012.

[13] P. ZEEMAN and P., "The Effect of Magnetisation on the Nature of Light Emitted by a Substance," *Nature*, vol. 55, pp. 347–347, 1897.

[14] P. T. Callaghan, *Principles of nuclear magnetic resonance microscopy*. Clarendon Press, 1993.

[15] A. Abragam, *Principles of Nuclear Magnetism. International Series of Monographs on Physics 32*. Oxford University Press, 1961.

[16] A. Karabanov, I. Kuprov, G. T. P. Charnock, A. van der Drift, L. J. Edwards, and W. Kockenberger, "On the accuracy of the state space restriction approximation for spin dynamics simulations," *The Journal of Chemical Physics*, vol. 135, p. 084106, 2011.

[17] D. Hoult and R. Richards, "The signal-to-noise ratio of the nuclear magnetic resonance experiment," *Journal of Magnetic Resonance (1969)*, vol. 24, pp. 71–85, 1976.

[18] D. Hoult and P. C. Lauterbur, "The sensitivity of the zeugmatographic experiment involving human samples," *Journal of Magnetic Resonance (1969)*, vol. 34, pp. 425–433, 1979.

[19] L. Ciobanu, D. Seeber, and C. Pennington, "3D MR microscopy with resolution by by," *Journal of Magnetic Resonance*, vol. 158, pp. 178–182, 2002.

[20] N. Zettili, "Quantum Mechanics Concepts and Applications Second Edition Library of Congress Cataloging-in-Publication Data," 2009.

[21] H. C. Torrey, "Bloch Equations with Diffusion Terms," *Physical Review*, vol. 104, pp. 563–565, 1956.

[22] D. I. Hoult and N. S. Ginsberg, "The quantum origins of the free induction decay signal and spin noise.," *Journal of magnetic resonance (San Diego, Calif. : 1997)*, vol. 148, no. 1, pp. 182–99, 2001.

[23] J. W. Cooley and J. W. Tukey, "An Algorithm for the Machine Calculation of Complex Fourier Series," *Mathematics of Computation*, vol. 19, 1965.

[24] H. Black, "Modulation theory. Bell Telephone Laboratories series," 1953.

[25] P. Callaghan and C. Eccles, "Sensitivity and resolution in NMR imaging," *Journal of Magnetic Resonance (1969)*, vol. 71, pp. 426–445, 1987.

[26] E. L. Hahn, "Spin Echoes," *Physical Review*, vol. 80, 1950.

[27] H. Y. Carr and E. M. Purcell, "Effects of Diffusion on Free Precession in Nuclear Magnetic Resonance Experiments," *Physical Review*, vol. 94, pp. 630–638, 1954.

[28] R. Freeman, *Handbook of nuclear magnetic resonance.* John Wiley and Sons,New York, NY, 1987.

[29] S. Meiboom and D. Gill, "Modified Spin-Echo Method for Measuring Nuclear Relaxation Times," *Review of Scientific Instruments*, vol. 29, pp. 688–691, 1958.

[30] P. Lauterbur, "Image formation by induced local interactions: examples employing nuclear magnetic resonance," 1973.

[31] P. Mansfield and P. Grannell, "NMR'diffraction'in solids," *Journal of Physics C: solid state*, 1973.

[32] A. Garroway, P. Grannell, and P. Mansfield, "Image formation in NMR by a selective irradiative process," *Journal of Physics C: Solid*, 1974.

[33] P. Mansfield and P. K. Grannell, ""Diffraction" and microscopy in solids and liquids by NMR," *Physical Review B*, vol. 12, pp. 3618–3634, 1975.

[34] P. Mansfield and A. Maudsley, "Medical imaging by NMR," *The British journal of radiology*, 1977.

[35] A. Haase, J. Frahm, D. Matthaei, W. Hänicke, and K.-D. Merboldt, "Flash imaging: Rapid nmr imaging using low flip-angle pulses," *Journal of Magnetic Resonance*, vol. 213, no. 2, pp. 533 – 541, 1986.

[36] A. Haase, "Snapshot flash mri. applications to t1, t2, and chemical-shift imaging," *Magnetic Resonance in Medicine*, vol. 13, pp. 77–89, 1990.

[37] P. Mansfield, "Multi-planar image formation using NMR spin echoes," *Journal of Physics C: Solid State Physics*, vol. 10, pp. L55–L58, 1977.

[38] J. Hennig, A. Nauerth, and H. Friedburg, "RARE imaging: A fast imaging method for clinical MR," *Magnetic Resonance in Medicine*, vol. 3, pp. 823–833, 1986.

[39] L. Ciobanu and C. Pennington, "3D micron-scale MRI of single biological cells," *Solid State Nuclear Magnetic Resonance*, vol. 25, pp. 138–141, 2004.

[40] S.-C. Lee, K. Kim, J. Kim, S. Lee, J. Han Yi, S. Woo Kim, K.-S. Ha, and C. Cheong, "One Micrometer Resolution NMR Microscopy," *Journal of Magnetic Resonance*, vol. 150, pp. 207–213, 2001.

[41] S. Lovesey, "Electricity and Magnetism, Volume 1: Third Edition, Electricity and Magnetism, Volume 2: Third Edition, by B.I. Bleaney and B. Bleaney," *Contemporary Physics*, vol. 55, pp. 141–142, 2014.

[42] P. Callaghan, L. Forde, and C. Rofe, "Correlated susceptibility and diffusion effects in NMR microscopy using both phase-frequency encoding and phase-phase encoding," *Journal of Magnetic Resonance, Series*, 1994.

[43] J. Hrabe, G. Kaur, and D. N. Guilfoyle, "Principles and limitations of NMR diffusion measurements.," *Journal of medical physics*, vol. 32, pp. 34–42, 2007.

[44] E. O. Stejskal and J. E. Tanner, "Spin Diffusion Measurements: Spin Echoes in the Presence of a Time-Dependent Field Gradient," *The Journal of Chemical Physics*, vol. 42, pp. 288–292, 1965.

[45] N. J. Rogers, F. Hill-Casey, K. F. Stupic, J. S. Six, C. Lesbats, S. P. Rigby, J. Fraissard, G. E. Pavlovskaya, and T. Meersmann, "Molecular hydrogen and catalytic combustion in the production of hyperpolarized 83Kr and 129Xe MRI contrast agents.," *Proceedings of the National Academy of Sciences of the United States of America*, vol. 113, pp. 3164–8, 2016.

[46] S. Appelt, A. B.-A. Baranga, C. J. Erickson, M. V. Romalis, A. R. Young, and W. Happer, "Theory of spin-exchange optical pumping of 3 He and 129 Xe," *Physical Review A*, vol. 58, pp. 1412–1439, 1998.

[47] A.-m. Vapors, *Spin-Exchange Optical Pumping with alkali-metal vapours*. PhD thesis, UNIVERSITY OF WISCONSIN-MADISON, 2005.

[48] M. L. Hirsch, N. Kalechofsky, A. Belzer, M. Rosay, and J. G. Kempf, "Brute-Force Hyperpolarization for NMR and MRI," *Journal of the American Chemical Society*, vol. 137, pp. 8428–8434, 2015.

[49] X. Ji, A. Bornet, B. Vuichoud, J. Milani, D. Gajan, A. J. Rossini, L. Emsley, G. Bodenhausen, and S. Jannin, "Transportable hyperpolarized metabolites.," *Nature communications*, vol. 8, p. 13975, 2017.

[50] D. G. Gadian, K. S. Panesar, A. J. Perez Linde, A. J. Horsewill, W. Kockenberger, J. R. Owers Bradley, G. G. Green, I. G. Khazal, J. Lopez-Serrano, and D. C. Williamson, "Preparation of highly polarized nuclear spin systems using brute-force and low-field thermal mixing," *Physical Chemistry Chemical Physics*, vol. 14, p. 5397, 2012.

[51] D. T. Peat, M. L. Hirsch, D. G. Gadian, A. J. Horsewill, J. R. Owers-Bradley, J. G. Kempf, K. Vandoorne, K. Nicolay, K. M. Brindle, I. Park, G. Reed, L. Carvajal, E. J. Small, P. Munster, V. K. Weinberg, J. H. Ardenkjaer-Larsen, A. P. Chen, R. E. Hurd, L. I. Odegardstuen, F. J. Robb, J. Tropp, and J. A. Murray *Phys. Chem. Chem. Phys.*, vol. 18, pp. 19173–19182, 2016.

[52] F. Jahnig, G. Kwiatkowski, and M. Ernst, "Conceptual and instrumental progress in dissolution DNP," *Journal of Magnetic Resonance*, vol. 264, pp. 22–29, 2016.

[53] Chan-Gyu Joo., Kan-Nian Hu., Jeffrey A. Bryant., and Robert G. Griffin*, "In Situ Temperature Jump High-Frequency Dynamic Nuclear Polarization Experiments: Enhanced Sensitivity in Liquid-State NMR Spectroscopy," 2006.

[54] D. Ferguson and J. Haw, "Transient methods for in situ NMR of reactions on solid catalysts using temperature jumps," *Analytical Chemistry*, 1995.

[55] M. Sharma, G. Janssen, J. Leggett, A. Kentgens, and P. van Bentum, "Rapid-melt Dynamic Nuclear Polarization," *Journal of Magnetic Resonance*, vol. 258, pp. 40–48, 2015.

[56] P. van Bentum, M. Sharma, S. van Meerten, and A. Kentgens, "Solid Effect DNP in a Rapid-melt setup," *Journal of Magnetic Resonance*, vol. 263, pp. 126–135, 2016.

[57] D. Yoon, M. Soundararajan, C. Caspers, F. Braunmueller, J. Genoud, S. Alberti, and J.-P. Ansermet, "500-fold enhancement of in situ 13 C liquid state NMR using gyrotron-driven temperature jump DNP," *Journal of Magnetic Resonance*, vol. 270, pp. 142–146, 2016.

[58] A. Macor, E. de Rijk, G. Annino, S. Alberti, and J. Ansermet, "THz-waves channeling in a monolithic saddle-coil for Dynamic Nuclear Polarization enhanced NMR," *Journal of Magnetic Resonance*, vol. 212, pp. 440–449, 2011.

[59] A. Comment, "Dissolution DNP for in vivo preclinical studies," *Journal of Magnetic Resonance*, vol. 264, pp. 39–48, 2016.

[60] J. H. Ardenkjaer-Larsen, "On the present and future of dissolution-DNP," *Journal of Magnetic Resonance*, vol. 264, pp. 3–12, 2016.

[61] T. Harris, G. Eliyahu, L. Frydman, and H. Degani, "Kinetics of hyperpolarized 13c1-pyruvate transport and metabolism in living human breast cancer cells," *Proceedings of the National Academy of Sciences*, vol. 106, no. 43, pp. 18131–18136, 2009.

[62] C. Hilty and S. Bowen, "Applications of dynamic nuclear polarization to the study of reactions and reagents in organic and biomolecular chemistry," *Organic & biomolecular chemistry*, vol. 8, no. 15, pp. 3361–3365, 2010.

[63] S. Bowen and C. Hilty, "Time-resolved dynamic nuclear polarization enhanced nmr spectroscopy," *Angewandte Chemie*, vol. 120, no. 28, pp. 5313–5315, 2008.

[64] F. A. Gallagher, M. I. Kettunen, S. E. Day, D.-E. Hu, J. H. Ardenkjær-Larsen, P. R. Jensen, M. Karlsson, K. Golman, M. H. Lerche, K. M. Brindle, *et al.*, "Magnetic resonance imaging of ph in vivo using hyperpolarized 13 c-labelled bicarbonate," *Nature*, vol. 453, no. 7197, p. 940, 2008.

[65] F. A. Gallagher, S. E. Bohndiek, M. I. Kettunen, D. Y. Lewis, D. Soloviev, and K. M. Brindle, "Hyperpolarized 13c mri and pet: in vivo tumor biochemistry," *Journal of Nuclear Medicine*, vol. 52, no. 9, pp. 1333–1336, 2011.

[66] S. J. Nelson, J. Kurhanewicz, D. B. Vigneron, P. E. Larson, A. L. Harzstark, M. Ferrone, M. van Criekinge, J. W. Chang, R. Bok, I. Park, *et al.*, "Metabolic imaging of patients with prostate cancer using hyperpolarized [1-13c] pyruvate," *Science translational medicine*, vol. 5, no. 198, pp. 198ra108–198ra108, 2013.

[67] T. B. Rodrigues, E. M. Serrao, B. W. Kennedy, D.-E. Hu, M. I. Kettunen, and K. M. Brindle, "Magnetic resonance imaging of tumor glycolysis using hyperpolarized 13 c-labeled glucose," *Nature medicine*, vol. 20, no. 1, p. 93, 2014.

[68] C. H. Cunningham, J. Y. Lau, A. P. Chen, B. J. Geraghty, W. J. Perks, I. Roifman, G. A. Wright, and K. A. Connelly, "Hyperpolarized 13c metabolic mri of the human heartnovelty and significance: Initial experience," *Circulation research*, vol. 119, no. 11, pp. 1177–1182, 2016.

[69] J. Leggett, R. Hunter, J. Granwehr, R. Panek, A. J. Perez-Linde, A. J. Horsewill, J. McMaster, G. Smith, W. Kockenberger, F. Engelke, C. Griesinger, K. Golman, and J. H. Ardenkjaer Larson, "A dedicated spectrometer for dissolution DNP NMR spectroscopy," *Physical Chemistry Chemical Physics*, p. 5883, 2010.

[70] T. R. Carver and C. P. Slichter, "Experimental Verification of the Overhauser Nuclear Polarization Effect," *Physical Review*, vol. 102, pp. 975–980, 1956.

[71] A. Abragam and M. Goldman, "Principals of dynamic nuclear polarisatoin," *Rep. Prog. Phys*, vol. 41, 1978.

[72] T. V. Can, M. A. Caporini, F. Mentink-Vigier, B. Corzilius, J. J. Walish, M. Rosay, W. E. Maas, M. Baldus, S. Vega, T. M. Swager, and R. G. Griffin, "Overhauser effects in insulating solids," *The Journal of Chemical Physics*, vol. 141, p. 064202, 2014.

[73] N. JH and R. Schirmer, "The Nuclear Overhauser Effect-Chemical Applications," *Ac-ademic Press, New York*, 1971.

[74] T. Prisner, V. Denysenkov, and D. Sezer, "Liquid state DNP at high magnetic fields: Instrumentation, experimental results and atomistic modelling by molecular dynamics simulations," *Journal of Magnetic Resonance*, vol. 264, pp. 68–77, 2016.

[75] M. D. Lingwood, T. A. Siaw, N. Sailasuta, B. D. Ross, P. Bhattacharya, and S. Han, "Continuous flow Overhauser dynamic nuclear polarization of water in the fringe field of a clinical magnetic resonance imaging system for authentic image contrast.," *Journal of magnetic resonance (San Diego, Calif. : 1997)*, vol. 205, pp. 247–54, 2010.

[76] A. A. Smith, B. Corzilius, A. B. Barnes, T. Maly, and R. G. Griffin, "Solid effect dynamic nuclear polarization and polarization pathways," *The Journal of Chemical Physics*, vol. 136, p. 015101, 2012.

[77] W. T. Wenckebach, "The Solid Effect," *Applied Magnetic Resonance*, vol. 34, pp. 227–235, 2008.

[78] Y. Hovav, A. Feintuch, and S. Vega, "Theoretical aspects of dynamic nuclear polarization in the solid state – The solid effect," *Journal of Magnetic Resonance*, vol. 207, pp. 176–189, 2010.

[79] T. Maly, G. T. Debelouchina, V. S. Bajaj, K. Hu, C. Joo, M. L. MakJurkauskas, J. R. Sirigiri, P. C. A. van der Wel, J. Herzfeld, R. J. Temkin, and R. G. Griffin, "Dynamic nuclear polarization at high magnetic fields," *The Journal of Chemical Physics*, vol. 128, p. 052211, 2008.

[80] A. B. Barnes, G. De Paepe, P. C. A. van der Wel, K. Hu, C. Joo, V. S. Bajaj, M. L. MakJurkauskas, J. R. Sirigiri, J. Herzfeld, R. J. Temkin, and R. G. Griffin, "High-Field Dynamic Nuclear Polarization for Solid and Solution Biological NMR," *Applied Magnetic Resonance*, vol. 34, pp. 237–263, 2008.

[81] A. Karabanov, A. van der Drift, L. J. Edwards, I. Kuprov, and W. Kockenberger, "Quantum mechanical simulation of solid effect dynamic nuclear polarisation using Krylov–Bogolyubov time averaging and a restricted state-space," *Physical Chemistry Chemical Physics*, vol. 14, p. 2658, 2012.

[82] Y. Hovav, A. Feintuch, and S. Vega, "Dynamic nuclear polarization assisted spin diffusion for the solid effect case," *The Journal of Chemical Physics*, vol. 134, p. 074509, 2011.

[83] G. J. Gerfen, L. R. Becerra, D. A. Hall, R. G. Griffin, R. J. Temkin, and D. J. Singel, "High frequency (140 GHz) dynamic nuclear polarization: Polarization transfer to a solute in frozen aqueous solution," *The Journal of Chemical Physics*, vol. 102, pp. 9494–9497, 1995.

[84] S. Bowen, "Multi-Field Cryogen Free Dissolution-DNP at 3.35, 6.70, and 10.05 T," 2017.

[85] K. W. Lipso, S. Bowen, O. Rybalko, and J. H. Ardenkjaer Larsen, "Large dose hyperpolarized water with dissolution-DNP at high magnetic field," *Journal of Magnetic Resonance*, vol. 274, pp. 65–72, 2017.

[86] K.-N. Hu, C. Song, H.-h. Yu, T. M. Swager, and R. G. Griffin, "High-frequency dynamic nuclear polarization using biradicals: A multifrequency EPR lineshape analysis," *The Journal of Chemical Physics*, vol. 128, p. 052302, 2008.

[87] B. Corzilius, "Theory of solid effect and cross effect dynamic nuclear polarization with half-integer high-spin metal polarizing agents in rotating solids," *Phys. Chem. Chem. Phys.*, vol. 18, pp. 27190–27204, 2016.

[88] V. Atsarkin, "Dynamic nuclear polarization: Yesterday, today, and tomorrow," in *Journal of Physics: Conference Series*, vol. 324, p. 012003, IOP Publishing, 2011.

[89] K. R. Thurber and R. Tycko, "Theory for cross effect dynamic nuclear polarization under magic-angle spinning in solid state nuclear magnetic resonance: The importance of level crossings," *The Journal of Chemical Physics*, vol. 137, p. 084508, 2012.

[90] Y. Hovav, A. Feintuch, and S. Vega, "Theoretical aspects of dynamic nuclear polarization in the solid state – The cross effect," *Journal of Magnetic Resonance*, vol. 214, pp. 29–41, 2012.

[91] A. Karabanov, G. Kwiatkowski, and W. Kockenberger, "Quantum Mechanical Simulation of Cross Effect DNP Using Krylov–Bogolyubov Averaging," *Applied Magnetic Resonance*, vol. 43, pp. 43–58, 2012.

[92] D. Shimon, Y. Hovav, A. Feintuch, D. Goldfarb, and S. Vega, "Dynamic nuclear polarization in the solid state: a transition between the cross effect and the solid effect," *Physical Chemistry Chemical Physics*, vol. 14, p. 5729, 2012.

[93] V. K. Michaelis, T.-C. Ong, M. K. Kiesewetter, D. K. Frantz, J. J. Walish, E. Ravera, C. Luchinat, T. M. Swager, and R. G. Griffin, "Topical Developments in High-Field Dynamic Nuclear Polarization," *Israel Journal of Chemistry*, vol. 54, pp. 207–221, 2014.

[94] Y. Hovav, D. Shimon, I. Kaminker, A. Feintuch, D. Goldfarb, S. Vega, W. E. Maas, M. Baldus, S. Vega, T. M. Swager, and R. G. Griffin, "Effects of the electron polarization on dynamic nuclear polarization in solids," *Phys. Chem. Chem. Phys.*, vol. 17, pp. 6053–6065, 2015.

[95] W. Wenckebach, "Dynamic nuclear polarization via thermal mixing: Beyond the high temperature approximation," *Journal of Magnetic Resonance*, vol. 277, pp. 68–78, 2017.

[96] A. Karabanov, G. Kwiatkowski, C. U. Perotto, D. Wiśniewski, J. McMaster, I. Lesanovsky, and W. Kockenberger, "Dynamic nuclear polarisation by thermal mixing: quantum theory and macroscopic simulations," *Phys. Chem. Chem. Phys.*, vol. 18, pp. 30093–30104, 2016.

[97] V. A. Atsarkin, "Dynamic polarization of nuclei in solid dielectrics," *Soviet Physics Uspekhi*, vol. 21, pp. 725–745, 1978.

[98] Y. Hovav, A. Feintuch, and S. Vega, "Theoretical aspects of dynamic nuclear polarization in the solid state – spin temperature and thermal mixing," *Phys. Chem. Chem. Phys.*, vol. 15, pp. 188–203, 2013.

[99] M. Borghini, W. de Boer, and K. Morimoto, "Nuclear dynamic polarization by resolved solid-state effect and thermal mixing with an electron spin-spin interaction reservoir," *Physics Letters A*, vol. 48, pp. 244–246, 1974.

[100] A. A. Schweiger and G. Jeschke, "Principles of pulse electron paramagnetic resonance," p. 578, 2001.

[101] L. Lumata, Z. Kovacs, A. D. Sherry, C. Malloy, S. Hill, J. van Tol, L. Yu, L. Song, and M. E. Merritt, "Electron spin resonance studies of trityl OX063 at a concentration optimal for DNP," *Physical Chemistry Chemical Physics*, vol. 15, p. 9800, 2013.

[102] O. Haze, B. Corzilius, A. A. Smith, R. G. Griffin, and T. M. Swager, "Water Soluble Narrow Line Radicals for Dynamic Nuclear Polarization," *Journal of the American Chemical Society*, vol. 134, pp. 14287–14290, 2012.

[103] D. Banerjee, D. Shimon, A. Feintuch, S. Vega, and D. Goldfarb, "The interplay between the solid effect and the cross effect mechanisms in solid state 13C DNP at 95GHz using trityl radicals," *Journal of Magnetic Resonance*, vol. 230, 2013.

[104] W. E. Blumberg, "Nuclear Spin-Lattice Relaxation Caused by Paramagnetic Impurities," *Physical Review*, vol. 119, pp. 79–84, 1960.

[105] I. J. Lowe and D. Tse, "Nuclear Spin Lattice Relaxation via Paramagnetic Centers," *Physical Review*, vol. 166, pp. 279–291, 1968.

[106] J. H. Ardenkjaer-Larsen, C. Laustsen, S. Bowen, and R. Rizi, "Hyperpolarized H2O MR angiography," *Magnetic Resonance in Medicine*, vol. 71, no. 1, pp. 50–56, 2014.

[107] M. Hauge, J. Henrik, A. Capozzi, A. Coi, M. Karlsson, M. H. Lerche, and J. Ardenkjaer-Larsen, "Preparation of Radical-Free Hyperpolarized Water using Photo-induced non-persistent Radicals on a " SpinLab-like " dissolution-DNP Polarizer Preparation of Radical-Free Hyperpolarized Water using Photo-induced non-persistent Radicals on a "," 2017.

[108] A. Capozzi, J. N. Hyacinthe, T. Cheng, T. R. Eichhorn, G. Boero, C. Roussel, J. J. van der Klink, and A. Comment, "Photoinduced Nonpersistent Radicals as Polarizing Agents for X-Nuclei Dissolution Dynamic Nuclear Polarization," *The Journal of Physical Chemistry C*, pp. 22632–22639, 2015.

[109] A. Capozzi, T. Cheng, G. Boero, C. Roussel, and A. Comment, "Thermal annihilation of photo-induced radicals following dynamic nuclear polarization to produce transportable frozen hyperpolarized (13)C-substrates.," *Nature communications*, 2017.

[110] R. Carrascosa, A. Martini, M. Ponzio, J. Busso, A. Ponce, and J. Lacuara, "Storage of Chinchilla lanigera Semen at 4°C for 24 or 72 h with Two Different Cryoprotectants," *Cryobiology*, vol. 42, pp. 301–306, 2001.

[111] A. Kiswandhi, B. Lama, P. Niedbalski, M. Goderya, J. Long, and L. Lumata, "The effect of glassing solvent deuteration and Gd $^{3+}$ doping on $^{13}$C DNP at 5 T," *RSC Adv.*, vol. 6, pp. 38855–38860, 2016.

[112] A. Kiswandhi, P. Niedbalski, C. Parish, P. Kaur, A. Martins, L. Fidelino, C. Khemtong, L. Song, A. D. Sherry, and L. Lumata, "Impact of Ho 3+ -doping on 13 C dynamic nuclear polarization using trityl OX063 free radical," *Phys. Chem. Chem. Phys.*, vol. 41, no. 31, p. 395, 2016.

[113] B. Lama, J. H. P. Collins, D. Downes, A. N. Smith, and J. R. Long, "Expeditious dissolution dynamic nuclear polarization without glassing agents," *NMR in Biomedicine*, vol. 29, pp. 226–231, 2016.

[114] B. P. Mcgeorge and H. Msci, "Novel Acquisition Strategies for Dissolution Dynamic Nuclear Polarisation," 2017.

[115] J. Wolber, F. Ellner, B. Fridlund, A. Gram, H. Jóhannesson, G. Hansson, L. Hansson, M. Lerche, S. Månsson, R. Servin, M. Thaning, K. Golman, and J. Ardenkjær-Larsen, "Generating highly polarized nuclear spins in solution using dynamic nuclear polarization," *Nuclear Instruments and Methods in Physics Research Section A: Accelerators, Spectrometers, Detectors and Associated Equipment*, vol. 526, no. 1, pp. 173–181, 2004.

[116] J. Granwehr, R. Panek, J. Leggett, and W. Köckenberger, "Quantifying the transfer and settling in NMR experiments with sample shuttling," *The Journal of Chemical Physics*, vol. 132, p. 244507, 2010.

[117] N. Chattergoon, F. Martínez-Santiesteban, W. B. Handler, J. H. Ardenkjaer-Larsen, and T. J. Scholl, "Field dependence of $T_1$ for hyperpolarized [1-$^{13}$C]pyruvate," *Contrast Media & Molecular Imaging*, vol. 8, pp. 57–62, 2013.

[118] K. Ingvorsen, A. J. Zehnder, and B. B. Jørgensen, "Kinetics of Sulfate and Acetate Uptake by Desulfobacter postgatei.," *Applied and environmental microbiology*, vol. 47, pp. 403–8, 1984.

[119] R. L. Veech and W. L. Gitomer, "The medical and metabolic consequences of administration of sodium acetate.," *Advances in enzyme regulation*, vol. 27, pp. 313–43, 1988.

[120] H. F. Bunn, K. H. Gabbay, and P. M. Gallop, "The glycosylation of hemoglobin: relevance to diabetes mellitus.," *Science (New York, N.Y.)*, vol. 200, pp. 21–7, 1978.

[121] A. Varki, *Essentials of glycobiology*. Cold Spring Harbor Laboratory Press, 2009.

[122] A. Maier, B. Völker, E. Boles, and G. F. Fuhrmann, "Characterisation of glucose transport in Saccharomyces cerevisiae with plasma membrane vesicles (countertransport) and intact cells (initial uptake) with single Hxt1, Hxt2, Hxt3, Hxt4, Hxt6, Hxt7 or Gal2 transporters," *FEMS Yeast Research*, vol. 2, pp. 539–550, 2002.

[123] G. W. Gould, H. M. Thomas, T. J. Jess, and G. I. Bell, "Expression of human glucose transporters in Xenopus oocytes: kinetic characterization and substrate specificities of the erythrocyte, liver, and brain isoforms," *Biochemistry*, vol. 30, pp. 5139–5145, 1991.

[124] S. Jeong, R. Eskandari, S. M. Park, J. Alvarez, S. S. Tee, R. Weissleder, M. G. Kharas, H. Lee, and K. R. Keshari, "Real-time quantitative analysis of metabolic flux in live cells using a hyperpolarized micromagnetic resonance spectrometer," *Science Advances*, vol. 3, p. e1700341, 2017.

[125] K. M. Brindle, "Imaging Metabolism with Hyperpolarized 13C-Labeled Cell Substrates," *Journal of the American Chemical Society*, vol. 137, pp. 6418–6427, 2015.

[126] R. Schmidt, C. Laustsen, J.-N. Dumez, M. I. Kettunen, E. M. Serrao, I. Marco-Rius, K. M. Brindle, J. H. Ardenkjaer-Larsen, and L. Frydman, "In vivo single-shot 13C spectroscopic imaging of hyperpolarized metabolites by spatiotemporal encoding," *Journal of Magnetic Resonance*, vol. 240, no. 240, pp. 8–15, 2014.

[127] I. Marco-Rius, M. C. D. Tayler, M. I. Kettunen, T. J. Larkin, K. N. Timm, E. M. Serrao, T. B. Rodrigues, G. Pileio, J. H. Ardenkjaer-Larsen, M. H. Levitt, and K. M. Brindle, "Hyperpolarized singlet lifetimes of pyruvate in human blood and in the mouse," *NMR in Biomedicine*, vol. 26, pp. 1696–1704, 2013.

[128] S. J. Nelson, Et Al., and J. Tropp, "Proof of Concept Clinical Trial of Hyperpolarized C-13 Pyruvate in Patients with Prostate Cancer," *Proceedings International Society for Magnetic Resonance in Medicine*, vol. 20, p. Abstract 0274, 2012.

[129] M. Federspiel, K. Stahr, A. Hansen, L. HÃ¸jgaard, and A. KjÃ¦r, *The Journal of nuclear medicine : JNM.*, vol. 57. Society of Nuclear Medicine, 2016.

[130] S. Broer, H. P. Schneider, A. Bröer, B. Rahman, B. Hamprecht, and J. W. Deitmer, "Characterization of the monocarboxylate transporter 1 expressed in Xenopus laevis oocytes by changes in cytosolic pH.," *The Biochemical journal*, vol. 333 ( Pt 1), pp. 167–74, 1998.

[131] L. Lumata, Z. Kovacs, C. Malloy, A. D. Sherry, and M. Merritt, "The effect of 13C enrichment in the glassing matrix on dynamic nuclear polarization of [1-13C]pyruvate.," *Physics in medicine and biology*, vol. 56, pp. N85–92, 2011.

[132] K. Nordengen, C. Heuser, J. E. Rinholm, R. Matalon, and V. Gundersen, "Localisation of N-acetylaspartate in oligodendrocytes/myelin," *Brain Structure and Function*, vol. 220, pp. 899–917, 2015.

[133] J. C. Chatham and S. J. Blackband, "Nuclear magnetic resonance spectroscopy and imaging in animal research.," *ILAR journal*, vol. 42, pp. 189–208, 2001.

[134] T. B. Patel and J. B. Clark, "Synthesis of N-acetyl-L-aspartate by rat brain mitochondria and its involvement in mitochondrial/cytosolic carbon transport.," *The Biochemical journal*, vol. 184, pp. 539–46, 1979.

[135] B. Ross and S. Bluml, "Magnetic resonance spectroscopy of the human brain," *The Anatomical Record*, vol. 265, pp. 54–84, 2001.

[136] S. M. Kazan, S. Reynolds, A. Kennerley, E. Wholey, J. E. Bluff, J. Berwick, V. J. Cunningham, M. N. Paley, and G. M. Tozer, "Kinetic modeling of hyperpolarized $^{13}$ C pyruvate metabolism in tumors using a measured arterial input function," *Magnetic Resonance in Medicine*, vol. 70, pp. 943–953, 2013.

[137] P. Miéville, P. Ahuja, R. Sarkar, S. Jannin, P. Vasos, S. Gerber-Lemaire, M. Mishkovsky, A. Comment, R. Gruetter, O. Ouari,

P. Tordo, and G. Bodenhausen, "Scavenging Free Radicals To Preserve Enhancement and Extend Relaxation Times in NMR using Dynamic Nuclear Polarization," *Angewandte Chemie International Edition*, vol. 49, pp. 6182–6185, 2010.

[138] M. Batel, M. Krajewski, K. Weiss, O. With, A. Däpp, A. Hunkeler, M. Gimersky, K. P. Pruessmann, P. Boesiger, B. H. Meier, S. Kozerke, and M. Ernst, "A multi-sample 94GHz dissolution dynamic-nuclear-polarization system," *Journal of Magnetic Resonance*, vol. 214, pp. 166–174, 2012.

[139] J. W. Ekin, *Experimental techniques for low-temperature measurements : cryostat design, material properties, and superconductor critical-current testing*. Oxford University Press, 2006.

[140] J. H. Ardenkjaer-Larsen, B. Fridlund, A. Gram, G. Hansson, L. Hansson, M. H. Lerche, R. Servin, M. Thaning, and K. Golman, "Increase in signal-to-noise ratio of $> 10,000$ times in liquid-state NMR.," *Proceedings of the National Academy of Sciences of the United States of America*, vol. 100, pp. 10158–63, 2003.

[141] K. P. Pruessmann, M. Weiger, M. B. Scheidegger, and P. Boesiger, "SENSE: Sensitivity encoding for fast MRI," *Magnetic Resonance in Medicine*, vol. 42, no. 5, pp. 952–962, 1999.

[142] W. Fong, "Handbook of mri pulse sequences," *Medical Physics*, vol. 32, no. 5, pp. 1452–1452, 2005.

[143] M. Lustig, D. Donoho, J. Santos, and J. Pauly, "Compressed Sensing MRI," *IEEE Signal Processing Magazine*, vol. 25, no. 2, pp. 72–82, 2008.

[144] H.-Y. Chen, P. E. Larson, J. W. Gordon, R. A. Bok, M. Ferrone, M. van Criekinge, L. Carvajal, P. Cao, J. M. Pauly, A. B. Kerr, *et al.*, "Technique development of 3d dynamic cs-epsi for hyperpolarized 13c pyruvate mr molecular imaging of human prostate cancer," *Magnetic resonance in medicine*, 2018.

[145] Y. Feng, J. W. Gordon, P. J. Shin, C. von Morze, M. Lustig, P. E. Larson, M. A. Ohliger, L. Carvajal, J. Tropp, J. M. Pauly, *et al.*, "Development and testing of hyperpolarized 13c mr calibrationless parallel imaging," *Journal of Magnetic Resonance*, vol. 262, pp. 1–7, 2016.

[146] B. P. Sutton, L. Ciobanu, X. Zhang, and A. Webb, "Parallel imaging for nmr microscopy at 14.1 tesla," *Magnetic resonance in medicine*, vol. 54, no. 1, pp. 9–13, 2005.

[147] M. A. Griswold, P. M. Jakob, M. Nittka, J. W. Goldfarb, and A. Haase, "Partially parallel imaging with localized sensitivities (PILS)," *Magnetic Resonance in Medicine*, vol. 44, no. 4, pp. 602–609, 2000.

[148] L. Ying and J. Sheng, "Joint image reconstruction and sensitivity estimation in SENSE (JSENSE).," *Magnetic resonance in medicine : official journal of the Society of Magnetic Resonance in Medicine / Society of Magnetic Resonance in Medicine*, vol. 57, no. 6, pp. 1196–202, 2007.

[149] D. S. Taubman and M. W. Marcellin, *JPEG2000 Image Compression Fundamentals, Standards and Practice*. Boston, MA: Springer US, 2002.

[150] D. Donoho, "Compressed sensing," *IEEE Transactions on Information Theory*, vol. 52, pp. 1289–1306, 2006.

[151] M. Lustig, D. Donoho, and J. M. Pauly, "Sparse MRI: The application of compressed sensing for rapid MR imaging," *Magnetic Resonance in Medicine*, vol. 58, no. 6, pp. 1182–1195, 2007.

[152] R. Otazo, D. Kim, L. Axel, and D. K. Sodickson, "Combination of compressed sensing and parallel imaging for highly accelerated first-pass cardiac perfusion MRI," *Magnetic Resonance in Medicine*, vol. 64, no. 3, pp. 767–776, 2010.

[153] E. Gong, F. Huang, K. Ying, W. Wu, S. Wang, and C. Yuan, "PROMISE: Parallel-imaging and compressed-sensing reconstruction of multicontrast imaging using SharablE information," *Magnetic Resonance in Medicine*, vol. 73, no. 2, pp. 523–535, 2015.

[154] M. Weiger, K. P. Pruessmann, and P. Boesiger, "Cardiac real-time imaging using SENSE. SENSitivity Encoding scheme.," *Magnetic resonance in medicine : official journal of the Society of Magnetic Resonance in Medicine / Society of Magnetic Resonance in Medicine*, vol. 43, pp. 177–184, 2000.

[155] M. Weiger, K. P. Pruessmann, C. Leussler, P. Röschmann, and P. Boesiger, "Specific coil design for SENSE: a six-element cardiac array.," *Magnetic resonance in medicine : official journal of the Society of Magnetic Resonance in Medicine / Society of Magnetic Resonance in Medicine*, vol. 45, no. 3, pp. 495–504, 2001.

[156] B. Madore, "UNFOLD-SENSE: A parallel MRI method with self-calibration and artifact suppression," *Magnetic Resonance in Medicine*, vol. 52, no. 2, pp. 310–320, 2004.

[157] G. Chen, L. T. Muftuler, S. H. Ha, and O. Nalcioglu, "An optimization method for designing SENSE imaging RF coil arrays.," *Journal of magnetic resonance (San Diego, Calif. : 1997)*, vol. 186, no. 2, pp. 273–81, 2007.

[158] M. Ohliger and D. Sodickson, "An introduction to coil array design for parallel MRI," *NMR in Biomedicine*, 2006.

[159] A. G. Webb, "Radiofrequency microcoils in magnetic resonance," *Progress in Nuclear Magnetic Resonance Spectroscopy*, vol. 31, no. 1, pp. 1–42, 1997.

[160] J. W. Thorpe, D. Kidd, B. E. Kendall, P. S. Tofts, G. J. Barker, A. J. Thompson, D. G. MacManus, W. I. McDonald, and D. H. Miller, "Spinal cord MRI using multi-array coils and fast spin echo: I. Technical aspects and findings in healthy adults," *Neurology*, vol. 43, pp. 2625–2625, 1993.

[161] P. B. Roemer, W. a. Edelstein, C. E. Hayes, S. P. Souza, and O. M. Mueller, "The NMR phased array.," *Magnetic resonance in medicine : official journal of the Society of Magnetic Resonance in Medicine / Society of Magnetic Resonance in Medicine*, vol. 16, pp. 192–225, 1990.

[162] A. G. Webb, "Microcoil nuclear magnetic resonance spectroscopy.," *Journal of pharmaceutical and biomedical analysis*, vol. 38, no. 5, pp. 892–903, 2005.

[163] A. G. Webb, "Radiofrequency microcoils for magnetic resonance imaging and spectroscopy.," *Journal of magnetic resonance (San Diego, Calif. : 1997)*, vol. 229, pp. 55–66, 2013.

[164] H. Nyquist, "Thermal Agitation of Electric Charge in Conductors," *Physical Review*, vol. 32, no. 1, pp. 110–113, 1928.

[165] J. Mispelter, M. Lupu, and A. Briguet, *NMR Probeheads for Biophysical and Biomedical Experiments*. IMPERIAL COLLEGE PRESS, 2015.

[166] H. Fujita, T. Zheng, X. Yang, M. J. Finnerty, and S. Handa, "RF surface receive array coils: the art of an LC circuit.," *Journal of magnetic resonance imaging : JMRI*, vol. 38, no. 1, pp. 12–25, 2013.

[167] N. Bloembergen and R. V. Pound, "Radiation Damping in Magnetic Resonance Experiments," *Physical Review*, vol. 95, no. 1, pp. 8–12, 1954.

[168] J. Kraus and K. Carver, *Electromagnetics*. McGraw-Hill electrical and electronic engineering series, 1973.

[169] R. Subramanian, M. Lam, and A. Webb, "RF Microcoil Design for Practical NMR of Mass-Limited Samples," *Journal of Magnetic Resonance*, vol. 133, no. 1, pp. 227–231, 1998.

[170] C. E. Hayes and L. Axel, "Noise performance of surface coils for magnetic resonance imaging at 1.5 T," *Medical Physics*, vol. 12, no. 5, pp. 604–607, 1985.

[171] Y. Zur and S. Stokar, "A phase-cycling technique for canceling spurious echoes in NMR imaging," *Journal of Magnetic Resonance (1969)*, vol. 71, no. 2, pp. 212–228, 1987.

[172] X. Yan, R. Xue, and X. Zhang, "A monopole/loop dual-tuned RF coil for ultrahigh field MRI.," *Quantitative imaging in medicine and surgery*, vol. 4, no. 4, pp. 225–31, 2014.

[173] A. Webb, "Dielectric materials in magnetic resonance," *Concepts in Magnetic Resonance Part A*, vol. 38A, no. 4, pp. 148–184, 2011.

[174] T. Neuberger, V. Tyagi, E. Semouchkina, M. Lanagan, A. Baker, K. Haines, and A. Webb, "Design of a ceramic dielectric resonator for NMR microimaging at 14.1 tesla," *Concepts in Magnetic Resonance Part B: Magnetic Resonance Engineering*, vol. 33B, no. 2, pp. 109–114, 2008.

[175] K. Haines, T. Neuberger, M. Lanagan, E. Semouchkina, and A. Webb, "High Q calcium titanate cylindrical dielectric resonators for magnetic resonance microimaging," *Journal of Magnetic Resonance*, vol. 200, no. 2, pp. 349–353, 2009.

[176] X. Zhang, K. Ugurbil, and W. Chen, "Microstrip RF surface coil design for extremely high-field MRI and spectroscopy," *Magnetic Resonance in Medicine*, vol. 46, no. 3, pp. 443–450, 2001.

[177] C. Hilbert, J. Clarke, T. Sleator, and E. L. Hahn, "Nuclear quadrupole resonance detected at 30 MHz with a dc superconducting quantum interference device," *Applied Physics Letters*, vol. 47, no. 6, pp. 637–639, 1985.

[178] Y.-W. Kim, E. E. Magnuson, and D. C. Skvoretz, "Active Q-damping sub-system using nuclear quadrupole resonance and nuclear magnetic resonance for improved contraband detection," 2000.

[179] W. Everitt, "Output Networks for Radio-Frequency Power Amplifiers," *Proceedings of the IRE*, vol. 19, no. 5, pp. 723–737, 1931.

[180] F. D. Doty, "Probe Design and Construction," *eMagRes*, 2007.

[181] J. T. Vaughan, H. P. Hetherington, J. O. Otu, J. W. Pan, and G. M. Pohost, "High frequency volume coils for clinical NMR imaging and spectroscopy," *Magnetic Resonance in Medicine*, vol. 32, no. 2, pp. 206–218, 1994.

[182] A. Purea, T. Neuberger, and A. Webb, "Simultaneous NMR microimaging of multiple single-cell samples," *Concepts in Magnetic Resonance*, vol. 22B, no. 1, pp. 7–14, 2004.

[183] F. D. Doty, G. Entzminger, J. Kulkarni, K. Pamarthy, and J. P. Staab, "Radio frequency coil technology for small-animal MRI," *NMR in Biomedicine*, vol. 20, no. 3, pp. 304–325, 2007.

[184] D. Seeber, J. Jevtic, and A. Menon, "Floating shield current suppression trap," *Concepts in Magnetic Resonance*, vol. 21B, no. 1, pp. 26–31, 2004.

[185] R. F. Lee, R. O. Giaquinto, and C. J. Hardy, "Coupling and decoupling theory and its application to the MRI phased array," *Magnetic Resonance in Medicine*, vol. 48, no. 1, pp. 203–213, 2002.

[186] C. Constantinides and S. Angeli, "Elimination of mutual inductance in NMR phased arrays: The paddle design revisited," *Journal of Magnetic Resonance*, vol. 222, pp. 59–67, 2012.

[187] B. K. Li, H. Wang, A. Trakic, C. Engstrom, E. Weber, and S. Crozier, "An orthogonal-based decoupling method for MRI phased array coil design.," *NMR in biomedicine*, vol. 25, no. 6, pp. 835–42, 2012.

[188] K. L. Moody, N. A. Hollingsworth, F. Zhao, J.-F. Nielsen, D. C. Noll, S. M. Wright, and M. P. McDougall, "An eight-channel T/R head coil for parallel transmit MRI at 3T using ultra-low output impedance amplifiers," *Journal of Magnetic Resonance*, vol. 246, pp. 62–68, 2014.

[189] M. Schmitt, A. Potthast, D. E. Sosnovik, J. R. Polimeni, G. C. Wiggins, C. Triantafyllou, and L. L. Wald, "A 128-channel receive-only cardiac coil for highly accelerated cardiac MRI at 3 Tesla.," *Magnetic resonance in medicine*, vol. 59, no. 6, pp. 1431–9, 2008.

[190] Q.-X. Chu and H. Wang, "A Compact Open-Loop Filter With Mixed Electric and Magnetic Coupling," *IEEE Transactions on Microwave Theory and Techniques*, vol. 56, no. 2, pp. 431–439, 2008.

[191] P. Villa, J. J. Vaquero, S. Chesnick, and J. Ruiz-Cabello, "Probe efficiency improvement with remote and transmission line tuning and matching,"

[192] V. D. Kodibagkar and M. S. Conradi, "Remote Tuning of NMR Probe Circuits," *Journal of Magnetic Resonance*, vol. 144, no. 1, pp. 53–57, 2000.

[193] T. Peck, R. Magin, and P. Lauterbur, "Design and Analysis of Microcoils for NMR Microscopy," *Journal of Magnetic Resonance, Series B*, vol. 108, no. 2, pp. 114–124, 1995.

[194] Q. X. Yang, J. Wang, X. Zhang, C. M. Collins, M. B. Smith, H. Liu, X.-H. Zhu, J. T. Vaughan, K. Ugurbil, and W. Chen, "Analysis of wave behavior in lossy dielectric samples at high field," *Magnetic Resonance in Medicine*, vol. 47, no. 5, pp. 982–989, 2002.

[195] Y. Li, Z. Xie, Y. Pang, D. Vigneron, and X. Zhang, "ICE decoupling technique for RF coil array designs.," *Medical physics*, vol. 38, no. 7, pp. 4086–93, 2011.

[196] G. Duensing, H. Brooker, and J. Fitzsimmons, "Maximizing Signal-to-Noise Ratio in the Presence of Coil Coupling," *Journal of Magnetic Resonance, Series B*, vol. 111, no. 3, pp. 230–235, 1996.

[197] E. B. Joffe and K. Lock, "Grounding in Wiring Circuits and Cable Shields," in *Grounds for Grounding*, pp. 469–587, Hoboken, NJ, USA: John Wiley & Sons, Inc.

[198] M. Guéron and J. Leroy, "NMR of water protons. The detection of their nuclear-spin noise, and a simple determination of absolute probe sensitivity based on radiation damping," *Journal of Magnetic Resonance (1969)*, vol. 85, no. 1, pp. 209–215, 1989.

[199] J. P. Hornak, J. Szumowski, and R. G. Bryant, "Magnetic field mapping," *Magnetic Resonance in Medicine*, vol. 6, pp. 158–163, 1988.

[200] L. I. Sacolick, F. Wiesinger, I. Hancu, and M. W. Vogel, "B1 mapping by Bloch-Siegert shift," *Magnetic Resonance in Medicine*, vol. 63, no. 5, pp. 1315–1322, 2010.

[201] C. H. Cunningham, J. M. Pauly, and K. S. Nayak, "Saturated double-angle method for rapid B1+ mapping.," *Magnetic resonance in medicine : official journal of the Society of Magnetic Resonance in Medicine / Society of Magnetic Resonance in Medicine*, vol. 55, no. 6, pp. 1326–33, 2006.

[202] F. . Zelaya, W. U. Roffmann, S. Crozier, S. Teed, D. Gross, and D. M. Doddrell, "Direc visualisation of $B_1$ inhomogeneity by flip angle dependency," *Magnetic Resonake Imaging*, vol. 15, no. 4, pp. 497–504, 1997.

[203] J. F. Schenck, H. R. Hart, T. H. Foster, W. A. Edelstein, P. A. Bottomley, R. W. Redington, C. J. Hardy, R. A. Zimmerman, and L. T. Bilaniuk, "Improved MR imaging of the orbit at 1.5 T with surface coils.," *AJR. American journal of roentgenology*, vol. 144, no. 5, pp. 1033–6, 1985.

[204] P. Mansfield and P. Morris, "NMR Imaging in Biomedicine," *London: Academic Press*, 1982.

[205] A. Tannús and M. Garwood, "Adiabatic Pulses," *NMR in Biomed*, vol. 10, pp. 423–434, 1997.

[206] L. Ciobanu, A. Webb, and C. Pennington, "Magnetic resonance imaging of biological cells," *Progress in Nuclear Magnetic*, 2003.

[207] G. Finch, A. Yilmaz, and M. Utz, "An optimised detector for in-situ high-resolution NMR in microfluidic devices," *Journal of Magnetic Resonance*, vol. 262, pp. 73–80, 2016.

[208] R. Subramanian, M. Lam, and A. Webb, "RF Microcoil Design for Practical NMR of Mass-Limited Samples," *Journal of Magnetic Resonance*, vol. 133, pp. 227–231, 1998.

[209] M. Grisi, G. Gualco, and G. Boero, "A broadband single-chip transceiver for multi-nuclear NMR probes," *Review of Scientific Instruments*, vol. 86, no. 4, p. 044703, 2015.

[210] D. L. Olson, T. L. Peck, A. G. Webb, R. L. Magin, and J. V. Sweedler, "High-Resolution Microcoil $^1$H-NMR for Mass-Limited, Nanoliter-Volume Samples," *Science*, vol. 270, pp. 1967–1970, 1995.

[211] J. Anders, G. Chiaramonte, P. SanGiorgio, and G. Boero, "A single-chip array of NMR receivers.," *Journal of magnetic resonance (San Diego, Calif. : 1997)*, vol. 201, pp. 239–49, 2009.

[212] M. Woytasik, J.-P. Grandchamp, E. Dufour-Gergam, J.-P. Gilles, S. Megherbi, E. Martincic, H. Mathias, and P. Crozat, "Two- and three-dimensional microcoil fabrication process for three-axis magnetic sensors on flexible substrates," *Sensors and Actuators A: Physical*, vol. 132, no. 1, pp. 2–7, 2006.

[213] J. Bart, "Optimization of stripline-based microfluidic chips for high-resolution NMR," *Journal of Magnetic Resonance*, vol. 201, pp. 175–185, 2009.

[214] P. J. M. van Bentum, J. W. G. Janssen, A. P. M. Kentgens, J. Bart, and J. G. E. Gardeniers, "Stripline probes for nuclear magnetic resonance.," *Journal of magnetic resonance (San Diego, Calif. : 1997)*, vol. 189, pp. 104–13, 2007.

[215] M. Sharma, G. Janssen, J. Leggett, A. Kentgens, and P. van Bentum, "Rapid-melt Dynamic Nuclear Polarization," *Journal of Magnetic Resonance*, vol. 258, pp. 40–48, 2015.

[216] C. Massin, F. Vincent, A. Homsy, K. Ehrmann, G. Boero, and R. Popovic, "Planar microcoil-based microfluidic NMR probes," *Journal of Magnetic Resonance*, vol. 164, pp. 242–255, 2003.

[217] H. Ryan, S.-H. Song, A. Zaß, J. Korvink, and M. Utz, "Contact-less NMR Spectroscopy on a Chip," *Analytical Chemistry*, vol. 84, pp. 3696–3702, 2012.

[218] K. Ehrmann, N. Saillen, F. Vincent, M. Stettler, M. Jordan, F. M. Wurm, P.-A. Besse, and R. Popovic, "Microfabricated solenoids and Helmholtz coils for NMR spectroscopy of mammalian cells," *Lab on a Chip*, vol. 7, p. 373, 2007.

[219] K. Kratt, V. Badilita, T. Burger, J. G. Korvink, and U. Wallrabe, "A fully MEMS-compatible process for 3D high aspect ratio micro coils obtained with an automatic wire bonder," *Journal of Micromechanics and Microengineering*, vol. 20, p. 015021, 2010.

[220] N. Wu, T. Peck, A. Webb, L. Magin, and J. Sweedler, "1H-NMR Spectroscopy on the Nanoliter Scale for Static and On-Line Measurements," *Anal. Chem.*, vol. 66, pp. 3849–3857, 1994.

[221] C. Massin, *Microfabricated planar coils in nuclear magnetic resonance*. PhD thesis, 2004.

[222] C. Massin, G. Boero, F. Vincent, J. Abenhaim, P. Besse, and R. Popovic, "High-Q factor RF planar microcoils for micro-scale NMR spectroscopy," *Sensors and Actuators A: Physical*, vol. 97-98, pp. 280–288, 2002.

[223] K. Göbel, O. Gruschke, J. Leupold, J. Kern, C. Has, L. Bruckner-Tuderman, J. Hennig, D. Elverfeldt, N. Baxan, and J. Korvink, "Phased-array of microcoils allows mr microscopy of ex vivo human skin samples at 9.4 t," *Skin Research and Technology*, vol. 21, no. 1, pp. 61–68, 2015.

[224] Y. Zhu, C. Chen, Z. Wilson, I. Savukov, and C. Hilty, "Milli-tesla NMR and spectrophotometry of liquids hyperpolarized by dissolution dynamic nuclear polarization," *Journal of Magnetic Resonance*, vol. 270, pp. 71–76, 2016.

[225] "Development of low field nuclear magnetic resonance microcoils," *Review of Scientific Instruments*, vol. 76, p. 024101, 2005.

[226] M. Grisi, F. Vincent, B. Volpe, R. Guidetti, N. Harris, A. Beck, and G. Boero, "NMR spectroscopy of single sub-nL ova with inductive ultra-compact single-chip probes.," *Scientific reports*, vol. 7, 2017.

[227] T. Peck, R. Magin, J. Kruse, and M. Feng, "NMR microspectroscopy using 100 $\mu$m planar RF coils fabricated on gallium arsenide substrates," *IEEE Transactions on Biomedical Engineering*, vol. 41, pp. 706–709, 1994.

[228] B. Sorli, J. F. Chateaux, M. Pitaval, H. Chahboune, B. Favre, A. Briguet, and P. Morin, "Micro-spectrometer for NMR: analysis of small quantities in vitro," *Measurement Science and Technology*, vol. 15, pp. 877–880, 2004.

[229] "XXI. The magnetic susceptibilities of copper, silver and gold and errors in the Gouy method," *Philosophical Magazine*, vol. 1, pp. 223–236, 1956.

[230] M. Walper, J. Leupold, L. Dragonu, D. Elvefeld, Z. Maxim, and U. Wallrabe, "Magnetic properties of materials for MR engineering, micro-MR and beyond," *Journal of Magnetic Resonance*, vol. 242, pp. 233–242, 2014.

[231] F. D. Doty, G. Entzminger, and Y. A. Yang, "Magnetism in high-resolution NMR probe design. I: General methods," *Concepts in Magnetic Resonance*, vol. 10, pp. 133–156, 1998.

[232] S. Metz, R. Holzer, and P. Renaud, "Polyimide-based microfluidic devices," *Lab on a Chip*, vol. 1, 2001.

[233] D. Kang, Y.-S. Kim, G. Ornelas, M. Sinha, K. Naidu, and T. Coleman, "Scalable Microfabrication Procedures for Adhesive-Integrated Flexible and Stretchable Electronic Sensors," *Sensors*, vol. 15, pp. 23459–23476, 2015.

[234] S. Dayeh, D. Butler, and Z. Celik-Butler, "Micromachined infrared bolometers on flexible polyimide substrates," vol. 118, pp. 49–56, 2005.

[235] A. Mahmood, "Device level vacuum packaged microbolometers on flexible sybstrates," 2006.

[236] E. Koch and A. Dietzel, "Skin attachable flexible sensor array for respiratory monitoring," *Sensors and Actuators A: Physical*, vol. 250, pp. 138–144, 2016.

[237] O. Cherry, *Fabrication of an Atom Chip for Rydberg Atom-Metal Surface Interaction Studies*. PhD thesis, University of Waterloo, 2007.

[238] M. Aslam, "Bulk etching of silicon wafer and development of a polyimide membrane," *Journal of Physics: Conference Series*, vol. 439, p. 012029, 2013.

[239] B. Cristofori-Armstrong, M. S. Soh, S. Talwar, D. L. Brown, J. D. O. Griffin, Z. Dekan, J. L. Stow, G. F. King, J. W. Lynch, and L. D. Rash, "Xenopus borealis as an alternative source of oocytes for biophysical and pharmacological studies of neuronal ion channels," *Scientific Reports*, vol. 5, p. 14763, 2015.

[240] M. Ahmed and D. P. Butler, "Flexible substrate and release layer for flexible MEMS devices," *Journal of Vacuum Science & Technology B, Nanotechnology and Microelectronics: Materials, Processing, Measurement, and Phenomena*, vol. 31, p. 050602, 2013.

[241] J. K. Luo, D. P. Chu, A. J. Flewitt, S. M. Spearing, N. A. Fleck, and W. I. Milne, "Uniformity Control of Ni Thin-Film Microstructures Deposited by Through-Mask Plating," *Journal of The Electrochemical Society*, vol. 152, p. C36, 2005.

[242] P. Rai-Choudhury, *Handbook of microlithography, micromachining, and microfabrication*. SPIE Optical Engineering Press, 1997.

[243] A. Yaradanakul, D. Butler, and Z. Celik-Butler, "Uncooled infrared microbolometers on a flexible substrate," *IEEE Transactions on Electron Devices*, vol. 49, pp. 930–933, 2002.

[244] H. Chandra, Spencer A., S. Oberloier, N. Bihari, J. Gwamuri, and J. Pearce, *Open-Source Automated Mapping Four-Point Probe*, vol. 10. Molecular Diversity Preservation International, 2008.

[245] J. Marques and R. Bowtell, "Application of a fourier-based method for rapid calculation of field inhomogeneity due to spatial variation of magnetic susceptibility," *Concepts in Magnetic Resonance Part B: Magnetic Resonance Engineering*, vol. 25, no. 1, pp. 65–78, 2005.

[246] J. Sedlacik, A. Rauscher, and J. R. Reichenbach, "Quantification of modulated blood oxygenation levels in single cerebral veins by investigating their mr signal decay," *Zeitschrift für Medizinische Physik*, vol. 19, no. 1, pp. 48–57, 2009.

[247] C. Ziener, W. Bauer, and P. Jakob, "Frequency distribution and signal formation around a vessel," *Magnetic Resonance Materials in Physics, Biology and Medicine*, vol. 18, no. 4, pp. 225–230, 2005.

[248] J. Anders, G. Chiaramonte, P. SanGiorgio, and G. Boero, "A single-chip array of NMR receivers," *Journal of Magnetic Resonance*, vol. 201, pp. 239–249, 2009.

[249] J. Stocker, T. Peck, A. Webb, M. Feng, and R. Magin, "Nanoliter volume, high-resolution NMR microspectroscopy using a 60-$\mu$m planar microcoil," *IEEE Transactions on Biomedical Engineering*, vol. 44, no. 11, pp. 1122–1127, 1997.